Beyond vanilla new physics at the LHC

Humberto Reyes Gonzalez

To cite this version:

Humberto Reyes Gonzalez. Beyond vanilla new physics at the LHC. High Energy Physics - Phenomenology [hep-ph]. Université Grenoble Alpes [2020-..], 2020. English. NNT : 2020GRALY037 . tel-03144142

HAL Id: tel-03144142
https://tel.archives-ouvertes.fr/tel-03144142

Submitted on 17 Feb 2021

UGA
Université
Grenoble Alpes

THÈSE

Pour obtenir le grade de

DOCTEUR DE L'UNIVERSITÉ DE GRENOBLE

Spécialité : **Physique Subatomique et Astroparticules**

Arrêté ministériel : 25 mai 2016

Présentée par

Humberto REYES GONZÁLEZ

Thèse dirigée par **Sabine KRAML, DR1, Université Grenoble Alpes**

préparée au sein **Laboratoire Laboratoire de Physique Subatomique et Cosmologie**
dans **l'École Doctorale Physique**

Au-delà de la nouvelle physique standard au LHC

Beyond vanilla new physics at the LHC

Thèse soutenue publiquement le **8 octobre 2020**,
devant le jury composé de :

Madame GENEVIEVE BELANGER
DIRECTRICE DE RECHERCHE, CNRS DELEGATION ALPES, Président
Monsieur BENJAMIN FUKS
PROFESSEUR DES UNIVERSITES, SORBONNE UNIVERSITE -PARIS, Rapporteur
Monsieur TILMAN PLEHN
PROFESSEUR, UNIVERSITE DE HEIDELBERG, Rapporteur
Madame MARIE-HELENE GENEST
CHARGE DE RECHERCHE HDR, CNRS DELEGATION ALPES, Examinatrice
Madame ANA MARGARIDA TEIXEIRA
CHARGE DE RECHERCHE HDR, CNRS DELEGATION RHONE AUVERGNE, Examinatrice
Monsieur FELIX BRÜMMER
MAITRE DE CONFERENCES HDR, UNIVERSITE DE MONTPELLIER, Examinateur

If there's an answer to the questions we feel bound to ask
Show yourself destroy our fears release your mask...
We'll just keep on trying
Till the end of time.

Queen, *Innuendo.* Innuendo, Sony/ATV Music Publishing LLC (1991).

Acknowledgments.

I start by acknowledging non other than Sabine Kraml. Thank you for taking the bold chance of accepting me as your student. I appreciate you always giving the extra mile guiding, supporting and promoting my career. I couldn't have asked for a better mentor. Ah!, and thanks also for the hikes, the ski lessons, the climbing lessons...

I would also like to acknowledge the collaborators with whom I worked with and/or have shared stimulating discussions. In particular I'm grateful to Mark Goodsell, Sophie Williamson and Guillaume Chalons from the DG papers, to the `SModelS` collaboration, specially Wolfgang Waltenberger and Andre Lessa, and to the people I collaborated during the Les Houches 'Physics at TeV colliders' workshop 2019.

My stay at the LPSC Grenoble was always pleasant. I appreciate the nice ambient provided by the members of the theory group Christopher, Jèrêmy, Mariane, Ingo, Sabine, Aurélien, Killian, Kseniia, Selim, Mohammad, Pierre-Henri, Rola, Hoa, Gaël, Chloe, Lohan, Flora and Susanne. In particular, I'm thankful to Mohammad. I enjoyed our walks along the river, playing football and chatting about life. My appreciation also goes to David Maurin, for making sure that my PhD studies where always on track, and for all the rides to the football field, of course!

I'm also thankful to the members of my jury Geneviève Bélanger, Marie-Hélène Genest, Ana Teixeira, Felix Brümmer and to Benjamin Fuks and Tilman Plehn who also acted as referees.

I acknowledge the financial support provided by Consejo Nacional de Ciencia y Tecnología CONACYT under scholarship no. 291169. I also acknowledge the support given by the IN2P3 project 'Théorie LHCiTools' for attending schools and conferences.

I'm thankful to my parents for always cheering me from home. Since the beginning, you have been an example for me and have given me the tools I needed to get here. Thank you for showing me the way.

Last but not least, I'm forever thankful to you, Dalia. You have always supported me and encouraged me to follow my dreams. For dare moving halfway around the world with me. Finally, thank you for sharing the adventure of life with me. It has been an amazing journey with you.

Contents

Chapter 1

Introduction.

The summer of 2012 marked an important milestone on the history of the Large Hadron Collider (LHC). The ATLAS and CMS collaborations announced the observation of a resonance at 125 GeV in the di-photon spectra, corresponding to the resonant production of a scalar particle, with a 5σ confidence level. The Higgs boson had been discovered. Thus, the field spectra of the Standard Model (SM) of particle physics was completed. Since then, 8 years have passed and the SM remains unchallenged at the LHC. So far, all the observations from the ATLAS and CMS detectors remain faithful to the SM predictions, while no definite signs of deviations have been detected. However, we have good reasons to believe that the SM is not the final picture. Intrinsically, there are several phenomena raising questions for which we would like to find an answer for, such as why are the electroweak scale and Planck scale so far apart?, are the conservation of baryon and lepton numbers just accidental symmetries?, why is there no CP (Charge-Parity) violation in the QCD (Quantum Chromodynamics) sector?, etc. Furthermore, there are astrophysical and cosmological observations that lead us to believe that there is new physics beyond the SM: the matter-antimatter asymmetry, the accelerated expansion of the Universe and dark matter. Finally, the SM only describes three of the four fundamental forces we know, as it doesn't include gravity.

To solve the intrinsic puzzles of the SM and describe the observations that the SM can't, a plethora of Beyond Standard Model (BSM) theories have been proposed. So far, the most theoretically compelling ones, are the theories drawn from the supersymmetry paradigm, in which for every bosonic field a fermionic counterpart exists and viceversa. They can be invoked to address the majority, if not all, of the main SM problems and are predicted to be observed at the LHC. There is also a large number of non-supersymmetric extensions, such as theories with extra dimensions, multi-Higgs models and theories with new internal symmetries, which are often designed to describe specific SM problems. All together, the BSM theories form a vast sea of possibilities that should be thoroughly explored, as new physics can be found in any corner.

An extensive program of searches for new physics has been put forward at the LHC, aiming to cover new physics theories as much as possible. However, the vastness of BSM theories and scenarios within, makes it an impossible endeavor, for the experimental collaborations, to pursue on their own. Thus, a close communication between theorists and experimenters is necessary. This encourages new ideas on where to look for new physics. Furthermore, it promotes the preservation of the experimental results in such a way that they can be reinterpreted in the context of beyond vanilla or not yet though of theories. With this spirit, the LHC reinterpretation forum was funded as a joint effort between experimenters and theorist aimed to make the most of the LHC legacy.

It is within the framework of reinterpretation of LHC results that this thesis unfolds. On the phenomenological side, it explores the sensitivity of current LHC results to the Minimal Dirac

Gaugino Model (MDGSSM), a beyond vanilla SUSY theory where the gauginos are promoted to Dirac states[1]. Interestingly, the MDGSSM presents a considerably different phenomenology compared to SUSY models already considered at the LHC. The corresponding work involved the re-interpretation, following different approaches, of a variety of LHC analyses. On the tool development side, it regards the new developments of the `SModelS` reinterpretation tool presented in its version 1.2. My main contribution to this version was the development of a Interactive Plots Maker, to facilitate the comparison of `SModelS` output. Moreover, in this thesis we discuss the implementation of a tool to determine if signal regions (SRs) from different analyses are statistically independent from each other and hence, can be trivially combined.

On another note, we are living on a global era of big data which has translated in the development of sophisticated data science techniques. The interest on them has undoubtedly propagated to the field of particle physics. In both the collider and astrophysics fronts, a humongous amount of data is collected, which is utterly complicated to interpret without relying on modern data science. Thus, experimental collaborations have been increasingly adopting (and developing) modern machine learning (ML) techniques for their studies. The need to do the same in High Energy Physics (HEP) phenomenology is becoming ever more stringent. For one, to be able to properly interpret experimental results, a good understanding of the sophisticated techniques experimenters employ, is required. Furthermore, as pointed out, the LHC reinterpretation framework has as goal to cover the vast variety of proposed BSM theories. Most of this theories are made of a complicated interplay between their free parameters. The introduction of ML can definitely upgrade the exploration of such parameter spaces. Moreover, ML reopens the possibility of following the inverse problem. That is, to pursue data-driven searches for anomalies in experimental results, which could be later interpreted in the context of a BSM theory.

This thesis then also describes the first steps taken by the author, into the emergent subject of ML in HEP phenomenology. In concrete, I worked on implementing a neural network to accurately predict, with an estimated uncertainty, the production cross sections of the inert doublet Model. First results of this project were presented as part of contribution 22 of the New Physics Working Group Report of the Les Houches 2019 Physics at TeV Colliders workshop [1]. In there we also discuss the importance of providing uncertainties on ML predictions and on recommendations for sharing all the material involved in the production of ML applications. Furthermore, we present more examples of ML classifiers and regressors applied to HEP phenomenology.

The present manuscript is structured as follows. Chapter 2 serves as an introduction to the SM and our present quest to extend it. Regarding our motivation to go beyond the SM, we give special attention to dark matter, while in the new physics theory front, we emphasize on supersymmetry. Then, Chapter 3 presents the simplified model framework for interpreting LHC results, followed by a description of the main LHC analysis reinterpretation approaches. Chapter 4 starts by describing the general concept of the simplified model re-interpretation tool `SModelS`, to then focus on the developments presented in its most recent version, v1.2. In Chapter 5 we go beyond vanilla and explore the MDGSSM in the context of the LHC reinterpretation framework. In the first section we provide an introduction to the model and our motivations to study it. In the second, we present constraints on the gluinos and squarks of the model derived from the reinterpretation of appropriate LHC analyses. In the third, we turn to the electroweakino sector. We present our study of the collider phenomenology of the electroweakino parameter space where the lightest neutralino is a non-overabundant dark matter candidate that evades constraints from the DM direct detection searches, LEP and LHC Higgs measurements. The study was divided in two classes of scenarios: those with only promptly decaying electroweakinos and those with long lived charginos and/or neutralinos. This is followed by Chapter 6 where we discuss the implementation of TACO (Testing Analyses' COrrelations), a tool to determine the orthogonality

---

[1] As opposed to the minimal realization of a supersymmetric SM, where gauginos are Majorana particles.

of SRs from different LHC analyses. Afterwards, in Chapter 7 we discuss applications of ML regressors and classifiers in HEP phenomenology. Finally, the general concluding remarks are provided in Chapter 8.

Chapter 2

The journey beyond the Standard Model.

Ever since the times of the ancient Greek philosophers, *symmetries* were considered essential for the description of Nature. For the Pythagoreans, everything could be described by combinations of geometrical figures. From Aristotle to the dawn of the Renaissance, it was established that the movement of ethereal objects around the earth (and afterwards around the Sun) had to be composed of spherical shapes. In those times, complicated systems of perfect spheres were devised to accurately describe the dynamics of the Solar system. It was only until the beginning of the XVII century that Kepler realized, after a careful study of the data gathered by Tycho de Brahe, that planets followed elliptic trajectories around the Sun. Around the same time, the modern vision of *symmetries* in Nature started to emerge, as Galileo established a group of translational transformations following the idea that *the laws of Nature must be the same regardless of the observer*. The Galilean transformations were sufficient to leave *invariant* the laws of classical physics regardless of the observer. However, the invariance under these transformations didn't hold for the theory of electromagnetism established in the XIX, since Galileo didn't accounted for the behavior of physics near the speed of light. Hendrik Lorentz, thus came up of with an improved group of transformations by which the laws of physics at high speeds were respected, regardless of the reference frame, while still comprising classical motions. This, together with the discovery of the constant speed of light, led to Einstein's postulation of the Theory of Special Relativity. Following from this notion of symmetry, Emmy Noether proved in her theorem that *for every differentiable symmetry of the action of a physical system has a corresponding conservation law*. This translates into the outstanding fact that the conserved laws of Nature can be described by continuous symmetric groups. Noether's theorem was essential in the establishment of the current Standard Model of Particle Physics (SM), which describes the fundamental components of known matter and its interactions. And furthermore, it remains indispensable for any new description of the fundamental laws of physics.

In Sec. 2.1 we provide a condensed description of the SM and the symmetries it is based on (for more comprehensive reviews see e.g [2, 3]). This is followed by Sec. 2.2 describing the main theoretical and observational motivations for journeying beyond the SM. Then, an overview on BSM theories is given in Sec. 2.3, with emphasis on supersymmetry (see e.g. [4, 5, 6] for more on BSM theories). Finally, we present in Sec. 2.4 the LHC, our main machine to study the SM and its possible extensions.

2.1 The Standard Model of Particle Physics.

The SM is a Quantum Field Theory (QFT) based on a combination of global and internal symmetries. The global symmetries act on the coordinates of space-time. They include rotations, translations and boosts and form the Poincaré group. Furthermore, they are connected to the conservation of mass-energy, linear momentum and angular momentum. The internal symmetries are related to the gauge invariance of the SM under the $SU(3) \times SU(2)_L \times U(1)_Y$ group. The $SU(2)_L \times U(1)_Y$ is spontaneously broken into $U(1)_{EM}$ at the electroweak scale by the Brout-Englert-Higgs mechanism. These internal symmetries are connected to the conservation of strong, weak and electromagnetic charges. The field content of the SM, shown in 2.1, can be divided in fermionic (spin 1/2), vector bosonic (spin 1) and scalar bosonic (spin 0) parts. The fermionic part is comprised by three families with identical quantum numbers but distinguishable masses. Each family is made of four fermions, two quarks and two leptons. The quarks are colored, i.e. charged under strong interactions; one has electromagnetic charge 2/3 (up-quark) and the other -1/3 (down-quark). The two leptons are colorless; one with electromagnetic charge -1 (charged lepton) and one 0 (neutrino). Each fermion has two irreducible representations of the Lorentz group, known as chiralities, described together as Dirac spinors. Fermions are then left-handed (LH) or right-handed (RH), according to their chirality. The LH quarks and leptons are doublets under $SU(2)_L$, while the RH counterparts are singlets. The exception is the neutrino, since only their LH chirality has been observed so far (more on neutrinos below). The bosonic part comprehends the gauge bosons that mediate the three fundamental interactions associated with the gauge groups of the SM. The gluons g propagate the strong interactions, the W^+, W^- and Z^0 the weak interactions and the photon γ the electromagnetic one. The Z^0 and γ are a mixture of B and the neutral W^3, as a consequence of the spontaneous electroweak symmetry breaking. Finally, the picture is completed by the scalar part. It is made of a complex scalar Higgs field, which transform as doublet under $SU(2)_L$ and is responsible for the EWSB.

Names	Symbol	$SU(3)$, $SU(2)$, $U(1)_Y$
Quarks	$Q = (u_L, d_L)$	$(\mathbf{3}, \mathbf{2}, 1/6)$
	u_R	$(\mathbf{3}, \mathbf{1}, 2/3)$
(×3 families)	d_R	$(\mathbf{3}, \mathbf{1}, -1/3)$
Leptons	$L = (\nu_{eL}, e_L)$	$(\mathbf{1}, \mathbf{2}, -1/2)$
(×3 families)	e_R	$(\mathbf{1}, \mathbf{1}, 1)$
Higgs	$H = (\phi^+, \phi^0)^T$	$(\mathbf{1}, \mathbf{2}, 1/2)$
Gluons	G	$(\mathbf{8}, \mathbf{1}, 0)$
W boson	$(W^1\ W^2\ W^3)^T$	$(\mathbf{1}, \mathbf{3}, 0)$
B boson	B	$(\mathbf{1}, \mathbf{1}, 0)$

Table 2.1: Field content in the SM.

The mathematical description of the SM fields and their interactions is given by the Lagrangian

$$\mathcal{L}_{\text{SM}} = \mathcal{L}_{\text{G}} + \mathcal{L}_{\text{F}} + \mathcal{L}_{\text{S}} + \mathcal{L}_{\text{Y}}, \tag{2.1}$$

where

$$\mathcal{L}_{\text{G}} = -\frac{1}{4} G^a_{\mu\nu} G^{\mu\nu}_a - \frac{1}{4} W^a_{\mu\nu} W^{\mu\nu}_a - \frac{1}{4} B_{\mu\nu} B^{\mu\nu} \tag{2.2}$$

$$\mathcal{L}_{\text{F}} = i\bar{\chi} \not{D} \chi \tag{2.3}$$

$$\mathcal{L}_{\text{S}} = (D_\mu H)^\dagger (D^\mu H) - V(H) \tag{2.4}$$

$$\mathcal{L}_{\text{Y}} = y_e^{ij}\ \bar{L}_i\ H\ e_{Rj} + y_u^{ij}\ \bar{Q}_i\ \tilde{H}\ u_{Rj} + y_d^{ij}\ \bar{Q}_i\ H\ d_{Rj} + h.c. \tag{2.5}$$

$\mathcal{L}_{\mathrm{G}}$ contains the kinetic terms of the gauge fields, where $G_{\mu\nu}$, $W_{\mu\nu}$ and $B^{\mu\nu}$ are the field strength tensors corresponding to $SU(3)_C$, $SU(2)_{\mathrm{L}}$ and $U(1)_{\mathrm{Y}}$, respectively.

$\mathcal{L}_{\mathrm{F}}$ contains the kinetic terms of the fermionic field. In there, the covariant derivatives D_μ are defined, to ensure gauge invariance, as:

$$D_\mu = \partial_\mu - ig_s \frac{\lambda_a}{2} G^a_\mu - ig \frac{\sigma_j}{2} W^j_\mu - ig' Y B_\mu \tag{2.6}$$

where $\sigma_j, j = 1, 2, 3$ are the Pauli matrices and $\lambda_a, a = 1, ..., 8$ the Gell-Man matrices, representations of the $SU(2)_L$ and $SU(3)_C$ groups, respectively. These gauge invariant terms describe the gauge interactions of the fermions and the Higgs fields.

$\mathcal{L}_{\mathrm{S}}$ describes the scalar sector. The first term is the kinetic term of the Higgs field, while $V(H)$ is the corresponding potential, given by

$$V(H) = \mu^2 H^\dagger H + \lambda (H^\dagger H)^2, \tag{2.7}$$

where μ^2 is the only dimensionful operator in the SM. By setting $\mu^2 < 0$ and $\lambda > 0$, the Higgs potential acquires the well-known 'mexican hat' shape. In this configuration, the minimum of $V(H)$ is a continuous function $\mu^2/2\lambda \equiv v/2$, where v is defined as the vacuum expectation value (vev). The result is the spontaneous breaking of the electroweak symmetry $SU(2)_L \times U(1)_Y$ into the $U(1)_{EM}$ group related to the conservation of the electrical charge. To ensure that the neutral photon remains massless, the minimum of the Higgs potential corresponds to a non-zero v only for the neutral scalar field, thus we choose

$$\langle H \rangle_0 = \begin{pmatrix} 0 \\ \frac{v}{\sqrt{2}} \end{pmatrix}. \tag{2.8}$$

Writing the Higgs potential as fluctuations around the minimum we obtain

$$H = \frac{1}{\sqrt{2}} \begin{pmatrix} \theta_2 + i\theta_1 \\ (v + h) - i\theta_3 \end{pmatrix}. \tag{2.9}$$

After symmetry breaking we end up with one physical scalar h and three massless Goldstone bosons that ultimately yield their corresponding longitudinal degrees of freedom to the $W^\pm$ and Z bosons, trough the Higgs mechanism. As a consequence, the $W^\pm$ and Z bosons acquire masses

$$M_W^2 = \frac{1}{4} g^2 v^2, \quad M_Z^2 = \frac{1}{4} (g'^2 + g^2) v^2. \tag{2.10}$$

Finally, $\mathcal{L}_{\mathrm{Y}}$ describe the *Yukawa* interactions between the scalar and Dirac fields. In there, $\tilde{H} = i\sigma^2 H^*$. After symmetry breaking, the diagonalisation of the Yukawa interactions leads to the fermion masses,

$$m_e = \frac{v}{\sqrt{2}} y_e, \quad m_u = \frac{v}{\sqrt{2}} y_u, \quad m_d = \frac{v}{\sqrt{2}} y_d. \tag{2.11}$$

Note that, the up- and down-type quarks mass matrices are diagonalised separately, by two distinct unitary matrices $V_{u,d}$. This translates into the mismatch between the mass and weak eigenstates of the quarks that give rise to the flavor changing charged-current interactions, described by the Cabbibo-Kobayashi-Maskawa (CKM) matrix $V_{CKM} = V_u V_d^\dagger$.

It is important to note also that neutrinos remain massless in the SM, since they don't have RH components. However, from the observation of neutrino oscillations it follows that they actually have tiny masses. This leads to the definition of an equivalent of the CKM matrix in the lepton sector, the Pontecorvo-Maki-Nakagawa-Sakata (PMNS) matrix. Furthermore, the massiveness of the neutrinos already calls for an extension of the SM. To describe massive LH neutrinos, RH counterparts must be invoked, assuming they are of Dirac nature. The small masses of the LH neutrinos could then be realized trough the see-saw mechanism, which relates them to the large difference between the electroweak and the grand unification scale. Currently, we only know the relation between the masses of the three neutrino generations and not their exact mass scales. Also, we don't know if they are Dirac (like the other fermions) or Majorana particles. Dedicated experiments are being carried out that could potentially lead to the characterization of neutrinos in the upcoming years. Bounds on the mass scales can be derived from cosmological probes [7], the observation of the neutrinoless double beta decay [8] and the tritium beta decay [9]. Finally, the Dirac/Majorana nature of neutrinos could be determined by the negative/positive observation of the neutrinoless double beta decay (see [10] for recent results).

The SM has been a very successful theory. It provides our current best description of the elementary building blocks of Nature and their fundamental interactions (gravity aside). It has shown an outstanding predictive power, with important examples being the precise electroweak measurements on the Z resonance performed by LEP [11] and the detection of the Higgs boson by the ATLAS and CMS LHC experiments [12, 13]. As for today, no deviation from the SM has been observed at any collider experiment, instead we are reaching an ever more precise understanding of the theory.

2.2 Why do we look for new physics?

Despite the large success of the theory, there are clear indications that the SM is not the fundamental description of Nature. The most obvious one is the fact gravity is not incorporated in the SM. However, quantum gravity effects are only expected to be relevant at the Planck scale $M_{PI} \approx 10^{19}$ GeV, 16 orders of magnitude above the reach of the LHC or any foreseen experiment in the near future. Our motivations to extend the SM can be divided as theoretical and observational. The theoretical motivations are not originated by inconsistencies in the SM, per se, but come mainly from a desire of a better understanding of certain aspects of the theory and from questioning its behavior at higher energy scales. They will be discussed in Sec. 2.2.1. The observational ones are actually observed astrophysical and cosmological phenomenons that cannot be explained by the SM. In sec. 2.2.2 we will focus on one of the main ones: Dark Matter.

2.2.1 Theoretical motivations.

- **The hierarchy problem** is often considered as the most dazzling theoretical argument to extend the SM. It refers to the enormous energy distance between the electroweak scale and the Planck scale. The former is dictated by EWSB, after which the physical Higgs boson acquires a mass of 125GeV, through self-interaction. The latter is expected to be the fundamental scale. Hence, we assume that the SM is valid up to a high cut-off scale $\Lambda_{SM} \approx M_P$. This assumption leads to a strong fine-tuning on the Higgs mass, since it receives radiative corrections that grow quadratically with the energy (as opposed to logarithmically like the other particles), from the virtual effects of every particle the field interacts with. For instance, at one loop the contribution from interaction with a Dirac fermion is

  $$\Delta m_H^2 = \frac{y_f^2}{8\pi^2}\Lambda_{SM}, \tag{2.12}$$

  which makes manifest that a high cut-off Λ_{SM} would lead to a Higgs mass a lot larger than the one we observe. Thus, a severe amount of fine-tuning is required so the radiative corrections cancel each other almost completely, without invoking new physics below the Planck scale.

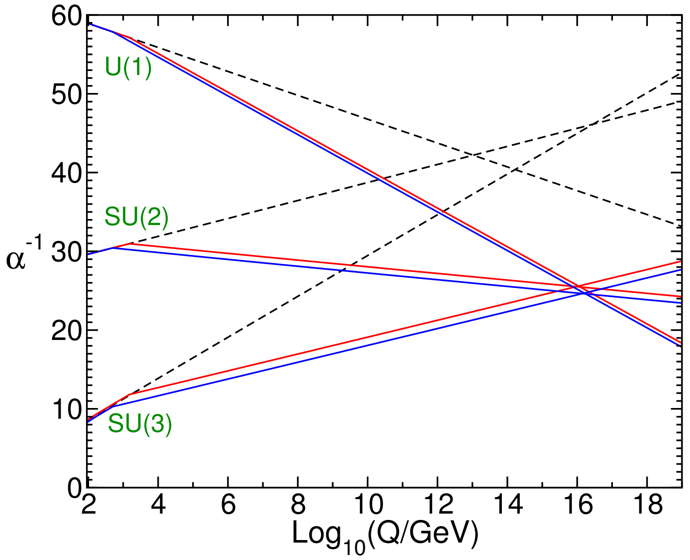

Figure 2.1: Two-loop renormalization group evolution of the SM gauge couplings, from [15]. In here $\alpha_i^{-1} = (g_i^2/4\pi)^{-1})$, where $g_1 = \sqrt{5/3}g'$, $g_2 = g$ and $g_3 = g_s$. The dashed lines correspond to the SM, while the solid lines correspond to MSSM scenarios with a common sparticle mass threshold of 750 GeV (blue) or 2.5 TeV (red).

Note that we have followed the case of the momentum cut-off regularization scheme, which renders the hierarchy problem very apparent. However, even when adopting dimensional regularization, where m_H^2 only receives a correction of the order of the heaviest mass (the top quark, in the SM), contribution cancellations are still necessary. Furthermore, the fact that the Higgs mass is extremely sensitive to higher scales remains, even if it's less apparent.

- **The strong CP problem.** So far there isn't any experimental indication of CP violation in the QCD sector of the SM. However, in the QCD lagrangian a CP violating term of the form $\theta_{\rm QCD} G_{\mu\nu}\tilde{G}^{\mu\nu}$, where $\theta_{\rm QCD}$ is the QCD vacuum angle, should be *naturally* present, since there isn't, a priori, any theoretical restriction to it. Hence, a very small value for $\theta_{\rm QCD}$ (if not zero), is needed to describe the experimental observations. This is known as the strong CP problem. A proposed solution, that avoids fine tuning, is the $U(1)_{PQ}$ Peccei-Quinn theory [14] which involves the addition of a new pseudoscalar particle, the axion.

- **Grand unification.** From the realization of the unification of the electromagnetic and weak forces at the electroweak scale and the unification of electricity and magnetism before that, it became natural to think about the possibility of a larger gauge symmetry group that contained the strong and electroweak forces. Such realization could provide an explanation (missing in the SM) for charge quantisation and for the exact cancellation of proton and electron charges. This is the idea behind the Grand Unification Theories (GUTs), where the strong and electroweak interactions are unified at a higher energy scale. The simplest example of a GUT, that embeds the three gauge groups and fits the known fermionic fields, is the one based on the $SU(5)$ group, described in Sec. 2.3.2. A necessary condition for a GUT is that all the gauge couplings unify at some energy scale. This can be tested by using the renormalization group equations (RGE) to extrapolate the three couplings at high energies. The result corresponds to the dashed lines in 2.1, from which one

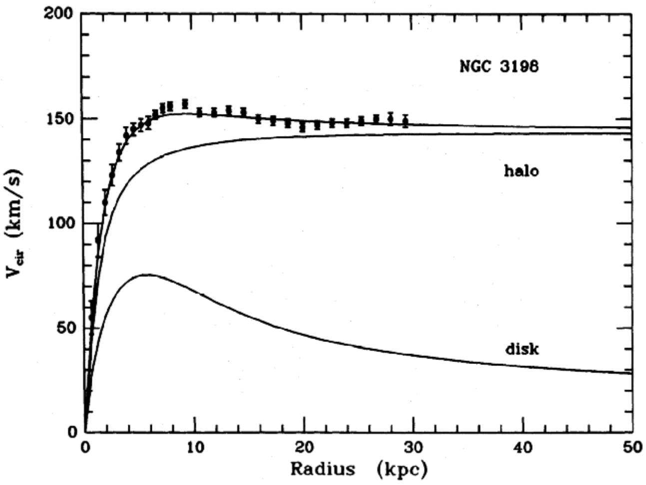

Figure 2.2: Rotation curve of the galaxy NGC-3198, as shown in [23]. The velocity measurements are compared to the expectations from visible matter only ('disk' line) and dark matter only ('halo' line).

concludes that gauge unification is not quite realized within the SM. However, when considering supersymmetric extensions it is possible to achieve unification around the 10^{16}GeV scale. The red and blue lines in 2.1 show this behavior for two scenarios of the minimal supersymmetric extension of the SM.

- **The fermionic sector.** There are several features on the fermionic sector that may hint the presence of underlying symmetries not described by the SM. For starters, the mass and mixing patterns are not well understood. On the one side, there is a large mass difference among the fermions. Between the up quark to the top quark masses there are five orders of magnitude and the difference becomes even more evident when considering the tiny masses of the neutrinos. On the other side, the structure of the CKM and PMNS mixing matrices is non-trivial. In the former, the mixing is small and the matrix is almost diagonal while in the former the mixing angles are fairly large. Furthermore, there are some consistency conditions that seem to be *accidentally* fulfilled. Namely, the baryon and lepton numbers are conserved (allowing stable protons) and all gauge anomalies are canceled.

2.2.2 Observational motivation: Dark Matter.

There is strong cosmological and astrophysical evidence of new physics beyond the SM. On the astrophysical front, we have the observation of a clear matter-antimatter imbalance, implying a baryon asymmetry in the early Universe achieved if the three Sakharov conditions [16] are fulfilled: baryon number violation, C and CP violation and out of equlibrium interactions. While C and CP violation is realised in the weak sector, the violation of B only occurs trough non-perbutavie processes in the SM. The third condition requires the existence of an electroweak transition phase for which the Higgs mass would need to be lighter than the measured value [17]. Thus, the need for new physics. In the cosmological front, the description of accelerated expansion of the Universe requires new physics to avoid relying on a very fined-tuned cosmological constant. But probably the most pressing motivation is the observation of Dark Matter (DM). Thus, we dedicate this section to its description. For more detailed discussions on DM see, for instance, [18, 19, 20, 21, 22]. The first evidence of DM dates back to 1933 [24], when Fritz Zwicky measured an anomalous mass over luminosity ratio from the Coma Cluster, that hinted a large presence of undetected matter. However, it was until the first observations of unexpected galaxy rotation curves in the 1970s [25], that the DM problem acquired notoriety. The phenomenon is well schematized in Fig. 2.3, where the rotation curve of the galaxy NGC-3198 [23] is shown as a function of the galactic radius r. In there, the 'disk' line represents the expected behavior of the rotation curve when taking only the visible matter into account. The visible matter is concentrated in the center of the galaxy, hence the 'disk' line follows a $1/\sqrt{r}$ function for larger r. However, velocity measurements of stars in NGC-3198, depicted by the upper line of Fig. 2.3, show a constant rotation curve outside the center. This behavior can be reproduced when assuming the presence of a constant halo of invisible matter permeating the galaxy, as represented by the 'halo' line. Further astrophysical evidence comes from gravitational lensing, Lymman-α and cluster collisions. The latter is specially important, since it cements the particle DM paradigm. When two clusters collide, the average velocity of baryonic matter should considerably reduce, while the DM halo, decoupled from the baryons and assumed not strongly self-interacting, is expected to remain mostly unaffected by the collision. This was confirmed after studying the Buller Cluster [26]. From X-ray emissions the baryonic matter distribution was inferred and found to be decoupled from the overall mass inferred from weak lensing. This phenomenon can not be explained by the alternative hypothesis of modified gravity, which implies a correlation between the overall mass and the baryonic matter, but is well in compliance with the particle DM paradigm.

Finally, the study of thermal anisotropies in the Cosmological Microwave Background (CMB) measured by the WMAP and Planck satellites [27, 28], provides a very important cosmological evidence of DM, since it allows for an estimation of it's present density. This is possible since the angular power spectrum of the CMB anisotropies depend on the baryonic and non-baryonic matter abundance in the Universe. Within the standard cosmological model ΛCDM, the relic density measured by the Planck collaboration [28] is

$$\Omega h^2 = 0.12 \pm 0.0012 \tag{2.13}$$

where h is the Hubble constant in units 100km/(s·Mpc), and Λ is the ratio between the DM density and the critical density of the Universe ρ_{DM}/ρ_c. When comparing (2.13) with the baryonic matter density $\Omega_b h^2 = .02237 \pm 0.00015$ we find that the DM abundance is more than five times larger than its baryonic counterpart!

From the evidence discussed above little is known about the exact nature of DM. Besides its abundance, we only know that it has to be stable (or at least have a lifetime larger than the age of the Universe), not electrically charged, almost not self-interacting and cold (i.e. not relativistic at keV temperatures to allow structure formation). Nonetheless, this is sufficient to discard any SM explanation. Hence, the need for invoking new massive particles that can conform the DM.

The WIMP scenario.

A very popular hypothesis is that DM is made of Weakly Interacting Massive Particles (WIMPs), i.e. that they are coupled to the SM via weak interactions. It is assumed that the WIMPs were in thermal equilibrium with the SM in the early Universe. Then, as the Universe expands and its temperature drops, the WIMPs decoupled from the thermal bath, since the interaction rate could no longer compensate the expansion. The point where the WIMPs become effectively decoupled from the SM, and their density stabilizes is known as freeze-out. After it, the WIMP becomes non-relativistic for $T < m_\chi$, where T is the temperature and χ a generic WIMP. The remaining DM relic density must then match (or at least not exceed) the observed abundance from eq. (2.13). This is known as the WIMP scenario. It is quite promising since it could imply the sought out new physics at the electroweak scale and could be directly detected via its weak interaction to the SM.

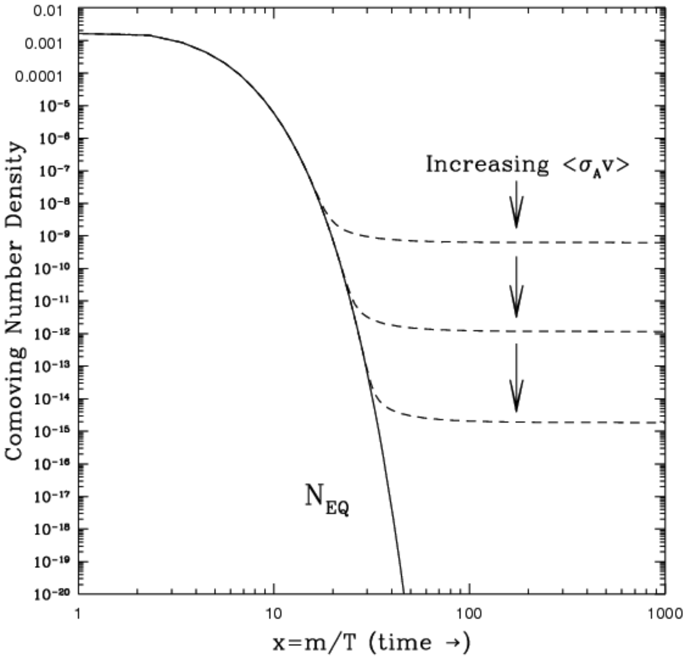

Figure 2.3: Variation of comoving number density of a WIMP in the early Universe as a function off $x = m/T$, as shown in [29].

For a given model with a WIMP component χ, the relic density at freeze-out can be computed from the Boltzmann equation for the number density evolution of χ

$$\frac{\mathrm{d}n}{\mathrm{d}t} = -3Hn_\chi - \langle\sigma_{ann}v\rangle\,(n_\chi^2 - (n_\chi^{eq})^2), \tag{2.14}$$

where n_χ is the DM number density, H the Hubble constant, $\langle\sigma_{ann}v\rangle$ the thermally averaged annihilation cross section and n_χ^{eq} the DM number density at equilibrium. Although there are standard approximate analytical solutions (for example see [20, 30, 31, 32]), in general eq. (2.14) can only be solved numerically. Fortunately, numerical relic density solutions can be efficiently obtained for generic models via dedicated tools such as `MicrOMEGAs` [33, 34] and `MadDM` [35, 36], while a further option for supersymmetric models is `DarkSUSY` [37, 38]. Numerical solutions of the Boltzmann equations are shown in fig. 2.3 as a variation of comoving number density dependent on $x = m_\chi/T$. When freeze-out occurs (dashed lines), the comoving number density becomes constant and corresponds to the DM relic density. The solid line, corresponding to thermal equilibrium, continuously drops to very small values. Furthermore, fig. 2.3 shows that the resulting relic density is proportional to $\langle\sigma_{ann}v\rangle$. The reason is that for larger values of $\langle\sigma_{ann}v\rangle$, the decoupling from thermal bath occurs later, hence the remaining DM abundance is reduced. A common assumption ensuring non-relativistic WIMPs by the time of departure from the thermal bath, is that freeze-out is reached at $T \simeq m_\chi/20$. In that case, the resulting relic density is approximately given by

$$\Omega h^2 \approx \frac{3\times 10^{-27}\mathrm{cm}^3\mathrm{s}^{-1}}{\langle\sigma_{ann}v\rangle}. \tag{2.15}$$

for which the observed abundance is obtained if m_χ is of the order of $\mathcal{O}(100)$ GeV and the WIMP presents typical electroweak couplings. This is known as the 'WIMP miracle'.

Other scenarios.

The WIMP scenario is certainly not the only picture that could explain the observed DM relic abundance. A well-known alternative is that DM is made of Feebly Interacting Massive Particles (FIMPs) that were never in equilibrium with the thermal bath, thus the observed abundance is obtained trough an alternative mechanism known as freeze-in [39]. Qualitatively, it is explained as follows. At temperature T the SM particles are in thermal equilibrium while the DM particle χ interacts very feebly with the thermal bath, so it remains thermally decoupled. Usually, it is assumed that the χ abundance is negligibly small in the early Universe. At first, some χ production is possible trough the small interactions with the bath; however, FIMP production dominantly occurs when T drops below m_χ (provided that χ is heavier than the particles in the bath). The χ abundance then 'freezes-in' with a relic density that increases with the interaction strength of χ with the bath.

The freeze-out and freeze-in can be viewed as opposite mechanisms. In the former, the initial DM abundance is the full thermal number density, which then drops when T reaches below m_χ and the resulting relic density is in inverse proportion to the DM-thermal bath interaction strength. In the latter, the initial abundance is negligible but is enhanced when $T < m_\chi$, and the subsequent stable abundance is directly proportional to the interaction strength with the bath. There are two standard FIMP scenarios, either the FIMP itself is the DM or the frozen-in FIMPs later decay to a lighter DM particle yielding the observed abundance. Finally, like the WIMPs, FIMPs can also have masses of the order of the weak scale, as long as they are lighter than the reheating temperature after inflation and heavier than the keV scale to avoid structure formation constraints. However, their direct detection becomes quite challenging since their SM interaction cross sections may be of orders of magnitude below the sensitivity of current experiments.

A further alternative, is that the DM is solely produced from gravitational interactions. This is well motivated from the fact that DM has indeed only been observed so far trough gravitational effects. Gravitational particle production can be achieved as a consequence of the expansion of the Universe or the time dependence of the cosmic scale factor [40, 41]. For instance, [42] discusses the possibility of particle creation during the transition from the inflation phase to the matter dominated or radiation dominated one. Following that idea, in [43, 44] is proposed that DM is made of super-heavy particles produced at the end of the inflation period. Another possibility, detailed in [45, 46] is that particle production happens during the inflation oscilation regime. In [47] the gravitational production of DM is studied for different inflation models and is shown that for certain combination of models and DM masses the right abundance is obtained. Of course, a purely gravitational nature of DM would impose a big challenge for its detection. Nonetheless, it has been proposed that gravitational production may lead to curvature fluctuations [48] or non-gaussianities [49] detectable in the CMB.

(WIMP) Dark matter detection.

If the DM is actually constituted by WIMPs we should be able to detect them trough their weak interaction with the SM. This could happen directly, by WIMP scattering with nuclei, indirectly by measuring their annihilation products, or they could be produced at a collider.

Direct detection experiments are designed to observe a potential nuclear recoil produced by WIMP scattering off the nucleus. The WIMP-nucleon interaction is often classified as spin dependent (axial vector) or spin independent (scalar). Stronger constraints are derived from the latter as protons and neutrons contribute equally and the total amplitude grows with the atomic mass. In contrast, the former is proportional to $J(J + 1)$, where J is the spin of the nucleus; hence, is not enhanced by a larger number of nuclei. Since the interaction cross sections are expected to be very low, detectors use heavy elements, such as xenon and germanium, as target

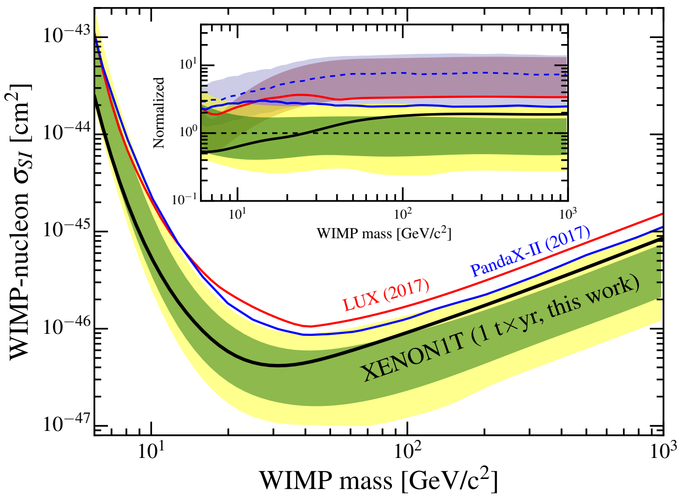

Figure 2.4: 90 % confidence level upper limits on the spin independent WIMP-nucleon cross sections as a function of the WIMP mass, taken from [51].

nuclei to improve their sensitivity. Furthermore, they are often placed underground to suppress background contamination. A compelling review on direct detection experiments is found in [50]. So far, no direct hints for DM have been observed. The current bounds on spin independent WIMP-nucleon cross sections, coming from the XENON1T experiment[51], are shown in Fig. 2.4. Finally, the same experiment has recently reported a possible excess in electronic recoil events, predominantly around the 2-3 keV region [52].

Indirect detection of DM could be realized from different astrophysical messengers such as photons, neutrinos, positrons and antiprotons, product of WIMP self-annihilation. Depending on the type and source of the messenger we could make inferences on the nature of the DM particle. However, compared to direct detection experiments, larger uncertainties are often encountered in indirect detection experiments. The modeling of the background is quite challenging. As an example, a γ-ray excess from the galactic center was observed by Fermi-LAT that would hint the presence of DM [53]. However, further studies showed that it may come from unresolved point sources incompatible with the DM halo description. Although it is still notably that similar excesses have been observed in other galaxies, it is clear that a deeper understanding of all possible sources is required. Nonetheless, there are exceptions. Robust constaints on light WIMPs have been derived by observing photons coming from dwarf spheroidal galaxies [54]. Another promising signal has been recently obtained from observations of the Experiment to Detect the Global EoR Signature (EDGES), an experiment focused on radio detection of hydrogen signatures from the Epoch of Reionization (EoR). In [55] an unexpected deep absorption radiation in the 78MHz was reported. The absorption profile is consistent with the expected 21cm redshifted signal induced by early stars. However the best-fitting amplitude of the signal is more that twice as larger than predicted. So far, the best explanation for the discrepancy seems to be a cooling of the hydrogen gas due to the interaction of DM with baryons.

Finally, DM could also be produced at colliders. This requires DM pair-production associated with an SM particle coming from initial state radiation. The dedicated LHC searches are known as mono-X, where X stands for the associated SM particle. Furthermore, DM production at colliders also opens the opportunity for FIMP detection on the light of Long Lived Particle (LLP) searches. The strategies for detecting DM at colliders will be presented in Sec. 3.1 where we discuss the LHC searches for new physics.

2.3 Theories of new physics.

2.3.1 Supersymmety.

The basic principle of supersymmetry (SUSY) is the presence of fermionic generators that transform the spin of the fields they act on by a factor of 1/2. This means that in a supersymmetric theory, for each boson there must be a fermionic counterpart and viceversa. The motivations for the SUSY framework are manifold. From the purely aesthetical point of view, it is the only way to non-trivially extend the Poincaré space-time symmetries. In the theoretical sense, it provides a natural solution to the hierarchy problem as the fermionic and bosonic contributions to the Higgs mass can cancel each other out. Also, it allows for a unification of the electroweak and strong forces (see Fig. 2.1). Furthermore, it can be invoked to explain unsolved astrophysical observations. Notably, SUSY theories with a conserved R-parity provide excellent DM candidates. And if that is not enough, certain SUSY breaking mediation mechanisms may suggest a connection to gravity at high energy scales whose influence may even be observed at the weak scale. Undoubtedly, this makes SUSY a very appealing framework, thus it has strongly influenced the search for new physics (as we will learn in Sec. 3.1). In this section the basic parts of the supersymetric Lagrangian will be presented, followed by an overview on the Minimal Supersymmetric Standard Model (MSSM) and its possible signals at hadron colliders. Comprehensive reviews on SUSY and the MSSM can be found, for instance, in [15, 56], while [57] is a standard textbook on the subject.

It is convenient to describe the supersymmetric Lagrangian in the superfield formalism where bosonic and fermionic fields are grouped together in single entities. The superspace coordinates are composed by the usual x_μ 'bosonic' space-time coordinates and four 'fermionic' counterparts, described by the anticommuting Grassmann variables θ_a. A superfield $\hat{\mathcal{S}}(x,\theta)$ is then a function of a 4-component bosonic field and a Majorana spinor with an equal number of degrees of freedom. Let us express the Majorana spinors as

$$\psi = \begin{pmatrix} \chi_L \\ -\sigma_2 \chi_L^* \end{pmatrix} \tag{2.16}$$

where χ_L is a left-handed two component Weyl spinor, and $-\sigma_2\chi_L^*$ transform as a right-handed spinor. By defining the usual projection $\psi_{L,R} = P_{L,R}\psi$ a Dirac spinor can be recovered from the combination of the two Majorana spinors.

A minimal supersymmetric prescription requires two kinds of superfields[1]. The first ones are the chiral superfields which describe the fermion and Higgs fields and their respective superpartners. A left-chiral superfield contains a complex scalar field $\mathcal{S}$, a fermion field ψ_L and auxiliary field $\mathcal{F}$. The latter leaves the action invariant, i.e. it is not physical, but is added to properly describe invariances under SUSY transformations. By defining $\hat{x}_\mu = x_\mu + \frac{i}{2}\bar{\theta}\gamma_5\gamma_\mu\theta$ the left-chiral superfield is expressed as:

$$\hat{\mathcal{S}}_L(x,\theta) = \mathcal{S}(\hat{x}) + i\sqrt{2}\bar{\theta}\psi_L(\hat{x}) + i\bar{\theta}\theta_L\mathcal{F}(\hat{x}). \tag{2.17}$$

The interactions between fermions and scalars are described by an holomorfic function of the left-chiral superfields, known as the superpotential. In general renormalizable form is given by

$$\mathcal{W} = L_i\hat{\mathcal{S}}_L^i + \frac{1}{2}M_{ij}\hat{\mathcal{S}}_L^i\hat{\mathcal{S}}_L^j + \frac{1}{6}y_{ijk}\hat{\mathcal{S}}_L^i\hat{\mathcal{S}}_L^j\hat{\mathcal{S}}_L^k, \tag{2.18}$$

where M_{ij} represents the mass terms of the fermions, y_{ijk} the yukawa couplings and L_i are mass-dimension parameters that only affect the scalar potential part of the Lagrangian. The latter term is only allowed when $\hat{\mathcal{S}}_L^i$ is a gauge singlet. Such cases will not be described here.

---

[1] There are also hyperfields, graviton superfields...

Secondly, we have the gauge superfields describing the gauge (vector) fields V^μ and their superpartners, the gauginos λ. Analogously to the chiral superfields, an auxiliary field $\mathcal{D}$ is also included. The gauge superfield is the written as

$$\hat{H}_A = \frac{1}{2}(\bar{\theta}\gamma_5\gamma_\mu\theta)V_A^\mu + i\bar{\theta}\gamma_5\theta\bar{\theta}\lambda_A - \frac{1}{4}(\bar{\theta}\gamma_5\theta)^2\mathcal{D}_A. \tag{2.19}$$

The gauge kinetic terms are described by defining a curl superfield, a generalized supersymmetric description of the field strength tensor. This encompasses the gauge-invariant kinetic terms of λ as well as the kinetic terms of the vector fields.

Finally, the gauge invariant kinetic terms are given by the Kähler potential

$$K = \hat{\mathcal{S}}_L^\dagger e^{-2gt_A\hat{H}_A}\hat{\mathcal{S}}_L, \tag{2.20}$$

from which, in addition to gauge invariant kinetic terms for the scalar and fermionic fields, we obtain interactions between the gauginos and the components of $\hat{\mathcal{S}}_L$ proportional to the corresponding gauge couplings.

Soft supersymmetry breaking.

As can be inferred from eq. (2.18), in a SUSY invariant theory all the fermionic and bosonic fields must have a corresponding superpartner with an equal mass. In such case, the superpartners of the SM fields would have been easily detected. However, since no signs of them have been found, SUSY must be broken. Nonetheless, it should only be broken $softly$, so to no reinvoke the hierarchy problem. This means that we shall be careful not to introduce terms with quadratic divergences. We are then left with linear, bilinear and trilinear interactions together with scalar and gaugino mass terms as options for soft supersymmetry breaking. Without any assumption on the nature of SUSY breaking, one should take all terms into account. Nonetheless, it is expected that SUSY breaking happens in a 'hidden sector' whose effect is somehow mediated to the visible sector. Depending on the mediation mechanism, specific patterns on the soft SUSY breaking parameters emerge reducing the total degrees of freedom. Several ideas have been proposed. SUSY breaking could be gravity mediated (SUGRA), in which case the hidden sector would give rise to a gravitino (superpartner of the hypothetical graviton), that in turn generates soft SUSY breaking terms trough radiative corrections. Its minimal setup, known as minimal supergravity, is parametrized by only five parameters: a common scalar mass m_0, a common gaugino and higgsino mass $m_{1/2}$, a common trilinear coupling A_0, $tan\beta$ and sing(μ) (for the definition of the last two parameters see 2.3.1). Although in general, m_0, $m_{1/2}$ and A_0 are actually dependent on the gravitino mass, in the minimal version they are taken as independent.

Another possibility is anomaly-mediated SUSY breaking (AMSB). In this scenario soft breaking terms are generated trough anomalous violation of a local superconformal invariance. Its minimal setup is described by 3 parameters: the scalar mass m_0, the gravitino mass $m_{3/2}$ and $\tan\beta$. At the weak scale, AMSB leads to a specific hierarchy for the gaugino mass terms. The other alternative is gauge-mediated SUSY breaking (GMSB). In this picture SUSY breaking mass terms are generated via SM gauge couplings at one loop. An interesting phenomenological feature of GMSB is the prediction of a gravitino as the lightest supersymmetric particle (LSP). This differentiates the GMSB from the AMSB and SUGRA scenarios where the LSP is normally a linear combination of the electroweak gauginos and higgsinos.

The Minimal Supersymmetric Standard Model.

The MSSM constitutes the minimal realization of a supersymmetric SM. The fermionic fields, written in terms of Majorana spinors, are embedded in left-chiral superfields, while the SM gauge bosons are described by gauge superfields. In the MSSM two Higgs doublet fields are required to give masses to all fermions which are included in left-chiral superfields. The resulting field content is summarized in Table 2.2. The superpotential of the MSSM is

Names	Superfield	Spin 0	Spin 1/2	Spin 1	$SU(3)$, $SU(2)$, $U(1)_Y$
Quarks	$\hat{Q}$	$\tilde{Q}=(\tilde{u}_L,\tilde{d}_L)$	(u_L,d_L)		$(\mathbf{3},\ \mathbf{2},\ 1/6)$
	$\hat{u^c}$	$\tilde{u}^c_R$	u^c_R		$(\bar{\mathbf{3}},\ \mathbf{1},\ \text{-}2/3)$
(×3 families)	$\hat{d^c}$	$\tilde{d}^c_R$	d^c_R		$(\bar{\mathbf{3}},\ \mathbf{1},\ 1/3)$
Leptons	$\hat{L}$	$(\tilde{\nu}_{eL},\tilde{e}_L)$	(ν_{eL},e_L)		$(\mathbf{1},\ \mathbf{2},\ \text{-}1/2)$
(×3 families)	$\hat{e^c}$	$\tilde{e}^c_R$	e^c_R		$(\mathbf{1},\ \mathbf{1},\ 1)$
Higgs	$\hat{H}_u$	(H_u^+,H_u^0)	$(\tilde{H}_u^+,\tilde{H}_u^0)$		$(\mathbf{1},\ \mathbf{2},\ 1/2)$
	$\hat{H}_d$	(H_d^0,H_d^-)	$(\tilde{H}_d^0,\tilde{H}_d^-)$		$(\mathbf{1},\ \mathbf{2},\ \text{-}1/2)$
Gluons	$\hat{G}$		$\tilde{g}$	g	$(\mathbf{8},\ \mathbf{1},\ 0)$
W	$\hat{W}$		$\tilde{W}^\pm,\tilde{W}^0$	$W^\pm,W^0$	$(\mathbf{1},\ \mathbf{3},\ 0)$
B	$\hat{B}$		$\tilde{B}$	B	$(\mathbf{1},\ \mathbf{1},\ 0\ )$

Table 2.2: Field content in the MSSM.

$$\mathcal{W}=\mu\hat{H}_u\hat{H}_d+\mathbf{y_u}\hat{Q}\hat{H}_u\hat{U}^c+\mathbf{y_d}\hat{Q}\hat{H}_d\hat{D}^c+\mathbf{y_e}\hat{L}\hat{H}_d\hat{E}^c, \tag{2.21}$$

where $\mathbf{y_i}$ are 3×3 matrices in flavor space and μ is the mass parameter of the Higss-higgsino superfield. In principle, baryon number (B) and lepton number (L) violation is allowed by supersymmetry (and by the SM gauge symmetries). However, the phenomenon is experimentally constrained, particularly by the proton lifetime estimation. Thus, B and L violating terms are explicitly suppressed in (2.21) by introducing a discrete symmetry, the R-parity. It is defined as

$$R=(-1)^{3(B-L)+2s}, \tag{2.22}$$

where s is the particle spin. Under R-parity, all the SM particles and the Higgs bosons are even ($R=1$) while their superpartners are odd ($R=-1$). As a consequence, the superpartners can only be produced in pairs and the LSP is stable. If the LSP is electrically neutral, it could be a prime WIMP dark matter candidate. Without assuming any scenario for SUSY breaking mediation, the soft SUSY breaking sector of the MSSM is read as

$$\begin{aligned}\mathcal{L}_{soft}=&-\frac{1}{2}(M_3\tilde{g}\tilde{g}+M_2\tilde{W}\tilde{W}+M_1\tilde{B}\tilde{B}+h.c.)\\&+(\mathbf{a_u}\epsilon_{ab}\tilde{Q}^aH_u^b\tilde{u}_R^\dagger+\mathbf{a_d}\tilde{Q}H_d\tilde{d}_R^\dagger-\mathbf{a_e}\tilde{L}H_d\tilde{e}_R^\dagger+h.c.)\\&-\tilde{Q}^\dagger\mathbf{m_Q^2}\tilde{Q}-\tilde{L}^\dagger\mathbf{m_L^2}\tilde{L}-\tilde{u}_R^\dagger\mathbf{m_U^2}\tilde{u}_R-\tilde{d}_R^\dagger\mathbf{m_D^2}\tilde{d}_R-\tilde{e}_R^\dagger\mathbf{m_E^2}\tilde{e}_R\\&-m_{H_u}^2H_u^*H_u-m_{H_d}^2H_d^*H_d+(bH_uH_d+h.c.)\end{aligned} \tag{2.23}$$

where M_1, M_2 and M_3 correspond to the bino, wino and gluino mass terms, respectively, $\mathbf{a_i}$ are the 3×3 trilinear couplings and $\mathbf{m_i}$ are the 3×3 mass terms of the sfermions.

Electroweak symmetry breaking in the MSSM impose certain conditions on the free parameters ($|\mu|^2$, $m_{H_u}^2$, $m_{H_d}^2$ and b) of the potential. To express them we start by writing the vevs of the neutral scalar fields as

$$v_u=\frac{\langle h_u^0\rangle}{\sqrt{2}},\ v_d=\frac{\langle h_d^0\rangle}{\sqrt{2}} \tag{2.24}$$

which, after electroweak symmetry breaking, are parametrized as

$$v^2=v_u^2+v_d^2=2m_Z^2/(g^2+g'^2)=(246\text{GeV})^2. \tag{2.25}$$

Finally, by defining the ratio of v_u and v_d as

$$\tan\beta = \frac{v_u}{v_d} \tag{2.26}$$

we can write the conditions for electroweak symmetry as

$$b\mu = \frac{(m_{H_u}^2 + m_{H_d}^2 + 2\mu^2)\sin(2\beta)}{2}, \tag{2.27}$$

$$\mu^2 = \frac{m_{H_d}^2 - m_{H_u}^2\tan^2\beta}{\tan^2\beta - 1} - \frac{M_Z^2}{2}. \tag{2.28}$$

Note that to avoid a fine-tuned cancellation between the Higgs potential parameters, their values must lie around the electroweak scale. For $m_{H_u}^2$, $m_{H_d}^2$ and b this could be explained from a common SUSY breaking mediation origin. However, the μ term is SUSY conserving, which makes the parameter independent. Thus, μ remains fined-tuned. This known as the 'μ problem'. The scalar sector is then composed by five physical degrees of freedom. We have two CP-even neutral states h and H, a pair of charged Higgs bosons $H^{\pm}$ and a CP-odd neutral state A. Normally, h denotes the SM Higgs boson. A notable consequence of the electroweak symmetry breaking in the MSSM is that m_h is actually bounded from above. At tree level, we have the constraint

$$m_h < m_Z|\cos(2\beta)|, \tag{2.29}$$

which is incompatible with the measured value of the Higgs boson mass, $m_h = 125\text{GeV}$. This is solved in the MSSM by taking into account loop corrections, specially those coming from the tops and their superpartners, the stops[2]. They are given by

$$\Delta(m_h^2) = \frac{3}{4\pi^2}\cos^2\!\alpha\; y_t^2 m_t^2\left[\ln(m_{\tilde{t}_1} m_{\tilde{t}_2}/m_t^2) + \Delta_{\text{threshold}}\right], \tag{2.30}$$

where α is the scalar mixing angle determined by

$$\frac{\sin 2\alpha}{\sin 2\beta} = -\left(\frac{m_H^2 + m_h^2}{m_H^2 - m_h^2}\right), \tag{2.31}$$

and $\Delta_{\text{threshold}}$ corresponds to the finite threshold correction to the supersymmetric Higgs quartic coupling, given by

$$\begin{aligned}\Delta_{\text{threshold}} &= \cos^2\theta_{\tilde{t}}\sin^2\theta_{\tilde{t}}[(m_{\tilde{t}_2}^2 - m_{\tilde{t}_1}^2)/m_t^2]\ln(m_{\tilde{t}_2}^2/m_{\tilde{t}_1}^2) \\ &+ \cos^4\theta_{\tilde{t}}\sin^4\theta_{\tilde{t}}\left[(m_{\tilde{t}_2}^2 - m_{\tilde{t}_1}^2)^2 - \frac{1}{2}(m_{\tilde{t}_2}^4 - m_{\tilde{t}_1}^4)\ln(m_{\tilde{t}_2}^2/m_{\tilde{t}_1}^2)\right]/m_t^4,\end{aligned} \tag{2.32}$$

where $\theta_{\tilde{t}}$ is the top-squark mixing angle and $\tilde{t}_{1,2}$ are the two stops mass states, defined below in eq. (2.45).

The resulting mass content in the MSSM is enlisted as follows.

- **Gauge boson masses.** The masses of $W^{\pm}$ and Z continue to follow the relations of eq. (2.10) but with $v^2 = v_u^2 + v_d^2$.

- **Fermion masses.** The fermion masses now depend on $\tan\beta$. The mass matrices of the up quarks are proportional to $v_u = v\sin\beta$, while ones corresponding to the down quarks and charged leptons are proportional to $v_d = v\cos\beta$. Thus, at tree level the fermion masses are given by

$$m_u = \frac{v}{\sqrt{2}}y_u\sin\beta,\; m_d = \frac{v}{\sqrt{2}}y_d\cos\beta,\; m_e = \frac{v}{\sqrt{2}}y_e\cos\beta. \tag{2.33}$$

---

[2] In Sec. 5.1 we shall learn that the Higgs mass can be *naturally* enhanced at tree level when promoting the gauginos to Dirac states.

- **Higgs boson masses.** The Higgs boson masses are given as

$$m_A^2 = B\mu(\cot\beta + \tan\beta), \tag{2.34}$$

$$m_{H^\pm}^2 = B\mu(\cot\beta + \tan\beta) + M_W^2 \tag{2.35}$$

$$m_{h,H}^2 = \frac{1}{2}[(m_A^2 + M_Z^2) \mp \sqrt{(m_A^2 + M_Z^2)^2 - 4m_A^2 M_Z^2 \cos^2\beta}]. \tag{2.36}$$

  from which we derive the upper bound on m_h presented in eq. (2.29).

- **Gluino mass**. The $SU(3)_C$ group remains unbroken and thus the gluinos do not mix with the other fermions. Therefore, their masses at tree level are simply

$$m_{\tilde{g}} = M_3. \tag{2.37}$$

- **Neutralino and chargino masses.** Electroweak symmetry breaking implies that the higgsinos and the electroweak gauginos are mixed in blocks according to their electric charge. This results in four neutral mass eigenstates, referred to as neutralinos, and two charged mass eigenstates, denoted as charginos. In the electroweak basis $(\tilde{B}, \tilde{W}, \psi_{h_d^0}, \psi_{h_u^0})$ the neutralino mass matrix is given by

$$M_{\tilde{\chi}^0} = \begin{pmatrix} M_1 & 0 & -g'v_d/2 & g'v_u/2 \\ 0 & M_2 & gv_d/2 & -gv_u/2 \\ -g'v_d/2 & gv_d/2 & 0 & \mu \\ g'v_u/2 & -gv_u/2 & \mu & 0 \end{pmatrix}. \tag{2.38}$$

  By diagonalising the mass matrix with the unitary matrix V_n we obtain the neutral mass eigenstates $\tilde{\chi}_i^0$ as

$$\begin{pmatrix} \tilde{B} \\ \tilde{W} \\ \psi_{h_d^0} \\ \psi_{h_u^0} \end{pmatrix} = V_n \begin{pmatrix} \tilde{\chi}_1^0 \\ \tilde{\chi}_2^0 \\ \tilde{\chi}_3^0 \\ \tilde{\chi}_4^0 \end{pmatrix}. \tag{2.39}$$

  When M_1, M_2 and μ are well separated, the mixing is reduced and we can effectively classify the neutralinos as 'bino-like', 'wino-like' and 'higgsino-like'.

  Similarly, the chargino mixing matrix is given in the $(\tilde{W}^+, \psi_{h_u^+}; \tilde{W}^-, \psi_{h_d^-})$ basis by

$$M_{\tilde{\chi}^\pm} = \begin{pmatrix} M_2 & -gv_d/\sqrt{2} \\ -gv_u/\sqrt{2} & -\mu \end{pmatrix} \tag{2.40}$$

  The charged mass eigenstates are related to the corresponding gauge eigenstates by two unitary matrices U_n and W_n as

$$\begin{pmatrix} \tilde{\chi}_1^+ \\ \tilde{\chi}_2^+ \end{pmatrix} = W_n \begin{pmatrix} \tilde{W}^+ \\ \psi_{h_u^+} \end{pmatrix}, \quad \begin{pmatrix} \tilde{\chi}_1^- \\ \tilde{\chi}_2^- \end{pmatrix} = U_n \begin{pmatrix} \tilde{W}^- \\ \psi_{h_u^-} \end{pmatrix} \tag{2.41}$$

  The unitary matrices are chosen so that

$$U_n^* M_{\tilde{\chi}^\pm} W_n^{-1} = \begin{pmatrix} m_{\tilde{\chi}_1^\pm} & 0 \\ 0 & m_{\tilde{\chi}_2^\pm} \end{pmatrix} \tag{2.42}$$

- **The sfermion masses.** Analogously to gauginos and higgsinos, in principle sfermion mass states can also mix after electroweak symmetry breaking. Thus, assuming only mixing between $SU(2)$ doublet and singlet fermions of the same generations, we end up with a series of similarly constructed 2×2 sfermion mass matrices. For the case of stops $\tilde{t}$, the mass matrix is given by

  $$M_{\tilde{t}}^2 = \begin{pmatrix} m_{\tilde{t}_L}^2 + m_t^2 + D(\tilde{t}_L) & m_t(-A_t + \mu \cot\beta) \\ m_t(-A_t + \mu \cot\beta) & m_{\tilde{t}_R}^2 + m_t^2 + D(\tilde{t}_R) \end{pmatrix} \tag{2.43}$$

  where generically

  $$D = M_Z^2 \cos 2\beta (T_3 - Q \sin^2 \theta_W). \tag{2.44}$$

  The diagonal contributions to the stop mass matrix are, the soft term mass terms $m_{\tilde{t}_{L,R}}^2$, the fermion mass m_t^2 and the $D-$ terms denoting squark-Higgs boson interaction $D(\tilde{t}_{L,R})$, while $A_t \equiv (\mathbf{a_t}/y_t)$. From eq. (2.43) we deduce that the mixing between the 'left' and 'right' sfermion states depends on the mass of the corresponding fermion. This is considerable for the 3rd generation sfermions while for the rest it is often considered negligible given the smaller fermionic masses. For the stops the mixing can be parametrized by the angle $\theta_{\tilde{t}}$ as

  $$\begin{pmatrix} \tilde{t}_1 \\ \tilde{t}_2 \end{pmatrix} = \begin{pmatrix} \cos\theta_{\tilde{t}} & \sin\theta_{\tilde{t}} \\ -\sin\theta_{\tilde{t}} & \cos\theta_{\tilde{t}} \end{pmatrix} \begin{pmatrix} \tilde{t}_L \\ \tilde{t}_R \end{pmatrix} \tag{2.45}$$

  .

The general MSSM contains more than 100 free parameters. However, by taking into account a few phenomenological considerations it is possible to significantly reduce the parameter space while remaining agnostic about the SUSY breaking mediation mechanism. From experimental observations we can assume that

- possible new sources of CP-violation are suppressed,
- no terms inducing flavor changing neutral currents should appear,
- first and second generation universality is preserved.

The result is a simplified version of the MSSM with only 19 free parameters, known as the phenomenological MSSM (pMSSM). The remaining parameters are:

- Three gaugino mass terms: M_1, M_2 and M_3.
- Five first and second generation sfermion mass terms: $m_{\tilde{q}}$, $m_{\tilde{u}_R}$, $m_{\tilde{d}_R}$, $m_{\tilde{l}}$ and $m_{\tilde{e}_R}$.
- Five third generation sfermion mass terms: $m_{\tilde{Q}}$, $m_{\tilde{t}_R}$, $m_{\tilde{b}_R}$, $m_{\tilde{L}}$ and $m_{\tilde{\tau}_R}$.
- Three Higgs sector parameters: $\tan\beta$, M_A and μ.
- Three third generation trilinear couplings: A_t, A_b and A_τ

MSSM signals at hadron colliders.

It is important to understand how supersymmetric particles would be produced at the LHC. Thus, we provide a brief overview on sparticle production and their decay channels. In the following, we assume that the MSSM is R-parity conserved and that the lightest neutralino $\tilde{\chi}_1^0$ is the LSP.

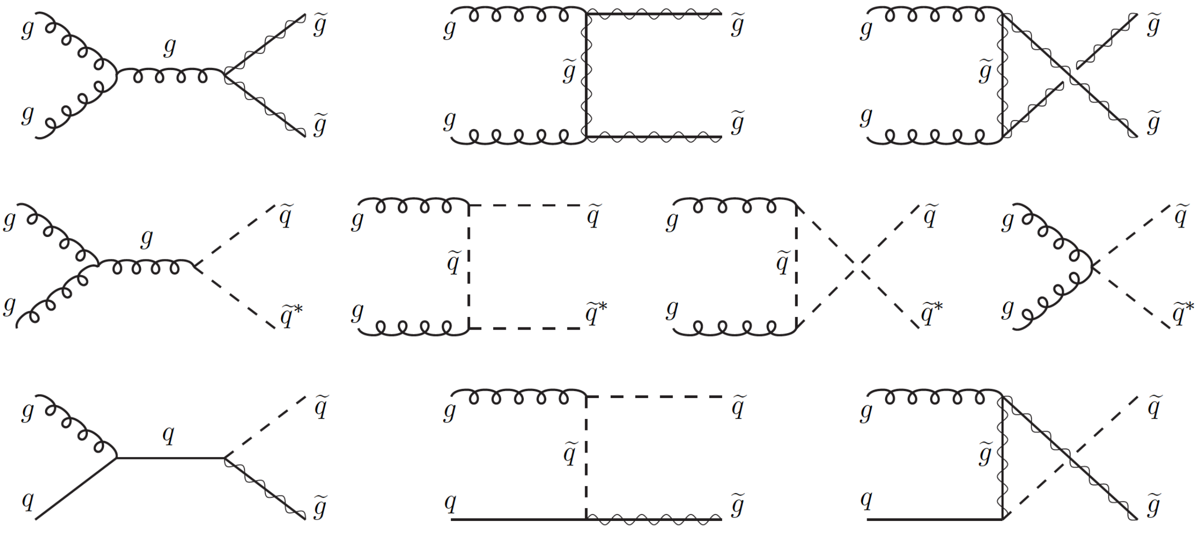

Figure 2.5: Feynman diagrams for strong production at hadron colliders via gluon-gluon and gluon-quark fusion, taken from [15].

Sparticle production. Sparticle production can happen trough strong or electroweak processes giving rise to gluinos and squarks or charginos, neutralinos and sleptons, respectively. Unless the gluino and squark masses are too large, strong production dominates in hadron collisions. The corresponding reactions are:

$$gg \to \tilde{g}\tilde{g},\ \tilde{q}_i\tilde{q}_j \tag{2.46}$$
$$gq \to \tilde{g}\tilde{q}_i, \tag{2.47}$$
$$q\bar{q} \to \tilde{g}\tilde{g},\ \tilde{q}_i\tilde{q}_j^*, \tag{2.48}$$
$$qq \to \tilde{q}_i\tilde{q}_j. \tag{2.49}$$

These final state combinations can arise from t-chanel exchange of either a squark or a gluino, depending on the final state, while the (2.46) and (2.48) processes receive further contributions from gluon s-channel processes. The relevant Feynman diagrams are shown in Figs. 2.5 and 2.6 corresponding to gluon-gluon and gluon-quark fusion and to strong quark-antiquark annihilation and quark-quark scattering, respectively.

Turning to electroweak production, charginos and neutralinos are produced as

$$q\bar{q} \to \tilde{\chi}_i^+\tilde{\chi}_j^-,\ \tilde{\chi}_k^0\tilde{\chi}_l^0, \tag{2.50}$$
$$u\bar{d} \to \tilde{\chi}_i^+\tilde{\chi}_k^0,\ d\bar{u} \to \tilde{\chi}_i^-\tilde{\chi}_k^0 \tag{2.51}$$

where $i, j = 1, 2$ and $k, l = 1, ..., 4$. While for sleptons we have

$$q\bar{q} \to \tilde{l}_i^+\tilde{l}_j^-,\ \tilde{\nu}_l\tilde{\nu}_l^* \tag{2.52}$$
$$u\bar{d} \to \tilde{l}_L\tilde{\nu}_l,\ d\bar{u} \to \tilde{l}_L\tilde{\nu}_l^* \tag{2.53}$$

The reactions in (2.50) and (2.52) can occur via electroweak bosons in the $s-$channel. Chargino and neutralino production also receive contributions from $t-$channel squark exchange which are generally subdominant because of a potentially large squark mass. The relevant Feynman diagrams of electroweak production are shown in 2.7.

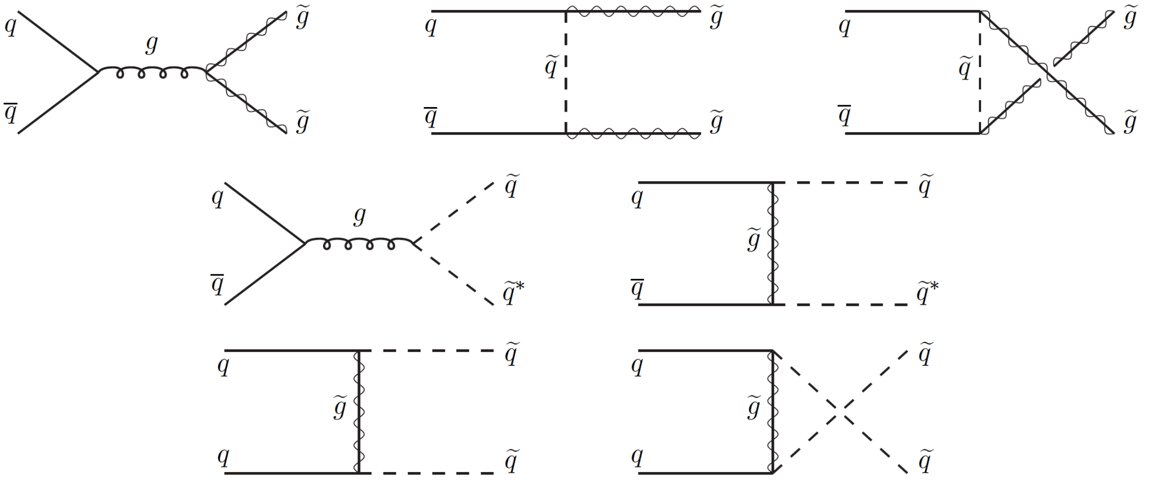

Figure 2.6: Feynman diagrams for strong production at hadron colliders via quark-antiquark annihilation and quark-quark scattering, taken from [15].

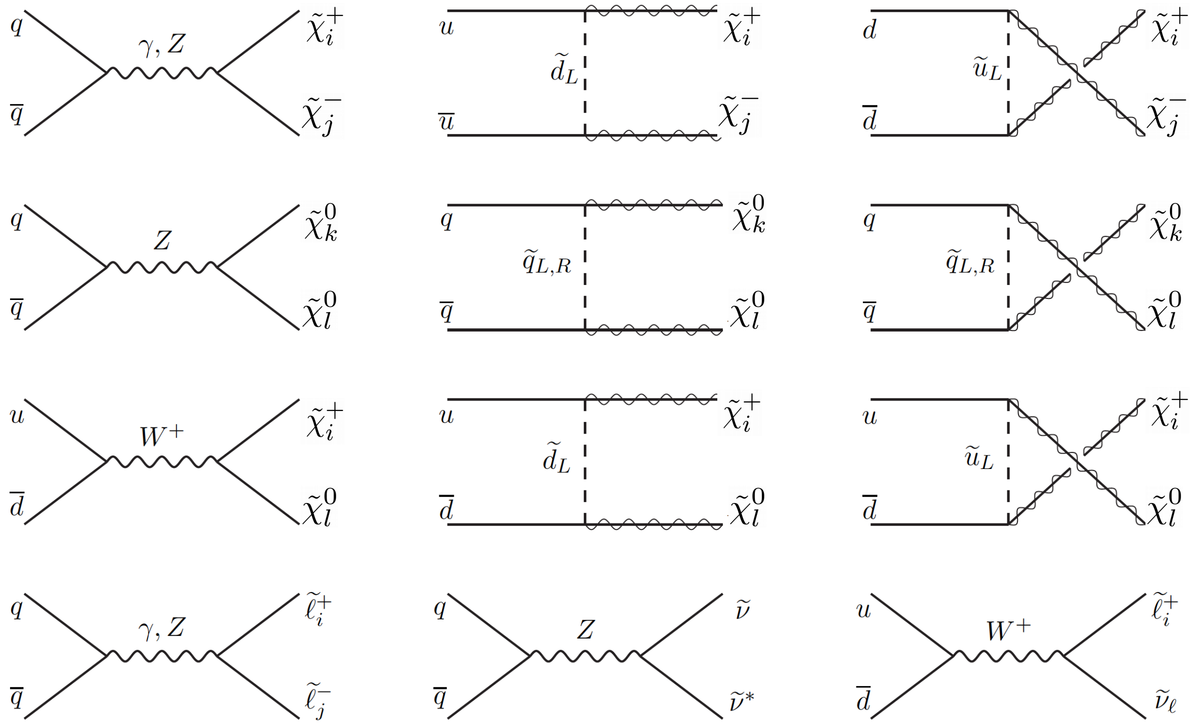

Figure 2.7: Relevant Feynman diagrams for elecroweakino production, taken from [15].

Decay channels. Let us now summarize the main sparticle decay patterns. For gluinos, when at least one squark is lighter than them, the predominant decay is

$$\tilde{g} \to q\tilde{q}. \tag{2.54}$$

Alternatively, when all the squarks are heavier, gluino decays happen through off-shelf squarks, resulting in the three body decays

$$\tilde{g} \to q\bar{q}\tilde{\chi}_i^0,\ qq'\tilde{\chi}_j^{\pm} \tag{2.55}$$

where again $i = 1, ..., 4$ and $j = 1, 2$. It is also possible that gluinos decay as $\tilde{g} \to g\tilde{\chi}_i^0$ through a quark-squark loop. This happens in very compressed $m_{\tilde{g}} - m_{\tilde{\chi}_i^0}$ scenarios, leading to long-lived gluinos. Sfermions may decay through gauge and Yukawa interactions as

$$\tilde{f} \to f\tilde{\chi}_i^0,\ \tilde{f} \to f'\tilde{\chi}_j^{\pm} \tag{2.56}$$

where $i = 1, ..., 4,\ j = 1, 2,\ f = l, \nu, q$ and decays to charginos involve up-type↔down-type switch of (s)quarks or a $l \leftrightarrow \nu$ one in the case of (s)leptons. Generally, direct decays to the LSP are kinematically favoured. However, in the case where sleptons are heavy, their decays to $\tilde{\chi}_1^{\pm}$ and $\tilde{\chi}_2^{\pm}$ may be preferred. Furthermore, left-handed fermions would also prefer to decay into $\tilde{\chi}_1^{\pm}$ and $\tilde{\chi}_2^{\pm}$, rather than to the LSP if the former are wino-like and kinematically allowed. Finally, if gluinos are lighter than the squarks, the strong two-body decay

$$\tilde{q} \to q\tilde{g} \tag{2.57}$$

would actually dominate.

Finally, charginos and neutralinos can decay via the two-body processes

$$\tilde{\chi}_i^0 \to Z\tilde{\chi}_k^0,\ W\tilde{\chi}_j^{\pm},\ h\tilde{\chi}_k^0,\ l\tilde{l}, \nu\tilde{\nu},\ q\bar{q}, [H\tilde{\chi}_k^0,\ A\tilde{\chi}_k^0, H^{\pm}\tilde{\chi}_k^{\mp}, q\tilde{q}], \tag{2.58}$$

$$\tilde{\chi}_j^{\pm} \to W\tilde{\chi}_l^0,\ Z\tilde{\chi}_1^{\pm},\ l\tilde{\nu},\ \nu\tilde{l}, q\bar{q}', [H\tilde{\chi}_1^{\pm},\ A\tilde{\chi}_1^{\pm}, H^{\pm}\tilde{\chi}_l^0, q\tilde{q}'] \tag{2.59}$$

where the final states in brackets are expected to be subdominant since the produced sparticles are normally heavier. Also, if charginos and neutralinos have a significant higgsino content and the process is kinematically allowed, the decays to third-family quark-squark pairs would be enhanced by the large top-quark Yukawa coupling. It the two-body decays are kinematically forbidden, it follows that the three-body decays

$$\tilde{\chi}_i^0 \to ff\tilde{\chi}_j^0,\ \tilde{\chi}_i^0 \to ff'\tilde{\chi}_j^{\pm},\ \tilde{\chi}_i^{\pm} \to ff'\tilde{\chi}_j^0 \text{ and } \tilde{\chi}_2^{\pm} \to ff\tilde{\chi}_1^{\pm}, \tag{2.60}$$

induced from the (now off-shell) gauge bosons, Higgs scalars, sleptons and squarks appearing in the two-body decays.

From the above we can infer that sparticles produced at hadron colliders would subsequently cascade decay into combinations of SM and SUSY particles until the LSP is generated. As an example, 2.8 shows some of the possible decay chains that gluinos can undergo. As a consequence, SUSY signatures are expected to be made of different combinations of jets and leptons plus missing energy (corresponding to the LSP) depending on the realized production and decay channels. The SUSY searching strategy at the LHC, described in Sec. 3.1, is based on this expectation.

Beyond the MSSM.

So far, we have focused on the minimal SUSY extension of the SM, the MSSM. The phenomenology of this supersymmetric realization has been widely studied; in fact, most searches at the LHC

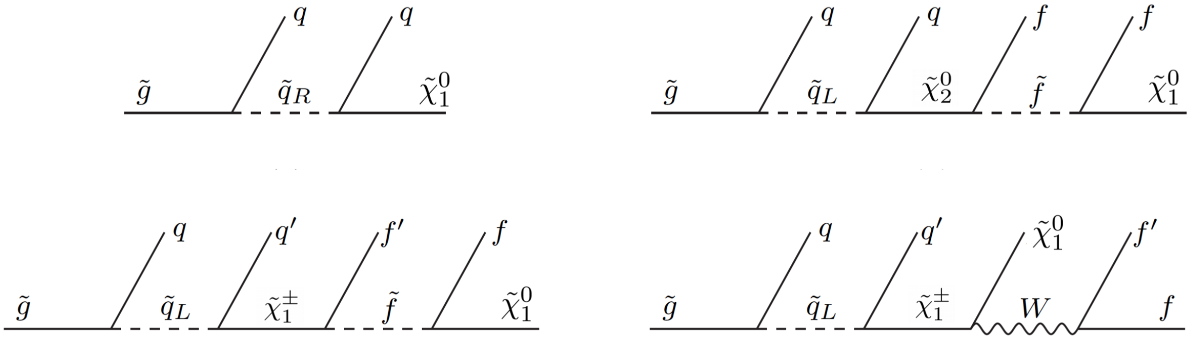

Figure 2.8: Several examples of gluino cascade decays, taken from [15].

are optimized in the context of this model. However, the MSSM is indeed not the only interesting SUSY theory. Several beyond vanilla extensions with distinctive properties have been proposed, which also deserve thorough phenomenological studies. The simplest one is known as the Next-to-Minimal Supersymmetric Standard Model (NMSSM) [58], in which an SM singlet chiral superfield $\hat{S}$, composed by a complex scalar field S and a fermionic singlino $\tilde{S}$ is added. In the simplest scenario the superpotential is extended by

$$\mathcal{W} = \lambda \hat{S} \hat{H}_u \cdot \hat{H}_d + \frac{\kappa}{3} \hat{S}^3 \tag{2.61}$$

The NMSSM was proposed to address the μ problem. When the $\tilde{S}$ superfield acquires a vacuum expectation value s an effective μ term is obtained as

$$\mu_{eff} = \lambda_s, \tag{2.62}$$

now connected to the SUSY breaking scale. Several phenomenological differences are expected from the NMSSM as compared to the MSSM. For instance, we obtain additional tree level contributions to the Higgs mass and the possibility of a singlino-like neutralino LSP. The latter as a consequence of the mixing of the singlino with gauginos and higgsinos.

Another interesting example is the so-called MSSM+RN [59, 60]. In there, the MSSM is extended by a RH neutrino superfield (RN) $\hat{N}$ composed by an RH neutrino and a corresponding sneutrino $\tilde{N}$, yielding Dirac neutrino masses. The $\tilde{N}$ sneutrino can mix with the $\tilde{\nu}_L$, allowing for a mostly RH sneutrino LSP as a viable DM candidate.

Furthermore, the MSSM can also be extended by a $U(1)'$ gauge group, forming what is known as the UMSSM. The symmetry group of the model is

$$SU(3) \times SU(2)_L \times U(1)_Y \times U(1)'. \tag{2.63}$$

The UMSSM is well-motivated, for instance, in the context of superstring models [61] and GUTs [62] . Interesting properties of the UMSSM include: obtaining a m_h of 125 GeV without relying on large contributions from the stops, SM like tree-level couplings of h and, similarly to the NMSSM, the μ problem can be addressed by the vev of a singlet field, responsible for $U(1)$ symmetry breaking. Moreover, as in the MSSM+RN the DM candidate can be either a neutralino or an sneutrino.

Finally, another well-motivated extension of the MSSM is to allow Dirac masses for the gauginos, an idea originally proposed to allow the gluino to be massive [63]. Models with Dirac Gauginos (DG) have interesting features such as providing a tree level boost to the Higgs mass, being able to be associated to $N = 2$ supersymmetry, possibility of preserving R-symmetry and increase naturalness. The MDGSSM constitutes the minimal extension of the MSSM with Dirac gaugino states. It is obtained from the addition of one adjoint chiral superfield for each gauge group. This indeed translates into a different phenomenology from that of the MSSM. For instance, the electroweakino sector is enriched by 2 new neutral states, one bino and one wino, and one charged wino state, yielding a total of 6 neutralinos and 3 charginos. Furthermore, the MDGSSM includes an explicit, but soft R-symmetry breaking term, B_μ. As a consequence, small mass splittings are induced between the bino-like and wino-like electroweakinos, yielding the possibility of LLP signatures. In Chapter 5 we will present the MDGSSM in more detail and discuss the collider phenomenology of the colored and electroweakino sectors. We will also delimit the regions of the former sector, where the lightest neutralino is a viable DM candidate.

2.3.2 Non-SUSY extensions.

There are, of course, several alternatives to the SUSY framework. They usually address specific theoretical or observational puzzles. Without intention of completeness, we provide here an overview on non-SUSY extensions of the SM.

- **SU(5), the simplest GUT.**

  As an example GUT, let us briefly describe the simplest one, the $SU(5)$. It is the minimal group that can accommodate all the particles of the SM which can be broken exactly into its gauge groups
  $$SU(5) \to SU(3) \times SU(2) \times U(1) \tag{2.64}$$
  by the vacuum expectation value of the nuetral component of the adjoint irreducible representation (irrep) **24**.

  In the $SU(5)$ GUT, the left-handed quarks and leptons are accommodated in irreps of $SU(5)$ as $\bar{\mathbf{5}} = [d^c_R, L]$ and $\mathbf{10} = [Q, u^c_R, e^c_R]$, while left-handed anti-neutrinos can be added as $\mathbf{1} = [v^c_R]$. The gauge bosons fit in the adjoint irrep **24**, together with 12 new fractionally charged bosons with both lepton and baryon numbers, known as leptoquarks. Since leptons and bosons are assembled in the same irreps, B and L numbers are not conserved individually, but the B-L combination is. This can lead to proton decay through leptoquark exchange, a distinctive signature in many GUTs. Finally, the Higgs boson is accommodated in either a **5** or a $\bar{\mathbf{5}}$ irrep, which will decompose in triplets of $SU(3)$ and doublets of $SU(2)$ after $SU(5)$ symmetry breaking. The colored Higgs triplets are another source of B and L violation and mediate fast proton decay, unless they are very heavy. Thus, fine tuning is required to be left with the doublets at the electroweak scale while leaving the triplets in the GUT one. This is known as the doublet-triplet splitting fine tuning problem.

- **Extra dimensions.** Another way to journey beyond the SM is considering new extra spatial dimensions. Since we only experience four dimensions (3 space and 1 time), these new dimensions must be 'compactified'. However, according to the universal extra dimension (UED) model [64, 65], the SM can propagate into the extra dimensions. Originally proposed (100 years ago) to unify electromagnetism and scalar gravity, theories with extra dimensions have been found to have interesting properties. For instance, they can address the hierarchy problem [66, 67] and provide DM candidates [68]. Furthermore, they are the basis for modern superstring and brane theories.

  Let us consider here the simplest case of one extra compactified dimension y and its effect on a massless scalar field. This will be sufficient to suggest the presence of a DM candidate.

The action of a massless scalar field in five dimensions is given by

$$S = -\int d^5x \frac{1}{2}\partial_M \Psi(x^\mu, y)\partial^M \Psi(x^\mu, y) \tag{2.65}$$

where $M = 1, ..., 5$ and $\mu = 1, ..., 4$. The y dimension is compactified over a circle of radius R; thus, the field has the periodic boundary conditions

$$\Psi(x^\mu, y) = \Psi(x^\mu, y + 2\pi R) \tag{2.66}$$

which allow the Fourier expansion

$$\Psi(x^\mu, y) = \Psi_n(x^\mu, y)\exp(iny/R). \tag{2.67}$$

After substituting the above in eq. (2.65) and integrating out the y dimension one obtains

$$S = \int d^4x(\partial_\mu \Psi^0 \partial_\mu \Psi^0 + \sum_n^\infty (\partial_\mu \Psi^{n\dagger}\partial^\mu \Psi^n - \frac{n^2}{R^2}\Psi^{n\dagger}\Psi^n)) \tag{2.68}$$

where $\Psi_n \equiv \sqrt{2\pi R}\Psi_n$. Thus, we obtain a zero mode Φ_0 and an infinite tower of massive complex scalar fields, known as Kaluza-Klein (KK) modes. Each KK mode has a mass given by $m_n = n/R$ where n is a quantum number called Kaluza-Klein number. The KK number represents the quantized momentum in the compactified dimension which is conserved. Hence, the lightest KK mode is stable hinting a possible DM candidate[3]. In the context of the UED model, this can be the first KK partner of the B boson.

- **Axions.** As discussed in Sec. 2.2.1, the strong CP problem can be solved by extending the SM by a $U(1)_{PQ}$ symmetry [14]. This symmetry is spontaneously broken giving place to a Nambu-Goldstone boson, the axion. The CP problem is solved by replacing the CP-violating angle θ_{QCD} with the dynamical CP-conserving axion. An standard review on axions and the CP problem is provided by Peccei himself [70].

  The axions can also be DM candidates. In the hot early Universe axions were massless, since the motion of the axion field occurs in the angular direction of its Mexican hat shaped potential and the curvature of the potential in this direction is zero at high temperatures. Then, as the Universe cools down to a temperature of a few hunderd MeV, the axion field starts oscillating around the minimum of the potential acquiring a non-zero mass due to nontrivial QCD vacuum effects. These oscillations remain undamped in the present epoch, making it possible for the axions to make up for (or a portion of) the observed dark matter. Despite their small masses

$$m \approx 6 \times 10^{-6}\text{eV}\frac{10^{12}\text{GeV}}{f_a} \tag{2.69}$$

  (where f_a is the axion decay constant ranging between 10^9GeV and 10^{12}GeV) axions can be cold dark matter candidates as they are never in thermal equilibrium in the early universe. The mechanism trough which axions are produced depends on whether the PQ symmetry breaks before or after inflation. For more details on axions as DM see [71] and references therein.

- **Multi-Higgs models.**

  It is possible to extend the SM without adding new continuous symmetries (or spatial dimensions). This is commonly done by extending the scalar sector with new scalar $SU(2)$

---

[3] See [69] for pioneering work on Lightest Kaluza Klein particles as DM candidates.

doublets, forming what are known as N Higgs Doublet Models (NHDM). The case of the 2HDM has been widely studied (for instance, see [72]). One of its simplest realizations is the Inert Doublet Model (IDM) [73], known as the prototype model for including Higgs dark matter. In there, the SM is extended by one scalar doublet that doesn't generate a vev. Furthermore, the new scalar doublet is defined as Z_2-odd while the rest of the SM is Z_2-even. The result is an inert doublet containing four physical degrees of freedom: two charged, one neutral scalar and one pseudo scalar Higgs where either (or both) of the former is the DM candidate.

Another popular extension is the so-called scotogenic model [74], constituted by 3 right handed neutrinos and an inert scalar doublet. In there, the left-handed neutrinos acquire small Majorna masses through one-loop radiative corrections involving the new scalars. Furthermore, it can accommodate two types of DM particles, one fermionic (the lightest RH neutrino) and one bosonic (the lightest inert scalar).

Furthermore, multi-Higgs models have been proposed in connection with flavor symmetries. For instance, in the 3HDM with S_3 family simmetry, the discrete symmetry is extended to the scalar sector [75]. As a result, a CKM matrix in accordance with the experimental results and the prediction of a non-zero reactor neutrino mixing angle θ_{13} is obtained while preserving the S_3 symmetry in the flavor sector. This model was later extended to a 4HDM (occupying all the irreducible representations of the S_3 group) to allow for DM candidates without tempering with its original properties [76].

2.4 The Large Hadron Collider.

Consisting of a 27 km ring of superconducting magnets, the Large Hadron Collider is currently the world's most powerful particle accelerator[4]. It collides very energetic hadrons with the purpose of exploring the physics at the electroweak scale. On the one hand, it allows for precision measurements of SM interactions, and on the other, to search for signals of new physics (see Sec. 3.1) at said scale. The first operational run (Run 1) of the machine collided protons at a 7-8 TeV center of mass energy and reached an integrated luminosity of 30 fb^{-1} per experiment. Notably, by the end of this run the Higgs boson was discovered. As for today, the LHC has finished Run 2 where protons were collided at a 13 TeV center of mass energy, and a total integrated luminosity of 150 fb^{-1} was achieved[5].

The highly energetic proton collisions occurring at the LHC can be described under the parton model framework. Following the QCD factorization theorem, the scattering amplitudes of hadronic reactions with large momentum transfer can be factorized into a product of the parton-level scattering and the corresponding parton distribution functions (PDFs). Thus, the cross section corresponding to the scattering of two hadrons A and B producing a final state F is given by

$$\sigma(AB \to F\ X) = \sum_{a,b} \int dx_a dx_b\ f_{a/A}(x_a, Q^2) f_{b/B}(x_b, Q^2)\ \hat{\sigma}(ab \to F), \tag{2.70}$$

where X is the scattering remnant. The hard scattering cross section $\hat{\sigma}(ab \to F)$ is obtained from a phase space integration over the corresponding matrix element. The PDF $f_{a/A}(x_a, Q^2)$

---

[4] Several options for a next generation collider have been discussed in the HEP community. In the 2020 update of the European Strategy for Particle Physics a high priority has been given to the construction of an electron-positron collider that would serve as a 'Higgs factory'.

[5] Currently, major upgrades are undergo at the LHC, heading us to the high-luminosity era. A total of 3000 fb^{-1} integrated luminosity is expected by the end of the LHC's lifetime.

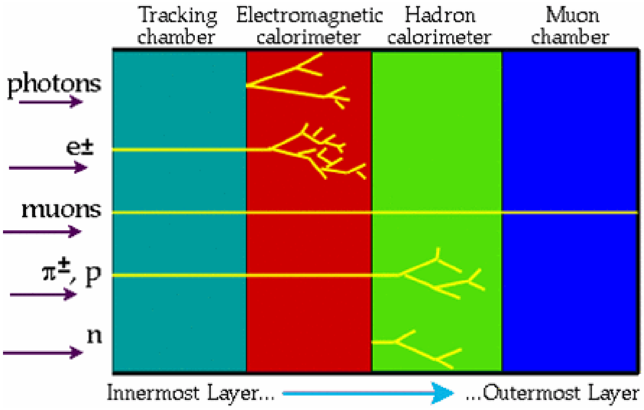

Figure 2.9: Scheme of particle identification at ATLAS and CMS, taken from [81].

($f_{b/B}(x_b, Q^2)$) describe the fractional longitudal momentum x_a (x_b) of a parton a (b) inside an hadron A (B) and depends on the squared four-momentun transfer Q^2. PDFs are fitted from data of numerous deep inelastic scattering experiments and their change rate over different energy scales is determined from the DGLAP evolution equations [77, 78, 79]. For detailed discussions on LHC physics, see [80, 81, 82, 83].

There are four major detectors placed around the LHC ring aimed to study the particles produced in hadron collisions. The ALICE (A Large Ion Collider Experiment) is a heavy-ion detector designed to study the quark-gluon plasma formed at extreme energy densities. The LHCb (Large Hadron Collider beauty) is primarily intended to study CP violation in beauty-hadron interactions which could possibly explain the observed matter-antimatter asymmetry in the Universe. The other two are the multipurpose detectors, ATLAS (A Toroidal LHC Apparatus) and CMS (Compact Muon Solenoid), and are the ones we are interested on here.

The ATLAS and CMS detectors are designed to cover a wide range of physics, and thus constitute our main tools to study the large variety of proposed BSM theories. Although not exactly the same[6], the overall design of the detectors is similar. They are made of four main stages:

- **The inner-chamber.** It is made of a silicon tracker designed to detect the tracks left by the charged particles that pass trough it, and to measure their momentum. Its placement, very close to the interaction point, permits the identification of heavy quark decays occurring away from the primary interaction vertex.

- **The Electromagnetic Calorimeter (ECAL).** The second layer of the multi-purpose detectors is the ECAL. It is designed to measure the energies of electromagnetically interacting particles.

- **The Hadronic Calorimeter (HCAL).** Analogously to the ECAL, its purpose is to measure the energy of hadrons.

- **The muon chambers.** Muons interact only feebly with the calorimeters. Thus, a muon spectrometer has been placed in the outer layer of the ATLAS and CMS apparatuses to measure their energy.

The four-stage design of ATLAS and CMS permits the identification of the (quasi-)stable particles constituting the final-states of the proton collision (see Fig. 2.9). They are namely,

---

[6] For instance, their magnetic systems follow different designs.

- **Jets.** They are made of traveling bunches of hadrons originated from the showering and hadronization (see Sec. 3.3.2) of the initially produced partons. The jet components can be electrically charged or neutral. In the former case, they would be *seen* in the tracking chamber and the ECAL before deposing the rest of their momentum in the HCAL. In the latter case, they would only be detected by the HCAL.

- **b-jets.** They are originated by a hard bottom quark. The typical lifetime of b-hadrons is enough for them to travel a measurable distance before decaying. Thus, b-jets are distinguished from the ordinary jets by reconstruction of the secondary vertex associated with the b-hadron decay.

- **Photons.** They typically depose their energy in the ECAL but since they are electrically neutral, they don't leave a track in the inner chamber.

- **Electrons.** After leaving a track in the inner chamber, they lose most of their energy in the ECAL.

- **Muons.** They leave a track, loose some energy at the ECAL, but most of their energy is deposed in the muon chamber.

- **Missing energy.** The missing transverse energy E_T^{miss} quantifies the transverse energy of the undetected particles produced in a collision event. It is defined as

  $$|\vec{p}_T^{\,miss}| = -\sum_i \vec{p}_T^{\,i}, \tag{2.71}$$

  where $\vec{p}_T^{\,miss}$ is the negative sum of the momentum $\vec{p}_T$ of all the detected particles. In the SM, the only particles that would pass undetected are the neutrinos.

At ATLAS and CMS an event can be defined as the occurrence of a combination of the above particles identified by the detector, together with their kinematic properties. The distributions of these events, can potentially be matched to the eq. (2.70) cross sections, allowing us to study the properties of the underlying theory to which they correspond.

Chapter 3

(Re)Interpretation of LHC searches.

In Sec. 2.3 we learned that a plethora of theories has been proposed to extend the SM. The diverse nature of these theories translates into a vast variety of different new signals that could be searched for at the LHC. The ATLAS and CMS detectors are multi-purpose instruments capable of covering a huge range of possibilities. The humongous amount of data that can be collected is an essential asset of the LHC and its adjacent detectors, but it comes with its challenges. The first one is that it's impossible to record the totality of events detected by ATLAS and CMS (and by the rest of the LHC experiments), hence it is primordial to select which events are worth saving. Afterwards, it is necessary to be able to distinguish a potential new signal from the SM background in the saved data. To overcome these challenges, it is useful to study where new signals are expected to be observed over the detector object parameter space, in the context of concrete BSM theories. With this in mind, the ATLAS and CMS collaborations have put forward an extensive and ever growing program of searches for new physics, aiming to cover popular new physics theories as much as possible. In Sec. 3.1 a brief overview on this program will be given. Presently, most LHC searches intepret their results as constrains on simplified models [84, 85]. In this way, the theory dependence of the interpretations are reduced, allowing for generic descriptions of the experimental impact on the kinematical parameters of a BSM theory. The simplified model framework will be presented in Sec. 3.2. Finally, to extend the coverage of new physics theories, LHC searches should be re-interpreted in the context of BSM scenarios not yet tested. This inspired the creation of the LHC reinterpretation forum, a joint effort beteween experimenters and theorists intended to make the most of the LHC results. The latest report of the forum, including a list of recommendations for presenting LHC results, can be found in [86]. An overview on the LHC reinterpretation effort is given in Sec. 3.3.

3.1 LHC searches for new physics.

The extensive program of searches for new physics performed by ATLAS and CMS can be roughly divided in 3 categories: missing energy, long lived particle and resonance searches. While they are introduced in the following lines, detailed reviews are provided in [87, 80].

- **Missing energy searches.** As mentioned in Sec. 2.4 the only SM particles that would pass undetected are the neutrinos, thus they account for all the E_T^{miss} in an SM event assuming a %100 efficiency of the detector. However, in many BSM theories the E_T^{miss} is expected to be enhanced since they often include stable neutral particles (i.e. DM candidates). Hence, BSM theories can be looked for in regions with high E_T^{miss}. This has motivated a large number of different searches, here classified as SUSY and Dark Matter searches.

  SUSY searches. As mentioned in Sec. 2.3.1, R-symmetric SUSY models are very attractive

BSM theories as they can lead to unification at large energy scales without compromising the stability of the proton, solve the hierarchy problem, account for dark matter, etc. In them, the superpartners can only be produced in pairs that subsequently cascade decay into it an stable, preferably neutral, LSP. At the LHC, pair production of particles from such models, would be observed as SM final states plus E_T^{miss} corresponding to the neutral LSP. For instance, in a scenario with $m_{\tilde{g}} > m_{\tilde{q}}$, squarks can decay as $\tilde{q} \to q + \text{LSP}$, leading to a 2-jet+$E_T^{miss}$ signature after squark production. ATLAS and CMS have performed a large number of SUSY searches targeting different SM+E_T^{miss} final states depending on the initially produced sparticle. Some examples are:

- $E_T^{miss} + \text{jets} + X$: inclusive jets plus missing energy (X = anything).
- $E_T^{miss} + \text{jets} + 0l$: lepton veto.
- $E_T^{miss} + nl$: multilepton.
- $E_T^{miss} + \text{jets} + 1l$: jets plus one lepton.
- $E_T^{miss} + \text{jets} + 2l$ with $Q(l_1 = -Q(l_2))$: jets plus opposite-sign dileptons.
- $E_T^{miss} + \text{jets} + 2l$ with $Q(l_1 = +Q(l_2))$: jets plus same-sign dileptons.

Moreover, despite these searches are tagged as 'SUSY' for historical reasons, they can also be applied to a more general class of models which present similar signatures form cascade decays, e.g. to some UED and Little Higgs scenarios.

Dark Matter searches. Searching for the direct production of dark matter particles has the small predicament of having a completely invisible signature, given that $\sum_i \vec{p}_T^{\,i} = 0$ so $E_T^{miss} = 0$. However, it is possible that a SM particle X recoils from the collision in the opposite direction of the dark matter particles, allowing the computation of a non trivial E_T^{miss} and yielding a $X + E_T^{miss}$ signature. For example, if X is a jet we can search for signal events with at least one high p_T jet associated with a large E_T^{miss}. This type of searches are known as mono-X searches.

A fundamental step in missing energy searches, is to determine the SRs in which the BSM signal is expected to dominate over the background (SM) expectation. To construct them, experiments often employ the 'cut-based' strategy[1], in which a series of cuts on detector objects are imposed (e.g. a minimum E_T^{miss}) to subtract the background while enhancing the signal expectation. Once that the SRs are constructed it is possible to compare the SM expectation to the number of experimentally observed events to make a statement about the expected BSM signal. Due to the typically low number of expected background events, the dedicated statistical procedure known as the CLs prescription [88], is generally used for limit setting in searches.

- **Long Lived Particle searches.** In the context of LHC physics, an LLP typically refers to a new physics particle with a lifetime of the order of the detector scale or larger, i.e. that decays at least 1mm away from the main collision vertex. There is a large number of theories in which LLPs can be realized. For example, they appear in SUSY theories with approximate R symmetry [89, 90, 91] or in scenarios with quasi degenerate multiplets [92, 93] (as we will see in Sec. 5.3). Other examples include gauge-portal theories where new vector mediators produce LLPs (e.g. [94]) and Dark Matter theories with non-thermal freeze-in scenarios [39]. See [95] for a comprehensive overview of theoretical models with

---

[1] In recent years, strategies based on modern ML algorithms, such as BDTs, have been gaining terrain over the classic 'cut-based' searches as they are proven to be very efficient on constructing SRs. However, as ML algorithms become more complex, the matter of reproducibility has risen. In [86] is recommended that relevant material, such as the implemented algorithm and the 'learned' ML model, be shared for re-interpretation purposes.

LLPs. The large variety of scenarios translates into a considerable amount of possible LLP signatures. They can be classified by the nature of their gauge interaction as electrically neutral, electrically charged or color charged[2].

Neutral LLPs can only be distinguished if they decay within the detector, otherwise they would count as E_T^{miss}. Typical expected signatures are those with displaced jets, leptons, or photons plus E_T^{miss}. The displaced objects are tagged as such because their reconstructed track doesn't point back to the main collision vertex.

Different search strategies have been performed by ATLAS and CMS, depending on the nature of the displaced objects and the detector position they arise from. Regarding displaced hadronic decays, ATLAS has searches with neutral LLPs, decaying in the HCAL [96, 97], in the inner tracker or muon chambers [98], in the inner tracker with large associated E_T^{miss} [99] and inner tracker decays with large E_T^{miss}, jets or leptons [100]. Searches focusing on inner tracker decays rely on standard triggering to select events with high-p_T jets, E_T^{miss}, or leptons. While for the HCAL and muon chamber decays the *CalRatio* (Calormeter Ratio trigger) and *MuonRol* (Muon Region of Interest cluster trigger) dedicated triggers are used. The former is designed to select events with long-lived neutral particles in the outer radius of the ECAL or within the HCAL by triggering on signals with at least one narrow jet with small energy deposit in the ECAL and no charged tracks pointing back to the jet. The latter looks for decays occurring in the outermost layers of the HCAL or in the muon spectrometer. On the other hand, CMS have performed inclusive searches for displaced jets [101, 102, 103]. They are based on an displaced jet tagging algorithm to identify displaced jet pairs in the inner tracker, while triggering is focused on large $H_T = \sum |p_T|$ values. Turning to displaced leptonic decays, both ATLAS and CMS have searched for lepton pairs originating from a displaced vertex [100, 104, 105]. While CMS has an additional search requiring exactly one isolated muon and one isolated electron with impact parameters between 0.2 cm $< |d_0| <$10cm [106]. The CMS searches trigger on reconstructed electrons or muons using inner tracker information [104] or reconstructed muons relying only on the muon chamber [105]. The [100] ATLAS search triggers on muons without an inner track, electrons or photons. For selecting events it requires one muon with $p_T > 50$ GeV, or one electron with $p_T > 110$ GeV, or one photon with $p_T > 130$ GeV, or a electron, photon or electron-photon pair with a minimum p_T for each object of 38-48 GeV. The displaced leptons must be of opposite sign and arise at least 4mm away from the primary vertex. The [107] ATLAS search focus on displaced muons with $|d_0| < 200$ cm. For more details on searches for these and other displaced objects, see [108].

An electrically charged LLP could give a very clear signature. If it traverses the whole detector, it would look like a very energetic muon and be considered as a Heavy Stable Charged Particle (HSCP), while if it decays in the inner tracker into a stable neutral particle, it would leave a disappearing track (DT) signature. The latter assumes that the SM decay products of the charged LLP are very soft, thus are not reconstructed. HSCP searches [109, 110, 111, 112, 113] trigger on large E_T^{miss} or high-p_T muons. They rely on two main charachteristics. One, massive particles or with an electric charge $\neq e$, have an ionization loss dE/dx distinguishable from that of the SM particles. Two, the traveling speed of heavy particles is measurably smaller than the speed of light. DT searches [114, 115, 115] trigger on large E_T^{miss} in association with initial state radiation jets with high p_T.

A bit more complicated is the case of color charged LLPs, e.g. the gluino in the split SUSY scenarios [116, 117]. The initially produced gluino will hadronize and form charged

---

[2] The latter can be subdivided again by their electric charge.

or neutral 'R-hadrons' [118, 119]. The fraction of charged R-hadrons strongly depends on the unknown hadronization model and can have a strong impact on the interpretation of a search. A reference study split SUSY collider phenomenology can be found in [117].

  An extensive list of LLP signatures is presented in [108]. Notably, LLP signatures are rarely observed from pure SM events, making it very easy to distinguish the signal from the background. This, together with the fact that new physics hasn't been found (yet) in resonance or missing energy searches, has lead to a large interest of the HEP community on this kind of searches despite the challenges they impose for their implementation.

- **Resonance searches.** A common method for searching new physics at colliders is to look for new resonances in the production rates of SM particles. Resonances provide very distinctive signatures. They appear as large narrow peaks (depending on the decay width) in the M_{inv} spectrum of the final states, around the pole mass of the resonant particle. For instance, the SM Higgs bosons was discovered as a resonance in the di-photon M_{inv} spectrum [12, 13]. It is also possible to search for a new resonance decaying partly into invisible final states, by considering the E_T^{miss}. W bosons are typical examples of such resonances since they decay as $W \to l\nu$.

  Resonance searches for new physics aim to observe peaks in the M_{inv} spectra of the SM final state particles, consequence of the resonant production of BSM particles. For instance, the Z', realized in $U(1)$ SM extensions, has been searched in the M_{inv} spectra of e^+e^- and $\mu^+\mu^-$ above the Drell-Yan background. Other examples are W' bosons from $SU(2)$ extensions and graviton excitations in KK models.

  The determination of discovery (or exclusion) of a resonant BSM particle follows from the application of a dedicated statistical procedure, such as the BUMPHUNTER algorithm [120]. By systematically comparing the measured data (signal) with the SM expectation (background) at different energy bins of M_{inv} spectra, CLs on the background or on the background+signal hypotheses can be derived. If the tested region of an M_{inv} distribution is in agreement with the SM at a 95% CL, the mass of the predicted BSM particle is considered as excluded in that energy region.

While the interpretation of resonance searches is generally straightforward and model independent (as long as interference effects are depreciable), the case of missing energy and LLP searches is more complex. For instance, the MSSM is composed by a large number of free parameters yielding a complicated interpretation of its collider signatures. If the number of parameters is reduced by considering (minimal) SUSY breaking scenarios, model specific patterns are introduced and potential interpretations could not be translated to alternative scenarios. Furthermore, optimizing a search for an specific scenario would mean that the general MSSM would be only partially tested. To overcome these issues, the concept of Simplified Model Spectra (SMS), also denoted as simplified models, has been introduced [84, 121, 122, 85]. The SMS approach was originally introduced in SUSY searches but their usage has now been extended to DM and LLP searches. The next section is dedicated to an overview on simplified models and their interpretation.

3.2 Simplified Model Spectra.

Simplified Model Spectra are sets of effective Lagrangian descriptions, called simplified models, designed to characterize a new physics model with a small number of kinematic parameters related to collider physics, namely particle masses, production cross-sections, and branching

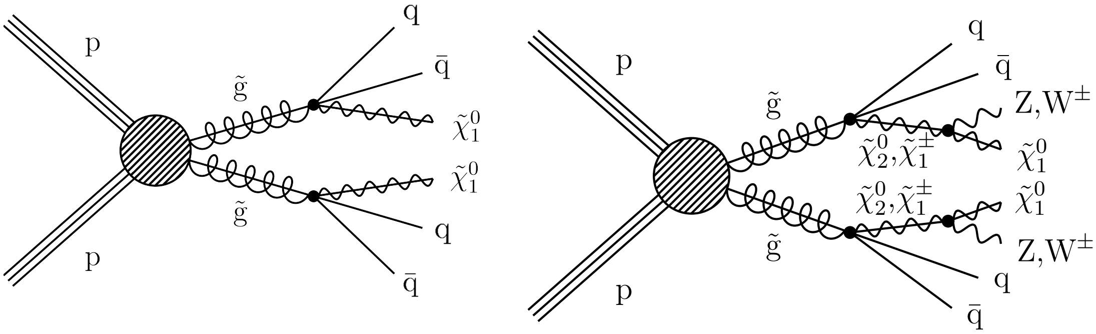

(a) T1

(b) T5WW,T5ZZ,T5WZ

Figure 3.1: Graphic representations of the T1 (left) and the superposition of the T5WW, T5ZZ and T5WZ topologies (right).

fractions[3], in a manner that is assumed to be sufficient to describe the essential phenomenology of the new physics model.

It is very advantageous to present new physics search results using simplified models. To start, it is desired that LHC searches cover as widely as possible popular BSM theories while remaining applicable to a broader range of theoretical models, in a straightforward manner. The SMS approach allows this. Furthermore, simplified model results encourage a strong communication between experimenters and theoreticians in the HEP community. They show a clear relation between the free parameters and the detector signatures yielding more transparent and instructive results. They allow experimenters to efficiently design and tune search strategies. Finally, they can be easily used to test a wide range of complete models that present similar topologies.

Simplified models were first introduced in new physics searches to represent generic scenarios of R-parity conserving SUSY models [123, 124, 125]. Their application was then rapidly extended to DM searches (see [126] for a compendium) and, more recently to LLP searches, with a list of topologies proposed by the LLP community found in [108]. Currently, most of ATLAS and CMS searches for new physics have chosen to present their results as constraints on simplified models [125, 124]. In them, a simplified model topology is defined by a set of hypothetical particles and a sequence of their production and decays and their corresponding signal-efficiency×acceptance ($\mathcal{A} \times \epsilon$) is computed for each signal region. From this, a 95% confidence level upper limit (UL) on the product of the cross section and branching fraction ($[\sigma \times \mathcal{B}]_{UL}$) is derived as a function of particle masses or, in the case of LLP searches, as a function of their lifetimes.
It is instructive to describe the general procedure to define a simplified model topology and derive its $[\sigma \times \mathcal{B}]_{UL}$ map trough an illustrative example. In here, we have chosen to use the T1 topology (schematized in 3.1(a)). Note that this topology corresponds to an R-parity conserving SUSY signature, hence proper of a missing energy SUSY search. At the end of this section, a few words on the key differences between SUSY, DM and LLP simplified models will be given.

The T1 topology corresponds to gluino pair production with both the gluinos directly decaying into a pair of light quarks and the lightest neutralino $\tilde{\chi}_1^0$:

$$\mathrm{p}\ \mathrm{p} \to \tilde{g}\ \tilde{g},\ \tilde{g} \to q\bar{q}'\tilde{\chi}_1^0. \tag{3.1}$$

leaving a signature of at least four hadronic jets plus missing energy in the ATLAS and CMS detectors. Since the produced gluinos have the same branching ratios (BRs), the legs in T1 are equal and the topology is considered symmetric.

---

[3] In LLP searches, lifetimes are also required.

This 3-body decay mode occurs in models where the squarks are heavy enough to become effectively decoupled. They arise from the operator

$$\mathcal{L}_{\text{int}} = \frac{\lambda_i^2}{M_i^2}\tilde{g}q_i\bar{q}_i\tilde{\chi}_1^0 + h.c., \tag{3.2}$$

where i runs over the different quark flavors, λ_i is the Yukawa coupling for the quark-squark-$\tilde{\chi}_1^0$ vertex, and M_i is the effective scale of the interaction.

Alternatively, a simplified model spectrum can include an intermediate state. For instance, the gluino can go trough a 3-body decay to either a chargino or a heavier neutralino that subsequently decays into a neutral LSP plus a charged boson ($W^{\pm}$) or a neutral boson (Z or H), respectively

$$\tilde{g} \to q\bar{q}'\tilde{\chi}^{\pm} \to q\bar{q}'(W^{\pm}\tilde{\chi}_1^0) \;\text{ or }\; \tilde{g} \to q\bar{q}'\tilde{\chi}'^{0} \to q\bar{q}'(Z\tilde{\chi}_1^0). \tag{3.3}$$

forming a one-step cascade decay. This translates into 3 possible topologies different from T1, namely T5WW, T5ZZ, and T5WZ. They are illustrated in Fig. 3.1(b)). In each one, is assumed that $\text{BR}(\tilde{\chi}_2^0 \to \tilde{\chi}_1^0 + Z) = \text{BR}(\tilde{\chi}_1^{\pm} \to \tilde{\chi}_1^0 + W) = 1$. It is important to note that the decays $W^{\pm}$ and Z^0 (or H) have different leptonic decay modes. In hadronic searches, this is seen as a different fraction of the events that are truly hadronic and the presence of $W^{\pm}$s decaying into non-vetoed leptons.

As mentioned before, a simplified model is described by a minimal set of parameters. The T1 topology is parametrized by $m_{\tilde{g}}$ and $m_{\tilde{\chi}_1^0}$ and $\sigma(\text{p p} \to \tilde{g}\;\tilde{g})$. In the case of the T5WW, T5ZZ, and T5WZ toplogies, the mass of the intermediate particle $m_{(\tilde{\chi}^{\pm},\tilde{\chi}'^{0})}$ and the BR of $\tilde{g}$ to $\tilde{\chi}^{\pm}, \tilde{\chi}'^{0}$ extend the number of parameters. To reduce the number of variables, is customary to set the BRs at 100% for each simplified model and construct linear combinations of them to study models with different decay modes. For further simplification, since it is difficult to present limits on a four-dimensional space (specially on printed paper), it is often preferred to set the mass of the intermediate particle as dependent on the parent particles (here $m_{\tilde{g}}$) and the daughter particles (here $m_{\tilde{\chi}_1^0}$) by following the relation

$$m_{(\tilde{\chi}^{\pm},\tilde{\chi}'^{0})} = m_{\tilde{\chi}_1^0} + r(m_{\tilde{g}} - m_{\tilde{\chi}_1^0}), \tag{3.4}$$

where r can be fixed to different values covering different kinematic cases.

Let us now describe the procedure to derive upper limit maps. As explained in [125], the first step is to apply event selection on simulated simplified model events to obtain the corresponding $\mathcal{A} \times \epsilon$ as the ratio between the number selected events and the total number of generated events. This is done for different values of the parent and daughter particles to form an $\mathcal{A} \times \epsilon$ map. As an example, in the left side of Fig. 3.2 an $\mathcal{A} \times \epsilon$ map corresponding to the T1 topology is shown as a function of $m_{\tilde{g}}$ ans $m_{\tilde{\chi}_1^0}$. Afterwards, the $\mathcal{A} \times \epsilon$ together with the background estimations and their uncertainties are used to compute a 95% confidence level upper limit on the cross section times branching ratio $[\sigma \times \mathcal{B}]_{UL}$, following the CLs criteria. Doing this for every point in the $\mathcal{A} \times \epsilon$ map results in a corresponding upper limit map like the one on the right side of Fig. 3.2. Finally, a lower limit on the particle masses of a simplified model is derived by comparing $[\sigma \times \mathcal{B}]_{UL}$ with the predicted σ.

Limits on particle masses derived from single simplified models are often conservative compared to the real exclusion line. The reason is that different simplified models can populate the same SR, increasing the signal expectation. For instance, T5WW, T5ZZ, and T5WZ all represent a 8-jet+ E_T^{miss} signature, so the same signal region is sensitive to all of them. In fact, limits from these toplogies have been presented directly in the form of a composite T5VV topology in [127]. Thus, a more accurate constrain can be obtained when combining topologies with similar expected signatures. The overall limit will then depend on the efficiencies of each topology and

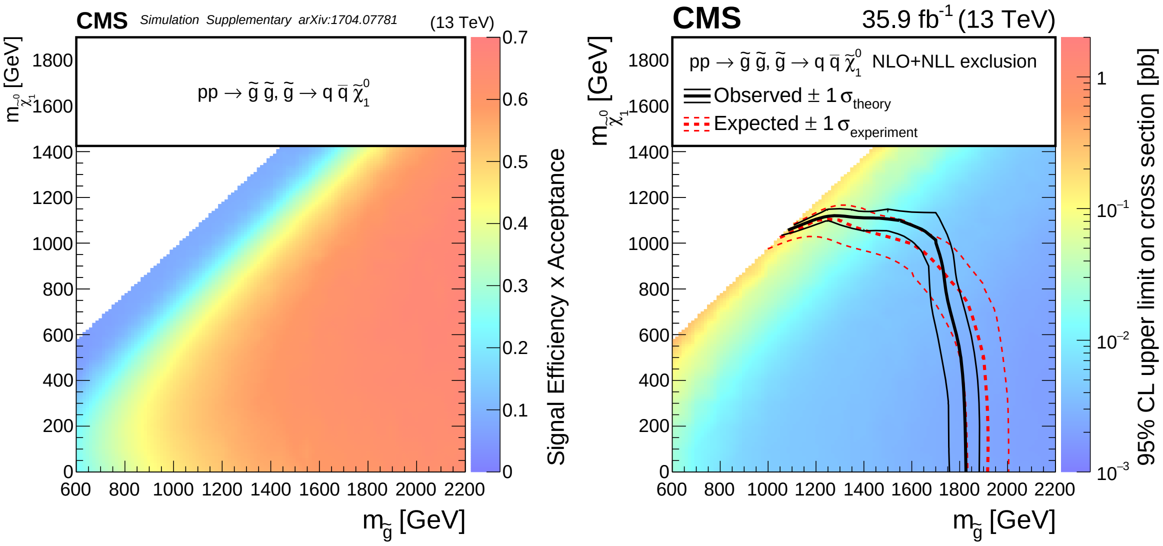

Figure 3.2: $\mathcal{A} \times \epsilon$ map (left) and upper limit map (right) of the T1 from CMS-SUS-16-033 [127].

on the relative branching ratio of decay into the allowed channels. The enhanced σ_{UL} limit is obtained by evaluating the appropriate efficiency for each component and adding the individual signal predictions, before comparing them against the total limit on the number of signal events N_{UL}. For simplicity, consider the case of two symmetric topologies A and B, with corresponding $\epsilon_{A,B}$ efficiencies and $\mathrm{BR}_{A,B}$ branching ratios. In there, σ_{UL} would be computed as:

$$\sigma_{UL} = \frac{N_{UL}}{\mathrm{BR}_A^2 \epsilon_A + \mathrm{BR}_B^2 \epsilon_B}, \tag{3.5}$$

where BR is squared to take the BRs of the two legs in each topology into account.

We close this section by sketching the key differences between the simplified models in SUSY, DM and LLP searches. In SUSY searches, simplified models often rely on a series of generalizations that reduce to model dependencies. To start, the production process is ignored and only on-shell particles are considered. Furthermore, only the on-shell decay products are described since virtual particles are replaced by an effective vertex. Thus, SUSY simplified models are solely described by the masses and decay rates of the involved BSM particles and by the production cross sections of the initial ones. In the case of DM simplified models, these assumptions usually don't hold. As discussed in Sec. 3.1 the identification of DM signals relies on the associated production of SM particles. This means that the interpretation of DM searches strongly depends on the detailed production processes. Hence, DM simplified models are designed with an explicit light mediator of the interaction between DM and SM particles. As for LLP simplifed models, a key feature that differentiates them from those SUSY and DM searchess, is their dependency on the lifetimes of the long lived components. Furthermore, the last final states are not necessarily E_T^{miss}, they can be an observed LLP like an HSCP or an R-hadron. The diverse variety of LLP signatures translate into several possibilities of interesting simplified models. In [108] a list of proposed topologies has been put forward aiming for a wide coverage of signatures by defining LLP simplified models as general as possible.

3.3 Reinterpretation of LHC results.

Regardless of the extensive program of searches performed by ATLAS and CMS, no new physics has been found yet at the LHC. Nonetheless, a vast portion of the BSM theory landscape has not been explored. On the one hand, mass limits derived in the context of simplified models are based on simple scenarios of a new physics model, thus can significantly change in more realistic realizations of the same theory. On the other hand, there is a long list of not-so-popular or beyond-vanilla theories that are not directly tested by the experiments. Hence, the re-interpretation of LHC searches is very well motivated and has become a very active field. An overview of it's current status is provided in [86], by the LHC Reinterpretation Forum.

There are mainly two approaches for re-interpretation of new physics searches. The first one is very fast but conservative. It is based on recasting $[\sigma \times \mathcal{B}]_{UL}$ and efficiency maps from simplified models, presented by the experiments, to directly compare them against the SMS topologies of a BSM theory. This approach will be only briefly presented in Sec. 3.3.1 while a more detailed discussion is offered in Sec. 4 in the context of the `SModelS` tool. The other one is a more general but more time consuming approach since it relies on full event simulation. It's main idea is to fully model the signal events and detector response followed from the production of new physics particles and then apply to them the signal selection cuts used by the experimental analyses to compute signal efficiencies.

Moreover, recent years have seen the appearance of re-interpretation boosted by ML techniques. They are being used in the process of generalization of likelihoods or exclusion limits. Model exclusion boundaries or likelihood (ratios) can be learned, explored and provided for further use using ML models. For example, SUSY-AI [128], is based on a neural network trained to classify parameter points from the pMSSM as excluded or allowed.

Finally, SM measurements can also be used to constrain BSM theories. This has been done both in the context of EFT Lagrangians [129, 130] and, more recently for explicit simplified BSM scenarios [131], without the need for further detector simulations[4]. An alternative approach, in which measurements are desgined with BSM measurements in mind, has been proposed in [132]. Given the scope of this thesis, reinterpretation of SM measurements will not be further discussed here but the interested reader is refered to [86].

3.3.1 Reinterpretation of SMS results.

Nowadays, most ATLAS and CMS searches for new physics present their results as upper limit and efficiency maps in the context of simplified models. Furthermore, they present limits on the masses of the particles that constitute the simplified model topologies. As described in Sec. 3.2, the outcome are efficiency and upper limit maps like the ones shown in Fig 3.2. However, such limits can significantly change for more realistic scenarios of the same theory [5] or for different theories presenting similar topologies. Fortunately, results presented in the simplified model framework are relatively straightforward to re-interpret in the context of different new physics models. This follows from the assumption that efficiencies or upper limits remain approximately valid for a generic model predicting the same signature as the simplified model. Thus, one can directly compare the $\sigma \times \mathcal{B}$ at given points of the generic model with the corresponding $[\sigma \times \mathcal{B}]_{UL}$. Alternatively, one can also use efficiency maps to compute the expected signal events and the corresponding yields. For example, in Sec. 5.2 we follow this approach to derive first limits on the gluinos and squarks of the MDGSSM. For that, we recasted, among others, the upper limits from Fig. 3.2.

Realistic models often have a large number of combinations of production channels and decay modes, thus the task of comparing each one of them to a corresponding experimental result turns into a very laborious one. Fortunately, dedicated tools have been implemented that automatically decompose BSM scenarios into simplified model topologies and automatically compare them with

---

[4] This is possible since SM measurements are presented in the context of truth-level (hadron-level) events.

[5] This was explicitly shown in [133] for the pMSSM.

the experimental results. Currently, a tool that applies this approach to generic BSM scenarios presenting a Z_2 symmetry is `SModelS` [134, 135]. The general concept behind this tool will be discussed until Chapter 4. There are also tools deviced for specific models, such as `HiggsBounds` [136, 137], intended for multi-Higgs models, `ZPEED`, [138] focused on Z' resonances, and `DarkCast` [139], devised for dark photon models.

3.3.2 Reinterpretation based on full event simulation.

When a tested parameter point splits into a large number of channels, as is typically the case of complex BSM models, or the cross section corresponding to missing topologies (i.e. the fraction of non available simplified model) is large, the limits that can be obtained with the SMS approach become very conservative. Alternatively, it is possible to reproduce an experimental analysis by means of full simulation of LHC events with Monte Carlo (MC) event generators followed by the simulation of the detector response. This is a more general and often more stringent approach, since it doesn't rely on the availability of simplified model results and can use the full spectra of the model to compute the signal efficiencies. However, it has the drawback of being more time consuming and harder to implement, as it requires the full simulation of a large number of events and a detailed description of the original experimental set-up. Furthermore, so far its only applicable to cut-based analyses.

The general idea of this approach is to compute the expected signal efficiencies of BSM processes that would be measured by a cut-based analysis. This is achieved by implementing the same selection cuts in the analyses and computing the ratio of selected events over the total number of events produced.

Evidently, it is essential to be able to accurately simulate the signal events resulting from a hard collision, given a new physics model. Furthermore, most searches for new physics are not unfolded, i.e. they are parametrized by detector-level (reconstruction-level) events, hence the detector response also has to be properly simulated. Fortunately, all this can be achieved with a set of dedicated tools.

The tools dedicated for event simulation are known as general purpose MC event generators. They are very important in high energy physics and a vital item in any experimenter's (and in many theorist's) tool-box, as they allow to make predictions on collider experiments for a theoretical model or in other words, to map the theoretical prediction of a measurement onto the experimental result. Furthermore, experimental collaborations often rely on Monte-Carlo event generation for designing and optimizing specific analysis strategies.

Before presenting the current landscape of reinterpretation tools based on full event simulation, let us briefly describe the complicated task of recreating the full process of a hard collision event all the way to the detector response. This can be divided in three steps: parton-level event generation, simulation of hadronisation and showering and emulation of the detector response. For each one, specific tools are used. Several frameworks, such as `MadGraph5_aMC@NLO` [140], interface them for an automatized production of events.

- *Parton-level event generators.* The first stage of an event, known as *parton-level*, is conformed by the elementary particle production resulting from proton collisions trough elementary processes. At this stage the effects of color confinement are not yet taken into account, hence the final states are mainly composed of bare quarks and gluons.

  Parton-level generators automatically generate matrix elements to describe a specific final state at leading order (LO) in perturbation theory, i.e. they compute the LO cross section of the production process. Recently, automatic calculations of NLO corrections have been included [140, 141]. To describe the incoming partons they employ implementations of PDFs, internally described or selected from the `LHAPDF` [142] framework. The probabilistic distribution of the outgoing particles are computed from the leading order perturbation theory description of the process. A widely used dedicated tool is `MadGraph5` [140] which outputs parton-level events using the `LHE` format [143].

- *Simulating showering and hadronization.*

  The resulting partons from the hard process (as well as the partons from initial state radiation) will branch out into a cascade of radiating partons with deacreasing momentum, forming a *parton-shower* that fills the space with mostly soft gluons. In MC generators the parton showers can be simulated as a sequential step-by-step process formulated as an evolution of a transferred momentum that decreases at each step until perturbation theory is no longer applicable. When this point is reached, color confinement takes over to group the partons into colorless hadrons, in a process known as *hadronization*. Dedicated tools such as `PYTHIA` [144, 145], `HERWIG` [146] and `Sherpa` [147, 148] are extensively used to simulate both the parton showering and hadronization giving as output hadronised events (often referred as truth- or particle-level MC events) on a `HEPMC` [149] format.

- *Detector simulation.*

  The last step is to emulate the detector response. There are mainly two ways currently used by the reintepretation community. The first one is to use the fast detector simulator `DELPHES` [150] as it provides a fast way of reproducing the detector response from hadronised events. In `DELPHES`, analysis objects, such as jets, missing energy and isolated electrons are reconstructed from a realistic simulation of the propagation of the stable (within the detector) SM particles trough the calorimeters, while their energy is deduced by smearing the long-lived particles' momenta according to the detector resolution. Futhermore, `DELPHES` is a multi-purpose simulator in the sense that it can be used to simulate the response of different LHC (or future) experiments. The other way is known as the 'smearing+efficiency' approach. This is implemented, for instance, in the `RIVET` framework [151, 152]. The main idea is the use of effective transfer functions to map physics objects from truth-level to detector-level. This is done by 'smearing' truth-level event kinematics with resolution functions in conjunction with reconstruction efficiencies.

Once with a set of simulated events, what follows is to apply the selection cuts implemented by the analyses. By doing so, one obtains the efficiency of the signal ϵ. Then, the number of expected signal events n_s are computed as:

$$n_s = \epsilon_s \mathcal{L} \sigma \tag{3.6}$$

where $\mathcal{L}$ is the integrated luminosity (provided by the experiment) and σ is the total cross section of the production process. Finally, n_s is used, together with the observed and expected number of (SM) background events provided by the analyses, to compute the 95% CL level of exclusion using the CLs prescription, or alternatively, the %95 CL upper limit on σ.

Currently, there are a number of public tools, that can either take detector level events or smear truth-level ones and apply selection cuts on them to derive constraints on new physics scenarios:

- `CheckMATE` [153, 154] takes the output from `DELPHES` to derive signal efficiencies using the cut-based analyses implemented in it's database. Since the release of `CheckMATE 2`, it is possible to generate events using `Pythia` or `MadGraph5_aMC@NLO` within the same framework. Furthermore, new analyses can be implemented by external users with the `CheckMATE` AnalysisManager [155].

- `MadAnalysis 5` [156, 157] also relies on `DELPHES` to obtain detector-level events. The list of available analyses is found in it's Public Analysis Database (PAD) [158, 157] which can be automatically installed locally. Users are encouraged to validate and add to the PAD any analysis implemented within the `MadAnalysis` framework. Furthermore, `MadAnalysis 5` has been integrated to `MadGraph5_aMC@NLO`. Finally, it is now possible to use efficiency and smearing functions for detector emulation with MadAnalysis [159].

- `ColliderBit` [160] is the `GAMBIT` framework [161] module devoted to reinterpretation of collider results. It follows the 'smearing+efficiency' approach for detector simulation by means of the `BuckFast` routines and the published efficiency functions from the individual experiments.

- `Rivet` [162, 151] was originally established as a toolkit and library of collider event analyses at truth level. However, since the release of v2.5.0 it comes with a detector efficiency and kinematic smearing system trough which truth-level events are passed, allowing the reinterpretation of reconstruction-level BSM search results.

- `adl2tnm` [163] and `CutLang` [164, 165] parse and run analysis logic written under the recently developed domain-specific language ADL [166, 1], designed with intuitive keywords to specify analysis objects and operators. Specifically, `adl2tnm` is a `Python` code that writes `C++` analysis code from ADL files while `CutLang` is runtime ADL interpreter. Both packages can take a variety of event formats. A repository of LHC analyses implemented in the ADL language is available in [167]. Furthermore, a parser from ADL to `Rivet` is also under development.

All the tools described above provide a clear road-map for re-interpreting searches for promptly decaying new particles. However, a standard framework doesn't exist yet for LLP searches. The reason being that this type of searches rely on detector-dependent definitions of reconstructed objects, hence fast detector simulators require to be significantly adapted. Nonetheless, several implementations of LLP searches have been performed by following different approaches. Some of them have been made public via the 'LLP Recasting Repository' or are available in some of the aforementioned frameworks. Two examples are:

Displaced jets with truth-level events. In [168] the CMS search for displaced di-jets [169] was implemented. The followed approach involved taking truth-level information and use it to reconstruct the various vertex, cluster, and track-level observables of each event. To estimate the reconstruction efficiencies, the authors computed truth-level efficiencies from signal models, identical to the ones used by the experiment, and normalized them to the analysis results. The obtained ratios were then used to re-scale truth-level efficiencies from other models. For validation, the ratios were compared for different LLP masses and kinematics, obtaining an agreement at a factor-of-two level.

Displaced Leptons with a customised `DELPHES` version. The CMS search for displaced leptons [106] has been implemented in `MadAnalysis` relying on a customized version of `DELPHES`[6] (dubbed `DELPHES-LLP`) available within the `MadAnalysis` framework [170]. It was originally designed to handle neutral LLPs decaying into leptons within the tracker but can be extended to simulate neutral LLPs decaying into muons outside the tracker or charged LLPs with leptonic decays.

---

[6] From v3.4.1, the standard DELPHES includes the features of the customised version.

Chapter 4

SModelS. Recent developments.

The nature of the SMS approach allows us the possibility of deriving constraints on a wide variety of BSM theories. Furthermore, since event simulation is not necessary, these constraints are rapidly derived. It is with this spirit that the `SModelS` tool was conceived.

In `SModelS` a general procedure to decompose BSM theories, presenting a Z_2 symmetry, into simplified model topologies is implemented. Followed by an automatic matching between the produced topologies and the corresponding simplified model results in its large database. It provides detailed information on the relevant topologies that are not covered by any result in the database. Moreover, `SModelS` comes with a set of auxiliary 'smodelsTools' that make for more efficient phenomenological studies.

`SModelS` is under constant development. In the first version of the tool, only UL maps from SUSY searches where included in the database, however by v1.1 efficiency maps started to be included. Afterwards, v1.2 (the current at the time of this writing) arrived with several new features. First, by considering the lifetime of Z_2-odd particles, the type of searches in the database was extended to include HSCP and R-hadron searches. Second, it now allows for a combination of signal regions in effciency map results by means of covariance matrices provided by the experiments. Third, smodelsTools now includes an interactive plots maker[1] for an easier visualization of the results from a model scan. Finally, several other improvements were included to increase the user-friendliness, such as the use of wildcards in the selection of experimental results and a faster database that can be given as a URL. The database is also constantly growing, with releases independent of the tool itself. Current version of the database is v1.2.3.

In Sec. 4.1 `SModelS` general concept is described, followed by an overview of the current database in Sec. 4.2. Afterwards, the main improvements in `SModelS` v1.2 will be detailed in Sec. 4.3, based on the official publication [135]. The complete description of the implementation, functionalities and general usage of `SModelS` can be found in the online manual[2].

4.1 General concept.

`SModelS` [134], is a public tool that, based on a general procedure to decompose BSM collider signatures into SMS topologies, provides a way to cast BSM predictions for the LHC in a model independent framework, which can be directly confronted with the relevant experimental constraints on simplified model topologies. `SModelS` currently focuses on BSM models with a Z_2 symmetry, SUSY or non-SUSY. As schematized in Fig. 4.1, it is made of three key ingredients

---

[1] The author of this thesis was heavily involved in the development of this tool.

[2] https://smodels.readthedocs.io/en/latest/index.html

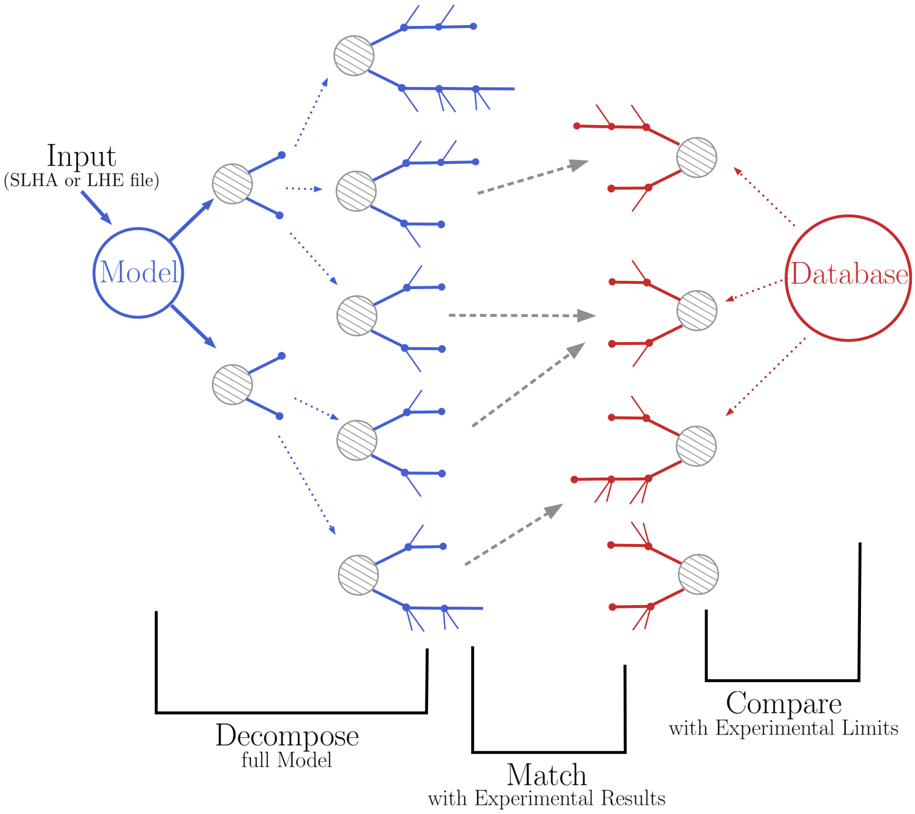

Figure 4.1: `SModelS` scheme.

- The decomposition of the BSM spectrum into SMS topologies.
- A database of experimental SMS results.
- The interface between decomposition and results database.

The `SModelS` implementation is based on assuming that the signal efficiencies from the experimental searches in its database depend mostly on the event kinematics and are just sightly affected by the details of the BSM model. For instance, simplified models from DM searches are not included in `SModelS` since they are generally model dependent. Furthermore, it remains the responsibility of the user to apply `SModelS` only to models and experimental results for which this assumption is approximately valid.

The general re-interpretation procedure of the `SModelS` framework, as detailed in [134] works as follows. First, all the signal topologies appearing in the full BSM spectrum are computed, together with their respective cross section times branching ratios $\sigma \times \mathcal{B}$, here called weights. Since only models with a Z_2 symmetry are considered, all the possible signal topologies will correspond to pair production of Z_2-odd particles P that decay as $P \to P' + \text{SM}$. The general picture of a resulting topology is shown in Fig. 4.2, where the production of a pair of Z_2-even BSM states and their subsequent cascade decay is schematized. All the relevant information in each topology is reduced to the number of vertices and SM final state particles in each vertex, the masses of all the conforming BSM particles, and the diagram weight $\sigma \times \mathcal{B}$.

As a consequence of the decompositon, the full model has been transformed into a group of SMS topologies, whose only information are the masses and weights $\sigma \times \mathcal{B}$ associated to each one of them. This prepares the next step of the procedure: confronting the obtained theoretical predictions of the group of SMS topologies with the experimental constraints. To do this, `SModelS`

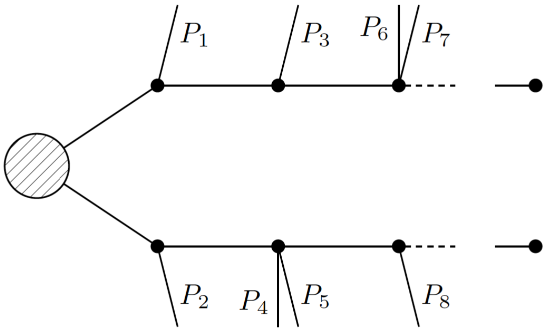

Figure 4.2: Graphic representation of a general SMS topology in a model with a Z_2 symmetry.

automatically compares each signal topology from the decompositon with the SMS topologies constrained by experimental analyses. This is fairly trivial when the analysis provide an $[\sigma\times\mathcal{B}]_{UL}$ map for a single toplogy as a function of the masses of the relevant BSM particles. For example, constraints on the T1 are normally presented individually as function of $m_{\tilde{g}}$ and $m_{\tilde{\chi}_1^0}$. However, it often happens that analyses constrain the sum of several topologies instead of the constituent ones. For instance. in [127] constraints are shown for the composite T5VV topology rather than on the T5WW, T5ZZ and T5WZ topologies individually. In such cases, `SModelS` combines the signal topologies according to the individual contributions to the total $\sigma\times\mathcal{B}_{UL}$ assumed by the experimental search. Once this is done, the resulting theoretical predictions for the cross sections of the combined topologies can be directly compared to the experimental upper limits. Finally, the result is presented as

$$r = \frac{\sigma\times\mathcal{B}}{[\sigma\times\mathcal{B}]_{UL}} \tag{4.1}$$

where if $r > 1$, the theoretical prediction would be considered as excluded.

Alternatively, `SModelS` can also use efficiency map results to confront theoretical predictions. These kind of results often provide the efficiencies corresponding to different signal regions at each point. The corresponding upper limits are computed using the number of observed and expected events and the corresponding uncertainties, for each SR at each point. By default, `SModelS` keeps only the UL of the best SR (i.e. largest ratio (theory prediction)/(expected limit)) or, if a covariance matrix is available, the UL after SR combination.

4.2 The database.

`SModelS` contains a large and regularly updated database of validated SMS results from ATLAS and CMS. Since v1.1 [171], two types of experimental results are used:

- *Upper Limit (UL) results* contain the experimental constraints on the cross section times branching ratio ($\sigma\times BR$) for simplified model or a combination of them. These constraints are typically given in the format of UL maps, which correspond to 95% CL upper limit values on $\sigma\times BR$ as a function of the respective parameter space (usually BSM masses or slices over mass planes). Their advantage is that the statistical evaluation drawn from the measured efficiencies, are already done by the experimental collaborations. Moreover, they usually assume the best signal region (for a given point in parameter space), a combination of them or more involved limits from other methods. However, this means that the interpretation of UL maps is restricted to constraining signal topologies individually.

- *Efficiency Map (EM) results* constrain the total signal ($\sum\sigma\times BR\times\epsilon$) in a specific signal region[3]. They correspond to a grid of simulated acceptance times efficiency ($\mathcal{A} \times \epsilon$) values for a specific signal region for a specific simplified model. Furthermore, additional information, such as the luminosity, number of observed and expected events is also stored in a EM-type result. EMs are either directly provided by the experimental collaborations or computed by the theory groups by means of full event simulation. A useful property of this kinds of results is that they can be used to constrain combinations of simplified models that contribute to the same SR. Moreover, when covariance matrices are provided by the experimental collaborations, contributions from different signal regions can be combined.

At the time of redacting this thesis, the current version of the database is v1.2.3 [172]. It comprises 3246 individual maps from 397 distinct signal regions and 96 different SMS topologies, from a total of 96 ATLAS and CMS analyses. From Run 1, it includes results from 25 ATLAS and 18 CMS 8 TeV searches. From Run 2, results from 23 ATLAS and 30 CMS 13 TeV searches are present, including 3 UL and 8 EM maps from CMS LLP searches. The complete list of the results that compose this version is found in https://smodels.github.io/docs/ListOfAnalyses.

4.3 Developments in `SModelS` v1.2.

With the publication of v1.2 [135], `SModelS` announced several new developments. First, while previous versions were restricted to missing energy signatures and assumed prompt decays within each decay chain, the current one now considers the lifetime of each Z_2-odd particle and appropriately takes into account missing energy, heavy stable charge particle and R-hadron signatures. This is detailed in Sec. 4.3.1. Second, `SModelS` now allows for a combination of signal regions in efficiency map results whenever a covariance matrix is available from the experiment. This important step towards fully exploiting the constraining power of efficiency map results, is explained in Sec. 4.3.2. Futhermore, smodelsTools now provides an interactive plots maker to conveniently visualize the results of a model scan. This is discussed in Sec. 4.3.3. Finally, several other improvements that increase the user-friendliness, such as the use of wildcards in the selection of experimental results, and a faster database which can be given as a URL are not discussed here but can be found in [135].

4.3.1 Combination of signal regions.

Methodology.

If the experiment provides a covariance matrix together with efficiency maps for SMS topologies, the signal contributions in different signal regions can be combined [173, 174].[4] This is implemented in `SModelS` v1.1.3 onwards following the (symmetric) simplified likelihood approach of [173], and easily extendible to the more general treatment described in [174] once experimental results are available in that format.

SModelS allows for a marginalization as well as a profiling of the nuisances, with profiling being the default. As CPU performance is a concern in `SModelS`, we try to aggregate the official results, which can comprise a very large number of signal regions, to an acceptable number of aggregate regions. Here “acceptable” means as few aggregate regions as possible without significant loss in precision or constraining power. The CPU time required scales roughly linearly with the number of signal regions, so aggregating e.g. from 80 to 20 signal regions means gaining a factor of four in computing time.

---

[3] Here $\epsilon \equiv \mathcal{A} \times \epsilon$.

[4] With or without covariances, EMs are needed *for all signal regions.* Since the best SR can change depending on the model being tested, a single map containing the efficiencies for the best SR in each bin cannot be used in a general way.

For the computation of the 95% confidence level from the likelihoods, a $\mathrm{CL}_s (= \mathrm{CL}_{sb}/\mathrm{CL}_b)$ limit [175] is computed from the test statistic q_μ, as described in section 2.4, Eq. (14), in [176]. We then search for $\mathrm{CL}_s = 0.95$ using Brent's bracketing technique through the SciPy optimize library, see [177].

When using `runSModelS.py`, the combination of signal regions is turned on or off with the parameter combineSRs described in the previous section. Per default, combineSRs=False, in which case only the result from the best expected signal region (best SR) is reported. If combineSRs=True, both the combined result and the result from the best SR are quoted. If the user writes his/her own python code, the combination of SRs is envoked by setting combinedResults=True in `theoryPredictionsFor()`. In the same instance, one can switch between profiling and mariginalizing with marginalize=True/False, False being the default. An explicit example is discussed in the "How To's" of the online manual [178].

Example case.

The CMS SUSY group is providing covariance matrices for most of their analyses, so far under the assumption of Gaussian errors. However, by the time `SModelS` v1.2 was released, only two CMS analyses also provide simplified-model efficiency maps for each SR: CMS-SUS-16-050 [179] and CMS-PAS-SUS-16-052 [180].[5] Since the former analysis has significantly non-Gaussian background uncertainties, as we have checked, the covariance matrix provided for it is not a good approximation [174]. For this reason, only the covariance matrix for CMS-PAS-SUS-16-052 was included in `SModelS` v1.2.

Concretely, CMS-PAS-SUS-16-052 is a search for supersymmetry with compressed mass spectra in events with at least one soft lepton, moderate to high values of missing transverse momentum $p_T^{\rm miss}$, and one or two hard jets, compatible with the emission of initial-state radiation. It targets scenarios of stop-pair production, $pp \to \tilde{t}_1\tilde{t}_1^*$, where the mass difference to the $\tilde{\chi}_1^0$ is smaller than the mass of the W boson. The analysis has 44 SRs. The simplified model interpretations assume either four-body stop decays, $\tilde{t} \to bf\bar{f}'\tilde{\chi}_1^0$ (T2bbWWoff) or decays via an intermediate chargino, $\tilde{t} \to b\tilde{\chi}_1^+$, $\tilde{\chi}_1^+ \to f\bar{f}'\tilde{\chi}_1^0$ (T6bbWWoff). Efficiency maps for all 44 SRs are provided for both simplified models.

Figure 4.3 shows validation plots for the T2bbWWoff simplified model, comparing the 95% CL cross section upper limit derived by `SModelS` to the official UL from CMS across the SMS mass plane for three cases: using only the best SR (top left), combining all 44 SRs (top right), and aggregating to 17 SRs before combination (bottom). The x and y axes are $m_{\tilde{t}}$ and $m_{\tilde{t}} - m_{\tilde{\chi}_1^0} \equiv \Delta m$, respectively, and the colour code shows $f_{\rm UL} \equiv \sigma_{95}^{ul}(\mathrm{CMS})/\sigma_{95}^{ul}(\mathrm{SModelS})$. A value of $f_{\rm UL} = 0.8$ means that our SR combination gives a 20% weaker limit than the official CMS result, a value of $f_{\rm UL} = 1.2$ means that it is 20% too aggressive. Also shown are the official exclusion line (black) and the exclusion line derived from `SModelS` (grey).

We see that using only the best SR leads to too weak a limit: the mean $f_{\rm UL}$ is about 0.6 and the mass limit is up to about 150 GeV too low—compared to the maximum reach of $m_{\tilde{t}} \approx 500$ GeV this is significant. In contrast, the combination of all 44 SR performs much better for reproducing the official CMS result. Aggregating the 44 original SRs to 17 speeds up the calculation by more than a factor 2 while still giving a result very close to the full combination. The same holds true for the T6bbWWoff topology. We therefore included the efficiency maps for 17 aggregated SRs as CMS-PAS-SUS-16-052-agg in the `SModelS` database. The covariance matrix is given in the `globalInfo.txt` file in the same folder. Combining 17 SRs takes less than 2 sec on an average 4-core Intel i5 desktop computer.

---

[5] Other CMS Run 2 SUSY analyses provide covariance matrices but no efficiency maps. ATLAS analyses typically give efficiencies for the best SR only; moreover they do not provide covariances.

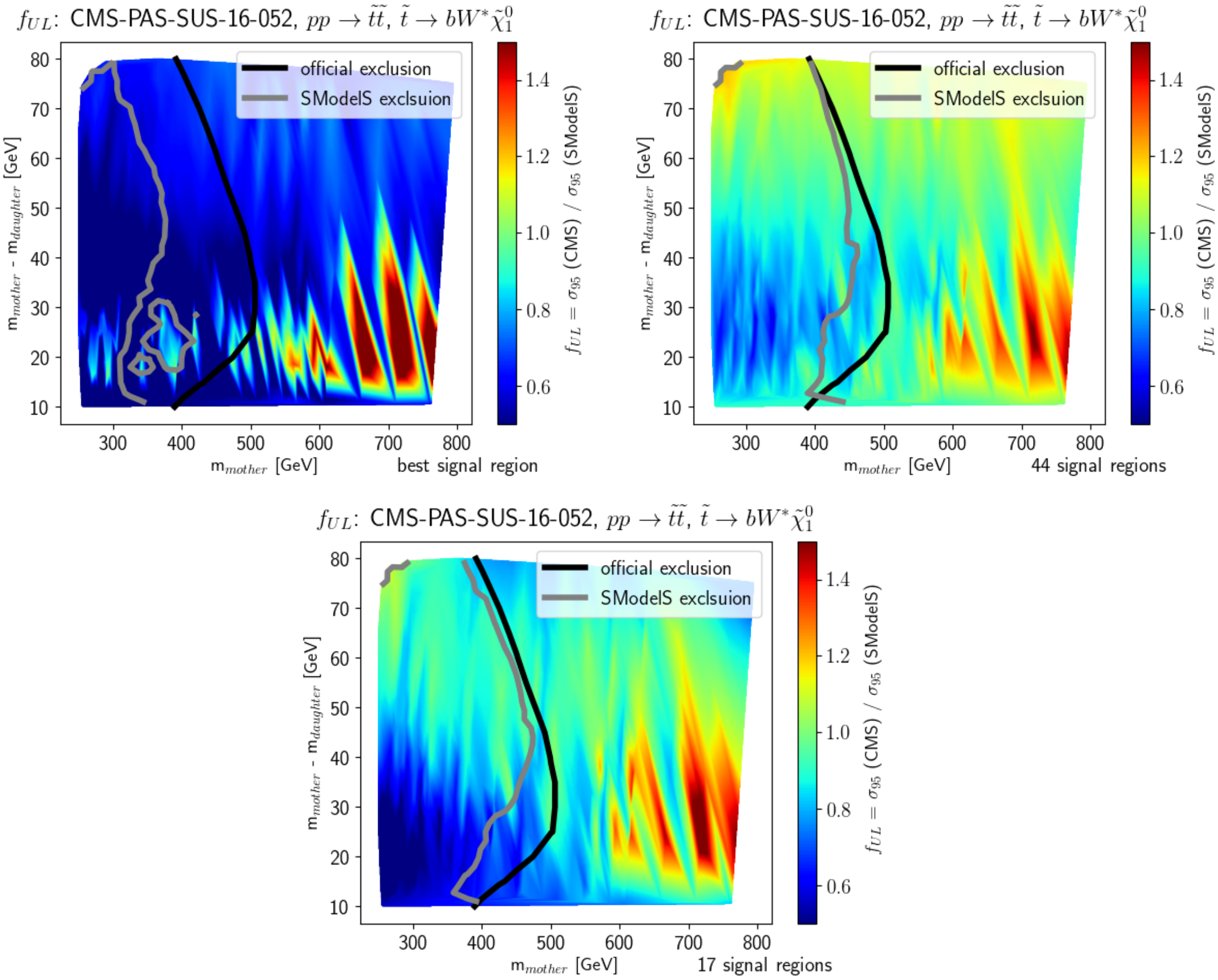

Figure 4.3: Comparison of exclusion curves from CMS-PAS-SUS-16-052 efficiency maps for the T2bbWWoff simplified model, using only the best signal region (top left), the combination of all 44 signal regions (top right) and the combination of 17 aggregate signal regions (bottom). The color map shows the f_{UL}-value obtained from dividing the official limit by the one obtained with `SModelS`. The grey lines indicate the `SModelS` exclusion $r = 1$. For comparison, the black line shows the official CMS exclusion curve.

4.3.2 Implementation of HSCP and R-hadron signatures.

The implementation of HSCP and R-hadron signatures required several important changes in theSModelS code as detailed below. For the user this is noticeable only in an extended output format in particular in the reporting of missing topologies, and a set of 10 new txnames (SMS topology definitions), which serve as a short-hand notation for the HSCP and R-hadron topologies.

Extension of decomposition procedure.

Taking the BSM particle masses, quantum numbers, total decay widths, branching ratios and total production cross-sections as input, `SModelS` performs a decomposition of the collider signature of any Z_2 symmetric BSM model into a coherent sum of simplified-model topologies. The resulting topologies exhibit a two-branch structure emerging from the production of twoZ_2-

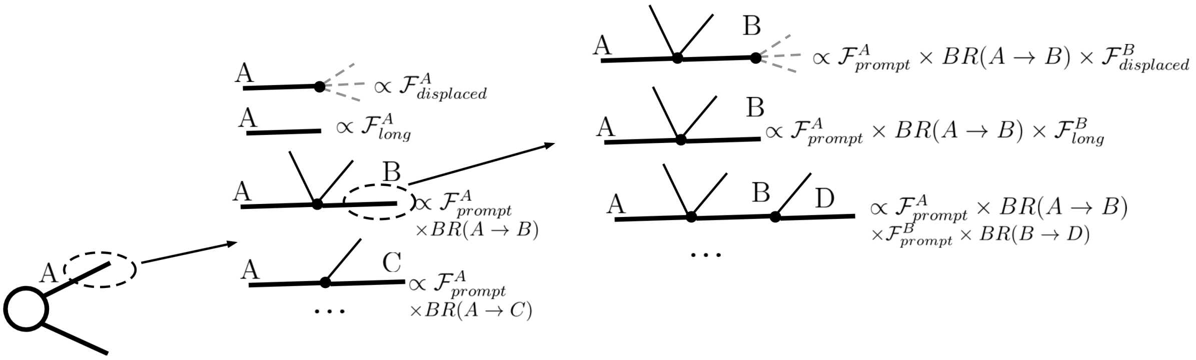

Figure 4.4: Decomposition into simplified model topologies and computation of weights in `SModelS` v1.2.

odd BSM states and their subsequent cascade decays. In the v1.0 and v1.1 releases, it was assumed that all BSM decays are prompt and that all cascade decays end in a stable neutral BSM particle leading to MET final states (otherwise, if `checkInput=True`, an error was issued). From v1.2 onwards this has been generalized in two ways.

First, instead of always assuming a MET final state, we allow each cascade decay to terminate in any BSM particle. Using the quantum numbers defined for the BSM particle, the final state is then classified as a MET signature, an HSCP or an R-hadron. If it does not fall in any of these categories, an error message is displayed.

Second, during the decomposition into simplified models, at each step in the cascade we compute the probabilities for the respective BSM particle to decay promptly ($\mathcal{F}_{\text{prompt}}$) and to decay outside the detector ($\mathcal{F}_{\text{long}}$) [181, 182]. The procedure is illustrated schematically in Fig. 4.4. The fraction of decays which take place inside the detector (labeled simply as "displaced decays") is approximated as $\mathcal{F}_{\text{displaced}} = 1 - \mathcal{F}_{\text{long}} - \mathcal{F}_{\text{prompt}}$. Note that the final states appearing in the displaced vertex are not stored during decomposition, since `SModelS` is currently not able to constrain displaced decay signatures; this is left for future work. As a result, for the time being, all elements with displaced decays will be identified as missing topologies.

Concretely, $\mathcal{F}_{\text{long}}$ and $\mathcal{F}_{\text{prompt}}$ are computed from the respective particle proper lifetime, τ, using the approximation

$$\mathcal{F}_{\text{prompt}} = 1 - \exp\left(-\frac{1}{c\tau}\left\langle\frac{\ell_{\text{inner}}}{\gamma\beta}\right\rangle_{\text{eff}}\right) \tag{4.2}$$

and

$$\mathcal{F}_{\text{long}} = \exp\left(-\frac{1}{c\tau}\left\langle\frac{\ell_{\text{outer}}}{\gamma\beta}\right\rangle_{\text{eff}}\right) . \tag{4.3}$$

We choose $\langle \ell_{\text{inner}}/\gamma\beta\rangle_{\text{eff}} = 1\,\text{mm}$ and $\langle \ell_{\text{outer}}/\gamma\beta\rangle_{\text{eff}} = 7\,\text{m}$,[6] which provides a good approximation to the result of a full simulation as shown in Appendix B of [182].

After decomposition the respective weight $\tilde{\sigma}$ of each simplified-model topology is hence given by

$$\tilde{\sigma} = \sigma_{\text{prod}} \left(\prod_i \text{BR}_i \times \mathcal{F}^i_{\text{prompt}}\right) \mathcal{F}^X_{\text{long/displaced}} \mathcal{F}^Y_{\text{long/displaced}} , \tag{4.4}$$

where σ_{prod} is the production cross section of the mother particles and X, Y are the Z_2 final states of the two cascades. The index i runs over all intermediate $\mathbb{Z}_2$-odd particles. For each chain, the

---

[6] As we currently include CMS results only, ℓ_{outer} corresponds to the CMS detector size. For the inclusion of ATLAS results $\langle \ell_{\text{outer}}/\gamma\beta\rangle_{\text{eff}}$ would have to be adjusted accordingly.

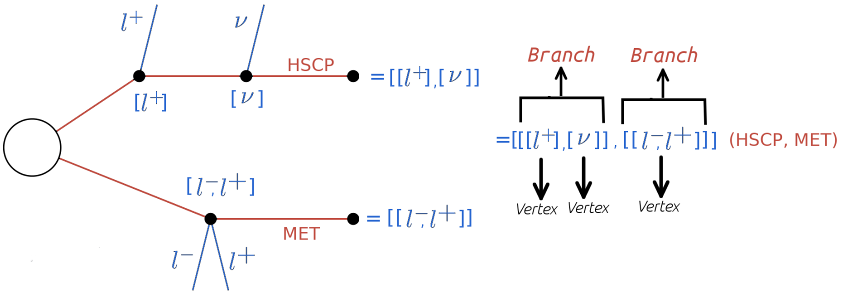

Figure 4.5: Extension of the `SModelS` bracket notation to include the $\mathbb{Z}_2$-odd final state description, in this example (HSCP, MET).

last probability factor is given by $\mathcal{F}_{\text{long}}$ for decays which take place outside the detector, or by $\mathcal{F}_{\text{displaced}}$ for displaced decays.

Extension of `SModelS` bracket notation

As explained in detail in [171], inside `SModelS` the structure and final states of elements are represented in textual form using a nested brackets notation. In order to fully specify all the information of a given SMS topology (an *element*), we must also include the list of masses for the Z_2-odd states, the list of Z_2-odd final states and the element weight. The masses for the Z_2-odd BSM states are represented by a mass array for each branch. An example is given in Fig. 4.5.

The quantum numbers of this BSM final state are essential for defining which type of signature this element represents. In an element the $\mathbb{Z}_2$-odd final state quantum numbers are mapped to final state signatures, as defined in the `particleNames` module. Currently the defined types of final states are: 'MET', 'HSCP', 'RHadronG', 'RHadronQ', the latter two being color-octet and color-singlet R-hadrons, respectively. New final state types can easily be added in this module.

HSCP and R-hadron results in the database

The v1.2.2 database includes results from the CMS searches for lepton-like HSCPs (carrying one unit of elementary charge), color-octet (gluino-like) R-hadrons and color-triplet (squark-like) R-hadrons at 8 TeV [110] and 13 TeV [109] center-of-mass energies. The relevant topologies and their short-hand notation ("txnames") in the `SModelS` database are summarized in Fig. 4.6.

We computed efficiency maps for the eight HSCP simplified-model topologies shown in Fig. 4.6. To this end, for the 8 TeV analysis we utilized the recasting provided in Ref. [183]. For the 13 TeV analysis we performed a dedicated recasting (see Appendix A of [182] for details). These efficiency maps are included in the `SModelS` v1.2.2 database.

For the R-hadron searches we only consider the direct production topologies TRHadGM1, TRHadQM1. As R-hadrons are strongly produced, their production via cascade decays is assumed to be less relevant and hence not considered here. We include the respective cross-section upper limits from Refs. [109, 110] considering the cloud hadronization model (assuming a 50% probability for gluino-gluon bound state formation as in [110]).

4.3.3 Interactive Plots Maker.

For a simple and quick visualization of results from a scan over input files, we now provide an "interactive plots maker" as part of `smodelsTools`. This tool allows to easily produce interactive plots which relate the `SModelS` output (*in python output format*) with information on the user's model stored in the SLHA files. It gives 2d plots in the parameter space defined by the user,

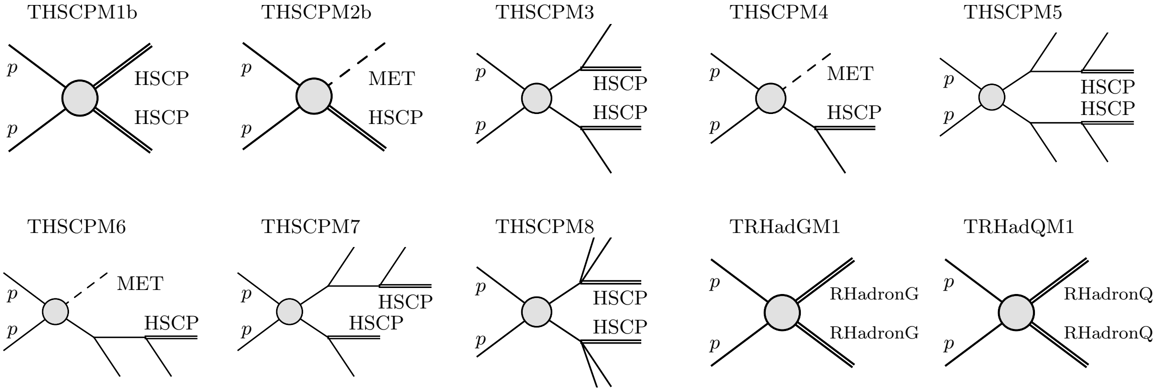

Figure 4.6: Simplified model topologies containing HSCP and R-hadron final states included in the `SModelS` v1.2.2 database. A double line represents an HSCP or R-hadron, while a dashed line represents an arbitrary decay chain terminating in a neutral LLP (providing a MET signature). The labels of the topologies correspond to the naming convention used in the database.

with additional user-defined information appearing in hover boxes. The output is in html format for viewing in a web browser. We stress that the aim is not to make publication-ready plots but simply to facilitate the user's analysis of, e.g., the properties of points in a scan.

The general usage of the `SModelS` interactive plots tool is:

```
smodelsTools.py interactive-plots [-h] [-p PARAMETERS]

       -f SMODELSFOLDER -s SLHAFOLDER [-o OUTPUTFOLDER]
       [-N NPOINTS] [-v VERBOSITY]
```

***arguments*:**

- **-h, --help** show this help message and exit.
- **-p PARAMETERS, --parameters PARAMETERS** path to the parameters file [./iplots_paramete
- **-f SMODELSFOLDER, --smodelsFolder SMODELSFOLDER** path to the smodels folder with the `SModelS` python output files.
- **-s SLHAFOLDER, --slhaFolder SLHAFOLDER** path to the SLHA folder with the SLHA input files.
- **-o OUTPUTFOLDER, --outputFolder OUTPUTFOLDER** path to the output folder, where the plots will be stored [./plots].
- **-N NPOINTS, --npoints NPOINTS** How many (randomly selected) points will be included in the plot. If -1, all points will be read and included [-1].
- **-v VERBOSITY, --verbosity VERBOSITY** Verbosity (debug, info, warning, error) [info].

The default values are given in [ ]. A typical usage example is:

```
./smodelsTools.py interactive-plots  \
    -f inputFiles/scanExample/smodels-output/  \
    -s inputFiles/scanExample/slha -p iplots_parameters.py  \
    -o results/iplots
```

The above command will read the `SModelS` output files (in python format) from the folder `inputFiles/scanExample/smodels-output`, the corresponding SLHA input files from `inputFiles/scanExample` and generate a set of HTML files with the interactive plots, which can be visualized with a regular web browser.

The settings in `iplots_parameters.py` include:

***plot_ title*:** main overall title for your plots, e.g. the model name.

***x and y axes:*:** axis label, SLHA block and PDG code number of the variables you want to plot, in a python dictionary form. Example:[7]

```
variable_x = {'m<sub>gluino</sub>': ['MASS', 1000021]}
variable_y = {'m<sub>LSP</sub>': ['MASS', 1000022]}
```

***spectrum hover information*:** defines which information from the input SLHA file will appear in the hover box. The syntax is again a python dictionary.

- `slha_hover_information`: information from the input SLHA file, e.g. model parameters or masses. Example:
  `slha_hover_information = {'m(gluino)': ['MASS', 1000021],`
  `'m(chi10)': ['MASS', 1000022]}`.
- `BR_hover_information`: defines for which particle(s) to display decay channels and branching ratios. Example:
  `BR_hover_information = {'BR(gluino)': 1000021}`.
  The output is written in the form .25[1000022, 1, −1], where the first number (0.25) is the branching ratio, and the numbers in [] are the PDG codes of the decay products.

  WARNING: Lists of branching ratios can be very long, so the may not fit in the hover box. One can define the number of entries with `BR_get_top` (default: 'all'); e.g. `BR_get_top = 3` will display only the three largest branching ratios.
- `ctau_hover_information`: displays the mean decay length in meter for the listed particle(s). Example:
  `ctau_hover_information = {'ctau(chi1+)': 1000024}`.

***SModelS hover information*:** defines, as a list of keywords, which information to display from the `SModelS` output. Example:

```
smodels_hover_information = ['SmodelS_excluded', 'r_max',
'Tx', 'Analysis', 'file'].
```

The options are:

- `SModelS_status`: prints whether the point is excluded or not by `SModelS`;
- `r_max`: shows the highest r-value for each parameter point ('False' if no experimental result applies);
- `chi2`: shows, if available, the χ^2 value associated to the highest r-value (if not, the output is 'False');

---

[7] Html notation like `<sub>NAME</sub>` for subscript and `<sup>NAME</sup>` for superscript works for axes labels and in the spectrum hover information, but not in the `SModelS` hover information.

- `Tx`: shows the topology/ies which give the highest r-value;
- `Analysis`: shows the experimental analysis from which the strongest constraint (r_max) comes from;
- `MT_max`: shows the missing topology with the largest cross section (in `SModelS` bracket notation);
- `MT_max_xsec`: shows the cross section of MT_max in fb;
- `MT_total_xsec`: shows the total missing cross section in fb, i.e. the sum of all missing topologies cross sections;
- `MT_long_xsec`: shows the total missing cross section (in fb) in long cascade decays;
- `MT_asym_xsec`: shows the total missing cross section (in fb) in decays with asymmetric branches;
- `MT_outgrid_xsec`: shows the total missing cross section (in fb) outside the mass grids of the experimental results;
- `file`: shows the name of the input spectrum file.

Choice of plots to make :

- `plot_data`: choice of which points to plot; the options are: all, excluded, non-excluded points. Example:
  `plot_data = ['all', 'excluded', 'non-excluded']`.
- `plot_list`: which quantities to plot in the x, y plane; the same options as for `SModelS` hover information apply. Example:
  `plot_list = ['r_max', 'chi2', 'Tx', 'Analysis', 'MT_max', 'MT_max_xsec', 'MT_total_xsec']`.

The plotted quantities (r_max, chi2, Tx, Analysis, etc.) and kind of points (all, excluded, non-excluded by `SModelS`) are reflected in the interactive plots' filenames. Moreover, a file `index.html` is created for a convenient access to all plots.

Chapter 5

Constraining the Minimal Dirac Gaugino Model.

Most SUSY searches at the LHC are performed in the context of the MSSM, where gauginos are Majorana particles. By introducing Dirac gauginos, we obtain an enriched phenomenology, from which considerable differences in the LHC signatures and limits are expected as compared to the MSSM. Concretely, in the MDGSSM we have an electroweakino sector extended by two extra neutralino and one extra chargino eigenstates. Moreover, production cross sections are enhanced for gluinos, while for squarks they are suppressed. Furthermore, small mass splitting within both the bino- like and wino- like states may lead to the presence of LLPs.

The present chapter disscusses current constraints on the gluinos and squarks and on the electroweakino sector of the MDGSSM, mainly derived from reinterpreting LHC results but also from considering constraints from dark matter searches. In Sec. 5.1 the MDGSSM is introduced and general phenomenological considerations are discussed. In Sec. 5.2 we explore the consequences of the current LHC limits on gluinos and squarks in this model based on [184]. In Sec. 5.3 we focus on the electroweakino sector of the model. In there, we find the parameter space where the lightest neutralino is a viable DM candidate that avoids constrains from DM direct detection, LEP and LHC Higgs measurements. Followed by exploring the consequences for collider phenomenology of the DM compatible electroweakino parameter space. This section is based on [185].

5.1 The Minimal Dirac Gaugino Model.

To add Dirac masses for the gauginos, we need to add a Weyl fermion in the adjoint representation of each gauge group; these are embedded in chiral superfields $\mathbf{S}, \mathbf{T}, \mathbf{O}$ which are respectively a singlet, triplet and octet, and carry zero R-charge. The resulting field content is summarised in Table 5.1. The mass terms can then be written by the *supersoft* [186] operators

$$\mathcal{L}_{\text{supersoft}} = \int d^2\theta \Big[\sqrt{2}\, m_{DB}\theta^\alpha \mathbf{W}_{1\alpha}\mathbf{S} + 2\sqrt{2}\, m_{DW}\theta^\alpha \mathrm{tr}\left(\mathbf{W}_{2\alpha}\mathbf{T}\right) + 2\sqrt{2}\, m_{D3}\theta^\alpha \mathrm{tr}\left(\mathbf{W}_{3\alpha}\mathbf{O}\right) \Big] + h.c.\,, \tag{5.1}$$

where $\mathbf{W}_{i\alpha}$ are the supersymmetric gauge field strengths. While it is possible to write the masses through hard breaking operators [187], in spontaneously broken SUSY, Dirac masses should only appear through the above *supersoft* terms which have the remarkable property that they do not appear in the renormalisation group (RG) equations for any other operators [188, 186, 189]. This means that Dirac gauginos can, in principle, be taken much heavier than their Majorana

Names		Spin 0	Spin 1/2	Spin 1	$SU(3)$, $SU(2)$, $U(1)_Y$
Quarks	$\mathbf{Q}$	$\tilde{Q} = (\tilde{u}_L, \tilde{d}_L)$	(u_L, d_L)		$(\mathbf{3}, \mathbf{2}, 1/6)$
	$\mathbf{u^c}$	$\tilde{u}^c_R$	u^c_R		$(\overline{\mathbf{3}}, \mathbf{1}, \text{-}2/3)$
(×3 families)	$\mathbf{d^c}$	$\tilde{d}^c_R$	d^c_R		$(\overline{\mathbf{3}}, \mathbf{1}, 1/3)$
Leptons	$\mathbf{L}$	$(\tilde{\nu}_{eL}, \tilde{e}_L)$	(ν_{eL}, e_L)		$(\mathbf{1}, \mathbf{2}, \text{-}1/2)$
(×3 families)	$\mathbf{e^c}$	$\tilde{e}^c_R$	e^c_R		$(\mathbf{1}, \mathbf{1}, 1)$
Higgs	$\mathbf{H_u}$	(H_u^+, H_u^0)	$(\tilde{H}_u^+, \tilde{H}_u^0)$		$(\mathbf{1}, \mathbf{2}, 1/2)$
	$\mathbf{H_d}$	(H_d^0, H_d^-)	$(\tilde{H}_d^0, \tilde{H}_d^-)$		$(\mathbf{1}, \mathbf{2}, \text{-}1/2)$
Gluons	$\mathbf{W_{3\alpha}}$		$\tilde{g}_\alpha$	g	$(\mathbf{8}, \mathbf{1}, 0)$
W	$\mathbf{W_{2\alpha}}$		$\tilde{W}^\pm, \tilde{W}^0$	$W^\pm, W^0$	$(\mathbf{1}, \mathbf{3}, 0)$
B	$\mathbf{W_{1\alpha}}$		$\tilde{B}$	B	$(\mathbf{1}, \mathbf{1}, 0)$
DG-octet	$\mathbf{O_g}$	O_g	$\tilde{g}'$		$(\mathbf{8}, \mathbf{1}, 0)$
DG-triplet	$\mathbf{T}$	$\{T^0, T^\pm\}$	$\{\tilde{W}'^\pm, \tilde{W}'^0\}$		$(\mathbf{1}, \mathbf{3}, 0)$
DG-singlet	$\mathbf{S}$	S	$\tilde{B}'$		$(\mathbf{1}, \mathbf{1}, 0)$

Table 5.1: Chiral and gauge multiplet fields in the model. The red coloured section corresponds to the new chiral multiplets that complete the DG model. The rest are the usual multiplets found in the MSSM.

counterparts since, instead of inducing a logarithmic correction to the sfermion masses, they only induce a finite shift: when this hierarchy is maximally large (i.e. we start with zero soft masses for sfermions) it is known as the *supersoft scenario*, which would be realised e.g. in models of goldstone gauginos [190, 191].

The supersoft property when applied to the Higgs masses means that Dirac gaugino (DG) models are much more *natural* than Majorana ones, although they do not completely alleviate the little hierarchy problem by themselves [192]. On the other hand, the singlet and triplet fields can have new superpotential couplings with the Higgs,

$$W \supset \lambda_S \mathbf{S}\,\mathbf{H_u} \cdot \mathbf{H_d} + 2\lambda_T\,\mathbf{H_d} \cdot \mathbf{T}\mathbf{H_u}\,, \tag{5.2}$$

which naturally enhance the Higgs mass at tree level — and can also be associated with an $N = 2$ supersymmetry in the gauge-Higgs sector [193, 194]. An $N = 2$ SUSY in turn leads automatically to alignment [195] due to the $SU(2)$ R-symmetry of the two Higgs doublets (which form an $N = 2$ hypermultiplet) [196]. This alignment is surprisingly robust under quantum corrections, where there is an accidental cancellation of $N = 2$ breaking effects [195]. Moreover, it has been found that the R-symmetry also prevents chirality-flip diagrams, which significantly relaxes flavour constraints [197, 198, 199] and suppresses squark production at the LHC, rendering DG models “supersafe” [200, 201, 202, 203].

The above motivations led to many studies, and realisations being developed [204, 205, 186, 206, 193, 207, 208, 209, 210, 211, 212, 213, 214, 215, 216, 217, 218, 219, 220, 221, 222, 223, 224, 225, 226, 227, 228, 229, 230, 231, 232, 233, 234, 235, 190, 191, 236, 187, 237, 238, 239]. The models fall either into the class of those that preserve an exact R-symmetry, or allow a small amount of R-breaking. On the former side, the principal example is the Minimal R-Symmetric Supersymmetric Standard Model (MRSSM) [197]: this requires the addition of supplementary R-Higgs fields (in the same gauge representation as the MSSM Higgs doublets but with different R-charges) which do not obtain expectation values after electroweak symmetry breaking. However, the couplings in eq. (5.2) are forbidden, and the equivalent couplings between the Higgs and R-

Higgs fields do not give any tree-level enhancement to the Higgs mass, making the Higgs sector rather like the MSSM — except that stop mixing is forbidden by the R-symmetry, so that in order to obtain the correct value of the Higgs mass either the new superpotential couplings must be very large [237, 238, 239] or the stops should be in the $\mathcal{O}(10\text{–}100)$ TeV range [195].

Quantum gravity arguments tell us, however, that no continuous global symmetries should be exact, and so the R-symmetry should be broken at some scale. In this paper, we shall consider the minimal model: the MDGSSM, described by just the matter content of the MSSM and the adjoint chiral superfields. This model *requires* R-symmetry to be broken in the Higgs sector by a B_μ term, otherwise it would be spontaneously broken at the same time as electroweak symmetry and generate a massless R-axion in the Higgs sector. As in [206, 240, 224, 241, 242], we shall assume that this is the *only* source of R-symmetry breaking, and is motivated by minimality, naturalness (allowing the couplings $\lambda_{S,T}$) and the idea that the Higgs sector couples to a different source of SUSY breaking than the other fields (in order e.g. to generate the μ/B_μ terms of similar order etc). This is perfectly consistent at the level of the RG equations: the B_μ term does not generate other R-breaking operators on RG evolution. Consequently, the superpotential is

$$\begin{aligned} W^{\text{MDGSSM}} =& Y_u^{ij}\,\mathbf{U}_i\mathbf{Q}_j\cdot\mathbf{H_u} - Y_d^{ij}\,\mathbf{D}_i\mathbf{Q}_j\cdot\mathbf{H_d} - Y_e^{ij}\,\mathbf{E}_i\mathbf{L}_j\cdot\mathbf{H_d} \qquad (5.3)\\ &+\mu\mathbf{H_u}\cdot\mathbf{H_d} + \lambda_S\mathbf{S}\,\mathbf{H_u}\cdot\mathbf{H_d} + 2\lambda_T\,\mathbf{H_d}\cdot\mathbf{T}\mathbf{H_u}\,, \qquad (5.4)\end{aligned}$$

where $\mathbf{Q}_i, \mathbf{L}_j\mathbf{U}_i, \mathbf{D}_i, \mathbf{E}_i, , \mathbf{H_d}, \mathbf{H_u}$ are, respectively, the superfields for the left-handed (LH) squarks; LH sleptons; right-handed (RH) up-type squarks; RH down-type squarks; RH sleptons; down- and up-type Higgs fields as in the MSSM, and $Y_u^{ij}, Y_d^{ij}, Y_e^{ij}$ which are the standard Yukawa couplings of the MSSM. For the supersymmetry-breaking terms, we add just the supersoft operators eq. (5.1), and the *standard* soft terms

$$\begin{aligned} -\mathcal{L}_{\text{standard soft}} =& \bar{Q}^i(m_Q^2)_i^j Q_j + \bar{U}^i(m_U^2)_i^j U_j + \bar{D}^i(m_D^2)_i^j D_j + \bar{L}^i(m_L^2)_i^j L_j\\ &+\bar{E}^i(m_E^2)_i^j E_j + m_{H_u}^2|H_u|^2 + m_{H_d}^2|H_d|^2 + B_\mu(H_u\cdot H_d + \text{h.c.})\\ &+m_S^2|S|^2 + 2m_T^2\text{tr}(T^\dagger T) + m_O^2|O|^2 \qquad (5.5)\\ &+\Big[t_S S + \frac{1}{2}B_S S^2 + B_T\text{tr}(TT) + B_O\text{tr}(OO)\\ &+\frac{A_\kappa}{3}S^3 + A_{ST}S\text{tr}(TT) + A_{SO}S\text{tr}(OO) + \text{h.c}\Big].\end{aligned}$$

Importantly, the above *contains no SUSY-breaking squark trilinears*; but there is still some small mixing in the stop/sbottom sector due to the μ-term. For simplicity we shall also take $A_\kappa = A_{ST} = A_{SO} = 0$ in the following, which is well justified in gauge mediation models [243], but we do not expect these parameters to affect our bounds in any significant way.

Both the MDGSSM and the MRSSM can be embedded in grand unified theories by adding additional electroweak-charged fields [241]; in the former case there is a constrained scenario, the CMDGSSM. For simplicity and generality we shall not include the extra fields, which in any case should not significantly affect the bounds on squarks and gluinos. Instead we shall take a phenomenological approach, choosing masses and couplings at the scale of the colorful superpartners. While the parameter space of such models is large, we shall argue that the constraints we find should be quite general for this class of models.

The present chapter re-examines LHC bounds on squarks and gluinos in the MDGSSM and on the electroweakino sector of the model. Squarks and gluinos which have so far been studied only for Run 1 data [200, 201, 202]. For the MRSSM there was a study of collider bounds on sleptons and electroweakinos in the MRSSM using Run 1 data [244], and a recent examination of bounds on charginos in a gauge-mediation scenario [245]. The scalar octet partners of the gluons, or "sgluons", have received more attention in the literature: Dirac gaugino models predict *two* real sgluons, a scalar and pseudoscalar, since they come from a (complex) chiral superfield. These have very interesting collider phenomenology [246, 247, 248, 249, 250, 231, 251, 252, 253, 254]; in particular, if CP is preserved then the pseudoscalar is likely to be relatively light and decay predominantly to tops, so they can be searched for in four-top events [243, 131].

5.1.1 General phenomenological considerations.

The electroweakino sector.

An interesting phenomenological consequence of adding the chiral superfields **S** and **T** is, that we obtain 6 neutralino and 3 chargino mass eigenstates (as compared to 4 and 2, respectively, in the MSSM). The neutralino mass matrix $\mathcal{M}_N$ in the basis $(\tilde{B}', \tilde{B}, \tilde{W}'^0, \tilde{W}^0, \tilde{H}_d^0, \tilde{H}_u^0)$ is given by

$$\mathcal{M}_N = \tag{5.6}$$

$$\begin{pmatrix} 0 & M_{DB} & 0 & 0 & -\frac{\sqrt{2}\lambda_S}{g_Y} m_Z s_W s_\beta & -\frac{\sqrt{2}\lambda_S}{g_Y} m_Z s_W c_\beta \\ M_{DB} & 0 & 0 & 0 & -m_Z s_W c_\beta & m_Z s_W s_\beta \\ 0 & 0 & 0 & M_{DW} & -\frac{\sqrt{2}\lambda_T}{g_2} m_Z c_W s_\beta & -\frac{\sqrt{2}\lambda_T}{g_2} m_Z c_W c_\beta \\ 0 & 0 & M_{DW} & 0 & m_Z c_W c_\beta & -m_Z c_W s_\beta \\ -\frac{\sqrt{2}\lambda_S}{g_Y} m_Z s_W s_\beta & -m_Z s_W c_\beta & -\frac{\sqrt{2}\lambda_T}{g_2} m_Z c_W s_\beta & m_Z c_W c_\beta & 0 & -\mu \\ -\frac{\sqrt{2}\lambda_S}{g_Y} m_Z s_W c_\beta & m_Z s_W s_\beta & -\frac{\sqrt{2}\lambda_T}{g_2} m_Z c_W c_\beta & -m_Z c_W s_\beta & -\mu & 0 \end{pmatrix},$$

where $s_W = \sin\theta_W$, $s_\beta = \sin\beta$ and $c_\beta = \cos\beta$; $\tan\beta = v_u/v_d$ is the ratio of the Higgs vevs; M_{DB} and m_{DW} are the bino and wino Dirac mass parameters; μ is the higgsino mass term, and λ_S and λ_T are the couplings between the singlet and triplet fermions with the Higgs and higgsino fields. By diagonalising eq. (5.6), one obtains pairs of bino-like, wino-like and higgsino-like neutralinos, with small mass splittings *within* the bino or wino pairs induced by λ_S or λ_T, respectively. For instance, if M_{DB} is sufficiently smaller than M_{DW} and μ, we find mostly bino/U(1) adjoint $\tilde{\chi}_{1,2}^0$ as the lightest states with a mass splitting given by

$$m_{\tilde{\chi}_2^0} - m_{\tilde{\chi}_1^0} = \left| 2\frac{M_Z^2 s_W^2}{\mu} \frac{(2\lambda_S^2 - g_Y^2)}{g_Y^2} c_\beta s_\beta \right| . \tag{5.7}$$

Turning to the charged EW-inos, the chargino mass matrix in the basis $v^+ = (\tilde{W}'^+, \tilde{W}^+, \tilde{H}_u^+)$, $v^- = (\tilde{W}'^-, \tilde{W}^-, \tilde{H}_d^-)$ is given by:

$$\mathcal{M}_C = \begin{pmatrix} 0 & M_{DW} & \frac{2\lambda_T}{g} m_W c_\beta \\ M_{DW} & 0 & \sqrt{2} m_W s_\beta \\ -\frac{2\lambda_T}{g} m_W s_\beta & \sqrt{2} m_W c_\beta & \mu \end{pmatrix}, \tag{5.8}$$

This can give a higgsino-like $\tilde{\chi}^\pm$ and two wino-like $\tilde{\chi}^\pm$ —the latter ones again with a small splitting driven by λ_T. Note that in both eqs. (5.6) and (5.8), Majorana mass terms are absent since we assume purely Dirac eigenstates in this model.

The mass splitting between the two lightest neutralinos determines the $\tilde{\chi}_2^0$ lifetime. If the splitting is very small, the $\tilde{\chi}_2^0$ can live long enough to effectively be a co-LSP on collider scales and appear only as MET. For larger mass splittings, the $\tilde{\chi}_2^0$ can decay promptly, leading to the complex signatures discussed in the paragraphs above. In between, the $\tilde{\chi}_2^0$ is a long-lived neutral particle, whose decays can give signatures with displaced vertices, with soft displaced photons plus MET being the predominant one. Similarly, when $\tilde{\chi}_1^\pm$ is the NLSP, its lifetime is determined by the $m_{\tilde{\chi}_1^\pm} - m_{\tilde{\chi}_1^0}$ mass splitting. If $m_{\tilde{\chi}_1^\pm} - m_{\tilde{\chi}_1^0}$ is small enough, $\tilde{\chi}_1^\pm$ would be a long-lived charged particle that could leave a DT signature or be considered as an HSCP at the LHC, depending on its resulting lifetime. The collider phenomenology of scenarios with LL electroweakinos will be discussed in detail in Sec. 5.3.

Effect of R-symmetry breaking.

The mass-splittings in the neutralinos are due to the R-symmetry breaking effect of both the H_u and H_d fields obtaining an expectation value – hence they are proportional to $c_\beta s_\beta$ which vanishes for large and small $\tan\beta$. In addition, when $\lambda_S = g_Y/\sqrt{2}, \lambda_T = g_2/\sqrt{2}$, we have an effective global symmetry among the gauginos and higgsinos which allows the neutralinos and charginos to remain of Dirac type at tree-level – this is not actually the $SU(2)$ R-symmetry, of which the higgsinos are actually singlets.

This means that any Majorana masses for the neutralinos and charginos (which we are neglecting) should be smaller than the above splittings in order for the analysis in this paper to be valid: this makes a difference to the softness of the decays from $\tilde{\chi}^0_2$ to $\tilde{\chi}^0_1$, for example.

Turning to the gluinos, at tree level $\tilde{g}_{1,2}$ are exactly Dirac in our model; the two states are only split by a tiny difference at one loop from the small amount of mixing between the left- and right-handed squarks proportional to μ. Here, however, a modest Majorana mass could be tolerated, since the only effect would be to split the eigenstates and so be distinguishable in a detector as separate particles: in our benchmarks they shall be indistinguishable. Interestingly, in our model the octet fermion $\tilde{g}'$ only couples to the scalar octets, gluino and gluons. Hence the two gluino mass eigenstates, $\tilde{g}_1, \tilde{g}_2 = \frac{1}{\sqrt{2}}(\lambda_3 + \tilde{g}'), \frac{i}{\sqrt{2}}(\lambda_3 - \tilde{g}')$, couple only to the squarks and quarks through the component λ_3, and their couplings are the same up to a factor of i. This means that over the parameter space, their decays are *almost* identical, meaning that together they behave like a purely Dirac gluino—except for when the decay is highly non-relativistic.

In our model, the only relevant non-relativistic two-body decays of a gluino are when a squark becomes nearly degenerate with it; and so to obtain differences between $\tilde{g}_1$ and $\tilde{g}_2$ decays we would furthermore need a sizeable source of R-symmetry breaking, which means squark mixing. We can therefore expect a sizeable difference between the two gluino decays into stops or sbottoms only near the kinematic limit. This can be seen as follows: for a two-body decay $\tilde{g}_i \to q\tilde{q}$ for $i = 1, 2$ we can write the couplings (suppressing the gauge and Lorentz indices) as

$$\mathcal{L} \supset -\sqrt{2} g_3 \tilde{q}_L^* q_L \lambda_3 + \sqrt{2} g_3 \bar{q}_R \tilde{q}_R \bar{\lambda}_3 \tag{5.9}$$

and so if $\tilde{q}_L = \cos\theta_q \tilde{q}_1 + \sin\theta_q \tilde{q}_2$, $\tilde{q}_R^* = -\sin\theta_q \tilde{q}_1 + \cos\theta_q \tilde{q}_2$, then the coupling to say $\tilde{q}_1$ is

$$\mathcal{L} \supset -\tilde{q}_1^* \Big[c_L^i (q\tilde{g}_i) + c_R^i (\bar{q}\bar{\tilde{g}}_i) \Big], \qquad c_L^1 = \sqrt{2} g_3 \cos\theta_q, \quad c_R^1 = -\sqrt{2} g_3 \sin\theta_q, \tag{5.10}$$

while $c_L^2 = -i c_L^1, (c_R^2)^* = -i c_R^1$. The width for the gluino decays is then

$$\Gamma(\tilde{g}_i \to q\tilde{q}_i) = \frac{K}{32\pi m_{\tilde{g}_i}^3} \Big[(m_{\tilde{g}_i}^2 + m_q^2 - m_{\tilde{q}_i}^2)(|c_L|^2 + |c_R|^2) + 2 m_q m_{\tilde{q}_i} (c_L^* c_R + c_R^* c_L) \Big], \tag{5.11}$$

$$K \equiv \sqrt{(m_{\tilde{g}}^2 - m_q^2 - m_{\tilde{q}_i}^2)^2 - 4 m_q^2 m_{\tilde{q}_i}^2}. \tag{5.12}$$

So then when $m_{\tilde{g}_i} \sim m_q + m_{\tilde{q}_i}, m_{\tilde{q}_i} \gg m_q$, we have $(m_{\tilde{g}_i}^2 + m_q^2 - m_{\tilde{q}_i}^2) \simeq 2 m_q m_{\tilde{q}_i}$ and

$$\Gamma(\tilde{g}_i \to q\tilde{q}_i) \simeq \frac{K m_q g_3^2}{16\pi m_{\tilde{g}_i}^2} \Big[1 \pm 2\cos\theta_q \sin\theta_q \Big]. \tag{5.13}$$

Hence for maximal squark (stop or sbottom) mixing there is a complete suppression of one of the decays in this limit.

For three-body decays of a gluino to neutralinos and quarks, we shall argue below that in our model the neutralinos should be light, and so even though the neutralinos themselves significantly break the R-symmetry through their mixings, the quarks/neutralinos should be relativistic and we should not see a significant difference between the two gluino components.

Effects on the Higgs mass at tree-level.

In the (phenomenological) MSSM, it is reasonable to consider the bino/wino/higgsino masses as free parameters. However, in the MDGSSM (and in DG models generally) these have a large effect on the Higgs mass at tree level. Indeed, it is well known that in the supersoft limit the Higgs D-term potential is erased [186]; and a large μ-term has a similar effect. Moreover, the singlet and triplet scalars obtain tree-level masses m_{SR}, m_{TP} proportional to the Dirac mass terms:

$$m_{SR}^2 = m_S^2 + 4|m_{DY}|^2 + B_S, \qquad m_{TP}^2 = m_T^2 + 4|m_{D2}|^2 + B_T, \tag{5.14}$$

and so if m_{DY} or m_{D2} are large then the scalar singlet/triplet should be heavy. If we then integrate them out, then the correction to the Higgs quartic coupling is

$$\delta\lambda \sim \mathcal{O}\left(\frac{g_Y m_{DY}}{m_{SR}}\right)^2 + \mathcal{O}\left(\frac{\sqrt{2}\lambda_S m_{DY}}{m_{SR}}\right)^2 + \mathcal{O}\left(\frac{g_2 m_{D2}}{m_{TP}}\right)^2 + \mathcal{O}\left(\frac{\sqrt{2}\lambda_T m_{D2}}{m_{TP}}\right)^2, \tag{5.15}$$

The exact expressions for the Two-Higgs Doublet model parameters are given in [195]. This means that we need to make the singlet and triplet scalars heavy *relative to the gauginos and higgsinos* in order to not suppress the Higgs mass or even render the potential unstable. Without removing the scalars from the spectrum entirely and losing all trace of naturalness, this means keeping the gauginos/higgsinos well below a TeV.

Additionally, scalar triplet fields are well-known to generate a shift to the electroweak ρ-parameter at tree-level:

$$\Delta\rho = \frac{\Delta m_W^2}{m_W^2} = \frac{v^2}{m_{TP}^4}\left(\sqrt{2}\lambda_T \mu + g_2 m_{D2} c_{2\beta}\right)^2, \tag{5.16}$$

while the experimental best-fit value is [255]

$$\Delta\rho = (3.7 \pm 2.3) \times 10^{-4}, \tag{5.17}$$

leading to $m_{TP} \gtrsim 2$ TeV for typical values of $\mu, m_{D2} \sim 500$ GeV. Numerically we find it is hard to find satisfactory parameter points for gaugino/higgsino masses of $\mathcal{O}$(TeV) and so in our benchmark points we shall take them to be only a few hundred GeV.

On the other hand, in the decoupling limit, the light Higgs mass is given by

$$m_{h_1}^2 \simeq M_Z^2 \cos^2(2\beta) + \frac{(\lambda_S^2 + \lambda_T^2)}{2} v^2 \sin^2(2\beta) + \ldots \tag{5.18}$$

and so taking small $\tan\beta$ and moderate values of λ_S, λ_T we can enhance the Higgs mass at tree-level without having exceptionally heavy stops (given that the stop mixing will be small in the absence of SUSY-breaking trilinear couplings).

5.2 Collider limits on gluinos and squarks.

Previous studies of Dirac vs. Majorana gauginos highlighted a weakening of collider limits on squarks due to the absence of a chirality flip in the DG case [200, 201, 202, 203]. In the MSSM, squark–anti-squark production at the LHC ($pp \to \tilde{q}_L\tilde{q}_L^*$, $q_R\tilde{q}_R^*$) proceeds via s-channel gluon and t-channel gluino exchange; squark–squark production ($pp \to \tilde{q}\tilde{q}$, $q^*\tilde{q}^*$) of same (LL, RR) and mixed (LR) chirality via t-channel gluino exchange is another important contribution to the total squark production. Squark–squark production of same chirality however requires a chirality

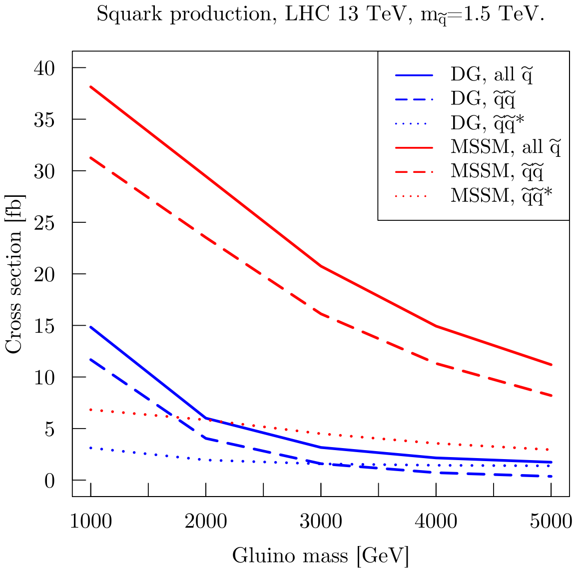

Figure 5.1: Squark production cross-sections at leading order (LO) for the 13 TeV LHC as a function of the gluino mass in the MSSM (in red) and in the DG case (in blue), for $m_{\tilde{q}} = 1.5$ TeV, assuming an 8-fold squark degeneracy ($\tilde{q} = \tilde{u}, \tilde{d}, \tilde{c}, \tilde{s}$). The dashed, dotted and full lines show the squark-squark, squark-antisquark and total squark production cross-sections, respectively.

flip, so it is absent in the DG case. Moreover, the other t-channel gluino exchange processes are suppressed by $|p|/m_{\tilde{g}}^2$ in the amplitude, where $|p|$ is the momentum in the propagator. This has a huge impact on the total squark production in the presence of a heavy Dirac gluino as illustrated in Fig. 5.1. This suppression of light-flavour squark production at the LHC is the perhaps best known consequence of Dirac gauginos.

There are also other interesting consequences, which may impact collider phenomenology. For one, the cross-section of gluino-pair production is enhanced in the DG case because of the larger number of degrees of freedom than in the MSSM (see [256] for a detailed discussion). Another important aspect is the more complex electroweak-ino spectrum. Concretely, while in the MSSM the neutralinos are a linear combination of the four neutral fermions, the bino $\tilde{B}$, wino $\tilde{W}^0$ and higgsinos $\tilde{H}_u^0$ and $\tilde{H}_d^0$, in the DG model this is supplemented by two adjoint fermions: a bino $\tilde{B}'$ and wino $\tilde{W}'^0$. In the chargino sector, the charged winos $\tilde{W}^\pm$ and higgsinos $\tilde{H}_u^+$, $\tilde{H}_d^-$ are supplemented by the triplet $\tilde{W}'^\pm$. We thus have six neutralino and three chargino mass eigenstates, which may appear in gluino and squark cascade decays.

One may therefore expect that LHC phenomenology, and constraints from current searches, are different in DG models as compared to the MSSM. In this section we will derive such limits on gluinos and squarks, on the light of run 2 LHC results.

5.2.1 Benchmark scenarios.

To quantitatively investigate how the aforementioned arguments affect LHC limits on gluinos and squarks, we chose four benchmark scenarios with different values of λ_S, λ_T. Concretely we take $m_{DY} < \mu < m_{2D}$ with, for the first three benchmarks,

$$m_{DY} = 200 \text{ GeV}, \quad \mu = 400 \text{ GeV}, \quad m_{D2} = 500 \text{ GeV}. \tag{5.19}$$

Moreover, to favor a large tree-level boost to m_{h_1}, we take $\tan\beta = 2$. This gives a hierarchical spectrum of bino-, higgsino- and wino-like states with masses of about 200, 400 and 500 GeV,

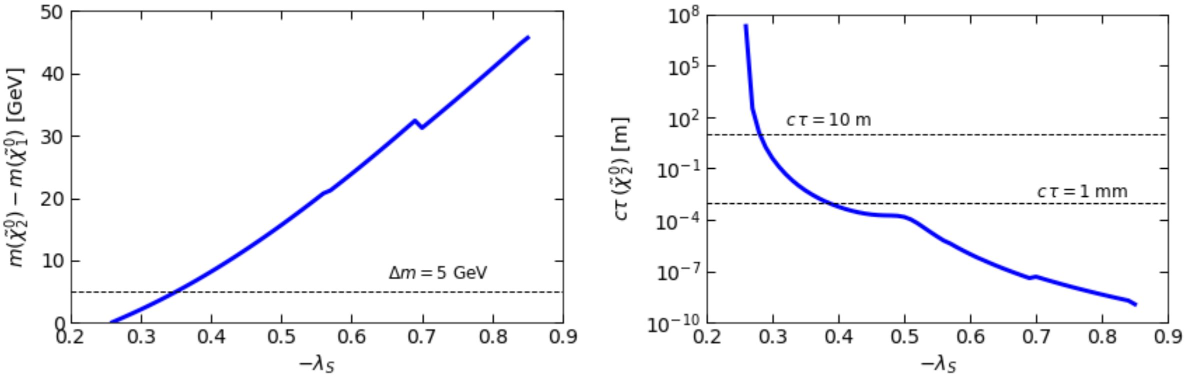

Figure 5.2: Influence of λ_S on the mass splitting between the two bino-like mass eigenstates $\tilde{\chi}_{1,2}^0$ (left) and on the lifetime of the $\tilde{\chi}_2^0$ (right) for the parameters of eq. (5.19) and $\tan\beta = 2$.

respectively. Finally, we set $\lambda_T = 0.2$ and choose two values of λ_S, $\lambda_S = -0.27$ and -0.74, to have cases with small and sizeable $\tilde{\chi}_{1,2}^0$ mass splittings. The dependence of the $\tilde{\chi}_{1,2}^0$ mass splitting and the $\tilde{\chi}_2^0$ lifetime on λ_S is shown in Fig. 5.2[1].

With this setup, the masses of gluinos and squarks are treated as free parameters (m_{3D} and a scalar soft mass-squared parameter), while the masses of the 3rd generation squarks are adjusted such that $m_{h_1} \in [123,\ 127]$ GeV. The calculation of the mass spectrum and decay branching ratios is done with `SARAH` [257, 258, 259, 260, 261] and `SPheno` [262], including Higgs mass calculation the 2-loop level [263, 264, 265]. We consider three distinct cases:

$$\begin{aligned} \text{DG1}: &\quad \lambda_S = -0.27;\ m_{\tilde{t}} \sim m_{\tilde{b}} \sim 3.6\,\text{TeV}, && (5.20)\\ \text{DG2}: &\quad \lambda_S = -0.74;\ m_{\tilde{t}} \sim m_{\tilde{b}} \sim 2.6\,\text{TeV}, && (5.21)\\ \text{DG3}: &\quad \lambda_S = -0.74;\ m_{\tilde{t}} \sim m_{\tilde{b}} \sim 1.6\,\text{TeV}. && (5.22) \end{aligned}$$

For DG1 with $\lambda_S = -0.27$, the two bino-like mass eigenstates $\tilde{\chi}_{1,2}^0$ are quasi-degenerate with sub-GeV mass splitting, and the $\tilde{\chi}_2^0$ has a mean decay length of nearly 3 km, so that it will appear as a co-LSP. For $\lambda_S = -0.74$ (DG2 and DG3), the two bino-like mass eigenstates $\tilde{\chi}_{1,2}^0$ have masses of about 182 GeV and 216–218 GeV, respectively, and the $\tilde{\chi}_2^0$ decays promptly into $\tilde{\chi}_1^0 f\bar{f}$ via an off-shell Z.

Since we are mostly interested in gluino and squark cascade decays, we consider also a fourth benchmark with heavy winos by moving m_{2D} above 1 TeV, thus on the one hand somewhat suppressing decays into wino-like states, and on the other hand changing the kinematic distributions of such cascades. Concretely,

$$\begin{aligned} \text{DG4}: \quad & m_{1D} = 200\ \text{GeV},\ \mu = 400\ \text{GeV},\ m_{2D} = 1175\ \text{GeV},\\ & \lambda_S = -0.79,\ \lambda_T = -0.37;\ m_{\tilde{t}} \sim m_{\tilde{b}} \sim 3\,\text{TeV}. \qquad (5.23) \end{aligned}$$

The main parameters and resulting masses for the four benchmark scenarios are summarised in Table 5.2. Examples of gluino and squark decay branching ratios are given in Table 5.3 and compared to the branching ratios in the MSSM with an equivalent bino/wino/higgsino spectrum.

The complete SLHA spectrum files produced with `SARAH/SPheno` are available at [266].[2] Note

---

[1] This results does not include 1 loop neutralino decays.

[2] For the sake of reproducibility of our results, we provide moreover the `SPheno` model and input files, as well as the UFO model and two helpful scripts for modifying the `SPheno` .spc files so they can be used for event generation with `MadGraph`/`Pythia`.

Parameters	DG1	DG2	DG3	DG4
m_{1D}	200	200	200	200
m_{2D}	500	500	500	1175
μ	400	400	400	400
$\tan\beta$	2	2	2	2
$-\lambda_S$	0.27	0.74	0.74	0.79
$\sqrt{2}\,\lambda_T$	0.14	0.14	0.14	-0.26
$m^2_{\tilde{Q}_3}$	1.25e7	6.5e6	2.26e6	8.26e6
$m^2_{\tilde{Q}_1}$	6.25e6	6.25e6	6.25e6	6.25e6
m_{3D}	1750	1750	1750	1750

Masses	DG1	DG2	DG3	DG4
$\tilde{\chi}^0_1$	201.35	182.1	181.8	182.4
$\tilde{\chi}^0_2$	201.72	218.0	216.6	213.2
$\tilde{\chi}^0_3$	403	400	396	408
$\tilde{\chi}^0_4$	419	445	441	437
$\tilde{\chi}^0_5$	537	536	535	1226
$\tilde{\chi}^0_6$	548	548	546	1227
$\tilde{\chi}^\pm_1$	400	395	391	398
$\tilde{\chi}^\pm_2$	536	536	534	1224
$\tilde{\chi}^\pm_3$	549	548	547	1229
$\tilde{t}_1$	3604	2607	1590	2894
$\tilde{t}_2$	3613	2637	1613	2927
h_1	124.0	125.0	125.3	125.2

Table 5.2: Parameters and masses of the four benchmark scenarios; m_{1D}, m_{2D}, μ, $\tan\beta$, λ_S, λ_T and the soft masses of the third generation ($m^2_{\tilde{Q}_3} = m^2_{\tilde{U}_3} = m^2_{\tilde{D}_3}$) are fixed for each benchmark, while m_{3D} and $m^2_{\tilde{Q}_1} = m^2_{\tilde{U}_1} = m^2_{\tilde{Q}_1}$ will be varied to scan over gluino and squark masses.

here, that our conventions differ (as usual) from the `SARAH DiracGauginos` implementation. We have

$$\begin{array}{|c|c|}\hline \text{Parameter} & \texttt{SARAH}\ \text{convention} \\ \hline \lambda_S & -\texttt{lam} \\ \lambda_T & \texttt{LT}/\sqrt{2} \\ \hline \end{array} \tag{5.24}$$

Scenarios DG1, DG2 and DG3 have heavy stops and sbottoms, so the gluino branching ratios in Table 5.3 will not change significantly with the gluino mass in the region accessible with current LHC data, as long as $m_{\tilde{g}} < m_{\tilde{q}}$ (if $m_{\tilde{g}} > m_{\tilde{q}}$, then of course $\tilde{g} \to q\tilde{q}$ decays dominate). This is different for DG3 which has stops and sbottoms at about 1.6 TeV. Here the gluino branching ratios vary a lot with $m_{\tilde{g}}$ up to 2 TeV, as shown in Fig. 5.3. We note that in this figure BR $(\tilde{g}_1)$ and BR$(\tilde{g}_2)$ are averaged over because R-symmetry breaking effects lead to differences in $\tilde{g}_1$ and $\tilde{g}_2$ decays near the threshold where 2-body decays into sbottoms/stops become kinematically allowed. These differences are however experimentally not observable.

5.2.2 Simplified model limits with `SModelS`.

As a first step, we applied the Simplified Model Limit approach using `SModelS` [171] to the DG1 and DG3 scenarios. The results are shown in Fig. 5.4.

For DG1, when $m_{\tilde{g}} < m_{\tilde{q}}$ the strongest constraint comes from the $pp \to \tilde{g}\tilde{g}$, $\tilde{g} \to q\bar{q}\tilde{\chi}^0_1$ simplified model (denoted as T1) and excludes gluino masses up to about 1250 GeV for LO cross-sections. When $m_{\tilde{q}} < m_{\tilde{g}}$, the strongest constraint mostly comes from the $pp \to \tilde{q}\tilde{q}^{(*)}$, $\tilde{q} \to q\tilde{\chi}^0_1$ simplified model (denoted as T2), excluding squark masses up to roughly 1300 GeV as long as the gluino is not too heavy. In the equivalent MSSM case (MSSM1 scenario in Table 5.3), the gluino mass limit would be only 1 TeV due to the smaller gluino pair-production cross-section while, conversely, the squark mass limit would be about 2 TeV for 2.6 TeV gluinos.

For DG3, which has stops around 1600 GeV and a $\tilde{\chi}^0_2$–$\tilde{\chi}^0_1$ mass splitting of about 35 GeV, the picture changes. On the one hand, over a large part of the region with $m_{\tilde{g}} < m_{\tilde{q}}$, the strongest constraint now comes from the $pp \to \tilde{g}\tilde{g}$, $\tilde{g} \to t\bar{t}\tilde{\chi}^0_1$ simplified model (denoted as T1tttt). Moreover, and more importantly, gluino and squark decays via the bino-like $\tilde{\chi}^0_2$ are followed by $\tilde{\chi}^0_2 \to \tilde{\chi}^0_1 f\bar{f}$ via an off-shell Z, which is a different topology in the simplified model

	DG1	DG2	DG3	DG4	MSSM1	MSSM4
Gluino decays, $m_{\tilde q} \approx 2$ TeV, $m_{\tilde g} \approx 2.6$ TeV						
$\tilde g \to q\bar q$ + binos	12%	6%	–	18%	10%	15%
$\tilde g \to b\bar b$ + binos	–	1%	–	6%	–	1%
$\tilde g \to t\bar t$ + binos	1%	4%	–	6%	1%	3%
$\tilde g \to (q\bar q^{(\prime)}, b\bar b)$ + heavy EW-inos	66%	36%	–	13%	66%	19%
$\tilde g \to (t\bar t, t\bar b, b\bar t)$ + heavy EW-inos	20%	53%	–	61%	23%	62%
$\tilde g \to t + \tilde t_{1,2}$	–	–	48%	–	–	–
$\tilde g \to b + \tilde b_{1,2}$	–	–	52%	–	–	–
Squark decays, $m_{\tilde q} \approx 2$ TeV, $m_{\tilde g} \approx 2.6$ TeV						
$\tilde q_R \to q$ + binos	99%	99%	98%	99%	92%	92%
$\tilde q_L \to q$ + heavy EW-inos	99%	99%	99%	97%	98%	97%

Table 5.3: Branching ratios of gluino and squark decays for DG1–DG4. For gluino decays we consider the mass hierarchy $m_{\tilde q} < m_{\tilde g_{1,2}}$, for squark decays the mass hierarchy $m_{\tilde g_{1,2}} > m_{\tilde q}$. The columns MSSM1 and MSSM4 give the comparison to the equivalent MSSM case with $M_1 = 200$ GeV, $\mu = 400$ GeV and $M_2 = 500$ GeV (MSSM1) or 1200 GeV (MSSM4); third generation squark masses are about 3.6 TeV for MSSM1 and 3 TeV for MSSM4, while $\tan\beta = 10$ and $A_t = -4$ TeV to achieve $m_h \approx 125$ GeV.

picture.[3] This drastically reduces the effective cross-section ($\sigma \times$ BRs) that goes into the T1, T1tttt or T2 topologies. Consequently, the excluded region is noticeably smaller for DG3 than for DG1, with a gluino mass limit of only 1 TeV (corresponding to the factor 2 reduction of the T1 cross-section which is also seen in the comparison between DG1 and MSSM1 above), and a squark mass limit below 1 TeV.

It is also worth pointing out that for heavy gluinos and squarks, the effective T1(tttt) or T2 cross-sections become too small and electroweak production of charginos followed by $\tilde\chi_i^\pm \to W^\pm \tilde\chi_1^0$ decays (denoted as TChiWW) takes over as the most constraining simplified model signature. Note however that TChiWW upper limit maps are available for 8 TeV only—neither ATLAS nor CMS have provided them for the 13 TeV data—and do not exclude any of the scan points.

We have to keep in mind, however, that the constraints which can be derived in the context of simplified models considerably weaken in realistic scenarios where the gluinos (squarks) share out their branching ratios over several decay channels [133]. For instance, in the DG1 scenario BR($\tilde g \to q\bar q\tilde\chi_1^0$) $\backsim 0.1$, which means that only 1% of the total gluino-pair production is constrained by the $pp \to \tilde g\tilde g$, $\tilde g \to q\bar q\tilde\chi_1^0$ simplified model. This clearly suggests that the simplified model limits are not sufficient for constraining complex scenarios as the ones considered here. Nonetheless, this approach provides a very fast way to derive results that can serve as lower bounds, when scanning for the true exclusion lines of such cases.

5.2.3 Recast of the ATLAS multi-jet plus E_T^{miss} analysis.

To derive the true exclusion limit, a full recasting of the experimental search(es) is necessary. With this aim, we implemented (see [267]) the 'Meff-based' signal regions of the ATLAS multijet search [268] for squarks and gluinos in final states with 2-6 jets and large missing transverse momentum, using 36 fb^{-1} of $\sqrt{s} = 13$ TeV pp collision data, in `MadAnalysis 5` [158].

We scanned over gluino and light-flavor squark masses for the DG1, DG2, DG3 and DG4 scenarios. For each scan point, we simulated 30K events with `MadGraph5_aMC@NLO` [140], with

---

[3] In `SModelS` txname notation, these would be constrained by, e.g., T5ZZoff or T6ZZoff results, which are however not available.

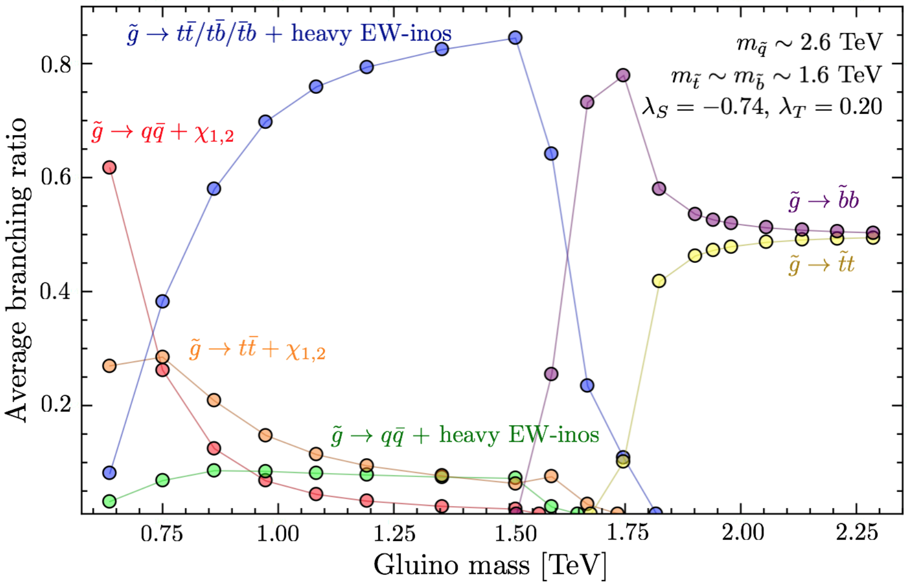

Figure 5.3: Branching ratios of gluino decays (averaged over $\tilde g_1$ and $\tilde g_2$) for DG3 as function of the gluino mass, for $m_{\tilde q} \approx 2.6$ TeV.

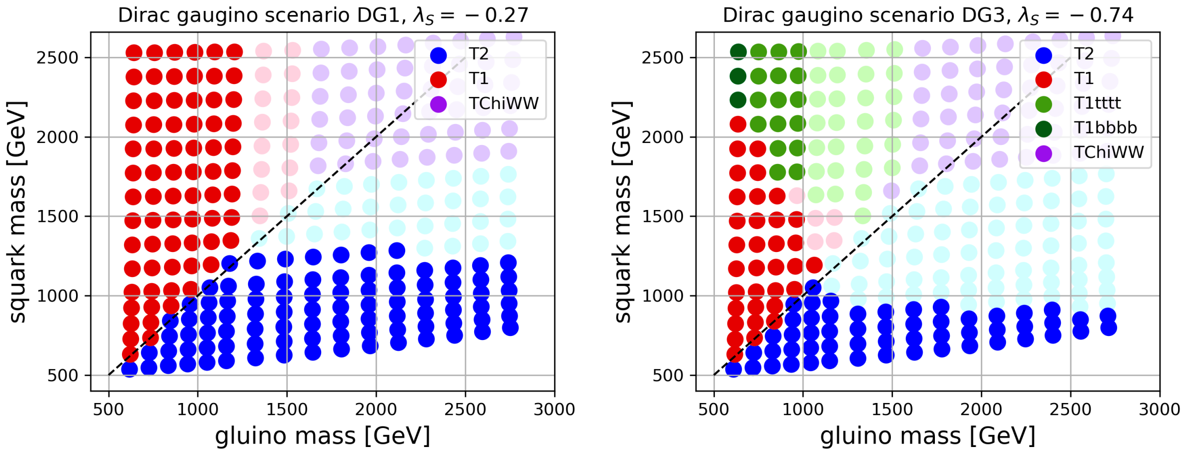

Figure 5.4: `SModelS` constraints in the gluino versus squark mass plane, on the left for DG1, on the right DG3. The colour code denotes the simplified model which gives the strongest constraint (T1: $pp \to \tilde g\tilde g$, $\tilde g \to q\bar q\tilde\chi^0_1$; T1tttt: $pp \to \tilde g\tilde g$, $\tilde g \to t\bar t\tilde\chi^0_1$; T2: $pp \to \tilde q\tilde q^{(*)}$, $\tilde q \to q\tilde\chi^0_1$; TChiWW: $pp \to \tilde\chi^\pm_i\tilde\chi^\pm_i$, $\tilde\chi^\pm_i \to W^\pm\tilde\chi^0_1$). Full-colour (non-transparent) points are excluded by `SModelS`, while light-shaded points escape the simplified model limits.

parton showering and hadronization done in `Pythia` 8.2 [145] and the simulation of the ATLAS detector with `Delphes` 3 [150]. Afterwards, the events were analyzed with `MadAnalysis` 5 and exclusion confidence levels (CL) were computed. Finally, for limit setting, since signal regions are inclusive, only the "best" (i.e. the statistically most sensitive) were used.

Figure 5.5 shows the 95% CL exclusion lines in the gluino vs. squark mass plane for the benchmark scenarios with light winos, and for MSSM1, an MSSM scenario equivalent to DG1. In the region $m_{\tilde q} > m_{\tilde g}$ we found a robust limit of $m_{\tilde g} \gtrsim 1.65$ TeV when squarks are very heavy, in

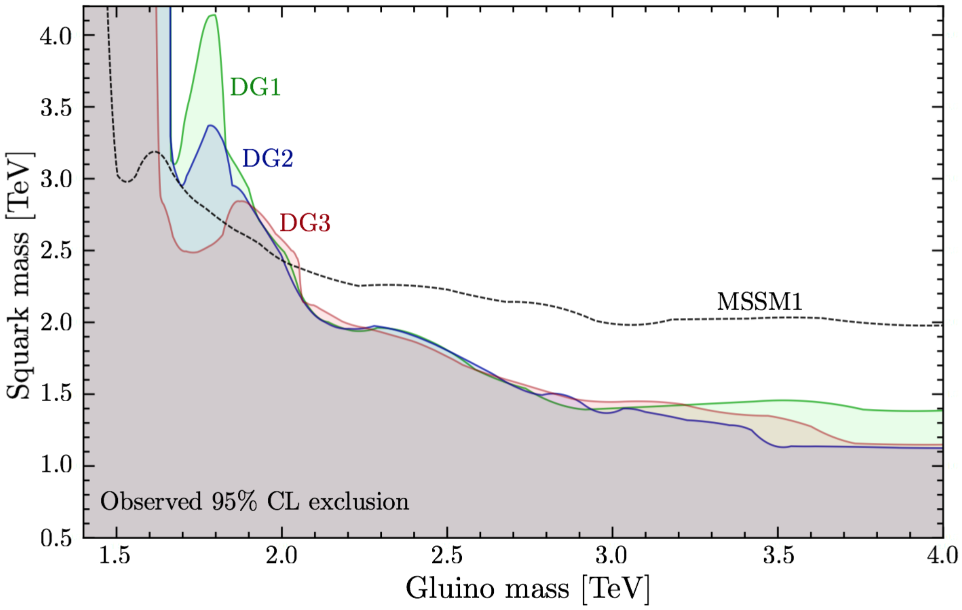

Figure 5.5: 95% CL exclusion limits in the gluino vs. squark mass plane for DG1 (green), DG2 (blue) and DG3 (red) contrasted with MSSM1 (black dashed line), derived from the recasting of the ATLAS 2–6 jets + MET analysis for 36 fb^{-1} at $\sqrt{s} = 13$ TeV. Only the most sensitive (=best expected) signal region is used for the limit setting.

all cases. In the region $m_{\tilde{g}} > m_{\tilde{q}}$, for DG2 and DG3 we obtained a squark limit of $m_{\tilde{q}} \gtrsim 1.1$ TeV, while for DG1 the limit reaches $m_{\tilde{q}} \gtrsim 1.4$ TeV. The difference is a consequence of the $\tilde{\chi}_2^0 \to Z^* \tilde{\chi}_1^0$ decays, which are present in DG3 and DG2 but not in DG1.

We also observe different "dips" in the exclusion contours for the different benchmark scenarios which originate from a switch of the best signal region from 6j-Meff-1800 (6 jets, $M_{\text{eff}} > 1800$ GeV) to 6j-Meff-2600 (6 jets, $M_{\text{eff}} > 2600$ GeV) at different, but close, values of gluino mass for each scenario.

To understand the shape of the exclusion contour, it is instructive to consider which signal regions are used for the limit setting and how the various production modes contribute to the final CLs value. To this end, Fig. 5.6 shows the CLs values in the best signal region from various proton-proton processes as a function of gluino mass, for medium heavy squarks of $m_{\tilde{q}} \sim 2.6$ TeV.

We see that the best signal region switches from 6j-Meff-1800 (6 jets, $M_{\text{eff}} > 1800$ GeV) to 6j-Meff-2600 (6 jets, $M_{\text{eff}} > 2600$ GeV) at different values of gluino mass for the three benchmark scenarios. In particular for DG3 this leads to the exclusion CL dropping below 0.95 for $m_{\tilde{g}} \sim 1.7$ TeV, where gluino decays into 3rd generation squarks become dominant, and getting back above 0.95 for $m_{\tilde{g}} \sim 1.8$–2 TeV. Moreover, we observe that taking into account gluino-pair production would only give a bound of $m_{\tilde{g}} \gtrsim 1.65$–1.7 TeV, as is also found in the limit of heavy squarks in Fig. 5.5. The inclusion of both gluino-pair and gluino-squark production is essential for a correct limit setting.[4]

Next, we compare in Fig. 5.7 the CLs values in different signal regions for DG1 and DG3. In order to cut across the dip-peak features in the exclusion contours, we here choose $m_{\tilde{q}} \sim 3.6$ TeV for DG1 and $m_{\tilde{q}} \sim 2.6$ TeV for DG3. We see again that for relatively light gluinos the best signal region is 6j-Meff-1800 and the observed CL value drops below 0.95 for gluino masses around 1.65 TeV. The 6j-Meff-2600 signal region, on the other hand, excludes higher gluino masses, up

---

[4] This was also pointed out in [133] in the context of simplified model limits.

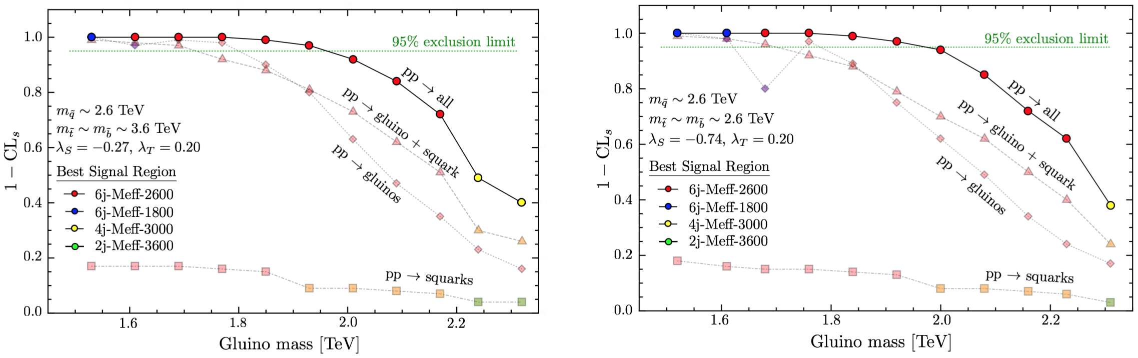

(a) DG1 (b) DG2

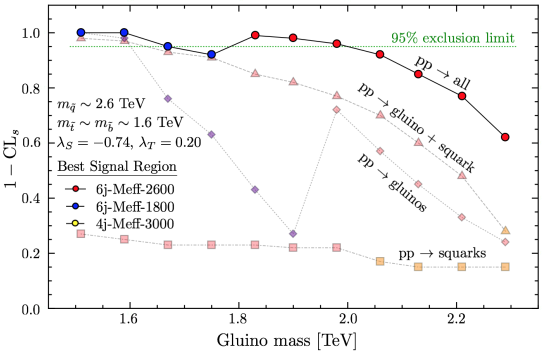

(c) DG3

Figure 5.6: 1-CLs values in the best signal regions from all proton-proton processes as a function of gluino mass for (a) DG1, (b) DG2, (c) DG3; $m_{\tilde q} \sim 2.6$ TeV in all three cases. Individual contributions to the total CLs (denoted by the solid black line labelled $pp \to$ all) are given by the faint dashed lines, namely gluino-pair production (diamonds); squark-pair production (triangles) and gluino-squark production (squares). The best signal region at each gluino mass value is identified by the colour code as indicated in the plot legends.

to about 1.8 TeV in DG1 with $m_{\tilde q} \sim 3.5$ TeV, and up to about 2 TeV in DG3 with $m_{\tilde q} \sim 2.6$ TeV. However, 6j-Meff-2600 becomes the "best" signal region (used for the limit setting in Fig. 5.5) only for gluino masses of 1.8 TeV onwards. This is responsible for the dip-peak structure in the exclusion curve in Fig. 5.5; using only the 6j-Meff-2600 signal region, the gluino mass limit would be stronger.

Turning to the squark exclusion limits, Fig. 5.8 shows the CLs values in the best signal regions as a function of squark mass, for fixed gluino mass. We again compare only DG1 and DG3, as DG2 is very similar to the latter. For $m_{\tilde g} \sim 2.4$ TeV, signal regions with 4 jets (first 4j-Meff-2600 and then 4j-Meff-3000) exclude squark masses up to 1.9 (1.8) TeV for DG1 (DG3). This is partly due to a substantial contribution from gluino-squark production. As the gluino mass is increased to ~ 4 TeV, both squark-pair and gluino-squark production cross-sections are suppressed, and the best signal region is typically one with only 2 jets. The exception is DG3 with squark masses around 1 TeV, where a 5-jet signal region with rather low M_{eff} cut (5j-Meff-1600) becomes the best one. This is again a consequence of the $\tilde\chi_2^0 \to Z^* \tilde\chi_1^0$ decays, which are present in DG3 (and DG2) but not in DG1.

Finally, turning to the heavy winos scenario, Fig. 5.9 show the 95% CL exclusion limits in the gluino vs. squark mass plane for the DG4 and its MSSM equivalent MSSM4 scenarios. Interestingly, when comparing these limits with the ones for DG2 and DG3, we find very similar

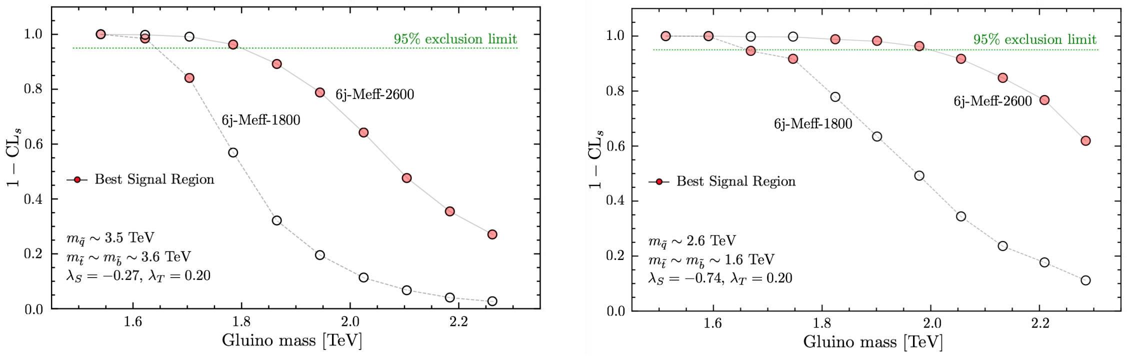

(a) DG1 (b) DG3

Figure 5.7: Comparison of 1-CLs values in the 6j-Meff-1800 and 6j-Meff-2600 signal regions as a function of gluino mass, for (a) DG1 with $m_{\tilde{q}} \sim 3.6$ TeV and (b) DG3 with $m_{\tilde{q}} \sim 2.6$ TeV. The best signal region is identified by full red circles.

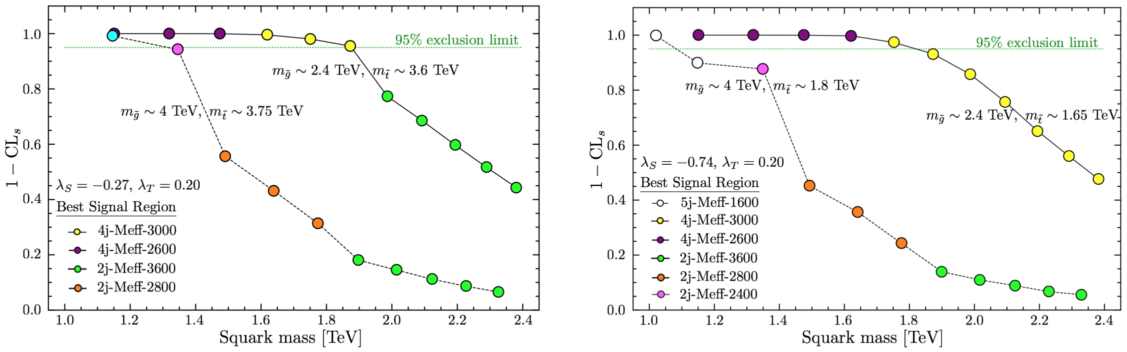

(a) DG1 (b) DG3

Figure 5.8: 1-CLs values in the best signal regions from all proton-proton processes as a function of squark mass for (a) DG1 and (b) DG3. The solid lines are for $m_{\tilde{g}} \sim 2.4$ TeV, while the dashed lines are for $m_{\tilde{g}} \sim 4$ TeV. (Since the input parameters are the soft masses, $m_{\tilde{t}}$ and $m_{\tilde{b}}$ vary slightly in the two cases.)

results; the main difference is a small increase of the squark limit by about 100–200 GeV, when winos are heavy. Regarding DG4 compared to MSSM4, the same arguments as for the light wino cases apply.

Before concluding this sector, a comment is in order on the effect of higher-order corrections. It is well known from the MSSM [269, 270] that K-factors for gluino-pair and gluino-squark production can be very large, of the order of a factor 2–3, depending on the PDF set used while K-factors for squark production are somewhat smaller but still sizeable. The reason for this comes from the fact that the K-factors for squark-pair final states are almost mass independent, while for final states involving gluinos the K-factor mass dependence is strong. This is particularly noticeable in the scenario where squarks and gluinos are almost mass degenerate. For a fixed gluino mass and increasing squark mass, the LO cross section decreases while the NLO correction increases, leading to larger K-factors. For the DG case, the next-to-leading order (NLO) corrections to squark production in the R-symmetric model were computed in [239], with the conclusion that NLO K-factors are generally larger than in the MSSM by the order of 10–20%. Since the cross-section of squark production falls off very steeply with increasing squark mass, K ≈ 2 has only little impact, pushing the gluino mass limit about 100 GeV higher. The higher-

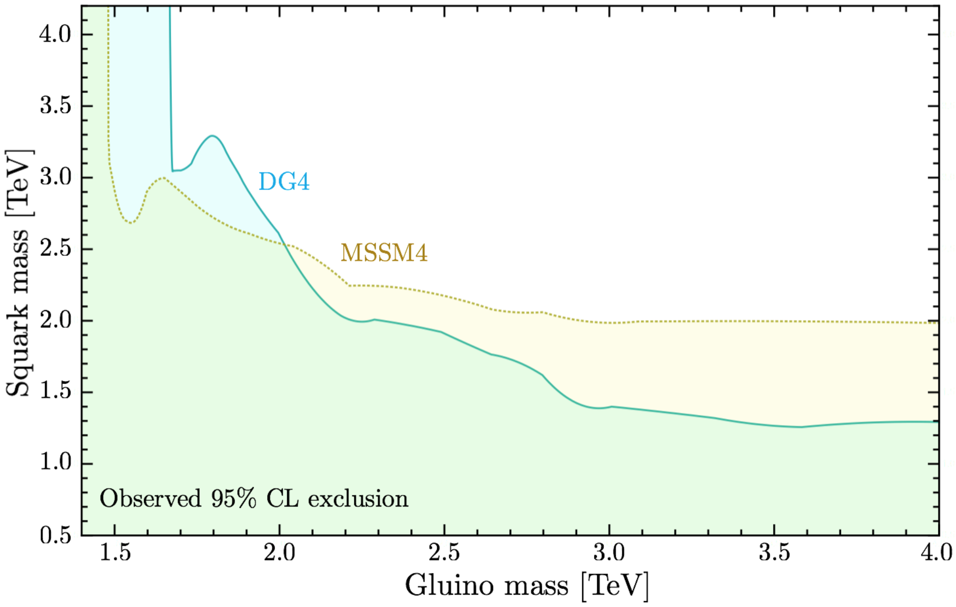

Figure 5.9: 95% CL exclusion limits in the gluino vs. squark mass plane for DG4, and comparison to MSSM4.

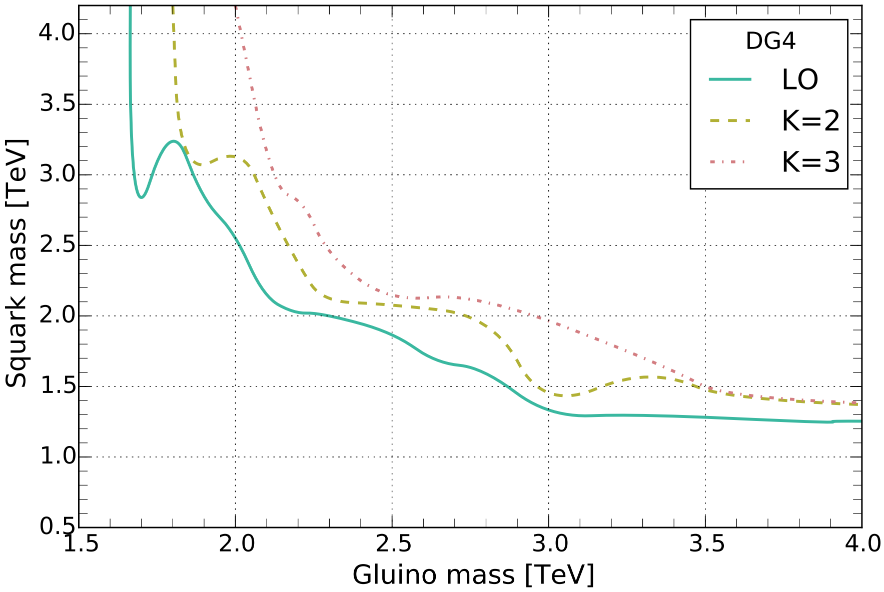

Figure 5.10: 95% CL exclusion limits in the gluino vs. squark mass plane for benchmark DG4 with K-factors 1 (LO), 2 and 3.

order corrections for Dirac gluino final states have not been computed explicitly, but we may assume they are not vastly different from the MSSM. Taking a K-factor of 2–3 as the reference, the gluino mass limit increases by roughly 200 GeV to $m_{\tilde{g}} \gtrsim 2$ TeV for heavy squarks, while for $m_{\tilde{g}} \approx m_{\tilde{q}}$ the limit is pushed to roughly 2.3–2.4 TeV. We illustrate this explicitly for the scenario DG4 in Fig. 5.10.

5.2.4 Conclusions

Most SUSY searches at the LHC are optimised for the MSSM, where gauginos are Majorana particles. Dirac gauginos are, however, an interesting and theoretically well-motivated alternative. Their phenomenological consequences at the LHC include that gluino-pair production is enhanced by a factor 2 as compared to the MSSM, while squark production is strongly suppressed due to a much faster decoupling of the gluino t-channel exchange. Moreover, the extended chargino and neutralino sector present in DG models can have important effects on the collider signatures.

Here, we have investigated the bounds from LHC searches on squarks and gluinos in the Minimal Dirac Gaugino Supersymmetric Standard Model for several representative benchmark scenarios. Since a typical MDGSSM scenario should have electroweakinos not too far above the electroweak scale, we chose, as a primary test case, scenarios with a bino-like LSP around 200 GeV, higgsinos around 400 GeV and winos around 500 GeV. Thus all charginos and neutralinos may appear in gluino and squark cascade decays. We also considered a scenario with heavier winos of about 1200 GeV, and we compared all these to the nearest equivalent models in the MSSM.

In the context of simplified model constraints, derived with `SModelS`, the large variety of possible decay modes in our benchmark scenarios led to very weak limits. The reason is, that in complex scenarios like the ones considered here, only a small fraction of the total SUSY production leads to simple signal topologies which are constrained by the available simplified model results.

We therefore went on to confront our benchmark scenarios with a full recasting of the ATLAS multi-jet + MET search [268] with `MadAnalysis 5`. By comparing the bounds in the DG benchmark scenarios to those in the MSSM, we confirmed and quantified by how much supersoft models are supersafe: for large gluino masses, the bounds on squarks are very significantly (by several hundred GeV) suppressed compared to the MSSM, and this should have consequences for the naturalness of allowed models. We showed that this statement is robust even including loop corrections to the production. On the other hand, for smaller gluino masses, the extra degrees of freedom lead to larger production cross-sections, and so the lower limit on the gluino mass in these models is somewhat higher than in the MSSM.

An important feature of the DG case, which we discussed in some detail here, is that the trilinear λ_S and λ_T couplings, which give a tree-level boost to the light Higgs mass, lead to small mass splittings within the bino and wino states. This is important for LHC phenomenology because, if the mass splitting between the two lightest states (in our benchmark scenarios the two binos) is very small, then the $\tilde{\chi}_2^0$ can live long enough to effectively be a co-LSP on collider scales and appear only as MET. For larger mass splittings, however, the $\tilde{\chi}_2^0$ may decay promptly into $f\bar{f}\tilde{\chi}_1^0$ via an off-shell Z-boson, leading to an additional step in part of the gluino and squark cascade decays. For $m_{\tilde{g}} \approx m_{\tilde{q}}$ this has no noticeable influence on the mass limits. For heavy gluinos or squarks, however, we showed that the mass limits slightly weaken when λ_S is large.

5.3 Constraining the electroweakino sector.

5.3.1 Introduction

The lightest neutralino [271, 272, 32] in supersymmetric models with conserved R-parity has been the prototype for particle dark matter (DM) for decades, motivating a multitude of phenomenological studies regarding both astrophysical properties and collider signatures. The ever tightening experimental constraints, in particular from the null results in direct DM detection experiments, are however severely challenging many of the most popular realisations. This is in particular true for the so-called well-tempered neutralino [273] of the MSSM, which is pushed into blind spots [274] of direct DM detection. One sub-TeV scenario that survives in the MSSM is bino-wino DM [275, 276, 277, 278], whose discovery is, however, very difficult experimentally [279, 280, 281].

It is thus interesting to investigate neutralino DM beyond the MSSM. While a large literature exists on this topic, most of it concentrates on models where the neutralinos – or gauginos in general – have Majorana soft masses. Models with Dirac gauginos have received much less attention, despite their excellent theoretical and phenomenological motivations. The phenomenology of neutralinos and charginos ("electroweakinos" or "EW-inos") in DG models is indeed quite different from that of the MSSM. Therefore, we here provide up-to-date constraints on this sector in the context of the MDGSSM.

Currently there is no reason that the electroweak fermions must be heavy, (LEP and LHC limits impose only weak constraints) and so far the only real constraints on them have been through DM studies. Therefore we shall begin by revisiting neutralino DM, previously examined in detail in [240] (see also [282, 242]), which we update in this work. We will focus on the EW-ino sector, considering the lightest neutralino $\tilde{\chi}_1^0$ as the Lightest Supersymmetric Particle (LSP), and look for scenarios where the $\tilde{\chi}_1^0$ is a good DM candidate in agreement with relic density and direct detection constraints. In this, we assume that all other new particles of the model are heavy and play no role in the phenomenological considerations.

While the measurement of the DM abundance and limits on its interactions with nuclei have been improved since previous analyses of the model, our major new contribution shall be the examination of up-to-date LHC constraints, in view of DM-collider complementarity. For example, certain collider searches are optimal for scenarios that can only over-populate the relic density of dark matter in the universe, so by considering both together we obtain a more complete picture.

Owing to the additional singlet, triplet and octet chiral superfields necessary for introducing DG masses, the EW-ino sector of the MDGSSM comprises six neutralinos and three charginos, as compared to four and two, respectively, in the MSSM. More concretely, one obtains pairs of bino-like, wino-like and higgsino-like neutralinos, with small mass splittings *within* the bino (wino) pairs induced by the couplings λ_S (λ_T) between the singlet (triplet) fermions with the Higgs and higgsino fields. As pointed out in 5.1 this can potentially lead to a long-lived $\tilde{\chi}_2^0$ and/or $\tilde{\chi}_1^{\pm}$. We will therefore discuss the potential of probing DG DM scenarios with LLP searches at the LHC.

This section is based on [185] and is organized as follows. In subsection 5.4 we explain our numerical analysis: concretely, the setup of the parameter scan, the tools used and constraints imposed, and how chargino and neutralino decays are computed for very small mass differences. In particular, when the phase-space for decays is small enough, hadronic decays are best described by (multi) pion states (rather than quarks), and we describe the implementation of the numerical code to deal with this. Furthermore, loop-induced decays of EW-inos into lighter ones with the emission of a photon can be important, and we describe updates to public codes to handle them correctly.

The results of our study are presented in subsection 5.5. We first delineate the viable parameter space where the lightest neutralino of the MDGSSM is at least part of the DM of the universe, and then discuss consequences for collider phenomenology. Re-interpreting ATLAS and CMS searches for new physics, we characterize the scenarios that are excluded and those that escape detection at the LHC. In addition, we give a comparison of the applicability of a simplified models approach to the limits obtained with a full recasting. We also briefly comment on the prospects of the MATHUSLA experiment. In section 5.6 we then propose a set of benchmark points for further studies. A summary and conclusions are given in section 5.7.

5.4 Setup of the numerical analysis

5.4.1 Parameter scan

We now turn to the numerical analysis. Focusing solely on the EW-ino sector, the parameter space we consider is:

$$0 < m_{DY},\, m_{D2},\, \mu < 2 \text{ TeV}; \quad 1.7 < \tan\beta < 60; \quad -3 < \lambda_S,\, \lambda_T < 3. \tag{5.25}$$

The rest of the sparticle content of the MDGSSM is assumed to be heavy, with slepton masses fixed at 2 TeV, soft masses of the 1st/2nd and 3rd generation squarks set to 3 TeV and 3.5 TeV, respectively, and gluino masses set to 4 TeV. The rest of parameters are set to the same values as in [184]; in particular trilinear A-terms are set to zero.

The mass spectrum and branching ratios are computed with `SPheno` v4.0.3 [283, 262], using the `DiracGauginos` model [284] exported from `SARAH` [258, 259, 257, 260]. This is interfaced to `micrOMEGAs` v5.2 [33, 285, 286][5] for the computation of the relic density, direct detection limits and other constraints explained below. To efficiently scan over the EW-ino parameters, eq. (5.25), we implemented a Markov Chain Monte Carlo (MCMC) Metropolis-Hastings algorithm that walks towards the minimum of the negative log-likelihood function, $-\log(L)$, defined as

$$-\log(L) = \chi^2_{\Omega h^2} - \log(p_{\mathrm{X1T}}) + \log(m_{\mathrm{LSP}})\,. \tag{5.26}$$

Here,

- $\chi^2_{\Omega h^2}$ is the χ^2-test of the computed neutralino relic density compared to the observed relic density, $\Omega h^2_{\mathrm{Planck}} = 0.12$ [28]. In a first scan, this is implemented as an upper bound only, that is
$$\chi^2_{\Omega h^2} = \frac{(\Omega h^2 - \Omega h^2_{\mathrm{Planck}})^2}{\Delta^2_\Omega} \tag{5.27}$$
if $\Omega h^2 > \Omega h^2_{\mathrm{Planck}}$, and zero otherwise. In a second scan, eq. (5.27) is applied as a two-sided bound for all Ωh^2. Allowing for a 10% theoretical uncertainty (as a rough estimate, to account e.g. for the fact that the relic density calculation is done at the tree level only), we take $\Delta^2_\Omega = 0.1\,\Omega h^2_{\mathrm{Planck}}$.

- p_{X1T} is the p-value for the parameter point being excluded by XENON1T results [51]. The confidence level (CL) being given by $1 - p_{\mathrm{X1T}}$, a value of $p_{\mathrm{X1T}} = 0.1$ (0.05) corresponds to 90% (95%) CL exclusion. To compute p_{X1T}, the LSP-nucleon scattering cross sections are rescaled by a factor $\Omega h^2/\Omega h^2_{\mathrm{Planck}}$.

- m_{LSP} is the mass of the neutralino LSP, added to avoid the potential curse of dimensionality.[6]

In order to explore the whole parameter space, a small jump probability is introduced which prevents the scan from getting stuck in local minima of $-\log(L)$. We ran several Markov Chains from different, randomly drawn starting points; the algorithm is outlined step-by-step in Appendix A.

---

[5] More precisely, we used a private pre-release version of `micrOMEGAs` v5.2, which does however give the same results as the official release.

[6] Due to the exponential increase in the volume of the parameter space, one risks having too many points with an m_{LSP} at the TeV scale. Current LHC searches are not sensitive to such heavy EW-inos.

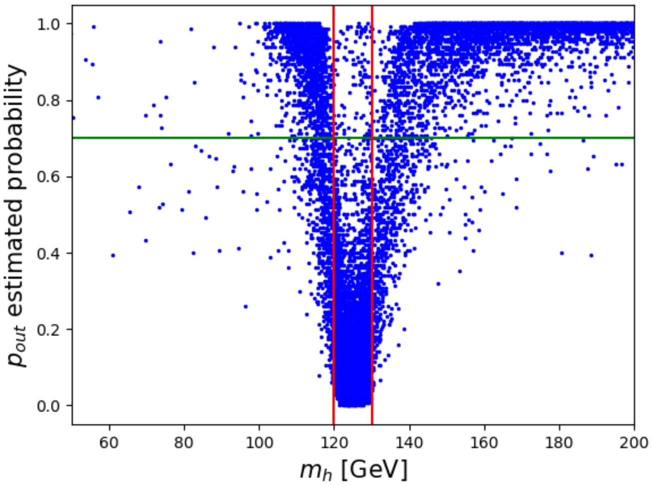

Figure 5.11: Distribution of the estimated probability for p_{out} as function of m_h obtained from the RFC. Points with an estimated probability above 70% (green line) of being outside the desired $120 < m_h < 130$ range (red lines) are discarded. Values in the $m_h > 200$ GeV and $m_h < 50$ GeV ranges are not depicted for clarity reasons.

5.4.2 Higgs mass classifier

A common drawback for the efficiency of phenomenological parameter scans, is finding the subset of the parameter space where the Higgs mass m_h is around the experimentally measured value. Our case is not the exception, as m_h depends on all the input variables considered in our study. This is clear for μ, the mass term in the scalar potential, and $\tan\beta$, the ratio between the vevs. For the soft terms, the dependence becomes apparent when one realises that in DG models, the Higgs quartic coupling receives corrections of the form

$$\delta\lambda \sim \mathcal{O}\left(\frac{g_Y m_{DY}}{m_{SR}}\right)^2 + \mathcal{O}\left(\frac{\sqrt{2}\lambda_S m_{DY}}{m_{SR}}\right)^2 + \mathcal{O}\left(\frac{g_2 m_{D2}}{m_{TP}}\right)^2 + \mathcal{O}\left(\frac{\sqrt{2}\lambda_T m_{D2}}{m_{TP}}\right)^2 , \tag{5.28}$$

where m_{SR} and m_{TP} are the tree-level masses of the singlet and triplet scalars, respectively, and are given large values to avoid a significant suppression on the Higgs mass[7].

To overcome this issue, we have implemented Random Forest Classifiers (RFCs) that predict, from the initial input values, if the parameter point has a m_h inside (p_{in}) or outside (p_{out}) the desired our $120 < m_h < 130$ GeV range. A sample of 50623 points was chosen so as to have an even distribution of inside/outside range points. The data was then divided as training and test data in a 67:33 split. We trained the classifier using the RFC algorithm in the `scikit-learn` python module with 150 trees in the forest (n_estimators=150).

The obtained mean accuracy score for the trained RFC was 93.75%. However, we are interested in discarding as many points with m_h outside of range as possible while keeping all the p_{in} ones. To do so we have rejected only the points with a 70% estimated probability of being p_{out}. In this way, we obtained an improved 98.8% on the accuracy for discarding p_{out} points while still rejecting 86% of them. The cut value of estimated probability for p_{out} was chosen as an approximately optimal balance between accuracy and rejection percentage. Above the 70%

---

[7] See for instance, Sec. 2.4 of [184] for a discussion on the effects of electroweak soft terms on the tree-level Higgs mass in DG models.

value there is no significant improvement in the accuracy, but the rejection percentage depreciates. This behaviour is schematised in Figure 5.11, where the estimated probability of p_{out} is shown as a function of m_h.

Finally, to estimate the overall improvement on the scan efficiency, we multiplied the percentage of real p_{out} (roughly 88%) by the p_{out} rejection percentage (86%) and obtained an overall 75% rejection percentage. Hence, the inclusion of the classifier yields a scan approximately four times faster.

In the various MCMC runs we kept for further analysis all points scanned over, which

1. have a neutralino LSP (charged LSPs are discarded);
2. have a light Higgs boson in the range $120 < m_h < 130$ GeV (see above);
3. avoid mass limits from supersymmetry searches at LEP as well as constraints from the Z boson invisible decay width as implemented in `micrOMEGAs` [285];
4. have $\Omega h^2 < 1.1\,\Omega h^2_{\text{Planck}}$ (or $\Omega h^2 = \Omega h^2_{\text{Planck}} \pm 10\%$) and
5. have $p_{\text{X1T}} > 0.1$.

With the procedure outlined above, many points with very light LSP, in the mass range below $m_h/2$ and even below $m_Z/2$, are retained. We therefore added two more constraints *a posteriori*. Namely, we require for valid points that

6. $\Delta\rho$ lies within 3σ of the measured value $\Delta\rho_{\text{exp}} = (3.9 \pm 1.9) \times 10^{-4}$ [287], the 3σ range being chosen in order to include the SM value of $\Delta\rho = 0$;
7. signal-strength constraints from the SM-like Higgs boson as computed with `Lilith-2` [288] give a p-value of $p_{\text{Lilith}} > 0.05$; this eliminates in particular points in which $m_{\text{LSP}} < m_h/2$, where the branching ratio of the SM-like Higgs boson into neutralinos or charginos is too large.

Points which do not fulfil these conditions are discarded. We thus collect in total 52550 scan points (out of $\mathcal{O}(10^6)$ tested points), which fulfil all constraints, as the basis for our phenomenological analysis.

5.4.3 Treatment of electroweakino decays

As argued above and will become apparent in the next section, many of the interesting scenarios in the MDGSSM feature the second neutralino and/or the lightest chargino very close in mass to the LSP. With mass splittings of $\mathcal{O}(1)$ GeV, $\tilde{\chi}_1^\pm$ or $\tilde{\chi}_2^0$ decays into $\tilde{\chi}_1^0+$ pion(s) and $\tilde{\chi}_2^{0,\pm}$ decays into $\tilde{\chi}_1^{0,\pm} + \gamma$ become important. These decays were in the first case not implemented, and in the second not treated correctly in the standard `SPheno`/`SARAH`. We therefore describe below how these decays are computed in our analysis; the corresponding modified code is available online [289].[8]

Note that the precise calculation of the chargino and neutralino decays is important not only for the collider signatures (influencing branching ratios and decay lengths), but can also impact the DM relic abundance and/or direct detection cross sections.

---

[8] We leave the decays $\tilde{\chi}_i^0$ to $\tilde{\chi}_j^\pm+$ pion(s) to future work.

Chargino decays into pions

When the mass splitting between chargino and lightest neutralino becomes sufficiently small, three-body decays via an off-shell W-boson, $\tilde{\chi}_1^{\pm} \rightarrow \tilde{\chi}_1^0 + (W_\mu^{\pm})^*$ start to dominate. However, as pointed out in e.g. Appendix A of [290] (see also [291] and references therein), when $\Delta m \lesssim 1.5$ GeV it is not accurate to describe the W^* decays in terms of quarks, but instead we should treat the final states as one, two or three pions (with Kaon final states being Cabibbo-suppressed)[9]; and for $\Delta m < m_\pi$ the hadronic channel is closed. Surprisingly, these decays have not previously been fully implemented in spectrum generators; `SPheno` contains only decays to single pions from neutralinos or charginos in the MSSM via an off-shell W or Z boson, and `SARAH` does not currently include even these. A full generic calculation of decays with mesons as final states for both charged and neutral EW-inos (and its implementation in `SARAH`) should be presented elsewhere; for this work we have adapted the results of [92, 290, 292] which include only the decay via an off-shell W:

$$\Gamma(\tilde{\chi}_1^- \rightarrow \tilde{\chi}_1^0 \pi^-) = \frac{f_\pi^2 G_F^2}{2\pi g_2^2} \frac{|\vec{k}_\pi|}{\widetilde{m}_-^2} \left\{ \left(|c_L|^2 + |c_R|^2\right) \left[\left(\widetilde{m}_-^2 - \widetilde{m}_0^2\right)^2 - m_\pi^2 \left(\widetilde{m}_-^2 + \widetilde{m}_0^2\right) \right] \right. \\ \left. + 4 \widetilde{m}_0 \widetilde{m}_- m_\pi^2 \mathrm{Re}\left(c_L c_R^*\right) \right. \tag{5.29}$$

$$\Gamma(\tilde{\chi}_1^- \rightarrow \tilde{\chi}_1^0 \pi^- \pi^0) = \frac{G_F^2}{192\pi^3 g_2^2 \widetilde{m}_-^3} \int_{4m_\pi^2}^{(\Delta m_{\tilde{\chi}_1})^2} dq^2 \left|F(q^2)\right|^2 \left(1 - \frac{4m_\pi^2}{q^2}\right)^{3/2} \lambda^{1/2}(\widetilde{m}_-^2, \widetilde{m}_0^2, q^2) \\ \left\{ \left[|c_L|^2 + |c_R|^2\right] \left[q^2 \left(\widetilde{m}_-^2 + \widetilde{m}_0^2 - 2q^2\right) + \left(\widetilde{m}_-^2 - \widetilde{m}_0^2\right)^2 \right] - 12 \mathrm{Re}(c_L c_R^*) q^2 \widetilde{m}_- \widetilde{m}_0 \right\}; \tag{5.30}$$

$$\Gamma(\tilde{\chi}_1^- \rightarrow \tilde{\chi}_1^0 3\pi) = \frac{G_F^2}{6912\pi^5 g_2^2 \widetilde{m}_-^3 f_\pi^2} \int_{9m_\pi^2}^{(\Delta m_{\tilde{\chi}_1})^2} dq^2 \lambda^{1/2}(\widetilde{m}_-^2, \widetilde{m}_0^2, q^2) \left|BW_a(q^2)\right|^2 g(q^2) \\ \left\{ \left[|c_L|^2 + |c_R|^2\right] \left[\widetilde{m}_-^2 + \widetilde{m}_0^2 - 2q^2 + \frac{\left(\widetilde{m}_-^2 - \widetilde{m}_0^2\right)^2}{q^2} \right] - 12 \mathrm{Re}(c_L c_R^*) \widetilde{m}_- \widetilde{m}_0 \right\}. \tag{5.31}$$

Here $\widetilde{m}_-, \widetilde{m}_0$ are the masses of the $\tilde{\chi}_1^-, \tilde{\chi}_1^0$ respectively, $\vec{k}_\pi = \lambda^{1/2}(\widetilde{m}_-^2, \widetilde{m}_0^2, m_\pi^2)/(2\widetilde{m}_-)$ is the pion's 3-momentum in the chargino rest frame, and $f_\pi \simeq 93$ MeV is the pion decay constant. The couplings c_L, c_R are the left and right couplings of the chargino and neutralino to the W-boson, which can be defined as $\mathcal{L} \supset -\overline{\tilde{\chi}_1^-} \gamma^\mu (c_L P_L + c_R P_R) \chi_0 W_\mu^-$. The couplings of the W-boson to the light quarks and the W mass are encoded in G_F; in `SARAH` we make the substitution $G_F^2 \rightarrow g_2^2 |c_L^{\overline{u}dW}|^2/(16 M_W^4)$, where $c_L^{\overline{u}dW}$ is the coupling of the up and down quarks to the W-boson.

While the single pion decay can be simply understood in terms of the overlap of the axial current with the pion, the two- and three-pion decays proceed via exchange of virtual mesons which then decay to pions. The form factors for these processes are then determined by QCD, and so working at leading order in the electroweak couplings we can use experimental data for processes involving the same final states; in this case we can use τ lepton decays. The two-pion decays are dominated by ρ and ρ' meson exchange, and the form factor $F(q^2)$ was defined in eqs. (A3) and (A4) of [290]. The expressions for the Breit–Wigner propagator BW_a of the a_1 meson (and *not* the a_2 meson as stated in [92, 290, 292]), which dominates 3π production, as well as for the three-pion phase space factor $g(q^2)$ can be found in eqs. (3.16)–(3.18) of [291]. As in [92, 290, 292] we use the propagator without "dispersive correction," and so include a factor

---

[9] As the mass difference is raised above $\Delta m = 1.5$ GeV is it found numerically that, with many hadronic decay modes being kinematically open, there is a smooth transition to a description in terms of quarks.

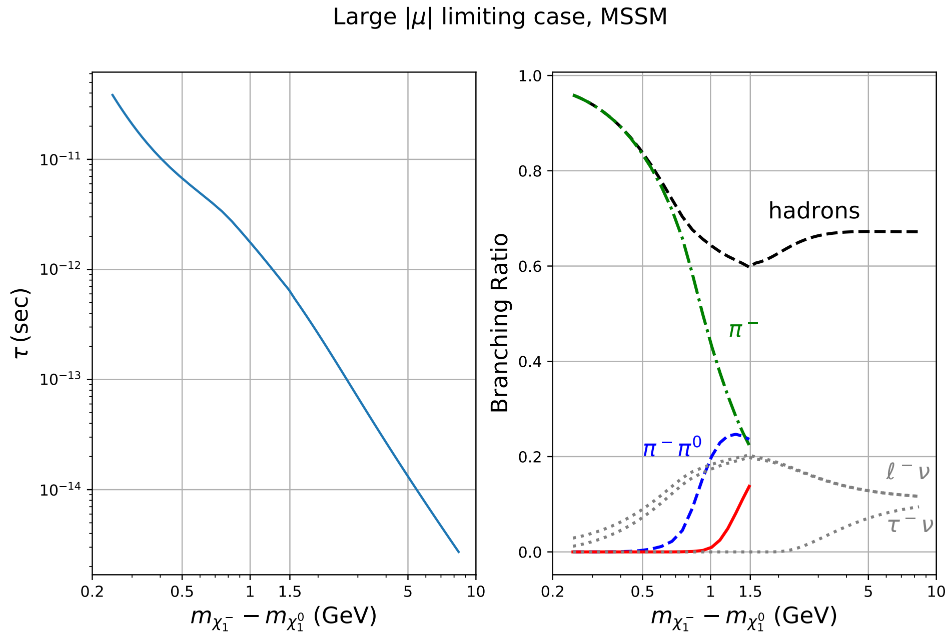

Figure 5.12: Chargino decays in the MSSM limit of our model; see text for details.

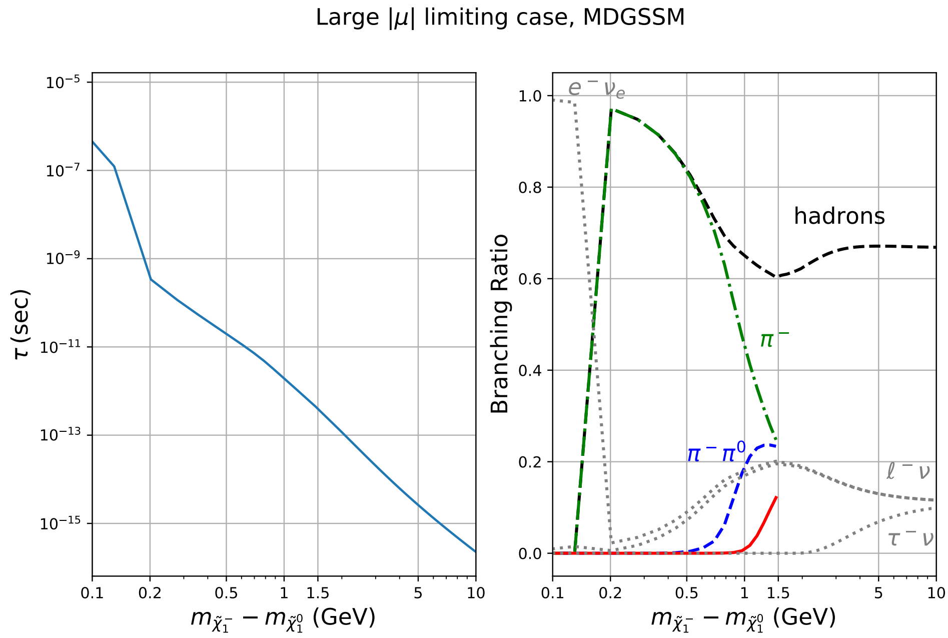

Figure 5.13: Chargino decays in the MDGSSM.

of 1.35 to compensate for the underestimate of $\tau^- \to 3\pi\nu_\tau$ decays by 35%. Note finally that the three-pion decay includes both $\pi^-\pi^0\pi^0$ and $\pi^-\pi^-\pi^+$ modes, which are assumed to be equal.

For comparison with [92, 290, 292], in Figure 5.12 we reproduce Fig. 6 from [290] (same as Fig. 1 in [292]) with our code by taking the MSSM-limit of our model; we add Majorana gaugino masses for the wino fixed at $M_2 = 200$ GeV and scan over values for the bino mass of $M_1 \in [210, 220]$ GeV while taking $\mu = 2000$ GeV and adding supersymmetric masses for the **S** and **T** fields of $M_S = M_T = 1$ TeV. Keeping $\tan\beta = 34.664$ and $B_\mu = (1\,\mathrm{TeV})^2$ we have a spectrum with effectively only Majorana charginos and neutralinos, which can be easily tuned in mass relative to each other by changing the bino mass.

In Figure 5.13 we show the equivalent expressions in the case of interest for this paper, where there are no Majorana masses for the gauginos. We take $\tan\beta = 34.664, \mu = 2$ TeV, $v_T = -0.568$ GeV, $v_S = 0.92$ GeV, $\lambda_S = -0.2$, $\sqrt{2}\lambda_T = 0.2687$, $m_{D2} = 200$ GeV, and vary m_{DY} between 210 and 221 GeV. We find identical behaviour for both models, except the overall decay rate is slightly different; and note that in this scenario we have $\tilde{\chi}^0_2$ almost degenerate with $\tilde{\chi}^0_1$, so we include decays of $\tilde{\chi}^\pm_1$ to *both* states of the pseudo-Dirac LSP.

Finally, we implemented the decays of neutralinos to single pions via the expression

$$\Gamma(\tilde{\chi}^0_2 \to \tilde{\chi}^0_1 \pi^0) = \frac{f_\pi^2 G_F^2 c_W^2}{2\pi g_2^2} \frac{|\vec{k}_\pi|}{\widetilde{m}_2^2} \bigg\{ \left(|c_L|^2 + |c_R|^2\right) \Big[\left(\widetilde{m}_2^2 - \widetilde{m}_1^2\right)^2 - m_\pi^2 \left(\widetilde{m}_2^2 + \widetilde{m}_1^2\right) \Big] + 4\widetilde{m}_1 \widetilde{m}_2 m_\pi^2 \mathrm{Re}\left(c_L c_R^*\right) \bigg\} \tag{5.32}$$

where now $\widetilde{m}_{1,2}$ are the masses of $\tilde{\chi}^0_{1,2}$ and c_L, c_R are the couplings for the neutralinos to the Z-boson analogously defined as above; since the neutralino is Majorana in nature we must have $c_R = -c_L^*$.

Neutralino decays into photons

In the MDGSSM, the mass splitting between the two lightest neutralinos is naturally small.[10] Therefore in a significant part of the parameter space the dominant $\tilde{\chi}^0_2$ decay mode is the loop-induced process $\tilde{\chi}^0_2 \to \tilde{\chi}^0_1 + \gamma$. This is controlled by an effective operator

$$\mathcal{L} = \overline{\Psi}_1 \gamma^\mu \gamma^\nu (C_{12} P_L + C_{12}^* P_R) \Psi_2 F_{\mu\nu}, \tag{5.33}$$

where $\Psi_i \equiv \begin{pmatrix} \chi_i^0 \\ \overline{\chi}_i^0 \end{pmatrix}$ is a Majorana spinor, and yields

$$\Gamma(\tilde{\chi}^0_2 \to \tilde{\chi}^0_1 + \gamma) = \frac{|C_{12}|^2}{2\pi} \frac{(m_{\tilde{\chi}_2}^2 - m_{\tilde{\chi}_1}^2)^3}{m_{\tilde{\chi}_2}^3}. \tag{5.34}$$

Our expectation (and indeed as we find for most of our points) is that $|C_{12}| \sim 10^{-5}$–$10^{-6}\,\mathrm{GeV}^{-1}$.

This loop decay process is calculated in `SPheno`/`SARAH` using the routines described in [261]. However, we found that the handling of fermionic two-body decays involving photons or gluons was not correctly handled in the spin structure summation. Suppose we have S-matrix elements $\mathcal{M}$ for a decay $F(p_1) \to F(p_2) + V(p_3)$ with a vector having wavefunction ε_μ, then we can decompose the amplitudes according to their Lorentz structures (putting v_i for the antifermion wavefunctions) as

$$\mathcal{M} = \varepsilon_\mu \mathcal{M}^\mu = \varepsilon_\mu(p_3) \Big[x_1 \overline{v}_1 P_L \gamma^\mu v_2 + x_2 \overline{v}_1 P_R \gamma^\mu v_2 + p_1^\mu x_3 \overline{v}_1 P_L v_2 + p_1^\mu x_4 \overline{v}_1 P_R v_2 \Big]. \tag{5.35}$$

This is the decomposition made in `SARAH` which computes the values of the amplitudes $\{x_i\}$. Now, if V is massless, and since $\mathcal{M}$ is an S-matrix element, the Ward identity requires $(p_3)_\mu \mathcal{M}^\mu = 0$ (note that this requires that we include self-energy diagrams in the case of charged fermions), and this leads to two equations relating the $\{x_i\}$:

$$x_3 = \frac{m_1 x_2 - m_2 x_1}{p_1 \cdot p_3}, \qquad x_4 = \frac{m_1 x_1 - m_2 x_2}{p_1 \cdot p_3}, \qquad \text{where } p_1 \cdot p_3 = \frac{1}{2}(m_1^2 - m_2^2). \tag{5.36}$$

---

[10] This could be even more so in the case of the MRSSM with a small R-symmetry violation.

Here, m_1 and m_2 are the masses of the first and second fermion, respectively. Performing the spin and polarisation sums naively, we have the matrix

$$\sum_{\text{spins, polarisations}} \mathcal{M}\mathcal{M}^* \equiv x_i \mathcal{M}_{ij} x_j^*, \tag{5.37}$$

$$\mathcal{M}_{ij} = \begin{pmatrix} 2(m_1^2+m_2^2) & -8m_1m_2 & 2m_1^2m_2 & m_1(m_1^2+m_2^2) \\ -8m_1m_2 & 2(m_1^2+m_2^2) & m_1(m_1^2+m_2^2) & 2m_1^2m_2 \\ 2m_1^2m_2 & m_1(m_1^2+m_2^2) & -m_1^2(m_1^2+m_2^2) & -2m_1^3m_2 \\ m_1(m_1^2+m_2^2) & 2m_1^2m_2 & -2m_1^3m_2 & -m_1^2(m_1^2+m_2^2) \end{pmatrix}.$$

When we substitute in the Ward identities and re-express as just x_1, x_2 we have

$$\sum_{\text{spins, polarisations}} \mathcal{M}\mathcal{M}^* = (x_1, x_2) \begin{pmatrix} 2(m_1^2+m_2^2) & -4m_1m_2 \\ -4m_1m_2 & 2(m_1^2+m_2^2) \end{pmatrix} \begin{pmatrix} x_1^* \\ x_2^* \end{pmatrix}. \tag{5.38}$$

This matrix will yield real, positive-definite widths for any value of the matrix elements x_1, x_2, whereas this is not manifestly true for eq. (5.37). For earlier versions of `SARAH`, instead of one of these expressions above, an incorrect formula was used. As of `SARAH` version `4.14.3` we implemented the spin summation for loop decay matrix elements given in eq. (5.38), i.e. in such decays we compute the Lorentz structures corresponding to x_1, x_2 and ignore x_3, x_4.

This applies to all $\tilde{\chi}^0_{i\neq 1} \to \tilde{\chi}^0_1\gamma$ and $\tilde{\chi}^\pm_{j\neq 1} \to \tilde{\chi}^\pm_1\gamma$ transitions.

5.5 Results

5.5.1 Properties of viable scan points

We are now in the position to discuss the results from the MCMC scans. We begin by considering the properties of the $\tilde{\chi}^0_1$ as a DM candidate. Figure 5.14((a)) shows the bino, wino and higgsino composition of the $\tilde{\chi}^0_1$ when only an upper bound on Ωh^2 is imposed; all points in the plot also satisfy XENON1T ($p_{\mathrm{X1T}} > 0.1$) and all other constraints listed in section 5.4.1. We see that cases where the $\tilde{\chi}^0_1$ is a mixture of all states (bino, wino and higgsino) are excluded, while cases where it is a mixture of only two states, with one component being dominant, can satisfy all constraints. Also noteworthy is that there are plenty of points in the low-mass region, $m_{\mathrm{LSP}} < 400$ GeV.

Figure 5.14((b)) shows the points where the $\tilde{\chi}^0_1$ makes for all the DM abundance. This, of course, imposes much stronger constraints. In general, scenarios with strong admixtures of two or more EW-ino states are excluded and the valid points are confined to the corners of (almost) pure bino, wino or higgsino. Similar to the MSSM, the higgsino and especially the wino DM cases are heavy, with masses $\gtrsim 1$ TeV, and only about a 5% admixture of another interaction eigenstate; in the wino case, the MCMC scan gave only one surviving point within the parameter ranges scanned over. Light masses are found only for bino-like DM; in this case there can also be slightly larger admixtures of another state: concretely we find up to about 10% wino or up to 35% higgsino components.

As mentioned, we assume that all other sparticles besides the EW-inos are heavy. Hence, co-annihilations of EW-inos which are close in mass to the LSP must be the dominating processes to achieve Ωh^2 of the order of 0.1 or below. The relation between mass, bino/wino/higgsino nature of the LSP, relic density and mass difference to the next-to-lightest sparticle (NLSP) is illustrated in Figure 5.15. The three panels of this figure show m_{LSP} vs. Ωh^2 for the points from Figure 5.14((a)), where the LSP is > 50% bino, wino, or higgsino, respectively. The NLSP–LSP mass difference is shown in colour, while different symbols denote neutral and charged NLSPs. Two things are apparent besides the dependence of Ωh^2 on $m_{\tilde{\chi}^0_1}$ for the different scenarios:

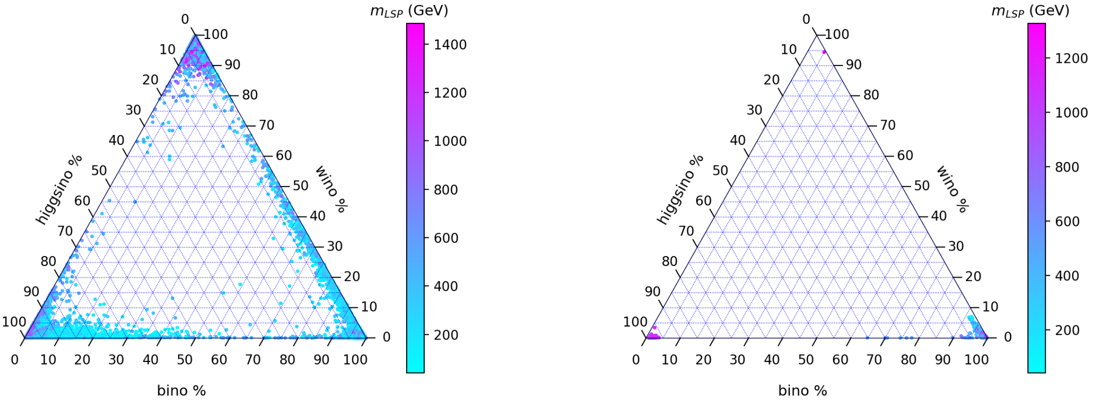

(a) $\Omega h^2 < 1.1\,\Omega h^2{}_{\text{Planck}}$.

(b) $\Omega h^2 = \Omega h^2{}_{\text{Planck}} \pm 10\%$.

Figure 5.14: Bino, wino and higgsino admixtures of the LSP in the region where it makes up for (a) at least a part or (b) all of the DM abundance; limits from XENON1T and all other constraints listed in section 5.4.1 are also satisfied. The colour denotes the mass of the LSP.

1. All three cases feature small NLSP–LSP mass differences. For a wino-like LSP, this mass difference is at most 3 GeV. For bino-like and higgsino-like LSPs it can go up to nearly 25 GeV, though for most points it is just few GeV.

2. The NLSP can be neutral or charged, that is in all three cases we can have mass orderings $\tilde{\chi}_1^0 < \tilde{\chi}_1^\pm < \tilde{\chi}_2^0$ as well as $\tilde{\chi}_1^0 < \tilde{\chi}_2^0 < \tilde{\chi}_1^\pm$.

For bino-like LSP points outside the Z and Higgs-funnel regions, a small mass difference between the LSP and NLSP is however not sufficient—co-annihilations with other nearby states are required to achieve $\Omega h^2 \leq 0.132$. Indeed, as shown in Figure 5.16, we have $m_{D2} \approx m_{DY}$, with typically $m_{D2}/m_{DY} \approx 0.9$–$1.4$, over much of the bino-LSP parameter space outside the funnel regions. This leads to bino-wino co-annihilation scenarios like also found in the MSSM. The scattered points with large ratios m_{D2}/m_{DY} have $\mu \approx m_{DY}$, i.e. a triplet of higgsinos close to the binos. Outside the funnel regions, the bino-like LSP points therefore feature $m_{\tilde{\chi}_1^\pm} - m_{\tilde{\chi}_1^0} \lesssim 30$ GeV and $m_{\tilde{\chi}_{3,4}^0} - m_{\tilde{\chi}_1^0} \lesssim 60$ GeV in addition to $m_{\tilde{\chi}_2^0} - m_{\tilde{\chi}_1^0} \lesssim 20$ GeV.

For completeness we also give the maximal mass differences found within triplets (quadruplets) of higgsino (wino) states in the higgsino (wino) LSP scenarios. Concretely we have $m_{\tilde{\chi}_2^0} - m_{\tilde{\chi}_1^0} \lesssim 15$ GeV and $m_{\tilde{\chi}_1^\pm} - m_{\tilde{\chi}_1^0} \lesssim 50$–$10$ GeV (decreasing with increasing $m_{\tilde{\chi}_1^0}$) in the higgsino LSP case. In the wino LSP case, $m_{\tilde{\chi}_1^\pm} - m_{\tilde{\chi}_1^0} \lesssim 4$ GeV, while $m_{\tilde{\chi}_2^0, \tilde{\chi}_2^\pm} - m_{\tilde{\chi}_1^0} \lesssim 20$ GeV (though mostly below 10 GeV). However, as noted before, either mass ordering, $m_{\tilde{\chi}_2^0} < m_{\tilde{\chi}_1^\pm}$ or $m_{\tilde{\chi}_1^\pm} < m_{\tilde{\chi}_2^0}$ is possible.

An important point to note is that the mass differences are often so small that the NLSP (and sometimes even the NNLSP) becomes long-lived on collider scales, i.e. it has a potentially visible decay length of $c\tau > 1$ mm. This is illustrated in Figure 5.17, which shows in the left panel the mean decay length of the LLPs as function of their mass difference to the LSP. Long-lived charginos will lead to charged tracks in the detector, while long-lived neutralinos could potentially lead to displaced vertices. However, given the small mass differences involved, the decay products of the latter will be very soft. The right panel in Figure 5.17 shows the importance of the radiative decay of long-lived $\tilde{\chi}_2^0$s in the plane of $\tilde{\chi}_1^0$ mass vs. $\tilde{\chi}_2^0$–$\tilde{\chi}_1^0$ mass difference. As can be seen, decays into (soft) photons are clearly dominant.

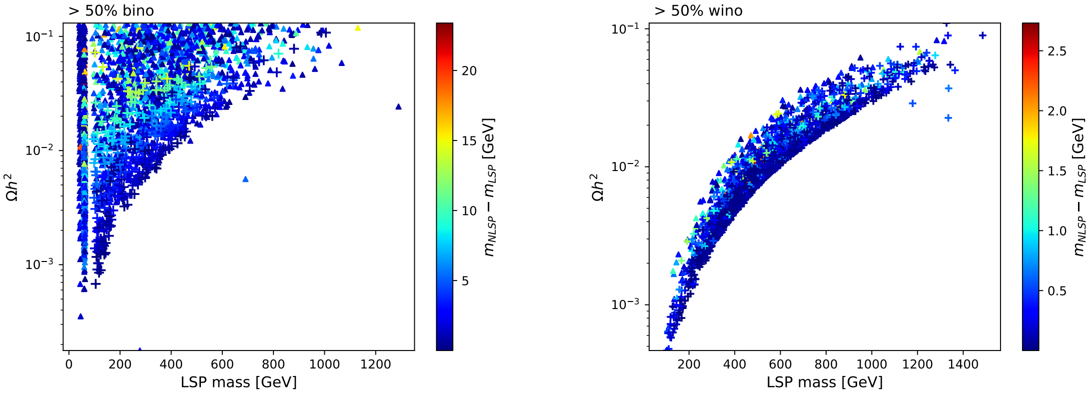

(a) LSP more than 50% bino.

(b) LSP more than 50% wino.

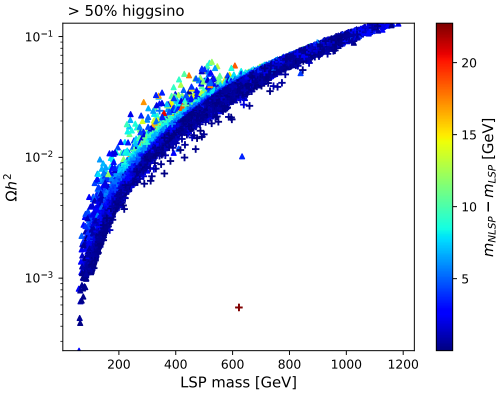

(c) LSP more than 50% higgsino.

Figure 5.15: m_{LSP} vs. Ωh^2 for points from Figure 5.14((a)), where (a) LSP $>$ 50% bino, (b) LSP $>$ 50% wino, and (c) LSP $>$ 50% higgsino. In color, the NLSP–LSP mass difference. Triangles represent neutral NLSPs while crosses represent charged NLSPs.

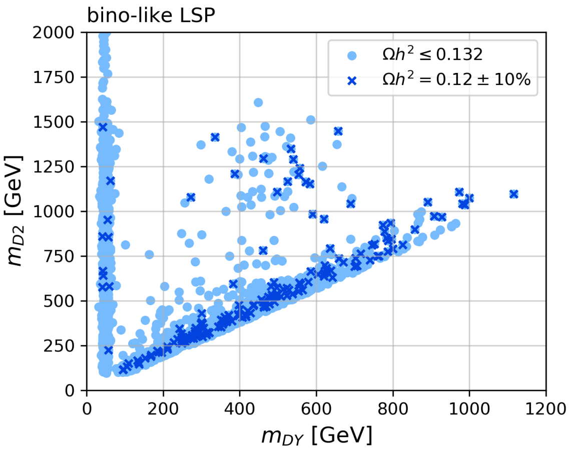

Figure 5.16: m_{DY} vs. m_{D2} for scan points with a bino-like LSP, cf. Figure 5.15(a).

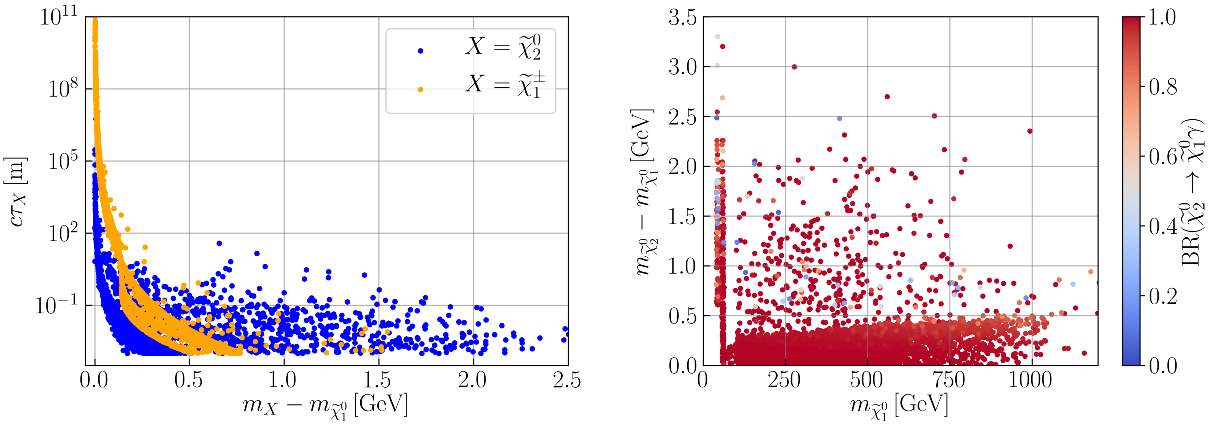

Figure 5.17: Left: Mean decay length $c\tau$ as a function of the mass difference with the LSP, for all points with long-lived particles ($c\tau > 1$ mm); blue points have a neutralino and orange points a chargino LLP. Right: $m_{\tilde{\chi}_1^0}$ vs. $m_{\tilde{\chi}_2^0} - m_{\tilde{\chi}_1^0}$ for points with long-lived neutralinos; the branching ratio of the loop decay $\tilde{\chi}_2^0 \to \tilde{\chi}_1^0 \gamma$ is indicated in colour.

Let us now turn to the region where the $\tilde{\chi}_1^0$ would account for all the DM. Figure 5.18 (left) shows the points with $\Omega h^2 = \Omega h^2_{\text{Planck}} \pm 10\%$ in the plane of $m_{\tilde{\chi}_1^0}$ vs. $m_{\tilde{\chi}_2^0} - m_{\tilde{\chi}_1^0}$. Points with bino-like, higgsino-like and wino-like $\tilde{\chi}_1^0$ are distinguished by different colours and symbols. As expected from the discussion above, there are three distinct regions of bino-like, higgsino-like and wino-like DM, indicated in blue, green and orange, respectively.

From the collider point of view, the bino-like DM region is perhaps the most interesting one, as it has masses below a TeV. We find that, in this case, the NLSP is always the $\tilde{\chi}_2^0$ with mass differences $m_{\tilde{\chi}_2^0} - m_{\tilde{\chi}_1^0}$ ranging from about 0.2 GeV to 16 GeV. As already pointed in [282, 240], this small mass splitting helps achieve the correct relic density through $\tilde{\chi}_{1,2}^0$ co-annihilation. In the region of $m_{\tilde{\chi}_1^0} = 100-1000$ GeV, it is induced by $-\lambda_S \simeq 0.05-1.26$.[11] For lower masses,

---

[11] Our conventions differ (as usual) from the `SARAH` `DiracGauginos` implementation: $\lambda_S \equiv -$`lam` and $\lambda_T \equiv$ `LT`$/\sqrt{2}$ in `SARAH` convention.

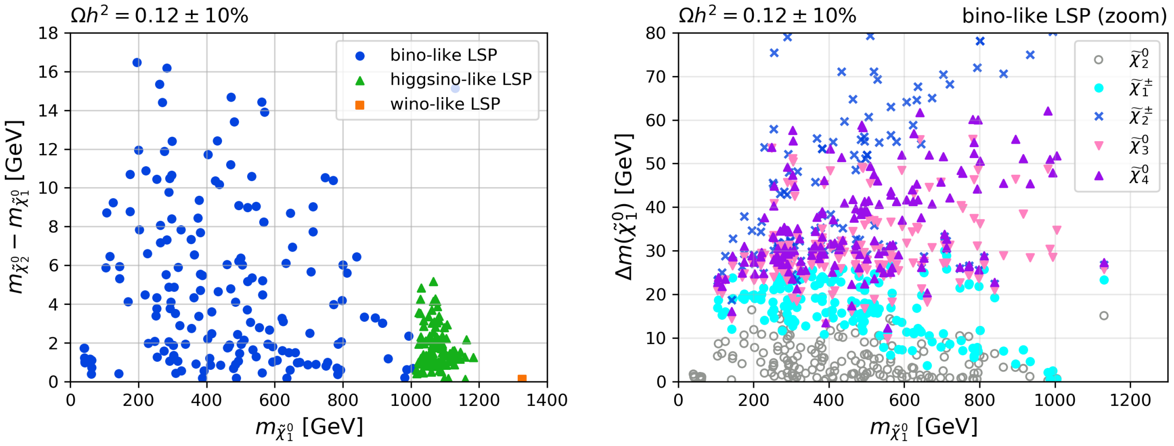

Figure 5.18: Left: $m_{\rm LSP}$ vs. NLSP–LSP mass difference for points from Figure 5.14((b)); points with bino-, higgsino-, and wino-like LSP are shown in blue, green and orange, respectively. Right: mass differences Δm of $\tilde{\chi}^0_{2,3,4}$ and $\tilde{\chi}^\pm_{1,2}$ to the $\tilde{\chi}^0_1$ as function of the $\tilde{\chi}^0_1$ mass, for the bino DM points of the right panel.

$m_{\tilde{\chi}^0_1} \simeq 40$ GeV or $m_{\tilde{\chi}^0_1} \simeq 60$ GeV, where the DM annihilation proceeds via the Z or h pole, and we have $\Delta m \simeq 0.4-1.7$ GeV and $|\lambda_S| \simeq 6 \times 10^{-4} - 0.26$ (with $\lambda_S \simeq -0.26$ to 0.02). With the exception of the funnel region, all the bino-like points in the left panel of Figure 5.18 also have a $\tilde{\chi}^\pm_1$ and $\tilde{\chi}^0_{3,4}$ close in mass to the $\tilde{\chi}^0_1$. This is shown explicitly in the right panel of the same figure. Concretely, we have $m_{\tilde{\chi}^\pm_1} - m_{\tilde{\chi}^0_1} \lesssim 30$ GeV and $m_{\tilde{\chi}^0_{3,4}} - m_{\tilde{\chi}^0_1} \approx 10$–$60$ GeV. Often, that is when the LSP has a small wino admixture, the $\tilde{\chi}^\pm_2$ is also close in mass. In most cases $m_{\tilde{\chi}^\pm_1} < m_{\tilde{\chi}^0_3}$ although the opposite case also occurs. All in all this creates peculiar compressed EW-ino spectra; they are similar to the bino-wino DM scenario in the MSSM, but there are more states involved and the possible mass splittings are somewhat larger. In any case, the dominant signatures are 3-body and/or radiative decays of heavier into lighter EW-inos; only the heavier $\tilde{\chi}^\pm_{2,3}$ and $\tilde{\chi}^0_{5,6}$ can decay via an on-shell W, Z or h^0.

Finally we show in Figure 5.19 the spin-independent ($\sigma^{\rm SI}$) and spin-dependent ($\sigma^{\rm SD}$) $\tilde{\chi}^0_1$ scattering cross sections on protons, with the p-value from XENON1T indicated in colour. While the bulk of the points has cross sections that should be testable in future DM direct detection experiments, there are also a few points with cross sections below the neutrino floor. We note in passing that the scattering cross section on neutrons (not shown) is not exactly the same in this model but can differ from that on protons by few percent.

5.5.2 LHC constraints

Let us now turn to the question of how the DG EW-ino scenarios from the previous subsection can be constrained at the LHC. Before reinterpreting various ATLAS and CMS SUSY searches, it is important to point out that the cross sections for EW-ino production are larger in the MDGSSM than in the MSSM. For illustration, Figure 5.20 compares the production cross sections for pp collisions at 13 TeV in the two models. The cross sections are shown as a function of the wino mass parameter, with $m_{D2} = 1.2\, m_{DY}$ ($M_2 = 1.2\, M_1$) for the MDGSSM (MSSM); the other parameters are $\mu \simeq 1400$ GeV, $\tan\beta \simeq 10$, $\lambda_S \simeq -0.29$ and $\sqrt{2}\lambda_T \simeq -1.40$. While LSP-LSP production is almost the same in the two models, chargino-neutralino and chargino-chargino

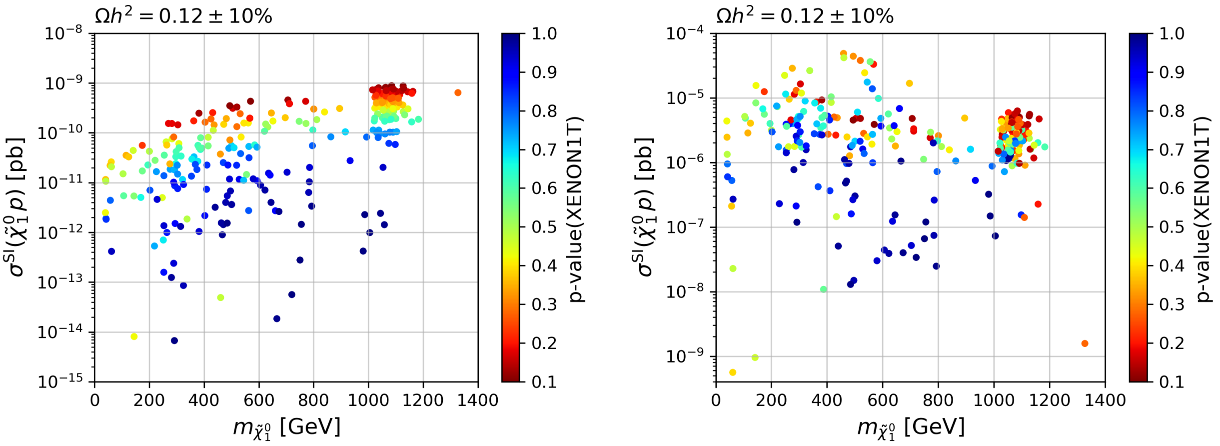

Figure 5.19: Spin-independent (left) and spin-dependent (right) $\tilde{\chi}_1^0$ scattering cross sections on protons as function of the $\tilde{\chi}_1^0$ mass, for the points with $\Omega h^2 = 0.12 \pm 10\%$. The colour code indicates the p-value for XENON1T.

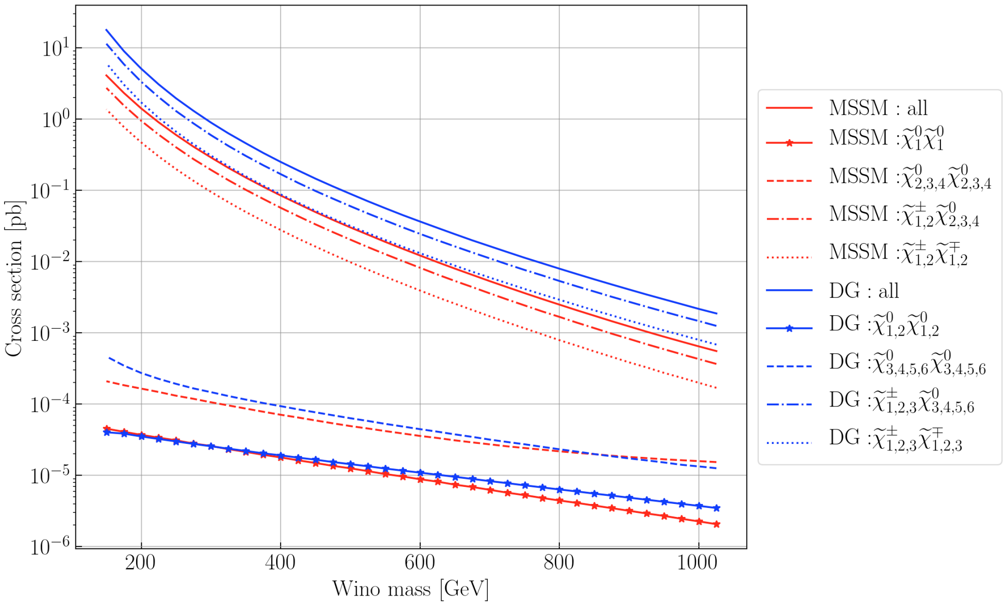

Figure 5.20: EW-ino production cross sections at the 13 TeV LHC as a function of the wino mass parameter, in blue for the MDGSSM and in red for the MSSM; the ratio of the bino and wino mass parameters is fixed as $m_{D2} = 1.2\, m_{DY}$ (MDGSSM) and $M_2 = 1.2\, M_1$ (MSSM), while $\mu \simeq 1400$ GeV, $\tan\beta \simeq 10$, $\lambda_S \simeq -0.29$ and $\sqrt{2}\lambda_T \simeq -1.40$.

production is about a factor 3–5 larger in the MDGSSM, due to the larger number of degrees of freedom.

Constraints from prompt searches

SModelS

We start by checking the constraints from searches for promptly decaying new particles with `SModelS` [134, 171, 293, 172]. The working principle of `SModelS` is to decompose all signatures occurring in a given model or scenario into simplified model topologies, also referred to as simplified model spectra (SMS). Each SMS is defined by the masses of the BSM states, the vertex structure, and the SM and BSM final states. After this decomposition, the signal weights, determined in terms of cross-sections times branching ratios, $\sigma \times \mathrm{BR}$, are matched against a database of LHC results. `SModelS` reports its results in the form of r-values, defined as the ratio of the theory prediction over the observed upper limit, for each experimental constraint that is matched in the database. All points for which at least one r-value equals or exceeds unity ($r_{\rm max} \geq 1$) are considered as excluded.

Concretely we are using `SModelS` v1.2.3 [172]. For our purpose, the most relevant "prompt" search results from Run 2 included in the v1.2.3 database are those from

- the ATLAS EW-ino searches with 139 fb^{-1}, constraining $WZ^{(*)} + E_T^{\rm miss}$ (ATLAS-SUSY-2018-06 [294]), $WH + E_T^{\rm miss}$ (ATLAS-SUSY-2019-08 [295]) and $WW^{(*)} + E_T^{\rm miss}$ (ATLAS-SUSY-2018-32 [296]) signatures arising from chargino-neutralino or chargino-chargino production, as well as
- the CMS EW-ino combination for 35.9 fb^{-1}, CMS-SUS-17-004 [297], constraining $WZ^{(*)} + E_T^{\rm miss}$ and $WH + E_T^{\rm miss}$ signatures from chargino-neutralino production.

One modification we made to the `SModelS` v1.2.3 database is that we included the combined $WZ^{(*)} + E_T^{\rm miss}$ constraints from Fig. 8a of [297]; the original v1.2.3 release has only those from Fig. 7a, which are weaker. It is interesting to note that the CMS combination [297] for 35.9 fb^{-1} sometimes still gives stronger limits than the individual ATLAS analyses [294, 295, 296] for full Run 2 luminosity.

The SLHA files produced with `SPheno` in our MCMC scan contain the mass spectrum and decay tables. For evaluating the simplified model constraints with `SModelS`, also the LHC cross sections at $\sqrt{s} = 8$ and 13 TeV are needed. They are conveniently added to the SLHA files by means of the `SModelS–micrOMEGAs` interface [285], which moreover automatically produces the correct `particles.py` file to declare the even and odd particle content for `SModelS`. Once the cross sections are computed, the evaluation of LHC constraints in `SModelS` takes a few seconds per point, which makes it possible to check the full dataset of 52.5k scan points.

The results are shown in Figures 5.21 and 5.22. The left panels in Figure 5.21 show the points excluded by `SModelS` ($r_{\rm max} \geq 1$), in the plane of $m_{\tilde{\chi}^0_1}$ vs. $m_{\tilde{\chi}^0_{3,4}}$ (top left) and $m_{\tilde{\chi}^\pm_j}$ vs. $m_{\tilde{\chi}^0_{3,4}}$ (bottom left), the difference between $\tilde{\chi}^0_{3,4}$ not being discernible on the plots. Points with bino-like or higgsino-like LSPs are distinguished by different colours and symbols: light blue dots for bino-like LSP points and magenta/pink triangles for higgsino-like LSP points. There are no excluded points with wino-like LSPs.

As can be seen, apart from two exceptions, all bino LSP points excluded by `SModelS` lie in the Z or h funnel region and have almost mass-degenerate $\tilde{\chi}^0_{3,4}$ and $\tilde{\chi}^\pm_1$ — actually most of the time they have mass-degenerate $\tilde{\chi}^0_{3,4}$ and $\tilde{\chi}^\pm_{1,2}$ corresponding to a quadruplet of wino states, as winos have much higher production cross sections than higgsinos. The reach is up to about 750 GeV for wino-like $\tilde{\chi}^0_{3,4}$, $\tilde{\chi}^\pm_{1,2}$. When the next-to-lightest states are higgsinos and winos are heavy, the exclusion reaches only $m_{\tilde{\chi}^0_{3,4}}$, $m_{\tilde{\chi}^\pm_1} \lesssim 400$ GeV.

The higgsino LSP points excluded by `SModelS` have $\tilde{\chi}^0_{1,2}$ and $\tilde{\chi}^\pm_1$ masses up to about 200 GeV and always feature light winos ($\tilde{\chi}^0_{3,4}$, $\tilde{\chi}^\pm_{2,3}$) below about 500 GeV. In terms of soft terms, the

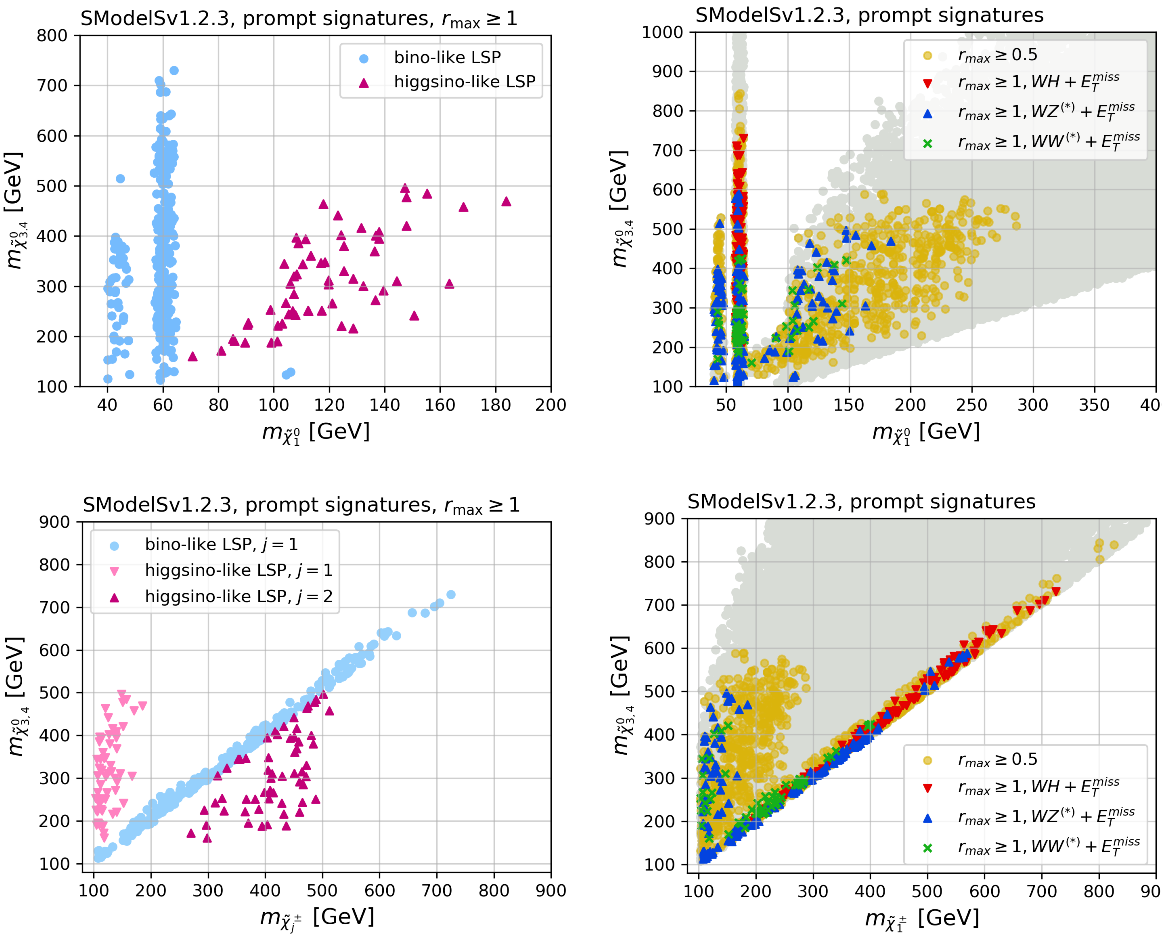

Figure 5.21: LHC constraints from prompt searches evaluated with `SModelS`. The left panels show the excluded points, $r_{\max} \geq 1$, in the $m_{\tilde{\chi}^0_1}$ vs. $m_{\tilde{\chi}^0_{3,4}}$ (top) and $m_{\tilde{\chi}^\pm_j}$ vs. $m_{\tilde{\chi}^0_{3,4}}$ (bottom) planes, with bino-like or higgsino-like LSP points distinguished by different colours and symbols as indicated in the plot labels. The right panels show the same mass planes but distinguish the signatures, which are responsible for the exclusion, by different colours/symbols (again, see plot labels); moreover the region with $r_{\max} \geq 0.5$ is shown in yellow, and that covered by all scan points in grey.

excluded bino LSP points have $m_{D2} < 750$ GeV or $\mu < 400$ GeV, while the excluded higgsino LSP points have $\mu < 200$ GeV and $m_{D2} < 500$ GeV (see Figure 5.22).

The right panels of Figures 5.21 and 5.22 show the same mass and parameter planes as the left panels but distinguish the signatures, which are responsible for the exclusion, by different colours/symbols. We see that $WH + E_T^{\text{miss}}$ simplified model results exclude only bino-LSP points in the h-funnel region, but can reach up to $m_{\tilde{\chi}^0_{3,4}} \lesssim 750$ GeV; all these points have $m_{DY} \approx 60$ GeV, $m_{D2} \lesssim 750$ GeV and $\mu \gtrsim m_{D2}$, cf. Figure 5.22 (right). The $WZ^{(*)} + E_T^{\text{miss}}$ ($WW^{(*)} + E_T^{\text{miss}}$) simplified model results exclude bino-LSP points in the Z- and h-funnel regions for winos up to roughly 600 (400) GeV, and higgsino-LSP points with masses up to roughly 200 (150) GeV when the wino-like states are below 500 (400) GeV. Correspondingly, in Figure 5.22 (right) the green crosses lie in the range $m_{D2} \lesssim 500$ GeV, while blue triangles lie in the region of $m_{D2} \lesssim 600$ GeV or $\mu \lesssim 400$ GeV.

For completeness, the right panels of Figures 5.21 and 5.22 also show the region with $r_{\max} \geq$

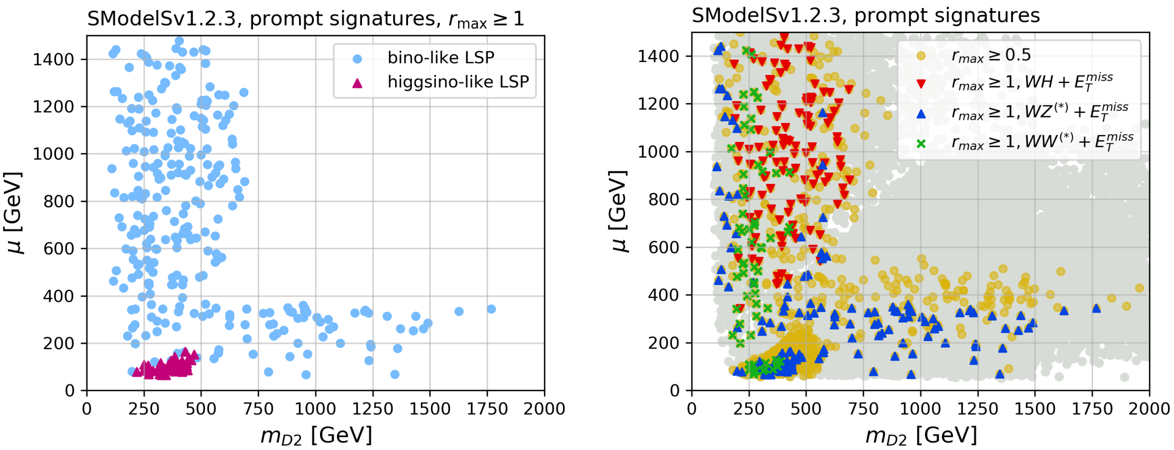

Figure 5.22: As Figure 5.21 but in the m_{D2} vs. μ plane.

0.5. This is primarily to indicate how the reach might improve with, e.g., more statistics. It also serves to illustrate the effect of a possible underestimation of the visible signal in the SMS approach, although in the comparison with `MadAnalysis 5` below we will see that the limits from simplified models and full recasting actually agree quite well.

We note that we have run `SModelS` with the default configuration of sigmacut=0.01 fb, minmassgap=5 GeV and maxcond=0.2. Long-lived $\tilde{\chi}_2^0$ are always treated as E_T^{miss} irrespective of the actual decay length, as the $\tilde{\chi}_2^0 \to \tilde{\chi}_1^0 + X$ decays (X mostly being a photon) are too soft to be picked up/vetoed by the signal selections of the analyses under consideration.[12] The excluded regions depend only slightly on these choices. Overall the constraints are very weak: of the almost 53k scan points, only 340 are excluded by the prompt search results in `SModelS`; 548 (1126) points have $r_{\max} > 0.8$ (0.5).

MadAnalysis 5

One disadvantage of the simplified model constraints is that they assume that charginos and neutralinos leading to $WZ^{(*)} + E_T^{\text{miss}}$ or $WH + E_T^{\text{miss}}$ signatures are mass degenerate. `SModelS` allows a small deviation from this assumption, but $\tilde{\chi}_i^{\pm}\tilde{\chi}_j^0$ production with sizeable differences between $m_{\tilde{\chi}_i^{\pm}}$ and $m_{\tilde{\chi}_j^0}$ will not be constrained. Moreover, the simplified model results from [294, 295, 296, 297] are cross section upper limits only, which means that different contributions to the same signal region cannot be combined (to that end efficiency maps would be necessary [171]). It is therefore interesting to check whether full recasting based on Monte Carlo event simulation can extend the limits derived with `SModelS`.

Here we use the recast codes [298, 299, 300] for Run 2 EW-ino searches available in `MadAnalysis 5` [156, 301, 158, 157].[13] These are

- two CMS searches in leptons $+E_T^{\text{miss}}$ final states for 35.9 fb^{-1} of Run 2 data, namely the multi-lepton analysis CMS-SUS-16-039 [302], for which the combination of signal regions via the simplified likelihood approach has recently been implemented in `MadAnalysis 5`

---

[12] To this end, we added `if abs(pid) == 1000023:  width = 0.0*GeV` in the `getPromptDecays()` function of `slhaDecomposer.py`; this avoids setting the $\tilde{\chi}_2^0$ decay widths to zero in the input SLHA files.

[13] See http://madanalysis.irmp.ucl.ac.be/wiki/PublicAnalysisDatabase.

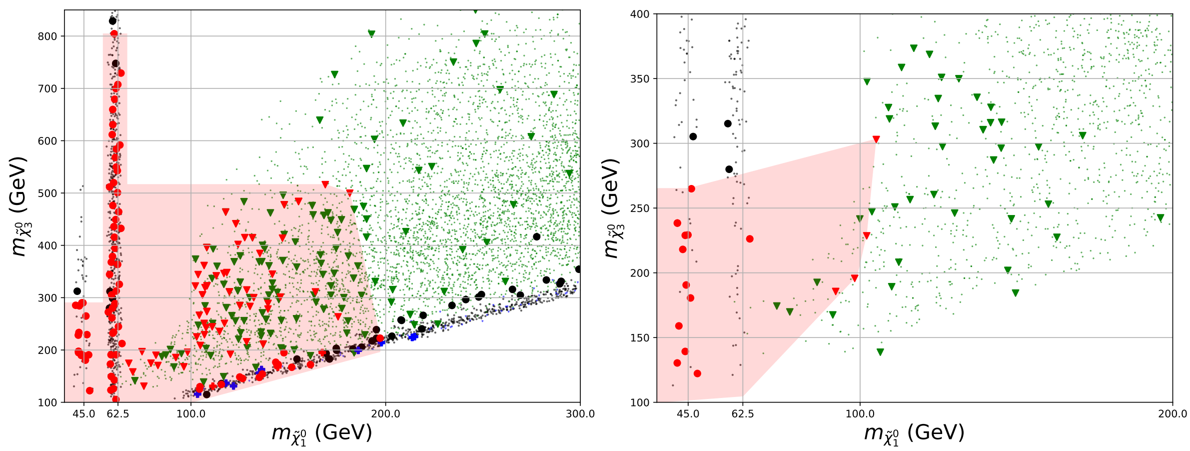

Figure 5.23: DM-compatible points found in our scan ($\Omega h^2 \leq 0.132$) in the plane of lightest neutralino vs. third lightest neutralino mass. The left plot shows points for which $m_{D2} < 900$ GeV, the right plot has $m_{D2} > 700$ GeV. Higgsino-like LSP points are shown in green, winos in blue and binos in black. The red transparent region surrounds all points that were found to be excluded using `MadAnalysis 5`; the location of the recast points are shown as large circles (binos), crosses (winos) and triangles (higgsinos). Excluded points are coloured red.

(see contribution no. 15 in [1]), and the soft lepton analysis CMS-SUS-16-048 [303], which targets compressed EW-inos; as well as

- the ATLAS search in the $1l + H(\to b\bar{b}) + E_T^{\rm miss}$ final state based on 139 fb^{-1} of data, ATLAS-SUSY-2019-08 [295], which targets the $WH + E_T^{\rm miss}$ channel and which we newly implemented for this study.

For these analyses we again treat the two lightest neutralino states as LSPs, assuming the transition $\tilde\chi^0_2 \to \tilde\chi^0_1$ is too soft as to be visible in the detector. For the CMS 35.9 fb^{-1} analyses, we simulate all possible combinations of $\tilde\chi^0_{1,2}$ with the heavy neutralinos, charginos, and pair production of charginos; while to recast the analysis of [295] we must simulate $pp \to \tilde\chi^\pm_i \tilde\chi^0_{j>2} + n$jets, where n is between zero and two. The hard process is simulated in `MadGraph5_aMC@NLO` [304] v2.6 and passed to `Pythia 8.2` [145] for showering. `MadAnalysis 5` handles the detector simulation with `Delphes 3` [150] with different cards for each analysis, and then computes exclusion confidence levels ($1 - \mathrm{CL}_s$), including the combination of signal regions for the multi-lepton analysis. For the two 35.9 fb^{-1} analyses we simulate 50k events, and the whole simulation takes more than an hour per point on an 8-core desktop PC. For the ATLAS 139 fb^{-1} analysis, we simulate 100k events (because of the loss of efficiency in merging jets, and targeting only b-jets from the Higgs and in particular the leptonic decay channel of the W) and each point requires 3 hours.

The reach of collider searches depends greatly on the wino fraction of the EW-inos. Winos have a much higher production cross section than higgsinos or binos, and thus we can divide the scan points into those where m_{D2} is "light" and "heavy." The results are shown in Figure 5.23. They show the distribution of points in our scan in the $m_{\tilde\chi^0_1} - m_{\tilde\chi^0_3}$ plane. In our model, there is always a pseudo-Dirac LSP, so the lightest neutralinos are nearly degenerate; for a higgsino- or wino-like LSP the lightest chargino is nearly degenerate with the LSP. However, $m_{\tilde\chi^0_3}$ gives the location of the next lightest states, irrespective of the LSP type. In this plane we show the points that we tested using `MadAnalysis 5`, and delineate the region encompassing all excluded points.

For "light" $m_{D2} < 900$ GeV, nearly all tested points in the Higgs funnel are excluded by [295] up to $m_{\tilde\chi_3} = 800$ GeV; the Z-funnel is excluded for $m_{\tilde\chi_3} \lesssim 300$ GeV. Otherwise we can find excluded points in the region $m_{\tilde{\chi}_1^0} \lesssim 200$ GeV, $m_{\tilde{\chi}_3^0} \lesssim 520$ GeV. While for small $m_{\tilde{\chi}_3^0} - m_{\tilde{\chi}_1^0}$ the ATLAS-SUSY-2019-08 search [295] is not effective, at large values of $m_{\tilde{\chi}_3^0}$ some points are excluded by this analysis, and others still by CMS-SUS-16-039 [302] and/or CMS-SUS-16-048 [303]. We note here that the availability of the covariance matrix for signal regions A of [302] is quite crucial for achieving a good sensitivity. It would be highly beneficial to have more such (full or simplified) likelihood data that allows for the combination of signal regions!

For "heavy" $m_{D2} > 700$ GeV,[14] we barely constrain the model at all: clearly Z-funnel points are excluded up to about $m_{\tilde{\chi}_3^0} = 260$ GeV; but we only find excluded points for $m_{\tilde{\chi}_1^0} \lesssim 100$ GeV, $m_{\tilde{\chi}_3} \lesssim 300$ GeV. Hence one of the main conclusions of this work is that higgsino/bino mixtures in this model, where $m_{D2} > 700$ GeV, are essentially unconstrained for $m_{\tilde{\chi}_1^0} \gtrsim 120$ GeV.

In general, as in [184], one may expect a full recast in `MadAnalysis 5` to be much more powerful than a simplified models approach. However, comparing the results from `MadAnalysis 5` to those from `SModelS`, a surprisingly good agreement is found between the r-values from like searches (such as the $WH + E_T^{\text{miss}}$ channel in the same analysis).[15] Indeed, from comparing Figures 5.23 with the upper two panels in Figure 5.21, we see that the excluded region is very similar, with perhaps a small advantage to the full `MadAnalysis 5` recasting at the top of the Higgs funnel and at larger values of $m_{\tilde{\chi}_3^0}$ for higgsino LSPs, while `SModelS` (partly thanks to more 139 fb^{-1} analyses) is more powerful in the Z-funnel region. A detailed comparison leads to the following observations:

- The $WZ + E_T^{\text{miss}}$ upper limits in `SModelS` can be more powerful than the recasting of the individual analyses implemented in `MadAnalysis 5`. As an example, consider the two neighbouring points with $(m_{DY}, m_{D2}, \mu, \tan\beta, -\lambda_S, \sqrt{2}\lambda_T) = \big(742.6,\ 435.7,\ 164.1,\ 5.83,\ 0.751,\ 0.491\big)$ and $\big(746.6,\ 459.9,\ 154.2,\ 12.77,\ 0.846,\ 0.466\big)$, with mass parameters in GeV units. They respectively have $(m_{\tilde{\chi}_1^0}, m_{\tilde{\chi}_3^0}, m_{\tilde{\chi}_5^0}) = (189, 474, 753)$ GeV and $(182, 500, 761)$ GeV, i.e. well spread spectra with higgsino LSPs. For the first point `SModelS` gives $r_{\max} = 0.99$ and for the second $r_{\max} = 0.84$ from the CMS EW-ino combination [297]. The $1 - \text{CL}_s$ values from `MadAnalysis 5` are 0.79 and 0.84, respectively, from the combination of signal regions A of the CMS multi-lepton search [302]; in terms of the ratio r_{MA5} of predicted over excluded (visible) cross sections, this corresponds to $r_{\text{MA5}} = 0.67$ and 0.71, so somewhat lower than the values from `SModelS`.

- The $WH + E_T^{\text{miss}}$ signal for the two example points above splits up into several components (corresponding to different mass vectors) in `SModelS`, which each give r-values of roughly 0.3 but cannot be combined. The recast of ATLAS-SUSY-2019-08 [295] with `MadAnalysis 5`, on the other hand, takes the complete signal into account and gives $1 - \text{CL}_s = 0.77$ for the first and 0.96 for the second point.

- The points excluded with `MadAnalysis 5` but not with `SModelS` typically contain complex spectra with all EW-inos below about 800 GeV, which all contribute to the signal.

- Most tested points away from the Higgs funnel region, which are excluded with `MadAnalysis 5` but not with `SModelS`, have $r_{\max} > 0.8$.

- There also exist points which are excluded by `SModelS` but not by the recasting with `MadAnalysis 5`. In these cases the exclusion typically comes from the CMS EW-ino combination [297]; detailed likelihood information would be needed to emulate this combination in recasting codes.

---

[14] The regions are only not disjoint so that we can include the entire constrained reach of the Higgs funnel in the "light" plot; away from the Higgs funnel there would be no difference in the "light" m_{D2} plot if we took $m_{D2} < 700$ GeV.

[15] We shall see this explicitly for some benchmark scenarios in section 5.6.

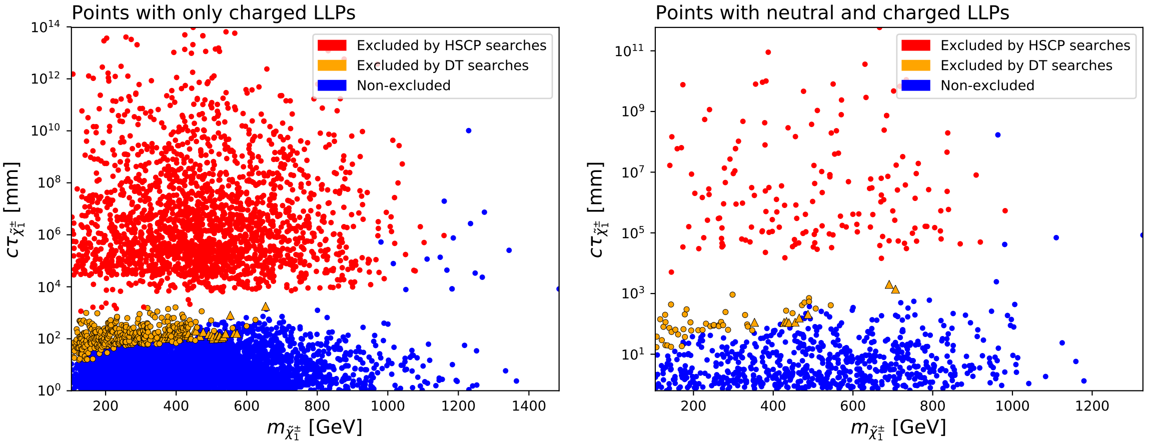

Figure 5.24: Exclusion plots for points with only charged LLPs (left) and points with neutral and charged LLPs (right), obtained in the simplified model approach. Red points are excluded by the HSCP searches implemented in `SModelS`, orange points are excluded by DT searches; the latter are plotted as circles if excluded at 36 fb^{-1} and as triangles if excluded at 140 fb^{-1}. Non-excluded points are shown in blue.

It would be interesting to revisit these conclusions once more EW-ino analyses are implemented in full recasting tools, but it is clear that, since adding more luminosity does not dramatically alter the constraints, the `SModelS` approach can be used as a reliable (and much faster) way of constraining the EW-ino sector; and that the constraints on EW-inos in Dirac gaugino models are still rather weak, particularly for higgsino LSPs where the wino is heavy.

Constraints from searches for long-lived particles

As mentioned in section 5.5.1, a relevant fraction (about 20%) of the points in our dataset contain LLPs. Long-lived charginos, which occur in about 14% of all points, can be constrained by Heavy Stable Charged Particles (HSCP) and Disappearing Tracks (DT) searches. Displaced vertex (DV) searches could potentially be sensitive to long-lived neutralinos; in our case however, the decay products of long-lived neutralinos are typically soft photons, and there is no ATLAS or CMS analysis which would be sensitive to these.

We therefore concentrate on constraints from HSCP and DT searches. They can conveniently be treated in the context of simplified models. For HSCP constraints we again use `SModelS`, which has upper limit and efficiency maps from the full 8 TeV [110] and early 13 TeV (13 fb^{-1}) [109] CMS analyses implemented. (The treatment of LLPs in `SModelS` is described in detail in Refs. [182, 293].) A new 13 TeV analysis for 36 fb^{-1} is available from ATLAS [111], but not yet included in `SModelS`; we will come back to this below.

For the DT case, the ATLAS [114] and CMS [115] analyses for 36 fb^{-1} provide 95% CL upper limits on $\sigma \times \text{BR}$ in terms of chargino mass and lifetime on `HEPData` [305, 306]. Here, $\sigma \times \text{BR}$ stands for the cross section of direct production of charginos, which includes $\tilde{\chi}_1^\pm \tilde{\chi}_1^\mp$ and $\tilde{\chi}_1^\pm \tilde{\chi}_1^0$ production, times $\text{BR}(\tilde{\chi}_1^\pm \to \tilde{\chi}_1^0 \pi^\pm)$, for each produced chargino. Using the `interpolate.griddata` function from `scipy`, we estimated the corresponding 95% CL upper limits for our scan points within the reach of each analysis[16] from a linear interpolation of the `HEPData` tables. This was then used to compute r-values as the ratio of the predicted signal over the observed upper limit, similar to

---

[16] This is $95 < m_{\tilde{\chi}_1^\pm} < 600$ GeV and $0.05 < \tau_{\tilde{\chi}_1^\pm} < 4$ ns ($15 < c\tau_{\tilde{\chi}_1^\pm} < 1200$ mm) for the ATLAS analysis [114], and $100 < m_{\tilde{\chi}_1^\pm} < 900$ GeV and $0.067 < \tau_{\tilde{\chi}_1^\pm} < 333.56$ ns ($20 < c\tau_{\tilde{\chi}_1^\pm} < 100068$ mm) for the CMS analysis [115].

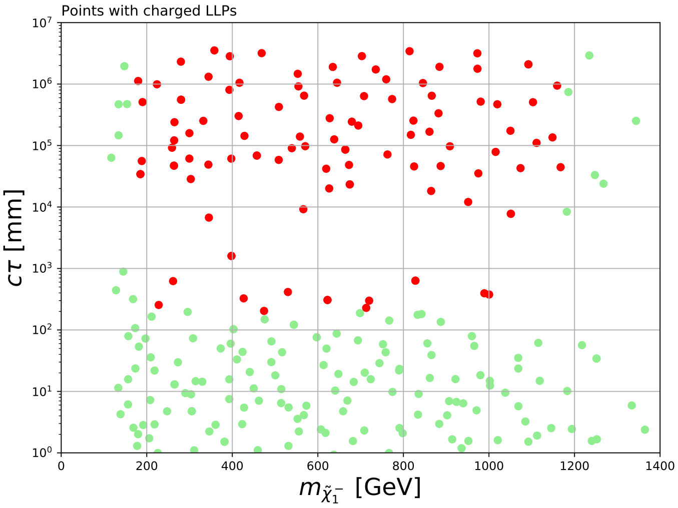

Figure 5.25: Exclusion for charged LLPs using A. Lessa's recast code for the ATLAS HSCP search [111] from https://github.com/llprecasting/recastingCodes; red points are excluded, green points are not excluded by this analysis.

what is done in `SModelS`. The points with only charged ($\tilde{\chi}_1^\pm$) LLPs and those with both charged and neutral ($\tilde{\chi}_2^0$) LLPs are treated on equal footing. However, for the points which have both a neutral and a charged LLP, if $m_{\tilde{\chi}_1^\pm} > m_{\tilde{\chi}_2^0}$, the $\tilde{\chi}_1^\pm\tilde{\chi}_2^0$ direct production cross section and the branching fraction of $\tilde{\chi}_1^\pm \to \tilde{\chi}_2^0\pi^\pm$ were also included.

There is also a new CMS DT analysis [307], which presents full Run 2 results for 140 fb^{-1}. At the time of our study, this analysis did not yet provide any auxiliary (numerical) material for reinterpretation. We therefore digitised the limits curves from Figures 1a–1d of that paper, and used them to construct linearly interpolated limit maps which are employed in the same way as described in the previous paragraph. Since the interpolation is based on only four values of chargino lifetimes, $\tau_{\tilde{\chi}_1^\pm} = 0.33$, 3.34, 33.4 and 333 ns, this is however less precise than the interpolated limits for 36 fb^{-1}.

The results are shown in Figure 5.24 in the plane of chargino mass vs. mean decay length; on the left for points with long-lived charginos, on the right for point with long-lived charginos and neutralinos. Red points are excluded by the HSCP searches implemented in `SModelS`: orange points are excluded by DT searches. The HSCP limits from [110, 109] eliminate basically all long-lived chargino scenarios with $c\tau_{\tilde{\chi}^\pm} \gtrsim 1$ m up to about 1 TeV chargino mass. The exclusion by the DT searches [114, 115] covers 10 mm $\lesssim c\tau_{\tilde{\chi}_1^\pm} \lesssim 1$ m and $m_{\tilde{\chi}_1^\pm}$ up to about 600 GeV; this is only slightly extended to higher masses by our reinterpretation of the limits of [307]. The white band in-between $c\tau \approx 10^3$–10^4 mm corresponds to $m_{\tilde{\chi}_1^\pm} - m_{\tilde{\chi}_1^0} \approx m_{\pi^\pm}$: the chargino lifetime changes significantly when decays into pions become kinematically forbidden.

To verify the HSCP results from `SModelS` and extend them to 36 fb^{-1}, we adapted the code for recasting the ATLAS analysis [111] written by A. Lessa and hosted at https://github.com/llprecasting/recastingCodes. This requires simulating hard processes of single/double chargino LLP production with *two* additional hard jets, which was performed at leading order with `MadGraph5_aMC@NLO`. The above code then calls `Pythia 8.2` to shower and decay the events, and process the cuts. It uses experiment-provided efficiency tables for truth-level events rather than detector simulation, and therefore does not simulate the presence of a magnetic field. However, the code was validated by the original author for the MSSM chargino case and found to give excellent agreement.

We wrote a parallelised version of the recast code to speed up the workflow (which is available upon request); the bottleneck in this case is actually the simulation of the hard process (unlike for the prompt recasting case in the previous section), and our sample was simulated on one desktop. We show the result in Figure 5.25. For decay lengths $c\tau_{\tilde{\chi}_1^\pm} > 1$ m, the exclusion is very similar to that from `SModelS`, only slightly extending it in the $m_{\tilde{\chi}_1^\pm} \approx$ 1–1.2 TeV range. For decay lengths of about 0.2–1 m, the recasting with event simulation allows the exclusion of points in the 0.2–1 TeV mass range; this region is not covered by `SModelS`. As with the `SModelS` results, we see that LLP searches are extremely powerful, and where a parameter point contains an LLP with a mass and lifetime in the correct range for a search, there is no possibility to evade exclusion.

5.5.3 Future experiments: MATHUSLA

We also investigated the possibility of seeing events in the MATHUSLA detector [95], which would be built $\mathcal{O}(100)$m from the collision point at the LHC, and so would be able to detect neutral particles that decay after such a long distance. Prima facie this would seem ideal to search for the decays of long-lived neutralino NLSPs; pseudo-Dirac states should be excellent candidates for this (indeed, the possibility of looking for similar particles if they were of $\mathcal{O}$(GeV) in mass at the SHiP detector was investigated in [308]). However, in our case the only states that have sufficient lifetime to reach the detector have mass splittings of $\mathcal{O}(10)$ MeV (or less), and decays $\tilde{\chi}_2^0 \to \tilde{\chi}_1^0 + \gamma$ vastly dominate, with a tiny fraction of decays to electrons.

In the detectors in the roof of MATHUSLA the photons must have more than 200 MeV (or 1 GeV for electrons) to be registered. Moreover, it is anticipated to reconstruct the decay vertex in the decay region, requiring more than one track; in our case only one track would appear, and much too soft to trigger a response. Hence, unless new search strategies are employed, our long-lived $\tilde{\chi}_2^0$ will escape detection.

5.6 Benchmark points

In this section we present a few sample points which may serve as benchmarks for further studies, designing dedicated experimental analyses and/or investigating the potential of future experiments. Parameters, masses, and other relevant quantities are listed in Tables 5.4 and 5.5.

Point 1 (`SPhenoDiracGauginos_667`) lies in the h-funnel region. It features almost pure bino $\tilde{\chi}_{1,2}^0$ with masses of 62–63 GeV, higgsino-like $\tilde{\chi}_1^\pm$ and $\tilde{\chi}_{3,4}^0$ with masses around 560–580 GeV, and heavy wino-like $\tilde{\chi}_{5,6}^0$ and $\tilde{\chi}_{2,3}^\pm$ around 1.2 TeV. A relic abundance in accordance with the cosmologically observed value is achieved through $\tilde{\chi}_1^0\tilde{\chi}_2^0$ co-annihilation into $b\bar{b}$ (63%), gg (17%) and $\tau^+\tau^-$ (13%) via s-channel h exchange.[17] Kinematically just allowed, invisible decays of the Higgs boson have a tiny branching ratio, BR$(h \to \tilde{\chi}_1^0\tilde{\chi}_2^0) = 5.2 \times 10^{-4}$, and thus do not affect current Higgs measurements or coupling fits. The main decay modes of the EW-inos are:

---

[17] This is one example where the precise calculation of the NLSP decays influences the value of the relic density. Without the $\tilde{\chi}_2^0 \to \tilde{\chi}_1^0\gamma$ loop calculation, $\Gamma_{\rm tot}(\tilde{\chi}_2^0) = 9\times10^{-18}$ GeV and $\Omega h^2 = 0.111$. Including the loop decay, we get $\Gamma_{\rm tot}(\tilde{\chi}_2^0) = 6.6 \times 10^{-17}$ GeV and $\Omega h^2 = 0.127$. Note also that one has to set `useSLHAwidth=1` in `micrOMEGAs` to reproduce these values with SLHA file input.

Point	**1**	**2**	**3**	**4**	**5**
m_{DY}	62.58	184.24	553.94	555.47	382.20
m_{D2}	1170.19	221.81	553.59	602.61	594.06
μ	605.67	1454.11	1481.55	1115.58	480.55
$\tan\beta$	15.63	10.44	7.92	12.28	28.05
$-\lambda_S$	0.016	1.13	0.97	0.60	0.27
$\sqrt{2}\lambda_T$	-1.26	-0.86	0.07	-1.2	-0.93
$m_{\tilde{\chi}_1^0}$	62.34	195.23	561.69	563.82	387.74
$m_{\tilde{\chi}_2^0}$	63.45	211.70	576.12	568.31	387.92
$m_{\tilde{\chi}_3^0}$	581.86	222.47	589.85	600.39	432.96
$m_{\tilde{\chi}_4^0}$	583.62	224.13	592.91	606.63	433.87
$m_{\tilde{\chi}_5^0}$	1233.07	1523.80	1532.71	1162.02	669.12
$m_{\tilde{\chi}_6^0}$	1234.85	1528.71	1536.34	1166.42	669.53
$m_{\tilde{\chi}_1^\pm}$	563.75	215.00	588.28	580.86	398.60
$m_{\tilde{\chi}_2^\pm}$	1212.35	229.86	592.69	626.84	619.96
$m_{\tilde{\chi}_3^\pm}$	1254.34	1521.61	1527.55	1184.63	703.47
$f_{\tilde{b}}$	0.997	0.95	0.97	0.96	0.997
$f_{\tilde{w}}$	$O(10^{-5})$	0.04	0.02	0.03	$O(10^{-5})$
$f_{\tilde{h}}$	$O(10^{-3})$	0.01	0.01	0.01	$O(10^{-3})$
Ωh^2	0.127	0.116	0.127	0.127	0.113
$\sigma^{\mathrm{SI}}(\tilde{\chi}_1^0 p)$	9.4×10^{-13}	2.2×10^{-11}	1.6×10^{-10}	1.2×10^{-10}	1.8×10^{-10}
$\sigma^{\mathrm{SD}}(\tilde{\chi}_1^0 p)$	2.7×10^{-7}	4×10^{-6}	1.9×10^{-6}	2.7×10^{-6}	1.1×10^{-8}
p_{X1T}	0.93	0.62	0.42	0.50	0.29
$r_{\max}$	0.39	–	–	–	–
$1 - \mathrm{CL}_s$	0.65	0.51	0.02	0.03	0.07
σ_{LHC13}	14.9	2581	41.2	35.9	87.8
σ_{LHC14}	18.0	2910	49.6	43.8	103.1

Table 5.4: Overview of benchmark points 1–5. Masses and mass parameters are in GeV, $\tilde{\chi}_1^0 p$ scattering cross sections in pb, and LHC cross sections in fb units. $f_{\tilde{b}}$, $f_{\tilde{w}}$ and $f_{\tilde{h}}$ are the bino, wino and higgsino fractions of the $\tilde{\chi}_1^0$, respectively. $r_{\max}$ is the highest r-value from `SModelS` (when relevant), while $1 - \mathrm{CL}_s$ is the exclusion CL from `MadAnalysis 5`. σ_{LHC13} and σ_{LHC14} are the total EW-ino production cross sections (sum over all channels) at 13 and 14 TeV computed with `MadGraph5_aMC@NLO`; the statistical uncertainties on these cross sections are 3% for Point 2, and about 5–7% otherwise.

Point	**6**	**7**	**8**	**9**	**10**
m_{DY}	1452.39	1919.27	1304.08	1365.50	809.67
m_{D2}	1459.01	1229.16	1269.15	848.28	446.83
μ	1033.56	1105.53	1957.19	572.96	224.68
$\tan\beta$	7.67	17.17	33.24	9.57	6.05
$-\lambda_S$	0.81	1.10	1.39	0.90	0.81
$\sqrt{2}\lambda_T$	0.42	0.29	0.05	0.31	0.37
$m_{\tilde{\chi}_1^0}$	1075.01	1158.96	1327.19	605.27	246.93
$m_{\tilde{\chi}_2^0}$	1079.15	1159.09	1327.31	605.71	247.19
$m_{\tilde{\chi}_3^0}$	1470.39	1295.59	1346.21	900.98	484.79
$m_{\tilde{\chi}_4^0}$	1473.61	1296.08	1356.92	901.04	485.79
$m_{\tilde{\chi}_5^0}$	1527.23	1951.32	2076.15	1380.78	821.83
$m_{\tilde{\chi}_6^0}$	1528.27	1957.08	2078.22	1383.37	821.86
$m_{\tilde{\chi}_1^\pm}$	1081.00	1159.38	1327.28	605.50	247.28
$m_{\tilde{\chi}_2^\pm}$	1526.26	1291.71	1331.70	898.31	480.35
$m_{\tilde{\chi}_3^\pm}$	1528.71	1299.64	2059.14	903.81	490.70
$f_{\tilde{b}}$	0.02	0.01	0.05	0.01	0.02
$f_{\tilde{w}}$	$O(10^{-4})$	0.03	0.94	$O(10^{-3})$	0.01
$f_{\tilde{h}}$	0.98	0.96	0.01	0.99	0.97
Ωh^2	0.112	0.124	0.11	0.04	0.006
$\sigma^{\rm SI}(\tilde{\chi}_1^0 p)$	4.1×10^{-10}	6.2×10^{-10}	6.4×10^{-10}	5.6×10^{-11}	1.2×10^{-9}
$\sigma^{\rm SD}(\tilde{\chi}_1^0 p)$	4.2×10^{-6}	2.3×10^{-7}	1.6×10^{-9}	1.3×10^{-6}	2.1×10^{-5}
p_{X1T}	0.35	0.20	0.28	0.92	0.46
$r_{\rm max}$	–	–	0.28	–	0.39
$1 - {\rm CL}_s$	–	–	–	–	0.73
$\sigma_{\rm LHC13}$	0.48	0.65	0.32	13.2	490.5
$\sigma_{\rm LHC14}$	0.64	0.90	0.45	16.3	557.3

Table 5.5: Overview of benchmark points 6–10. Notation and units as in Table 5.4. The statistical uncertainties on the LHC cross sections are about 10% for Points 6–8, 6–7% for Point 9 and 3–4% for Point 10.

mass	decays
1254 GeV	$\tilde{\chi}_3^\pm \to \tilde{\chi}_1^\pm Z$ (57%), $\tilde{\chi}_1^\pm h$ (42%)
1235 GeV	$\tilde{\chi}_6^0 \to \tilde{\chi}_3^0 Z$ (32%), $\tilde{\chi}_4^0 h$ (29%), $\tilde{\chi}_1^\pm W^\pm$ (36%)
1233 GeV	$\tilde{\chi}_5^0 \to \tilde{\chi}_4^0 Z$ (33%), $\tilde{\chi}_3^0 h$ (30%), $\tilde{\chi}_1^\pm W^\pm$ (36%)
1212 GeV	$\tilde{\chi}_2^\pm \to \tilde{\chi}_3^0 W^\pm$ (49%), $\tilde{\chi}_4^0 W^\pm$ (49%)
584 GeV	$\tilde{\chi}_4^0 \to \tilde{\chi}_1^0 h$ (33%), $\tilde{\chi}_2^0 h$ (25%), $\tilde{\chi}_2^0 Z$ (21%), $\tilde{\chi}_1^0 Z$ (20%)
582 GeV	$\tilde{\chi}_3^0 \to \tilde{\chi}_1^0 Z$ (30%), $\tilde{\chi}_2^0 Z$ (26%), $\tilde{\chi}_2^0 h$ (24%), $\tilde{\chi}_1^0 h$ (20%)
564 GeV	$\tilde{\chi}_1^\pm \to \tilde{\chi}_1^0 W^\pm$ (51%), $\tilde{\chi}_2^0 W^\pm$ (48%)
63 GeV	$\tilde{\chi}_2^0 \to \tilde{\chi}_1^0 \gamma$ (86%); $\Gamma_{\rm tot} = 6.6 \times 10^{-17}$ GeV ($c\tau \approx 3$ m)
62 GeV	$\tilde{\chi}_1^0$, stable

Regarding LHC signals, $pp \to \tilde{\chi}_1^\pm \tilde{\chi}_{3,4}^0$ production has a cross section of about 9 fb at $\sqrt{s} = 13$ TeV and leads to almost equal rates of $WZ + E_T^{\rm miss}$ and $WH + E_T^{\rm miss}$ ($H \equiv h$) signatures, accompanied by soft displaced photons in 3/4 of the cases. With $\tilde{\chi}_{3,4}^0$ masses only 1.7 GeV apart, `SModelS` adds up signal contributions from $\tilde{\chi}_1^\pm \tilde{\chi}_3^0$ and $\tilde{\chi}_1^\pm \tilde{\chi}_4^0$ production. This gives r-values of about 0.4 for the $WH + E_T^{\rm miss}$ topology (ATLAS-SUSY-2019-08 [295]) and about 0.3 for the $WZ + E_T^{\rm miss}$ topology (CMS-SUS-17-004 [297] and ATLAS-SUSY-2017-03 [309])[18] in good agreement with the exclusion confidence level (CL), $1 - {\rm CL}_s = 0.645$, obtained with `MadAnalysis 5` from recasting ATLAS-SUSY-2019-08 [295], and $1 - {\rm CL}_s = 0.26$ from the combination of signal regions A from CMS-SUS-16-039 [302].

Point 2 (`SPhenoDiracGauginos_50075`) has a $\tilde{\chi}_1^0$ mass of 195 GeV and a large $\tilde{\chi}_1^0$–$\tilde{\chi}_2^0$ mass difference of 16 GeV due to $\lambda_S = -1.13$. The LSP is 95% bino and 4% wino. The next-lightest states are the wino-like $\tilde{\chi}_{1,2}^\pm$ and $\tilde{\chi}_{3,4}^0$ with masses of 215–230 GeV ($m_{\tilde{\chi}_1^\pm} < m_{\tilde{\chi}_{3,4}^0} < m_{\tilde{\chi}_2^\pm}$). The higgsino-like $\tilde{\chi}_3^\pm$ and $\tilde{\chi}_{5,6}^0$ are heavy with masses around 1.5 TeV. A relic density of the right order, $\Omega h^2 = 0.116$, is achieved primarily through co-annihilations, in particular $\tilde{\chi}_1^0 \tilde{\chi}_1^\pm$ (29%) and $\tilde{\chi}_1^+ \tilde{\chi}_1^-$ (20%) co-annihilation into a large variety of final states; the main LSP pair-annihilation channel is $\tilde{\chi}_1^0 \tilde{\chi}_1^0 \to W^+ W^-$ and contributes 15%. The main decay modes relevant for collider signatures are:

mass	decays
230 GeV	$\tilde{\chi}_2^\pm \to \tilde{\chi}_1^0 W^*$ (82%), $\tilde{\chi}_1^\pm \gamma$ (11%)
220 GeV	$\tilde{\chi}_{3,4}^0 \to \tilde{\chi}_1^\pm W^*$ (98–99%), $\tilde{\chi}_1^0 \gamma$ (2–1%)
215 GeV	$\tilde{\chi}_1^\pm \to \tilde{\chi}_1^0 W^*$ (100%)
212 GeV	$\tilde{\chi}_2^0 \to \tilde{\chi}_1^0 \gamma$ (87%), $\tilde{\chi}_1^0 Z^*$ (13%); $\Gamma_{\rm tot} = 8.2 \times 10^{-10}$ GeV (prompt)
195 GeV	$\tilde{\chi}_1^0$, stable

Despite the large cross section for $\tilde{\chi}_{1,2}^\pm \tilde{\chi}_{3,4}^0$ ($\tilde{\chi}_{1,2}^+ \tilde{\chi}_{1,2}^-$) production of 1.6 (0.9) pb at $\sqrt{s} = 13$ TeV, the point remains unchallenged by current LHC results. Recasting with `MadAnalysis 5` gives $1 - {\rm CL}_s \approx 0.51$ from both the CMS soft leptons [303] and multi-leptons [302] + $E_T^{\rm miss}$ searches (CMS-SUS-16-048 and CMS-SUS-16-039), but no constraints can be obtained from simplified model results due to the complexity of the arising signatures. In fact, 86% of the total signal cross section is classified as "missing topologies" in `SModelS`, i.e. topologies for which no simplified model results are available. The main reason for this is that the $\tilde{\chi}_{3,4}^0$ decay via $\tilde{\chi}_1^\pm$, and thus $\tilde{\chi}_{1,2}^\pm \tilde{\chi}_{3,4}^0$ production gives events with softish jets and/or leptons from 3 off-shell Ws. It would be interesting to see whether the photons from $\tilde{\chi}_2^0 \to \tilde{\chi}_1^0 \gamma$ decays would be observable at, e.g., an e^+e^- collider.

---

[18] This drops to $r \lesssim 0.1$ if displaced $\tilde{\chi}_2^0 \to \tilde{\chi}_1^0 \gamma$ decays are not explicitly ignored in `SModelS`.

Point 3 (`SPhenoDiracGauginos_12711`) is similar to Point 2 but has a heavier bino-wino mass scale of 560–590 GeV. The $\tilde{\chi}_1^0$–$\tilde{\chi}_2^0$ mass difference is 14 GeV ($\lambda_S = -0.97$) and the LSP is 97% bino and 2% wino. The wino-like states are all compressed within 5 GeV around $m \simeq 590$ GeV. $\Omega h^2 = 0.127$ hence comes dominantly from co-annihilations among the wino-like states, with minor contributions from $\tilde{\chi}_1^0\tilde{\chi}_2^0 \to W^+W^-$ (3%) and $\tilde{\chi}_1^0\tilde{\chi}_1^\pm \to WZ$ or Wh (2% each). The collider signatures are, however, quite different from Point 2, given the predominance of photonic decays:

mass	decays
593 GeV	$\tilde{\chi}_2^\pm \to \tilde{\chi}_1^\pm\gamma$ (77%), $\tilde{\chi}_1^0 W^*$ (23%)
	$\tilde{\chi}_4^0 \to \tilde{\chi}_1^0\gamma$ (61%), $\tilde{\chi}_1^\pm W^*$ (27%), $\tilde{\chi}_2^0\gamma$ (7%)
590 GeV	$\tilde{\chi}_3^0 \to \tilde{\chi}_1^0\gamma$ (83%), $\tilde{\chi}_2^0\gamma$ (13%)
588 GeV	$\tilde{\chi}_1^\pm \to \tilde{\chi}_2^0 W^*$ (55%), $\tilde{\chi}_1^0 W^*$ (45%)
576 GeV	$\tilde{\chi}_2^0 \to \tilde{\chi}_1^0\gamma$ (92%), $\tilde{\chi}_1^0 Z^*$ (8%); $\Gamma_{\rm tot} = 3.3 \times 10^{-10}$ GeV (prompt)
562 GeV	$\tilde{\chi}_1^0$, stable

Moreover, the total relevant EW-ino production cross section is only 41 fb at $\sqrt{s} = 13$ TeV, compared to ≈ 2.6 pb for Point 2. Therefore, again, no relevant constraints are obtained from the current LHC searches. In particular, `SModelS` does not give any constraints from EW-ino searches but reports 34 fb as missing topology cross section, 64% of which go on account of $W^*(\to 2$ jets or $l\nu) + \gamma + E_T^{\rm miss}$ signatures.

Point 4 (`SPhenoDiracGauginos_2231`) has bino and wino masses of the order of 600 GeV similar to Point 3, but features a smaller $\tilde{\chi}_1^0$–$\tilde{\chi}_2^0$ mass difference of 4.5 GeV ($\lambda_S = -0.6$) and a larger spread, of about 46 GeV, in the masses of the wino-like states ($\sqrt{2}\lambda_T = 1.2$). The higgsinos are again heavy. $\Omega h^2 = 0.127$ comes to 46% from $\tilde{\chi}_1^+\tilde{\chi}_1^-$ annihilation; the rest is mostly $\tilde{\chi}_1^\pm$ co-annihilation with $\tilde{\chi}_{1,2,3}^0$. The $pp \to \tilde{\chi}_{1,2}^\pm\tilde{\chi}_{3,4}^0$ ($\tilde{\chi}_{1,2}^+\tilde{\chi}_{1,2}^-$) production cross section is 24 (12) fb at 13 TeV. Signal events are characterised by multiple soft jets and/or leptons $+E_T^{\rm miss}$ arising from 3-body decays via off-shell W- or Z- bosons as follows:

mass	decays
627 GeV	$\tilde{\chi}_2^\pm \to \tilde{\chi}_1^0 W^*$ (62%), $\tilde{\chi}_2^0 W^*$ (9%), $\tilde{\chi}_3^0 W^*$ (20%), $\tilde{\chi}_4^0 W^*$ (7%)
607 GeV	$\tilde{\chi}_4^0 \to \tilde{\chi}_1^\pm W^*$ (99.9%)
600 GeV	$\tilde{\chi}_3^0 \to \tilde{\chi}_1^\pm W^*$ (99.9%)
581 GeV	$\tilde{\chi}_1^\pm \to \tilde{\chi}_1^0 W^*$ (97%), $\tilde{\chi}_2^0 W^*$ (3%)
568 GeV	$\tilde{\chi}_2^0 \to \tilde{\chi}_1^0\gamma$ (98%), $\tilde{\chi}_1^0 Z^*$ (2%); $\Gamma_{\rm tot} = 3.8 \times 10^{-12}$ GeV (prompt)
564 GeV	$\tilde{\chi}_1^0$, stable

Point 5 (`SPhenoDiracGauginos_16420`) has the complete EW-ino spectrum below ≈ 700 GeV. With $m_{DY} < \mu < m_{D2}$ in steps of roughly 100 GeV, the mass ordering is binos < higgsinos < winos. Small $\lambda_S = -0.27$ and large $\sqrt{2}\lambda_T = -0.93$ create small mass splittings within the binos and larger mass splitting within the winos. Concretely, the $\tilde{\chi}_{1,2}^0$ are 99.7% bino-like with masses of 388 GeV and a mass splitting between them of only 200 MeV. The higgsino-like states have masses of about 400–430 GeV and the wino-like ones of about 620–700 GeV. $\Omega h^2 = 0.113$ is dominated by $\tilde{\chi}_1^+\tilde{\chi}_1^-$ annihilation, which makes up 60% of the total annihilation cross section; the largest individual channel is $\tilde{\chi}_1^+\tilde{\chi}_1^- \to Zh$ contributing 14%. Nonetheless $\tilde{\chi}_1^0\tilde{\chi}_1^\pm$ (13%) and $\tilde{\chi}_2^0\tilde{\chi}_1^\pm$ (12%) co-annihilations are also important. $\tilde{\chi}_1^0\tilde{\chi}_2^0$ co-annihilation contributes about 4%. The decay modes determining the collider signatures are as follows:

mass	decays
703 GeV	$\tilde{\chi}_3^\pm \to \tilde{\chi}_1^\pm Z$ (78%), $\tilde{\chi}_1^\pm h$ (16%), $\tilde{\chi}_{3,4}^0 W^\pm$ (6%)
670 GeV	$\tilde{\chi}_6^0 \to \tilde{\chi}_4^0 Z$ (45%), $\tilde{\chi}_1^\pm W^\pm$ (36%), $\tilde{\chi}_3^0 h$ (18%)
669 GeV	$\tilde{\chi}_5^0 \to \tilde{\chi}_3^0 Z$ (46%), $\tilde{\chi}_1^\pm W^\pm$ (35%), $\tilde{\chi}_4^0 h$ (18%)
620 GeV	$\tilde{\chi}_2^\pm \to \tilde{\chi}_3^0 W^\pm$ (50%), $\tilde{\chi}_4^0 W^\pm$ (50%)
434 GeV	$\tilde{\chi}_4^0 \to \tilde{\chi}_1^\pm W^*$ (99%)
433 GeV	$\tilde{\chi}_3^0 \to \tilde{\chi}_1^\pm W^*$ (99%)
399 GeV	$\tilde{\chi}_1^\pm \to \tilde{\chi}_2^0 W^*$ (58%), $\tilde{\chi}_1^0 W^*$ (42%)
388 GeV	$\tilde{\chi}_2^0 \to \tilde{\chi}_1^0 \gamma$ (100%); $\Gamma_{\rm tot} = 4.1 \times 10^{-16}$ GeV ($c\tau \approx 0.5$ m)
388 GeV	$\tilde{\chi}_1^0$, stable

The $\tilde{\chi}_i^+ \tilde{\chi}_j^-$ and $\tilde{\chi}_i^\pm \tilde{\chi}_k^0$ ($i, j = 1, 2, 3$; $k = 3...6$) production cross sections are 27 fb and 55 fb at the 13 TeV LHC, respectively, but again no relevant constraints can be obtained from reinterpretation of the current SUSY searches.

For the design of dedicated analyses it is relevant to note that $\tilde{\chi}_{2,3}^\pm \tilde{\chi}_{5,6}^0$ production would give signatures like $2W2Z + E_T^{\rm miss}$ or $3W1Z + E_T^{\rm miss}$, etc., accompanied by additional jets and/or leptons from intermediate $\tilde{\chi}_{3,4}^0 \to \tilde{\chi}_1^\pm W^*$ decays appearing in the cascade.

We also note that the $\tilde{\chi}_2^0$ is long-lived with a mean decay length of about 0.5 m. However, given the tiny mass difference to the $\tilde{\chi}_1^0$ of 180 MeV, the displaced photon from the $\tilde{\chi}_2^0 \to \tilde{\chi}_1^0 \gamma$ transition will be extremely soft and thus hard, if not impossible, to detect.

Point 6 (`SPhenoDiracGauginos_11321`) is a higgsino DM point with $m_{\tilde{\chi}_1^0} \simeq 1.1$ TeV and a rather large mass splitting between the higgsino-like states, $m_{\tilde{\chi}_2^0} - m_{\tilde{\chi}_1^0} \simeq 4$ GeV and $m_{\tilde{\chi}_1^\pm} - m_{\tilde{\chi}_1^0} \simeq$ 6 GeV. Here, $\Omega h^2 = 0.112$ results mainly from $\tilde{\chi}_1^0 \tilde{\chi}_2^0$ and $\tilde{\chi}_{1,2}^0 \tilde{\chi}_1^\pm$ co-annihilations. The main decay modes of the heavy EW-ino spectrum are:

mass	decays
1529 GeV	$\tilde{\chi}_3^\pm \to \tilde{\chi}_1^\pm Z$ (90%), $\tilde{\chi}_1^\pm h$ (8%)
1528 GeV	$\tilde{\chi}_6^0 \to \tilde{\chi}_1^0 Z$ (83%), $\tilde{\chi}_2^0 h$ (6%), $\tilde{\chi}_1^\pm W^\mp$ (7%), $\tilde{\chi}_2^0 Z$ (4%)
1527 GeV	$\tilde{\chi}_5^0 \to \tilde{\chi}_1^0 Z$ (62%), $\tilde{\chi}_2^0 Z$ (22%), $\tilde{\chi}_1^\pm W^\mp$ (8%), $\tilde{\chi}_2^0 h$ (6%)
1526 GeV	$\tilde{\chi}_2^\pm \to \tilde{\chi}_1^\pm Z^\pm$ (60%), $\tilde{\chi}_1^0 W^\pm$ (17%), $\tilde{\chi}_2^0 W^\pm$ (17%), $\tilde{\chi}_1^\pm h$ (6%)
1474 GeV	$\tilde{\chi}_4^0 \to \tilde{\chi}_1^0 Z$ (69%), $\tilde{\chi}_2^0 Z$ (15%), $\tilde{\chi}_1^\pm W^\mp$ (8%), $\tilde{\chi}_2^0 h$ (7%)
1470 GeV	$\tilde{\chi}_3^0 \to \tilde{\chi}_2^0 Z$ (79%), $\tilde{\chi}_1^\pm W^\mp$ (9%), $\tilde{\chi}_1^0 h$ (8%), $\tilde{\chi}_1^0 Z$ (5%)
1081 GeV	$\tilde{\chi}_1^\pm \to \tilde{\chi}_1^0 W^*$ (100%)
1079 GeV	$\tilde{\chi}_2^0 \to \tilde{\chi}_1^0 Z^*$ (89%), $\tilde{\chi}_1^0 \gamma$ (11%); $\Gamma_{\rm tot} = 9.9 \times 10^{-10}$ GeV (prompt)
1075 GeV	$\tilde{\chi}_1^0$, stable

The LHC production cross sections are however very low for such heavy EW-inos, below 1 fb at 13–14 TeV. This is clearly a case for the high luminosity (HL) LHC, or a higher-energy machine.

Point 7 (`SPhenoDiracGauginos_37`) is another higgsino DM point with $m_{\tilde{\chi}_1^0} \simeq 1.1$ TeV but small, sub-GeV mass splittings between the higgsino-like states, $m_{\tilde{\chi}_2^0} - m_{\tilde{\chi}_1^0} \simeq 120$ MeV and $m_{\tilde{\chi}_1^\pm} - m_{\tilde{\chi}_1^0} \simeq 400$ MeV. Co-annihilations between $\tilde{\chi}_1^0$, $\tilde{\chi}_2^0$ and $\tilde{\chi}_1^\pm$ result in $\Omega h^2 = 0.124$. The main decay modes are:

mass	decays
1957 GeV	$\tilde{\chi}_6^0 \to \tilde{\chi}_1^\pm W^\mp$ (33%), $\tilde{\chi}_{1,2}^0 Z$ (33%), $\tilde{\chi}_{1,2}^0 h$ (31%)
1951 GeV	$\tilde{\chi}_5^0 \to \tilde{\chi}_1^\pm W^\mp$ (33%), $\tilde{\chi}_{1,2}^0 Z$ (32%), $\tilde{\chi}_{1,2}^0 h$ (32%)
1300 GeV	$\tilde{\chi}_3^\pm \to \tilde{\chi}_1^\pm Z$ (55%), $\tilde{\chi}_1^\pm h$ (40%), $\tilde{\chi}_{1,2}^0 W^\pm$ (5%)
1296 GeV	$\tilde{\chi}_{3,4}^0 \to \tilde{\chi}_1^\pm W^\mp$ (44%), $\tilde{\chi}_{1,2}^0 Z$ (31%), $\tilde{\chi}_{1,2}^0 h$ (25%)
1292 GeV	$\tilde{\chi}_2^\pm \to \tilde{\chi}_1^0 W^\pm$ (49%), $\tilde{\chi}_2^0 W^\pm$ (50%)
1159 GeV	$\tilde{\chi}_1^\pm \to \tilde{\chi}_1^0 \pi^\pm$ (69%), $\tilde{\chi}_2^0 \pi^\pm$ (21%); $\Gamma_{\rm tot} = 3.4 \times 10^{-14}$ GeV ($c\tau \approx 6$ mm)
	$\tilde{\chi}_2^0 \to \tilde{\chi}_1^0 \gamma$ (100%); $\Gamma_{\rm tot} = 2.1 \times 10^{-15}$ GeV ($c\tau \approx 92$ mm)
1159 GeV	$\tilde{\chi}_1^0$, stable

The high degree of compression of the higgsino states causes both the $\tilde{\chi}_2^0$ and the $\tilde{\chi}_1^\pm$ to be long-lived with mean decay lengths of 92 mm and 6 mm, respectively. While the $\tilde{\chi}_2^0$ likely appears as invisible co-LSP, production of $\tilde{\chi}_1^\pm$ (either directly or through decays of heavier EW-inos) can lead to short tracks in the detector. Overall this gives a mix of prompt and displaced signatures as discussed in more detail for Points 9 and 10. Again, cross sections are below 1 fb in *pp* collisions at 13–14 TeV.

Point 8 (`SPhenoDiracGauginos_100`) is the one wino LSP point that our MCMC found (within the parameter space of $m_{DY}, m_{D2}, \mu < 2$ TeV), where the $\tilde{\chi}_1^0$ accounts for all the DM. Three of the wino-like states, $\tilde{\chi}_{1,2}^0$ and $\tilde{\chi}_1^\pm$, are quasi-degenerate at a mass of 1327 GeV, with the forth one, $\tilde{\chi}_2^\pm$, being 5 GeV heavier. The relic density is $\Omega h^2 = 0.11$ as a result of co-annihilations between all four winos. What is special regarding collider signatures is that the $\tilde{\chi}_2^\pm$ decays into $\tilde{\chi}_1^\pm + \gamma$, while the $\tilde{\chi}_1^\pm$ is quasi-stable on collider scales. Chargino-pair and chargino-neutralino production is thus characterised by 1–2 HSCP tracks, in part accompanied by prompt photons. In more detail, the spectrum of decays is:

mass	decays
2078 GeV	$\tilde{\chi}_6^0 \to \tilde{\chi}_4^0 Z$ (28%), $\tilde{\chi}_3^0 h$ (21%), $\tilde{\chi}_2^0 h$ (18%), $\tilde{\chi}_1^0 Z$ (14%), $\tilde{\chi}_2^\pm W^\mp$ (10%)
2076 GeV	$\tilde{\chi}_5^0 \to \tilde{\chi}_4^0 h$ (24%), $\tilde{\chi}_3^0 Z$ (24%), $\tilde{\chi}_2^0 Z$ (21%), $\tilde{\chi}_1^0 h$ (12%), $\tilde{\chi}_2^\pm W^\mp$ (11%)
2059 GeV	$\tilde{\chi}_3^\pm \to \tilde{\chi}_3^0 W^\pm$ (41%), $\tilde{\chi}_4^0 W^\pm$ (37%) $\tilde{\chi}_1^\pm Z$ (9%), $\tilde{\chi}_1^\pm h$ (9%)
1356	$\tilde{\chi}_4^0 \to \tilde{\chi}_1^\pm W^*$ (81%), $\tilde{\chi}_2^\pm W^*$ (19%)
1346	$\tilde{\chi}_3^0 \to \tilde{\chi}_1^\pm W^*$ (65%), $\tilde{\chi}_2^\pm W^*$ (35%)
1332 GeV	$\tilde{\chi}_2^\pm \to \tilde{\chi}_1^\pm \gamma$ (100%)
1327 GeV	$\tilde{\chi}_1^\pm \to \tilde{\chi}_1^0 e^\pm \nu$ (100%); $\Gamma_{\rm tot} = 2.3 \times 10^{-18}$ GeV ($c\tau \approx 84$ m)
	$\tilde{\chi}_2^0 \to \tilde{\chi}_1^0 \gamma$ (100%); $\Gamma_{\rm tot} = 1.6 \times 10^{-16}$ GeV ($c\tau \approx 1.2$ m)
1327 GeV	$\tilde{\chi}_1^0$, stable

Like for Points 6 and 7, the LHC cross sections are very low for such a heavy spectrum. Nonetheless `SModelS` gives $r_{\rm max} = 0.28$ from HSCP searches; from the `Pythia`-based recasting we compute $1 - {\rm CL_s} = 0.38$. We hence expect that this point will be testable at Run 3 of the LHC.

Point 9 (`SPhenoDiracGauginos_625`) is an example for higgsino-like LSPs at lower mass, around 600 GeV, where the $\tilde{\chi}_1^0$ is underabundant, constituting about 30% of the DM in the standard freeze-out picture. The higgsino-like states are highly compressed, $m_{\tilde{\chi}_1^\pm} - m_{\tilde{\chi}_1^0} \simeq 230$ MeV and $m_{\tilde{\chi}_2^0} - m_{\tilde{\chi}_1^0} \simeq 435$ MeV, which renders the $\tilde{\chi}_1^\pm$ long-lived with a mean decay length of 55 mm. Direct $\tilde{\chi}_1^\pm$ production has a cross section of about 10 fb at the 13 TeV LHC; more concretely $\sigma(pp \to \chi_1^\pm \chi_{1,2}^0) \simeq 8$ fb and $\sigma(pp \to \chi_1^+ \chi_2^-) \simeq 2$ fb. The $\tilde{\chi}_1^\pm$ can also be produced in decays of heavier EW-inos, in particular of the wino-like $\tilde{\chi}_{3,4}^0$ and $\tilde{\chi}_{2,3}^\pm$, which have masses around 900 GeV.

This gives rise to WZ, WH and WW events (with or without E_T^{miss}) accompanied by short disappearing tracks with a cross section of about 2 fb at 13 TeV. The classic, prompt WZ, WH, $WW + E_T^{\text{miss}}$ signatures also have a cross section of the same order (about 2 fb). While all this is below Run 2 sensitivity, it shows an interesting potential for searches at high luminosity. The detailed spectrum of decays is:

mass	decays
1383 GeV	$\tilde{\chi}^0_6 \to \tilde{\chi}^{\pm}_1 W^{\mp}$ (35%), $\tilde{\chi}^0_{1,2} Z$ (33%), $\tilde{\chi}^0_{1,2} h$ (31%)
1381 GeV	$\tilde{\chi}^0_5 \to \tilde{\chi}^{\pm}_1 W^{\mp}$ (34%), $\tilde{\chi}^0_{1,2} Z$ (33%), $\tilde{\chi}^0_{1,2} h$ (32%)
904 GeV	$\tilde{\chi}^{\pm}_3 \to \tilde{\chi}^{\pm}_1 Z$ (49%), $\tilde{\chi}^{\pm}_1 h$ (44%), $\tilde{\chi}^0_{1,2} W^{\pm}$ (7%)
901 GeV	$\tilde{\chi}^0_4 \to \tilde{\chi}^0_{1,2} Z$ (37%), $\tilde{\chi}^0_{1,2} h$ (31%), $\tilde{\chi}^{\pm}_1 W^{\mp}$ (33%)
	$\tilde{\chi}^0_3 \to \tilde{\chi}^{\pm}_1 W^{\mp}$ (34%), $\tilde{\chi}^0_{1,2} Z$ (33%), $\tilde{\chi}^0_{1,2} h$ (32%)
898 GeV	$\tilde{\chi}^{\pm}_2 \to \tilde{\chi}^0_{1,2} W^{\pm}$ (94%), $\tilde{\chi}^{\pm}_1 h$ (3%), $\tilde{\chi}^{\pm}_1 Z$ (3%)
606 GeV	$\tilde{\chi}^0_2 \to \tilde{\chi}^0_1 \gamma$ (87%), $\tilde{\chi}^0_1 \pi^0$ (11%); $\Gamma_{\text{tot}} = 2.5 \times 10^{-13}$ GeV ($c\tau \lesssim 1$ mm)
	$\tilde{\chi}^{\pm}_1 \to \tilde{\chi}^0_1 \pi^{\pm}$ (96%), $\tilde{\chi}^0_1 l^{\pm} \nu$ (4%); $\Gamma_{\text{tot}} = 3.6 \times 10^{-15}$ GeV ($c\tau \approx 55$ mm)
605 GeV	$\tilde{\chi}^0_1$, stable

Point 10 (`SPhenoDiracGauginos_236`) is another example of a low-mass higgsino LSP point with long-lived charginos. The peculiarity of this point is that the whole EW-ino spectrum lies below 1 TeV: the higgsino-, wino- and bino-like states have masses around 250, 500 and 800 GeV, respectively. The $\tilde{\chi}^0_1$ is highly underabundant in this case, providing only 5% of the DM relic density. Nonetheless the point is interesting from the collider perspective, as it has light masses that escape current limits. Moreover, with a mean decay length of the $\tilde{\chi}^{\pm}_1$ of about 13 mm, it gives rise to both prompt and DT signatures. Indeed, `SModelS` reports $r_{\max} = 0.39$ for the prompt part of the signal, concretely for $WZ + E_T^{\text{miss}}$ from ATLAS-SUSY-2017-03 ($\sigma = 17.51$ fb compared to the 95% CL limit of $\sigma_{95} = 44.97$ fb). The cross section for one or two DTs is estimated as 0.4 pb by `SModelS`, however the short tracks caused by $\tilde{\chi}^{\pm}_1$ decays are outside the range of the DT search results considered in section 5.5.2. Last but not least, DTs with additional gauge or Higgs bosons have a cross section of about 50 fb.[19] Recasting with `MadAnalysis 5` gives $1 - \text{CL}_s = 0.73$ (corresponding to $r = 0.6$) from the ATLAS-SUSY-2019-08 [295] analysis. The decay patterns of Point 10 are as follows:

mass	decays
822 GeV	$\tilde{\chi}^0_6 \to \tilde{\chi}^{\pm}_1 W^{\mp}$ (35%), $\tilde{\chi}^0_{1,2} Z$ (34%), $\tilde{\chi}^0_{1,2} h$ (29%)
	$\tilde{\chi}^0_5 \to \tilde{\chi}^{\pm}_1 W^{\mp}$ (35%), $\tilde{\chi}^0_{1,2} Z$ (33%), $\tilde{\chi}^0_{1,2} h$ (30%)
491 GeV	$\tilde{\chi}^{\pm}_3 \to \tilde{\chi}^{\pm}_1 Z$ (50%), $\tilde{\chi}^{\pm}_1 h$ (34%), $\tilde{\chi}^0_{1,2} W^{\pm}$ (15%)
486 GeV	$\tilde{\chi}^0_4 \to \tilde{\chi}^0_{1,2} Z$ (37%), $\tilde{\chi}^{\pm}_1 W^{\mp}$ (35%), $\tilde{\chi}^0_{1,2} h$ (28%)
485 GeV	$\tilde{\chi}^0_3 \to \tilde{\chi}^0_{1,2} Z$ (44%), $\tilde{\chi}^{\pm}_1 W^{\mp}$ (33%), $\tilde{\chi}^0_{1,2} h$ (22%)
480 GeV	$\tilde{\chi}^{\pm}_2 \to \tilde{\chi}^0_{1,2} W^{\pm}$ (90%), $\tilde{\chi}^{\pm}_1 h$ (5%), $\tilde{\chi}^{\pm}_1 Z$ (5%)
247 GeV	$\tilde{\chi}^{\pm}_1 \to \tilde{\chi}^0_1 \pi^{\pm}$ (92%), $\tilde{\chi}^0_1 l^{\pm} \nu$ (8%); $\Gamma_{\text{tot}} = 1.5 \times 10^{-14}$ GeV ($c\tau \approx 13$ mm)
	$\tilde{\chi}^0_2 \to \tilde{\chi}^0_1 \gamma$ (95%), $\tilde{\chi}^0_1 \pi^0$ (5%); $\Gamma_{\text{tot}} = 1.2 \times 10^{-13}$ GeV ($c\tau \approx 2$ mm)
247 GeV	$\tilde{\chi}^0_1$, stable

The SLHA files for these 10 points, which can be used as input for MadGraph, `micrOMEGAs` or `SModelS` are available via Zenodo [266]. The main difference between the SLHA files for `MadGraph5_aMC@NLO` or `micrOMEGAs` is that the `MadGraph5_aMC@NLO` ones have complex mixing

---

[19] See [182, 293] for details on the computation of the prompt and displaced signal fractions in `SModelS`.

matrices, while the `micrOMEGAs` ones have real mixing matrices and thus neutralino masses can have negative sign. The `SModelS` input files consist of masses, decay tables and cross sections in SLHA format but don't include mixing matrices. The CalcHEP model files for `micrOMEGAs` are also provided at [266]. The UFO model for `MadGraph5_aMC@NLO` is available at [284], and the `SPheno` code at [289].

5.7 Conclusions

Supersymmetric models with Dirac instead of Majorana gaugino masses have distinct phenomenological features. In this paper, we investigated the electroweakino sector of the Minimal Dirac Gaugino Supersymmetric Standard Model. The MDGSSM can be defined as the minimal Dirac gaugino extension of the MSSM: to introduce DG masses, one adjoint chiral superfield is added for each gauge group, but nothing else. The model has an underlying R-symmetry that is explicitly broken in the Higgs sector through a (small) B_μ term, and new superpotential couplings λ_S and λ_T of the singlet and triplet fields with the Higgs. The resulting EW-ino sector thus comprises two bino, four wino and three higgsino states, which mix to form six neutralino and three chargino mass eigenstates (as compared to four and two, respectively, in the MSSM) with naturally small mass splittings induced by λ_S and λ_T.

All this has interesting consequences for dark matter and collider phenomenology. We explored the parameter space where the $\tilde{\chi}_1^0$ is a good DM candidate in agreement with relic density and direct detection constraints, updating previous such studies. The collider phenomenology of the emerging DM-motivated scenarios is characterised by the richer EW-ino spectrum as compared to the MSSM, naturally small mass splittings as mentioned above, and the frequent presence of long-lived charginos and/or neutralinos.

We worked out the current LHC constraints on these scenarios by re-interpreting SUSY and LLP searches from ATLAS and CMS, in both a simplified model approach and full recasting using Monte Carlo event simulation. While HSCP and disappearing track searches give quite powerful limits on scenarios with charged LLPs, scenarios with mostly E_T^{miss} signatures remain poorly constrained. Indeed, the prompt SUSY searches only allow the exclusion of (certain) points with an LSP below 200 GeV, which drops to about 100 GeV when the winos are heavy. This is a stark contrast to the picture for constraints on colourful sparticles, and indicates that this sector of the theory is likely most promising for future work. We provided a set of 10 benchmark points to this end.

We also demonstrated the usefulness of a simplified models approach for EW-inos, in comparing it to a full recasting. While cross section upper limits have the in-built shortcoming of not being able to properly account for complex spectra (where several signals overlap), the results are close enough to give a good estimate of the excluded region. This is particularly true since it is a *much* faster method of obtaining constraints, and the implementation of new results is much more straightforward (and hence more complete and up-to-date). Moreover, the constraining power could easily be improved if more efficiency maps and likelihood information were available and implemented. This holds for both prompt and LLP searches.

We note in this context that, while this study was finalised, ATLAS made `pyhf` likelihood files for the $1l + H(\to b\bar{b}) + E_T^{\text{miss}}$ EW-ino search [295] available on `HEPData` [310] in addition to digitised acceptance and efficiency maps. We appreciate this very much and are looking forward to using this data in future studies. To go a step further, it would be very interesting if the assumption $m_{\tilde{\chi}_1^\pm} = m_{\tilde{\chi}_2^0}$ could be lifted in the simplified model interpretations.

Furthermore, the implementation in other recasting tools of more analyses with the full ≈ 140 fb^{-1} integrated luminosity from Run 2 would be of high utility in constraining the EW-ino sector. Here, the recasting of LLP searches is also a high priority, as theories with such particles are very easily constrained, with the limits reaching much higher masses than for searches for promptly decaying particles. A review of available tools for reinterpretation and detailed recommendations for the presentation of results from new physics searches are available in [86].

Last but not least, we note that the automation of the calculation of particle decays when there is little phase space will also be a fruitful avenue for future work.

Chapter 6

Determination of Independent SRs in LHC Searches for New Physics.

The LHC search programmes for new physics has produced hundreds of publications with an even larger number of individual SMS results. As discussed in sec. 3.2, results are typically presented as upper limits on production cross sections or signal efficiency “maps” for a small number of simplified models. In some cases, ATLAS and CMS also provide covariance matrices that allow for a combination of likelihoods derived from different signal regions. This is however, not general, and is restricted to signal regions within the same analysis. When perfoming a phenomenological study, a recasting of multiple analyses exploring different parts of the parameter space must often be carried out, which often raises the question: which analyses can be combined? Here, we propose a method to determine subsets of analyses whose event selection criteria do not overlap, and hence, can be trivially combined. This originated from the Les Houches ‘Physics at TeV Colliders’ workshop 2019 and appeared as contribution 16 in the BSM working group report [1].

6.1 Introduction.

Generally, analyses implemented by different collaborations (e.g. ATLAS *vs.* CMS) can safely be considered to be uncorrelated, as are those carried out at different centre of mass energies (e.g. 13 TeV *vs.* 7 TeV). In addition, within this work we looked only at signal regions, and do not considered possible correlations between control regions, as we assume such correlations to be second order effects and negligible for reinterpretation purposes. Our considerations thus focus on the signal regions, and we attempt to answer the question of whether any given pair of signal regions overlap in the space of all measured quantities or not. Using the analyses contained both in `SModelS` [134, 171, 135, 311] and `MadAnalysis 5` [156, 301, 158, 157], we want to determine the parameter space covered by the topologies that populate these signal regions and generate events to cover all the signal regions, enabling us to infer correlations between the analyses.

To determine which pairs of analyses are uncorrelated, we pursue the following strategy. Restricting ourselves to analyses implemented both in the `SModelS` v1.2.2 and `MadAnalysis 5` v1.8.20 frameworks, we use the `SModelS` database to extract the simplified models that a given analysis is sensitive to, alongside with the mass ranges for the BSM particles. We then sample this space of simplified model mass parameters and create random, realistic events from these simplified models using `MadGraph5_aMC@NLO` [140]. These events are then passed to a modified version of `MadAnalysis 5`, which as usual checks whether an event passes the cuts in each SR, but in addition records the corresponding set of SR cuts passed for every event. Using this information, a statistical bootstrap procedure is used to extract a correlation matrix relating every signal region through the events that co-populate them.

6.2 Implementation

To investigate the analysis correlations, we chose to use the overlap of analyses implemented both in `SModelS` and `MadAnalysis 5`: at the time of publication, these are ATLAS-SUSY-2015-06 [312], CMS-SUS-16-039 [302], CMS-SUS-16-033 [127] and CMS-SUS-17-001 [313], all being searches for SUSY. A description of the signal regions under consideration is shown in appendix B.

6.2.1 Topology identification.

Using the `SModelS` database, we extract the topologies that a certain analysis is sensitive to, as denoted in table 6.1, and consequently the mass parameter space the analysis can access. A topology describes a specific cascade decay, which, in the case of simplified models, is reduced to a 2- or 3- body decay with symmetric branches. A full list of the topologies contained in `SModelS` is given in `https://smodels.github.io/`. In the case of 3- body decays, the topology is reduced further so that the mass of the intermediate particle is fixed as a function of that of the mother and granddaughter.

Two analyses may both be sensitive to a given topology, but in different yet overlapping regions of the simplified model space that depends on the masses of the mother and daughter particles, denoted by m_0 and m_1 respectively. We want to generate events that randomly populate the union of the two regions without doubly populating the regions that are in common. We deduce this convex mass hull using the efficiency maps in `SModelS`: the efficiency maps provide upper limits on the production cross sections as a function of the masses of the simplified model particles. If the efficiency map of the point chosen in the parameter space is 0, then we move on to probe a different part of the parameter space until eventually a contour can be interpolated around the range of mass points that can be touched by the different analyses. For topologies involving two-body decays, this curve is obtained by sampling values of m_0, and determining the minimum and maximum m_1 values for which the regions are populated by the corresponding signal. When three-body decays are involved, the scan is expanded tri-dimensionally to determine minimum and maximum values of m_2 (the mass of the granddaughter particle) for a given m_1 and m_0 for which the SRs are populated.

6.2.2 Event generation and analysis.

We produce 50000 events evenly distributed over the corresponding convex mass hulls for each topology. These events have been generated with `MadGraph5_aMC@NLO`, using the standard MSSM UFO implementation shipped with the package [314]. Hard-scattering events have been matched with parton showers, as described with `Pythia` 8.2 [145] that has also handled hadronisation. As parameter inputs, we used template SLHA files [315], specific for each topology.

Hadron-level events are passed to `MadAnalysis 5`, whose expert mode (from v1.8.20 onwards) has been augmented by two new functions (`DumpSR` and `HeadSR`) dedicated to the writing to a file of the information on how a given event populates the various signal regions of the recasted analyses under consideration. In practice, the main executable of the recasting module (located in `tools/PAD/Build/Main/main.cpp`) has to be modified so that `HeadSR` is called prior to the event loop (in the `Execute` function), and that `DumpSR` is called within the event loop (*i.e.* for each event). The former function writes, as the first line of the output file, the signal regions as they are ordered internally in the code. The latter function writes, for each event, a set of 0 and 1 indicated whether the event populates each signal region (following the internal ordering). Both functions take an `ostream` object as argument.

Tag	Analysis	Topologies
A0(A-K,SS)	CMS-SUS-16-039	TChiWZ,TChiWZ(off), TChiWH, TChipmSlepL, TChiChipmStauStau, TChiChipmSlepStau
A1	CMS-SUS-16-033	T1, T1bbbb, T1tttt(off), T2, T2bb, T2tt(off)
A2	CMS-SUS-17-001	T2tt(off), T6bbWW
A3	ATLAS-SUSY-2015-06	T1, T2

Table 6.1: Table showing the sample of analyses investigated, with the names of the topologies reached and the tag-name used to refer to the analysis in the figures that follow.

6.2.3 Statistical framework.

The augmented `MadAnalysis 5` output consists in a grid of binary flags indicating the pass/fail status of each of N_{evt} event for each of the N_{SR} signal-region selections. In general, each event can have more than one "true" SR flag. This defines the correlation or co-population which makes analysis combination problematic, as a single unusual event could produce multiple observed analysis excesses. It would not make sense to count all such measures of the same event as if they were independent. To reduce this large matrix of binary flags to a more useful figure, we first make it much *larger*: by use of bootstrap sampling from a unit Poisson distribution, every event is multiplied by a set of N_{boot} "bootstrap samples", with sampled weights $w \sim \text{Pois}(\mu = 1)$ which replace the 0/1 binary SR weights. The total data structure is now a $N_{\text{evt}} \times N_{\text{SR}} \times N_{\text{boot}}$ tri-dimensional array of SR event weights - the SRs in each bootstrap history correlated through their common weight fluctuation. The event axis is then summed over, reducing to a two-dimensional $N_{\text{SR}} \times N_{\text{boot}}$ array of SR weight sums $W = \sum_{\text{evt}} w$, over the N_{boot} "histories". This two-dimensional array allows us to compute the correlation between two SRs i and j as usual via the covariance:

$$\text{cov}_{ij} = \langle W_i W_j \rangle - \langle W_i \rangle \langle W_j \rangle \,, \tag{6.1}$$

and

$$\rho_{ij} = \text{cov}_{ij} / \sqrt{\text{cov}_{ii} \text{cov}_{jj}} \,. \tag{6.2}$$

The averages here are computed over the bootstrap histories.

The correlations matrix ρ_{ij} acts as a sliding scale of event sharing between -1 and 1, and whether the combination of SRs i and j is acceptable can be decided by applying a cutoff $|\rho_{ij}| < \rho_{\text{max}}$. With asymptotic statistics, ρ_{ij} should be positive, as there is no mechanism (such as normalisation by the sum of SR yields) to generate true negative correlations where an increase in yield for one SR due to weight fluctuations leads to the active depopulation of another. But with finite statistics random negative correlations can occur, and empirical study of their distribution can help in setting the ρ_{max} cutoff.

We have implemented this bootstrap procedure in a `Python` program called TACO (*Testing Analyses' COrrelations*), available at `https://github.com/hreyes91/TACO`. TACO takes as input a data frame in which each column corresponds to a SR, each row to an event, and which is filled with 1 and 0 depending on whether the event passes the cuts of the corresponding signal region. The program then generates a user-defined number of N_{boot} histories (here taken as 1200) and computes the correlations between the considered SRs from the produced $N_{\text{SR}} \times N_{\text{boot}}$ matrix. Afterwards, TACO determines if the SRs are approximately uncorrelated based on a user-defined ρ_{max} cut-off (here 0.05) and substitutes the ρ_{ij} coefficients with a 0 (if $|\rho_{ij}| < \rho_{\text{max}}$) or a 1 (if $|\rho_{ij}| > \rho_{\text{max}}$) to produce an "independence matrix", which is the final value of the calculation.

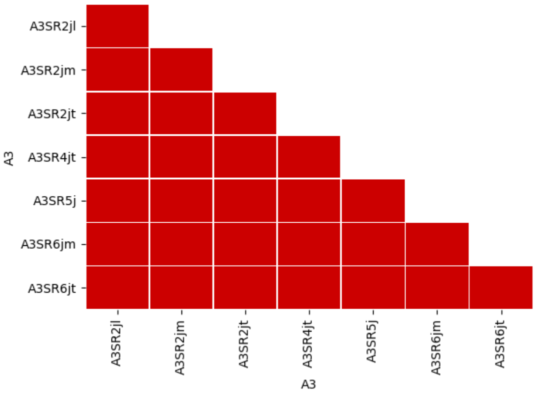

Figure 6.1: Matrix showing the correlation between the SRs of the A3 ATLAS analysis [312]. As expected for "inclusive" SRs, all the blocks in the matrix are red, denoting correlation between the SRs.

The implementation of the bootstrap procedure was applied to the signal regions populated with at least 300 events; this includes those in the A1, A2, A3 analyses and 11 SRs from the A0(A-K,SS) analysis (see table 6.1 for the naming scheme). In our results given in Figs 6.1 and 6.2, green blocks denote SRs which are independent, whereas red blocks are not. In all figures exhibiting correlations between signal regions within a sole analysis (Figs. 6.1, 6.2(a), 6.2(b), 6.2(c)), the anti-diagonal elements are trivially correlated. Fig. 6.1 depicts the results originating from the A3 ATLAS analysis. As expected for "inclusive" SRs, these are tagged as correlated. For the considered CMS analyses, results are shown in Fig. 6.2 where we can see that "exclusive" SRs are normally estimated as uncorrelated. For instance, Fig. 6.2(b) shows that most of the A1SR(1-5) regions, where the number of b-jets is $N_b = 0$, are uncorrelated with the set of A1SR(6-12) regions in which $N_b \geq 1$. In addition, the the pairs of SRs that seem correlated feature a ρ parameter very close to the $\rho_{\max} = 0.05$ threshold, with $\rho =\ 0.06$. They could thus be expected to be found uncorrelated as soon as more events are included. In this way, the results we present are on the conservative side in the sense that correlated SRs will surely be flagged as correlated, but independent SRs can erroneously be flagged correlated if the number of bootstrap iterations is too low. Moreover, in Figs. 6.2(d), 6.2(e) and 6.2(f) the determination of the independency between SRs of *different* analyses is presented. As a quick sanity check, we see for example that the SRs A0CSR017 and ASCSR018 in fig 6.2(a) are independent; this is because despite looking in the same dilepton invariant and stansverse mass ranges, the missing transverse energy p_T^{miss} ranges do not overlap. For the most part, the SRs from the A0(A-K,SS), A1 and A2 analyses were determined as independent from each other, while the rest of these SRs are expected to be determined as such once the number of populating events is increased.

6.3 Prospects.

We developed a probabilistic method for the determination of approximately uncorrelated pairs of analyses' SRs. It is based on simplified models, and first results were presented using the intersection of analyses present in both `SModelS` and `MadAnalysis 5`. It is our pronounced hope that the effort will be repeated with a wider set of analyses with the aim to compile a complete detailed list of analyses that can be treated as independent from each other. Specifically, `CheckMATE` [154, 153] and its database is a potential future target for this effort. Given such a database, a potential future extension of this work is to identify the subset of independently

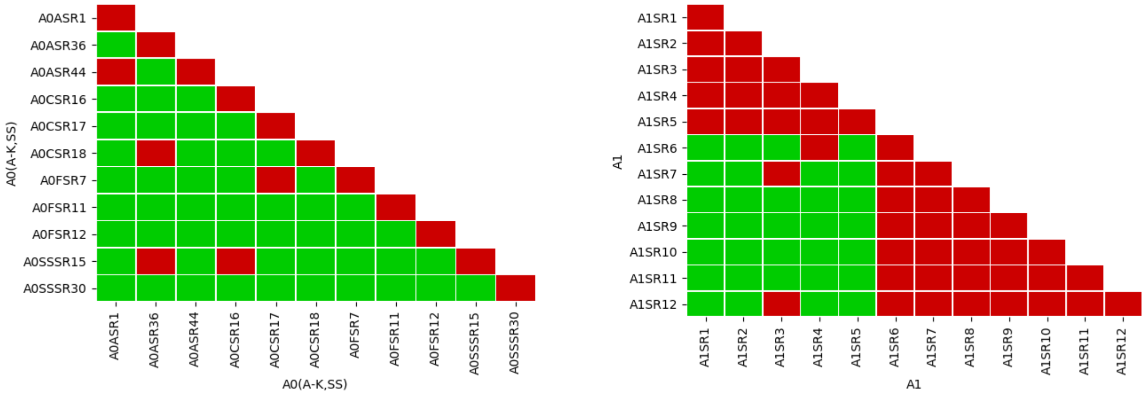

(a) A0(A-K,SS) vs. A0(A-K,SS)

(b) A1 vs. A1

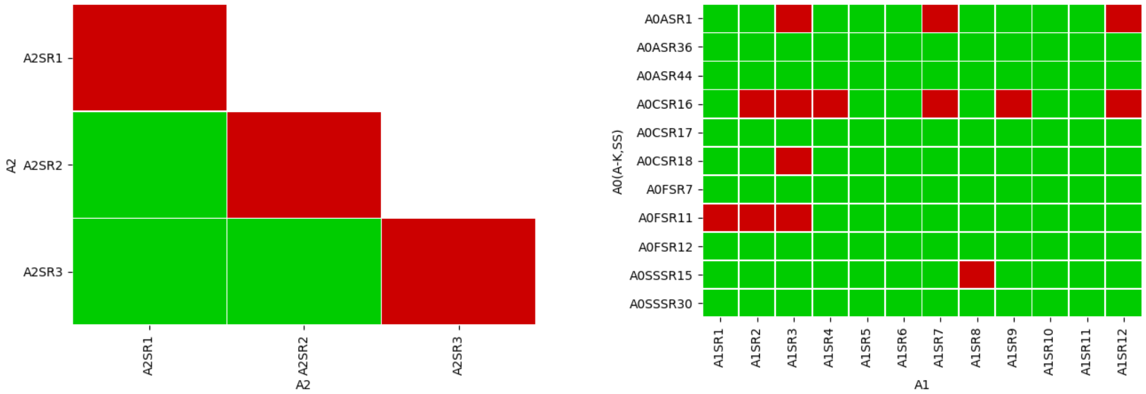

(c) A2 vs. A2

(d) A1 vs. A0(A-K,SS)

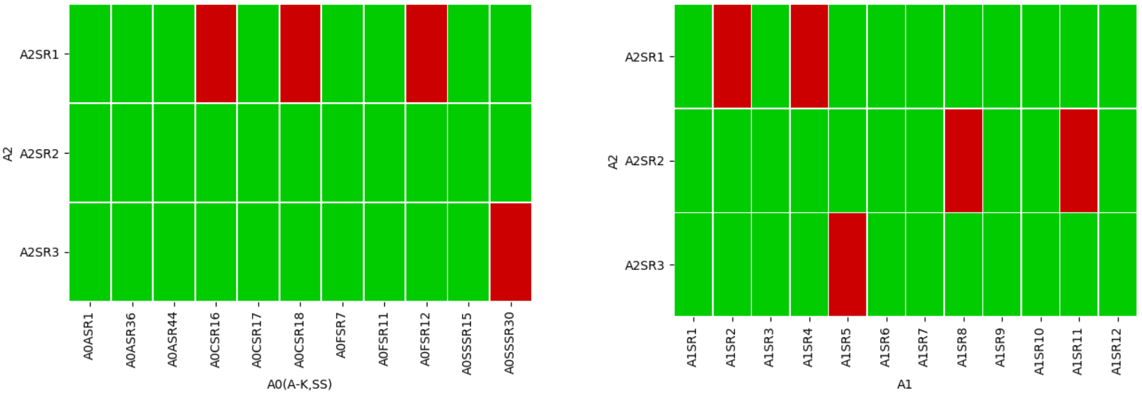

(e) A0 vs. A2

(f) A1 vs. A2

Figure 6.2: Matrices showing the correlations between the SRs of the CMS analyses under consideration that are populated with at least 300 events: A0(A-K,SS), A1 and A2. The green blocks denote that two SRs can be treated as approximately independent from each other, whereas the red blocks indicate that they are correlated.

populated SRs that maximises limit-setting power within a BSM parameter scan. The source code developed for this work can be accessed on Zenodo [316]. So far, only events originating from simplified model topologies were produced. In a future project, we wish to introduce also more complicated events to cover potential correlations that might be missed by too simplistic simplified models-based events.

Chapter 7

Practical Machine Learning for regression and classification and applications in HEP phenomenology.

This chapter regards contribution 22 of the BSM working group report from the Les Houches 'Physics at TeV Colliders' workshop 2019 [1]. In there, we discuss practical applications of ML in HEP phenomenology and in particular the possibility to examine HEP models of new physics in their full dimensionality. ML models can be trained to provide likelihood evaluations, cross-sections and exclusion boundaries given the parameters of the HEP model. We discuss ways to accelerate the applicability of ML, to evaluate uncertainties in the ML model and to provide a sustainable reuse of training data and ML model. Various examples are discussed. Namely, ML-based regression of cross sections in left-right symmetric models, of cross sections in the inert doublet model and the regression of likelihoods for the MSSM7 as provided by the GAMBIT collaboration. The second example was the was the responsibility of the author of this thesis. The other two where carried out by other collaborators of this project but are include here for completeness. Links to the training data can be found at `https://www.phenoMLdata.org`.

7.1 Introduction

In recent years machine learning has gained increasingly more traction in the particle physics community. Where machine learning was first used predominantly only in HEP experiments for the creation of metrics in a cut-and-count analysis, since a few years it also finds applications in various other branches of particle physics. This article is aimed at theorists and experimenters who want to understand how machine learning can be used for regression and classification in HEP phenomenology.

Many recent examples of the application of ML in phenomenology come from simulations and the exploration of theoretical models. Application range from simulations of particle physics events via so-called *generative* ML models [317, 318, 319, 320, 321, 322, 323] to proposals to search for new physics with the help of ML based *anomaly detection*, discussed in contribution 23 of [1]. Early ML applications in particle physics phenomenology and theory include the estimation of parton density functions [324] and various applications to jet physics as summarised in [325, 326]. Furthermore it has been demonstrated that high-parameteric model exclusion boundaries [128] or likelihood (ratios) can be learned, explored and provided for further use via the use of ML models, see e.g. [327]. The ML model is made by learning numbers based on theoretical calculations or experimental measurements (e.g. cross-sections, likelihoods, posteriors, confidence level for exclusion) from training data given the parameters of the physical model and including even the experimental nuisance parameters [328, 329]. Typically training data is provided by simulators (e.g. event generators) or by evaluating the likelihood of a given parameter set and theory with the help of experimental data. Examples could be a cross section of a new particle or an experimentally derived likelihood as a function of the parameters of a 20-dimensional BSM theory. Here, an effective high-dimensional sampling of the full model parameter space is needed.

Even though ML allows to explore physical parameters in their full dimensionality, the application of such an approach has so far been limited. The keen interest of the experimental and theoretical community at Les Houches led to this note describing ways to accelerate progress in researching ML models for phenomenology.

First, we wish to encourage the experimental and theoretical communities to study and release model data in its full dimensionality. The publication of high-dimensional data should become a standard practice. Furthermore, we propose in this contribution a standardized way to publish high-dimensional training data, a way to publish the trained ML model, and a code database to provide examples to quickly (re-)train ML models on such data. We also present various examples, worked out within the Les Houches workshop, that follow this approach.

7.2 Project description

The idea of this project is to simplify the creation and reuse of ML models made for HEP phenomenology. For this we like to encourage to save the ML model, the HEP data set and the code to train the ML models. If the construction of ML models can be simplified, any publication on HEP phenomenology could use ML models to store probabilities, cross sections, and limits also for multidimensional HEP models.

7.2.1 Classification and Regression with uncertainties

The majority of machine learning in high energy physics uses supervised learning. Within supervised learning there are two main branches: classification and regression. In classification the ML algorithm learns to classify new data into a discrete number of classes (e.g. excluded or not excluded parameter configurations), whereas in regression the ML algorithms learns to predict a continuous quantity (e.g. a cross section). Both these branches can be seen as a prediction of an output variable y (or a set of output variables $\vec{y}$) given a set of input variables $\vec{x}$. The machine learning algorithm created with the data estimates the mapping function $\hat{f}(x) = y$ between the two. This estimator of the true mapping function $f(x)$ is learned from n examples where x_i and the true function values $f(x_i)$ are known.

Determining the best parameters of a particular ML model (e.g. a neural network) is called training. The core of machine learning is that this determination of parameters is automated based on data (hence called training data). As this data has a big influence on the performance of the algorithm, having a data set that is both large and information dense enough is often key to training a good machine learning algorithm. In low dimensional problems (i.e. problems with few input variables) with a computationally cheap data generation procedure data can easily be generated with random sampling or grid sampling. In HEP phenomenology, however, data generation typically requires the execution of a chain of numerical integration programs, e.g. event generators or simulations and often even a (time-consuming) comparison to experimental data. HEP more often than not deals with high dimensional functions for which the truth values are computationally costly to acquire. Techniques like active learning can predominantly sample parameter regions that are difficult to learn for the ML algorithm and can help to mitigate these problems e.g. to learn exclusion boundaries of HEP models [330].

Since there is freedom in the choice of ML models/algorithms, a limited amount of training data and uncertainties in the data, there are two uncertainties to consider. So called *aleatoric* uncertainties are uncertainties inherent to the data or data collection procedure, e.g. noise. These cannot be removed or reduced by adding more data points. Second, *epistemic* uncertainties are uncertainties that are introduced with our ML model for the estimator $\hat{f}(x) \approx f(x)$. An example of this type of uncertainty is the uncertainty related to the trained values of the parameters (e.g. the weights of a neural network) of the ML algorithm. One way to estimate such uncertainties in neural networks is by applying *dropout* of nodes that stays turned on during inference [331]. As dropout randomly disables a fraction of the network parameters, the output of the network will again change at each inference step. The spread of the output can then be interpreted as a measure of model uncertainty.

7.2.2 Collection of Machine Learning Models

The core of this initiative is formed by a collection of trained ML models. These models, whether they are neural networks or other types of models, should be stored together with meta data which allows them to be read by an end-user package. Such an end-user package would allow external users to quickly use ML models and access the predictions made by these models.

The format of the trained ML model can differ based on which library was used to create the trained model. For scikit-learn [332] for example the authors suggest [333] to serialise the entire model object with the `joblib` package in Python. For more neural network based packages a more natural choice would be to store the model in an .onnx-file. Especially .onnx-files guarantee a cross-library support of trained networks, giving a strong guarantee that information encoded in trained networks will still be usable in the coming future.

As to where to store these trained models, we think we can best look at the current best practice in the machine learning research community. There they use primarily GitHub for this. Trained models are often stored together with their training and production code and instructions in a README file on how to use the included codes. As most papers use data from publicly available sources (e.g. the MNIST data set [334] or credit card data set [335]), data is most of the time not included, but instead referred to.

We suggest to adopt this practice for high energy physics, with the only exception being for the data. Most of the already published papers in our field generate their own data. This makes it impossible to just cite the data location; the data needs to be stored somewhere as well. As the standard platform to publish data in particle physics phenomenology is Zenodo we suggest using that as a default location to store the data sets used for creating machine learning algorithms. This includes both training and testing data.

For this collection of models to work the inclusion of meta data is crucial. It should contain for example what the inputs for the model should be and what its output(s) represent(s). It will furthermore contain information that will make the use of the model more robust against mistakes. By including information on the boundaries of the training region, the package's code can warn the user if a model is used outside of its intended range. The specifics of the meta data and the exact storage format are currently in the process of being developed.

The advantage of this methodology is that the trained model can be bundled together with the meta data, so that the model can easily be communicated by the creating user, and easily be used by the external user. In this way efficient communication of for example high-dimensional results becomes possible. To encourage this, a searchable library of publicly available models will be created, providing a single go-to location for neural networks in high energy physics.

7.2.3 Collection of Training Data

Alongside a trained model with meta data, each model instance should also come with a publicly accessible data set. For this we have set up webpage (https://www.phenoMLdata.org) and a Zenodo group[1], in which the high dimensional training data of each of the trained models will be published. We intend to also create a link with a tool like `SPOT` [336], which makes online and codeless visualisation of high dimensional data possible. A link to the data and the ML model could be added to the arXiv or `inSPIRE` entries of a HEP publication. This publishing of data is in our view essential to fully understand the trained models and to speed up the improvement of existing models.

7.2.4 Collection of Code to build Machine Learning models

To stimulate the adoption of machine learning in high energy physics even further each trained model will also have its training (and all other relevant) code published on platforms like GitHub. This code can then serve as example or as best-practice show case for both basic (e.g. how to train a network) to more complicated machine learning cases (e.g. how to extract epistemic and aleatoric uncertainties from a neural network).

7.3 Examples and best-practice

7.3.1 Examples of past phenomenological studies

Over the last years there are several examples where the use of ML techniques have shown to be very useful for phenomenology studies. Typically these methods have been applied to replace the event generation plus detector simulation chain using neural networks or Gaussian processes. This is usually the bottleneck of recasting and doing global fits of new physics models using LHC data.

The first use case was in the study of coverage properties on the constrained minimal supersymmetric standard model (cMSSM) parameter space inferred from a Bayesian posterior and the profile likelihood based on an ATLAS experiment sensitivity study [337]. The use of a shallow neural network allowed a fast prediction of the cMSSM mass spectrum gaining a factor of $\sim 10^4$ with respect to run a SUSY spectrum calculator as `softsusy` in sampling the cMSSM parameter space.

In a similar manner Buckley et al. [338] employed both a Bayesian deep neural network and a supported vectorial machine to interpolate between a grid of points in the cMSSM parameter space and therefore get fast predictions for the signal predicted by the model in the context of an ATLAS analysis.

Other phenomenological applications of ML in the SUSY context have been the development of SCYNeT [339] and SUSY-AI [128] packages. The first one uses neural network regression for a fast evaluation of the profile likelihood ratio using the 11-dimensional phenomenological minimal supersymmetric Standard Model (pMSSM) as an input. The authors have applied it to a global fit of the model including LHC data speeding up enormously the inference. Instead SUSY-AI does classification using a random forest algorithm which is trained with input data based in an analysis done by the ATLAS collaboration of the 19-dimensional pMSSM. Besides predicting whether a point of the model is excluded or not, it provides the epistemic uncertainty in the classification.

A recent application of deep neural networks have been developed to predict production cross sections of SUSY particles at the LHC. This is the case of DeepXS [340] which employs deep

---

[1] https://zenodo.org/communities/phenoml_database/

neural networks for a fast prediction of electro-weakino production cross-sections at the next-to-leading order in the pMSSM context. In this case the gain in speed is of order 10^7 compared with prospino [341] .

A further recent development has been the proposal of using deep neural networks for learning the full experimental information contained in the likelihood functions being used for the statistical inference in searches and measurements at the LHC [328]. The likelihoods learnt this way, so-called DNNLikelihoods, would allow a complete and framework-independent distribution of the physics analysis results, also enabling a precise combination with other experimental likelihoods, whenever the correlations among parameters are know.

Finally Kvellestad et al. [342] investigated the performance of deep neural networks to learn the signal mixture estimation of a ditau signal coming from a pair of degenerate Higgs bosons of opposite CP charge in the context of a Two-Higgs-Doublet model. They found a ~ 20 % improvement in the estimate of the uncertainty of signal mixture estimates, compared to estimates based on fitting, say, standard discriminating kinematic variables.

Moreover, recent papers have officially brought Bayesian networks into HEP. In [343] Bayesian classification for jet tagging has been introduced, while also serving as a clear introduction to Bayesian neural networks. The corresponding follow-up paper [344] presents Bayesian network regressors that predict the energy of a tagged top quark inside a fat jet. The work provides a good example on the usage of Bayesian networks to determine statistical and systematic uncertainties coming from the training sample.

In addition to deep neural networks, Gaussian processes have been applied as fast predictors of LHC analyses efficiencies in the context of the reconstruction of a natural SUSY scenario [345] and dark matter simplify models [346] using LHC simulated data.

So far there is a very limited number of works which have followed somehow the prescription in line of what is suggested in Sec. 7.2 to publish results. This is the case of the DeepXS (`https://github.com/SydneyOtten/DeepXS`) and DNNLikelihood (`https://github.com/riccardotorre/DNNLikelihood`) projects where weights of the trained models and python scripts with neural networks implementations have been published on GitHub so the user can train the data himself. Furthermore training data are also available in Zenodo [2]. In the case of SUSY-AI pickle files containing the trained weights are available (for details see `https://www.susy-ai.org`), whereas data were made public by the ATLAS collaboration. Finally another example is [326] as they also have made their training data avaliable on Zenodo [347].

7.3.2 Learning W_R Boson Production and Decay Rates

In light of its successful explanation of LHC data, the SM remains the best description of nature at high energies and short distances. Despite this success, there exists several experimental and theoretical motivations for the existence of new physics. One such example is the discovery [348, 349] of nonzero neutrino masses: in order to accommodate neutrino masses in a gauge-invariant and renormalizable manner, the SM must be extended by new particles and new couplings [350]. Such models that achieve this, known collectively as Seesaw models, can be tested at a variety of laboratory-based experiments, including the LHC and its potential successors [351, 352, 353, 354].

In practice, only benchmark and limiting cases of full, realistic, UV-complete Seesaw models are tested at the LHC due to the often cumbersome number of free parameters in the theory. For example: in the Left-Right Symmetric Model (LRSM) [355, 356, 357, 358, 359], which predicts the existence of a new W_R gauge boson and heavy Majorana neutrinos as shown in Fig. 7.1(a), one typically assumes that W_R bosons can only decay to one charged lepton flavor and one heavy neutrino. Such a scenario is unlikely to be realized in nature as it is weakly motivated

---

[2] Links to the training data can be found at `https://www.phenomldata.org`

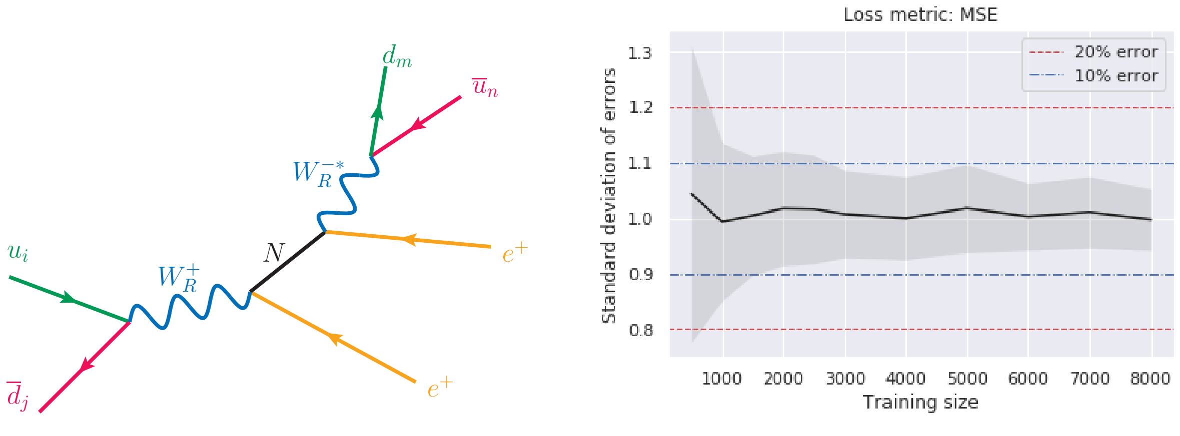

(a)

(b)

Figure 7.1: (a) Diagram within the LRSM containing a heavy neutrino and two new gauge bosons. (b) Spread of the prediction error made by the trained machine learning algorithm on the LRSM cross sections.

and not even observed in SM W boson decays. Were one able to efficiently interpolate and extrapolate from constraints on parameter space benchmarks, then LHC searches could be more fully utilized and subsequently make more general statements on new physics models. We explore this possibility here using ML techniques. As a first step, we attempt to quantify how efficiently a typical, off-the-shelf deep learning neural network can learn the production and decay cross sections for a W_R boson in the LRSM as a function of several (five) relevant mass and coupling parameters. Knowing then the acceptance and selection efficiencies as a function of inputs, which can be derived from Monte Carlo simulation, then one can in principle derive constraints on a fuller LRSM parameter space beyond that which was directly constrained.

Model and Model Inputs

For our purposes, it suffices to stipulate that the LRSM [355, 356, 357, 358, 359] is a gauge-extended scenario that postulates that the universe, in the UV limit, respects the gauge and parity symmetries $\mathcal{G}_{\text{LRSM}} = \text{SU}(3)_c \otimes \text{SU}(2)_L \otimes \text{SU}(2)_R \otimes \text{U}(1)_{B-L} \otimes \mathcal{P}_X$. Here, $\text{SU}(2)_R$ is a copy of the SM $\text{SU}(2)_L$ gauge group and describes maximally parity violating, right-handed interactions. In addition, $\mathcal{P}_X$ is a discrete parity that ensures $L \leftrightarrow R$ field exchange symmetry. To protect LRSM, one RH neutrino (N_R) for each fermion generation is required. The residual U(1) that protects against anomalies conserves the difference between baryon and lepton numbers ($B-L$). After Left-Right symmetry breaking at a scale $v_R \gg v_{\text{EW}} \approx 246$ GeV, the RH and $B-L$ gauge sector breaks down to the SM hypercharge gauge group, $\text{SU}(2)_R \otimes \text{U}(1)_{B-L} \otimes \mathcal{P} \rightarrow \text{U}(1)_Y$. This in turn reduces to QED when EWSB occurs.

In the mass basis, the relevant interaction Lagrangian that describes massive $W_R^\pm$ bosons from the $\text{SU}(2)_R$ gauge group coupling to RH quarks and leptons is given by

$$\Delta\mathcal{L} = \frac{g_R}{\sqrt{2}} W^-_{R\mu} \sum_{i,j} \left[\overline{d}^i_L V^{\text{R}}_{ij} \gamma^\mu P_R u^j_R \right] + \frac{g_R}{\sqrt{2}} W^-_{R\mu} \sum_{i,j} \left[\overline{e}^i_L Y^R_{ij} \gamma^\mu P_R N^j_R \right] + \text{H.c.} \tag{7.1}$$

The mixing matrices V^R and Y^R describe the mixing between RH quarks and RH leptons with their respective mass eigenstates, in analogy to the CKM and PMNS matrices. We ignore quark mixing and approximate both the CKM matrix and V^R with 3×3 identity matrices. The gauge couplings g_L, g_R controls the strength of LH, RH currents and set $g_R = g_L \approx 0.65$ in accordance with LR symmetry.

We consider at $\sqrt{s} = 14$ TeV the canonical LRSM signature featuring the production of same-sign leptons and two light quarks via an s-channel W_R and N_1, shown in Fig. 7.1(a) and given by [360]:

$$u_i\overline{d_j} \to W_R^\pm \to \ell_1^\pm N_1 \to \ell_1^\pm \ell_2^\pm d_i' \overline{u_j'}. \tag{7.2}$$

We decouple heavy neutrinos N_2 and N_3 and vary discretely the three mixing and two mass parameters

$$\begin{aligned} Y_{eN_1},\ Y_{\mu N_1},\ Y_{\tau N_1} &\in \{10^{-4}, 10^{-3}, 10^{-2}, 10^{-1}, 1\}, && (7.3)\\ m_{N_1} &\in \{15, 30, 45, 60, 75, 100, 150, 300, \\ &\qquad 450, 600, 750, 1000, 1500, 3000, 4500\}\ \text{GeV}, && (7.4)\\ M_{W_R} &\in \{1, 2, 3, 4, 5, 6, 8, 10, 12.5, 15, 17.5, 20\}\ \text{TeV}. && (7.5) \end{aligned}$$

Altogether, we compute a total of $N = 22.5$k cross sections, which constitutes our data set. We simulate the full $2 \to 4$ process at leading order and do not make the narrow width approximation. This means that a number of interesting kinematic limits are covered, including: non-resonant W_R production when $M_{W_R} \gtrsim \sqrt{s}$ [361, 362], the production of long-lived N_1 [362, 363], and boosted regimes such as when $m_{N_1} \ll M_{W_R} \ll \sqrt{s}$ [364, 365].

Computational Setup

To simulate the process in Eq. 7.2, we use `MadGraph5_aMC@NLO` [140] in conjunction with the `EffLRSM` UFO libraries [364, 365]. The NNPDF 3.1 NLO + LUXqed parton densities [366] are used and evolved using `LHAPDF6` [142]. Total widths for W_R and N_1 are computed on the fly for each parameter space point [367, 304]. The collinear factorization μ_f scale is dynamically to be half the sum of the transverse energy $E_T^k = \sqrt{p_T^{k2} + m_k^2}$ of all final-state particles k. No generator-level phase space cuts are applied.

Cross Section Learning

Using the generated data we trained a 3-layer neural network with elu [368] activation functions. As preprocessing we applied a base-10 logarithm to the input coupling strengths and to the cross sections that we aimed to predict. The data was z-score-normalized. The network was trained for 1000 epochs or until no mean squared error improvement was shown in 100 epochs (whichever occurred first).

Training was performed over random selections of the data in sizes of [500, 1000, 1500, 2000, 2500, 3000, 4000, 5000, 6000, 7000, 8000] events. 80% of the data was used for training, the remaining 20% for testing. For each of the training sizes the experiment was repeated 10 times (each with a new randomized selection of the total data). The test data was used to determine the relative error in the prediction of the cross section. This allowed us to determine the error made by the algorithm as function of the training size and, more importantly, when it becomes acceptable compared to the error made by the work-flow through which the data was generated in the first place. The results of this procedure can be found in Figure 7.1(b).

A more direct indication of the performance of the algorithm can be made in the form of a truth-prediction plot, in which the prediction of the algorithm is plotted against the value that the algorithm ought to predict. For a perfect algorithm the predictions would form a perfect diagonal line in such a plot. As seen in Figure 7.2(a), after training we find good agreement between predicted and truth rates.

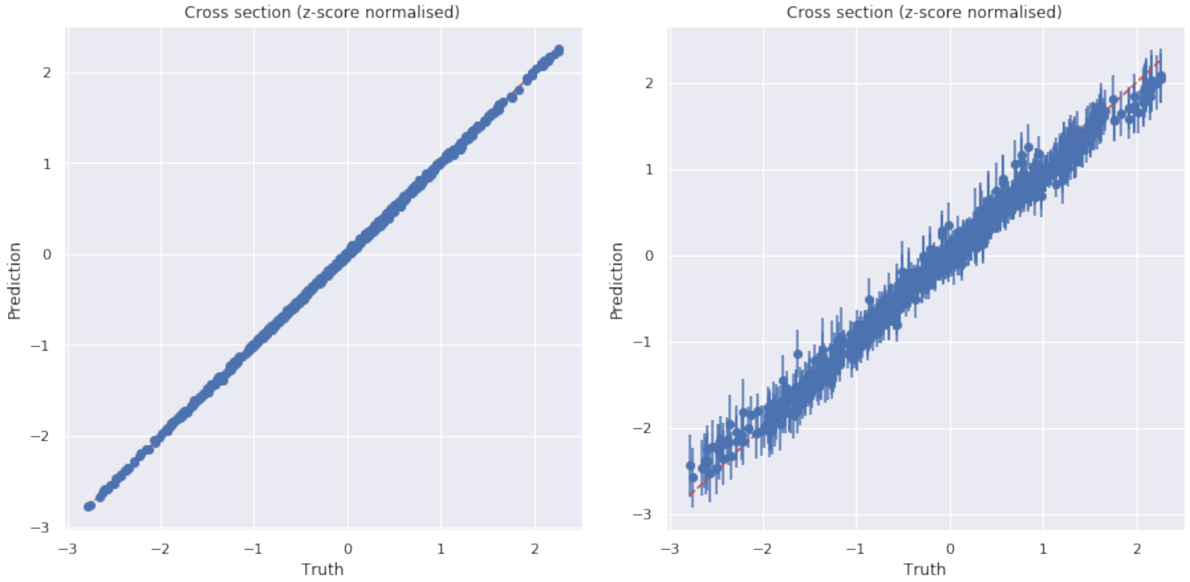

(a) (b)

Figure 7.2: Truth-prediction plots for the trained algorithm without Monte Carlo Dropout (a) and with Monte Carlo Dropout (rate: 0.2) (b) (tentative). The cross sections are z-score normalised to help the training of the algorithm.

When applying an algorithm such as the one we trained, the user is not only interested in the prediction of the algorithm, but also in the prediction uncertainty due to the algorithm. To take all related sources of uncertainty into account, one also has to determine the uncertainty due to the model configuration and training (i.e. the epistemic uncertainty), as explained in Section 7.2.1. Using the Monte Carlo Dropout technique discussed in Section 7.2.1, it is possible to determine the event-by-event uncertainty on the predictions made by the algorithm. Although work on estimating the uncertainty (including the aleatoric uncertainty) is ongoing, a tentative result of this can be seen in Figure 7.2(b) where the dropout rate was set to 0.2. To compensate the network capacity for this dropout rate, the width of the network layers is increased from [50, 50] to [60, 60].

From comparing Figure 7.2(a) and Figure 7.2(b) we see that the trained algorithm has a reduced accuracy when the epistemic uncertainty is determined alongside a prediction. This is expected as the inclusion of dropout can degrade the performance of the algorithm. However, by altering the configuration of the neural network it might be possible to counteract this loss in performance. To find this configuration, in future iterations of the network we plan on performing a hyperparameter scan for our model. Additionally, as our cross section data has some intrinsic uncertainty, as least from the Monte Carlo process through which it was calculated, we also plan on including aleatoric uncertainty determination.

7.3.3 Learning the production cross sections of the Inert Doublet Model.

One of the simplest extensions of the Standard Model (SM) is the addition of a second Higgs doublet in the so-called Two-Higgs-Double Models (2HDM). If a $\mathcal{Z}_2$ parity is further imposed, the model can easily avoid the bounds from flavor changing neutral currents and provide a dark matter candidate. This realisation of the 2HDM is the one known as the Inert Doublet Model [73], where the SM doublet ($\mathbf{H_1}$) is $\mathcal{Z}_2$-even and the new doublet ($\mathbf{H_2}$) is odd. The scalar potential in this case is given by:

$$\begin{aligned} V = \mu_1^2|\mathbf{H_1}|^2 + \mu_2^2|\mathbf{H_2}|^2 + \lambda_1|\mathbf{H_1}|^4 + \lambda_2|\mathbf{H_2}|^4 + \lambda_3|\mathbf{H_1}|^2|\mathbf{H_2}|^2 \\ +\lambda_4|\mathbf{H_1}^\dagger\mathbf{H_2}|^2 + \frac{\lambda_5}{2}[(\mathbf{H_1}^\dagger\mathbf{H_2})^2 + \text{h.c.}]\,. \end{aligned} \tag{7.6}$$

The above parameters are chosen so only the SM Higgs, h, acquires a vacuum expectation value (vev), thus maintaining the $\mathcal{Z}_2$ symmetry unbroken. After imposing the correct values for the Higgs mass and vev, the model contain five free parameters which we choose to be the masses of the new scalars (H^0, A^0 and $H^\pm$):

$$M_{H^0}^2 = \mu_2^2 + \frac{1}{2}(\lambda_3+\lambda_4+\lambda_5)v^2\,, \tag{7.7}$$

$$M_{A^0}^2 = \mu_2^2 + \frac{1}{2}(\lambda_3+\lambda_4-\lambda_5)v^2\,, \tag{7.8}$$

$$M_{H^\pm}^2 = \mu_2^2 + \frac{1}{2}\lambda_3 v^2\,, \tag{7.9}$$

and the two couplings:

$$\lambda_2 \quad \text{and} \quad \lambda_L \equiv \lambda_3+\lambda_4+\lambda_5\,. \tag{7.10}$$

In the above expressions, $v = 246$GeV is the Higgs vev.

Searches for the inert scalars at the LHC are particularly challenging due to their small (electroweak) production cross sections. Since the new states are $\mathcal{Z}_2$-odd, they are pair produced at the LHC and the following 8 processes can be relevant for LHC searches:

$$pp \to H^0H^0,\ A^0A^0,\ H^0A^0,\ H^0H^+,\ A^0H^+,\ H^+H^-,\ H^0H^- \text{ and } A^0H^-. \tag{7.11}$$

See [369] and references therein for a discussion of LHC signatures and limits. The goal of this project is to train a Deep Neural Network to accurately predict the above (leading order) cross sections given as input the five free parameters of the model. In other words, to create a function that maps the free parameters of the IDM to their corresponding production cross sections:

$$g_\phi : x_{\text{IDM}} \equiv (M_{H^0}, M_{A^0}, M_{H^\pm}, \lambda_L, \lambda_2) \to \sigma_{\text{IDM}} \tag{7.12}$$

where σ_{IDM} represents a vector containing the 8 cross section values.

As a first step, 50000 samples were generated following the method of jittered sampling [370], from a parameter space chosen as:

$$50 < M_{H^0},\ M_{A^0},\ M_{H^\pm} < 3000\text{GeV}; \quad -2\pi < \lambda_2,\ \lambda_L < 2\pi. \tag{7.13}$$

All the cross sections were computed at leading order using `MadGraph` 2.6.4 [140] and the IDM UFO implementation from the FeynRules data base [371, 369]. Since the expected integrated luminosity at the High-Luminosity LHC is about 3pb^{-1}, we imposed a lower limit on the cross sections of our data set of $\sigma_{\text{min}} = 10^{-7}$pb by discarding the cross sections below this limit. Afterwards, the remaining data was divided as training and test data in a 70:30 split.

An efficient training of the neural network requires some re-scaling of the input variables. For this, we followed the prescription and recommendations in [340] and pre-processed the model parameters via a z-score transformation:

$$x'_{\text{IDM}} = \frac{x_{\text{IDM}} - \mu(x_{\text{IDM}})}{\sigma(x_{\text{IDM}})}\,, \tag{7.14}$$

where $\mu(x_{\mathrm{IDM}})$ and $\sigma(x_{\mathrm{IDM}})$ are the mean and standard deviation of x_{IDM}, respectively. In addition the corresponding cross sections were logarithmically rescaled as:

$$\sigma'_{\mathrm{IDM}} = \log\left[\frac{\sigma_{\mathrm{IDM}}}{\min(\sigma_{\mathrm{IDM}})}\right]. \tag{7.15}$$

The hyperparameters of the training algorithm were set as follows. As initializer of the neural network weights we chose He normal. In each hidden layer, we set LeakyReLU as an activation function. In order to obtain an approximation of the Bayesian uncertainties [331] as Monte Carlo dropout a "permanent" dropout layer was implemented after each hidden layer, where "permanent" means that the dropout is present not only during training, but also for inferences. To take into account the pre-processing of the target values we used a custom loss function that minimises the mean absolute percentage error (MAPE) of the original cross sections:

$$L(\sigma'_{\mathrm{true}}, \sigma'_{\mathrm{pred}}) = \frac{1}{N}\sum_{i=1}^{N} |1 - \exp(\sigma'_{\mathrm{pred}} - \sigma'_{\mathrm{true}})|\,, \tag{7.16}$$

where N is the batch-size which we choose to be 32. Furthermore, we applied the Adam optimizer with an initial learning rate of $\alpha_{\mathrm{init}} = 10^{-3}$ and the EarlyStopping callback with a patience of 50. After 500 epochs have ended or EarlyStopping has terminated the iteration, the learning rate was divided by 2 and the training continues until 10 of those iterations were completed. To choose the best configuration, we ran a scan over the rest of the hyperparameters: the number of hidden layers, the number of artificial neurons, λ of the L2 regularization term and the dropout fraction, and trained a neural network with each combination for the $pp \to H^0H^0$ process. Finally, we trained one neural network for each of the remaining production processes using the configuration that better minimised the MAPE for the first process. This configuration is formed by 6 hidden layers with 192 artificial neurons, $\lambda = 10^{-5}$ and a dropout fraction of 1 %. The training data set, the code and the trained neural networks are presented in the GitHub repository `https://github.com/SydneyOtten/IDM_XS` fulfilling the criteria from sections 7.2.2, 7.2.3 and 7.2.4.

In order to test the performance of the neural network, 100 sample predictions were drawn for each point in the test data and their mean $\mu(\sigma_{pred})$ and standard deviation $\mathrm{std}(\sigma_{pred})$ was computed. From this, we computed the relative error (RE),

$$\mathrm{RE} = \left|\frac{(\sigma_{pred} - \sigma_{true})}{\sigma_{true}}\right|, \tag{7.17}$$

which quantifies the distance between $\mu(\sigma_{pred})$ and the true cross section σ_{true}, and the coefficient of variance (CV),

$$\mathrm{CV} = \frac{\mathrm{std}(\sigma_{pred})}{\mu(\sigma_{pred})}, \tag{7.18}$$

which describes the estimation of the Bayesian uncertainty.

The results are summarised in Table 7.1. For the processes of associated production of two different inert scalars, we obtained quite good results. The best one overall is for A^0H^+ production, with $\mu(\mathrm{RE}) \approx 0.005$, $\mu(\mathrm{CV}) \approx 0.03$, and the 1 std interval around the mean predicted cross section containing the true value for 99.97% of the test points. For the pair-production processes, however, the outcomes are not ideal: we observe large REs and CVs, specially the regions with large cross sections. The worst case is A^0A^0 production with $\mu(\mathrm{RE}) \approx 0.1$ and $\mu(\mathrm{CV}) \approx 0.19$, and 1 std around the mean prediction containing the true value for only 95.09% of the test points. The mean predicted vs. the true cross section for these two cases is shown in Fig. 7.3. We see here that 1. $\sigma(pp \to A^0A^0)$ reaches much higher values than $\sigma(pp \to A^0H^+)$ and

	H^0H^0	A^0A^0	H^+H^-	H^0A^0	H^0H^+	A^0H^+	H^0H^-	A^0H^-
μ(RE)	0.0303	0.1049	0.2259	0.0058	0.0076	0.0048	0.0057	0.0072
μ(CV)	0.0850	0.1880	0.1508	0.0272	0.0402	0.0276	0.0276	0.0287
within 1 std	0.9833	0.9509	0.9812	0.9981	0.9995	0.9997	0.9886	0.9817

Table 7.1: Summary of the accuracy of the predictions of the trained neural network from the test data: mean relative error, μ(RE), mean coefficient of variance, μ(CV), and fraction of test points whose true values lie within 1 std from the mean correspondent prediction, denoted as "within 1 std", for the eight production processes.

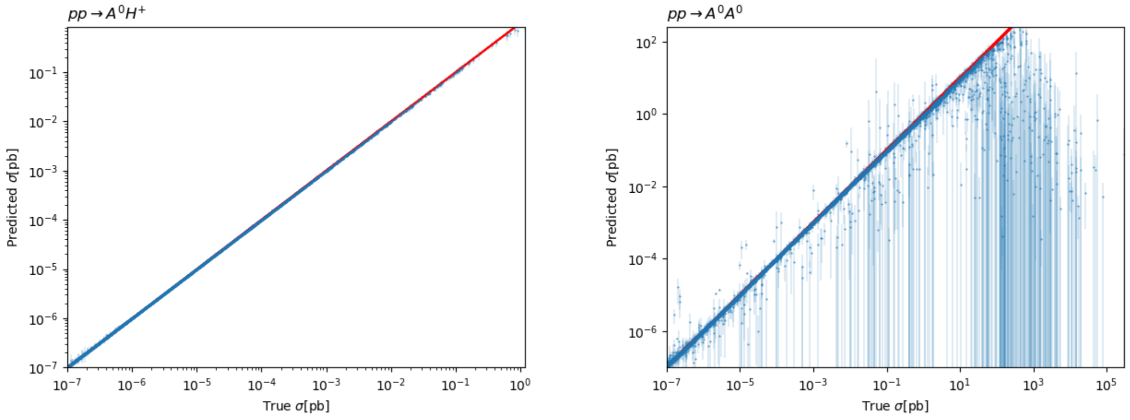

(a) $pp \to A^0H^+$ (b) $pp \to A^0A^0$

Figure 7.3: Mean predicted vs. true cross section for the processes with (a) the best and (b) the worst performance. The error bars correspond to 1 std from the mean prediction in each point.

2. the largest uncertainties arise for the highest cross sections. To understand this further, we plot in Fig. 7.4 the true cross section vs. the mass of the final state, with CV shown as color code. We observe that as the cross sections get larger so does the CV, a fact that is more notorious for the pair-production processes, which reach much higher values, specially when $2M_{A^0} \approx M_h$ where h-mediated production becomes kinematically allowed. Moreover, as expected, the cross sections peak towards low masses; in this region the density of points is rather low, which is also a cause of larger uncertainties. This suggests that the target values (i.e. the values of the cross sections) of the training sample should be more evenly distributed. Nevertheless, there is the positive conclusion that, in general, we observe a direct proportionality between the relative error and the standard deviation of the predictions. This can be deduced from Fig. 7.3 when comparing the size of the error bars for point with their respective distance from the red line (proportional to the error of the prediction). This is very important in order to ensure a correct interpretation of the uncertainty on the prediction.

In summary, we obtained first results from trained neural networks that predict the LHC production cross sections for inert scalars in the IDM, with an estimation of the Bayesian uncertainty. The next step of this project will focus on reducing this uncertainty and, by making sure that the true value is inside the 1 std uncertainty interval of the prediction, reducing the relative error of the predictions over the full parameter space for all the processes under consideration. One way to achieve this regards implementing Dropout-based Active Learning [372].

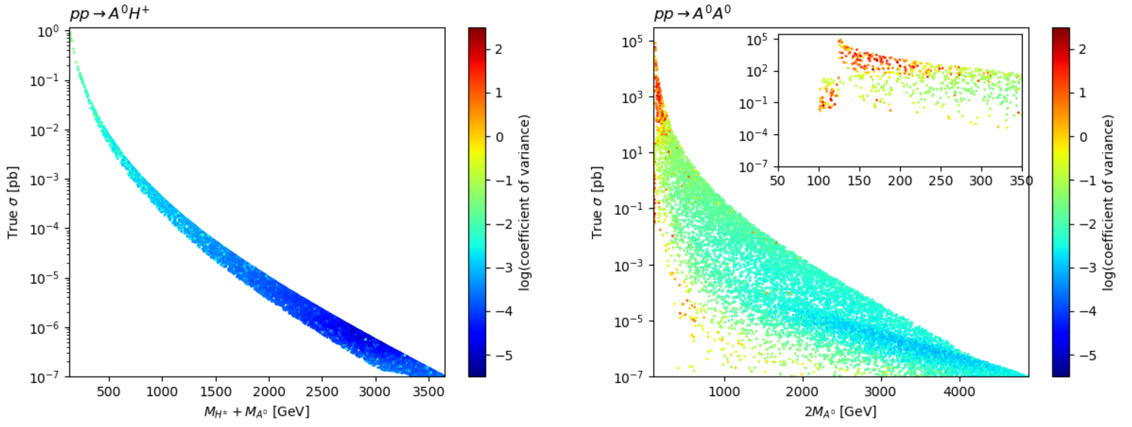

(a) $pp \to A^0H^+$

(b) $pp \to A^0A^0$

Figure 7.4: True cross section vs. effective mass for the processes with (a) the best and (b) the worst performance. In color, the logarithm of the coefficient of variance is shown.

7.3.4 Global fits of Gambit Zenodo data

The GAMBIT collaboration has released the data resulting from their global fits of a variety of beyond Standard Model models [373, 374, 375, 376, 377, 378, 379, 380] in Zenodo. These data can be trained using deep learning methods to predict, for instance, dark matter and LHC observables or likelihoods related with those observables for a posteriori interpolation.

One example is the seven-dimensional MSSM (MSSM7) [375] for which we have created a machine learning model in the form of two stacked deep neural networks to perform a regression on the MSSM7 combined likelihood. A total of 22.6 million samples were used for the training and evaluation of the models. Data exploration reveals that $\approx$ 595000 of those samples have a likelihood of 0 whereas all the other samples range from ≈ -450 to -255. The great void between -255 and 0 enhances the difficulty for a single neural network to perform well in every likelihood region. This particular inhomogeneity of the data raises the standard deviation from ≈ 7 when excluding the zero likelihoods to ≈ 42 when including them. Thus, it was no surprise to find an extraordinarily well performing deep network when excluding the zeros from the training procedure. However, when training a neural network on the full data set, we achieved an accuracy of 100 % for identifying zero likelihoods. We have implemented a stacking mechanism that combines the knowledge of two deep neural networks by merging them into a deep hybrid network.

Deep Hybrid Network Architecture and Training

The two neural networks comprising the hybrid architecture were constructed and trained with `Tensorflow` and `Keras`. Their most important difference is due to the data they were being trained on:

Net A is trained on the full data set including the samples with a likelihood of 0.

Net B is trained on the full data set excluding the samples with a likelihood of 0.

The stacking mechanism is therefore simple: firstly, the input is processed by net A. If it predicts a 0, the final prediction is 0. If it does not predict 0, query net B and give its prediction as the final result. Nets A and B share most of their hyperparameters. Thus, if not explicitly mentioned otherwise, the subsequent network features are true for the procedures of both nets:

Data Preprocessing: The input, as well as the output, are z-score normalised, i.e. for sample x_i, it is transformed into x'_i and

$$x'_i = \frac{x_i - \bar{\mu}(x)}{\sigma(x)}, \tag{7.19}$$

where $\bar{\mu}$ and σ are the mean and standard deviation. However, for the parameters Q and $\mathrm{sgn}(\mu)$, $\bar{\mu} = 0$ and $\sigma = 1$. After normalising the data, it is split into three parts: first of all, 5% of the $2.26 \cdot 10^7$ samples are stored as test samples the neural networks will not see at all during their training. The other 95% are then again split into training and validation samples with a ratio of 9:1 respectively. The training samples are the ones that the loss function gets to compare to the model predictions while the validation samples are only used as a monitor for the performance. However, as will be explained in the training paragraph, the Network will be slightly biased towards the validation set.

Network Topology: The input is processed by 8 layers of fully connected neurons with 64 (net A) or 100 (net B) neurons with the `selu` activation function. The initial weights are drawn from a normal distribution with $\mu = 0$, $\sigma_{\mathrm{netA}} = 0.125$ and $\sigma_{\mathrm{netB}} = 0.1$.

Training: The loss function measuring the deviation of the model predictions and true values is minimised by the `ADAM` [381] optimiser with default values beside the learning rate and a batch-size of 180000 and has been customised with respect to the data preprocessing. Our loss function is a modification of the mean absolute error (MAE):

$$\mathrm{Loss}\left(\mathrm{\hat{y}_i(x_i), y_i(x_i)}\right) = \frac{1}{\mathrm{N}} \sum_{\mathrm{i=1}}^{\mathrm{N}} \sigma(\mathrm{y}) \cdot |\mathrm{\hat{y}_i - y_i}| \,, \tag{7.20}$$

where $\hat{y_i}$ is the predicted and y_i is the true label for input x_i. Additionally, a learning rate scheduling with $\alpha_i = 0.01$, $\alpha_f = 10^{-5}$ and a factor of 1.7 dividing the learning rate for each iteration. One iteration is equivalent to 2500 epochs of training or until the `EarlyStopping` routine has ended the iteration with a patience of 200 epochs. For each iteration, the model parameters giving the best validation loss are loaded into the architecture and the optimisation continues which causes the bias mentioned earlier.

Performance measurement

To measure the performance of the model, we evaluate both neural networks by comparing their predictions to 5% of the corresponding data sets (the test sets). The test set of net A consists of 1.13 million points, including 50650 samples whose likelihood is 0. Although the training procedure for net A is a typical regression, its function in the stack is to classify whether the parameter space point corresponds to a likelihood of 0 or not. Therefore, the only interesting measure for net A is the binary classification accuracy which was 100 %. For net B, an evaluation plot is shown in Figure 7.5.

7.4 Conclusions

Machine learning can find various applications in HEP phenomenology. Here, the use of ML based regression and classification of information for high-dimensional HEP models was discussed with emphasis on best practices for a sustainable reuse of phenomenological information. To give an example, phenomenological studies of the likelihood of a particular HEP model should publish the multidimensional records of all likelihood evaluations. Such data can be used to train ML models which allow to evaluate the likelihood of this HEP model in its full dimensionality. The ML code

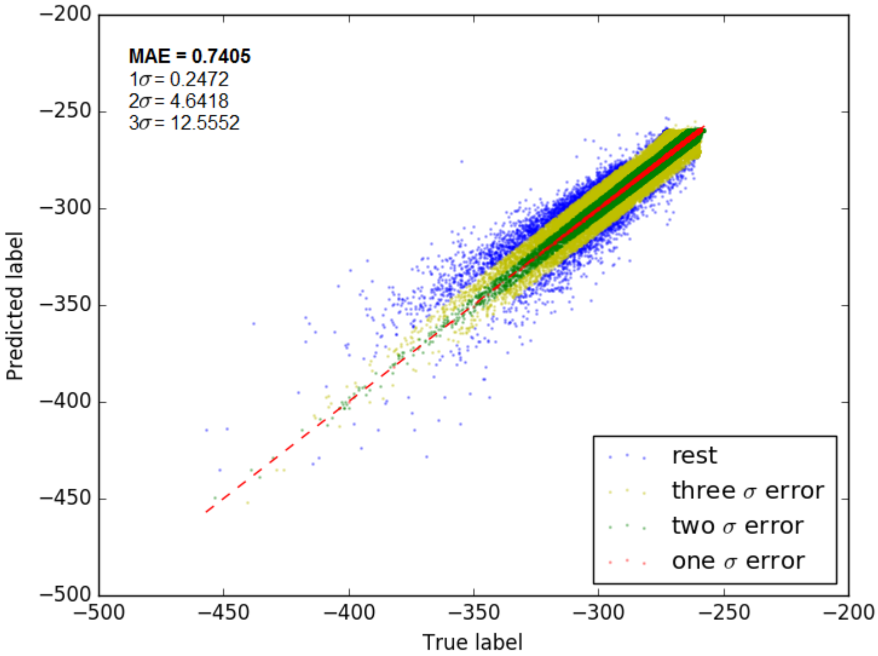

Figure 7.5: A validation plot of net B, showing the true label y_i on the x-axis and the predicted label $\hat{y}_i$ on the y-axis with a mean absolute error (MAE) of 0.7405. The test points are additionally showing the error bounds: 1σ in red, 2σ in green, 3σ in yellow and the rest in blue.

and the trained ML model should then be published with appropriate meta data specifying input and output variables, boundaries of the training regions, etc., to allow an easy reuse. We propose to build a HEP-wide framework storing such information.

As proof of concept and feasibility, we showed various examples of applications such as ML-based regression of cross sections in left-right symmetric models and in the inert doublet model and the regression of likelihoods for the minimal supersymmetric standard model as provided by the GAMBIT collaboration.

Chapter 8

Conclusions.

An extensive program of searches for new physics is being carried out by the ATLAS and CMS collaborations. In them, results are commonly interpreted in the context of simplified models. This approach allows a more clear understanding of the results and notably, facilitates their reinterpretation. However, mass limits derived from simplified models can significantly change when considering more realistic scenarios of a same theory. Furthermore, there is still a wide variety of new or beyond vanilla BSM theories that are no directly covered by the experimental collaborations. Thus, the presence of a very active framework of re-interpretation of LHC results. Carried within this context, the aim of this thesis was to study the collider phenomenology of beyond vanilla theories and to contribute on the development of tools to render more efficient such endeavor. Another aspect of this thesis, regarded the first steps taken by the author on the emergent subject of ML applications to HEP phenomenology.

In chapter 4 we discussed about the developments presented in version 1.2 of the `SModelS` reinterpretation tool. Namely, it now features the combination of signal regions whenever a covariance matrix and the corresponding efficiency maps are provided by the analysis. This is very useful to enhance the constraining power that can be derived from simplified models. Another major improvement is the implementation of HSCP and R-hadron signatures, considerably extending the types of topologies than can be tested by `SModelS`. Furthermore, version 1.2 presented the addition of an Interactive Plots Maker, a tool to efficiently visualize the `SModelS` output and compare it with the parameters of the model under study. Is in the development of this tool where I was mainly involved.

In chapter 5 we went beyond vanilla and explored the collider phenomenology of the coloured sector (in Sec. 5.2) and the electroweakino sector (in Sec. 5.3) of the MDGSSM. There are several motivations for studying this model. Among them, we find that a natural enhancement of the Higgs mass at tree level is induced. Furthermore, significant differences on collider constrains and signatures are expected with respect to the MSSM. In Sec. 5.1 we introduced the model together with some general phenomenological considerations.

In the first collider study of the MDGSSM, we derived LHC limits on the gluinos and squarks in the MDGSSM. As a first step, we used `SModelS` to quickly obtain bounds on the masses of the colored SUSY particles. However, since we were dealing with complex scenarios where the gluinos and squarks share out their branching ratios over several decay channels, the constrains that can be derived from simplified models are expected to be weak. Thus, we turned to recasting with full event simulation to obtain more realistic results. This required the implementation and validation of the ATLAS-SUSY-2016-07 multijet analysis into the `Madanalysis 5` framework. By comparing the finally obtained bounds to those in equivalent MSSM scenarios, we quantified their differences. On the one hand, when gluino masses are large, bounds on squarks are suppressed as compared to the MSSM. This is due to a forbidden chirality flip in the squark production via

t-channel gluino exchange process in the MDGSSM. On the other hand, when gluino production dominates, the constrains are enhanced in the MDGSSM case due to the extra gluino degrees of freedom.

In the second study, we constrained the electroweakinos of the MDGSSM. First, we delimited the parameter space where the lightest neutralino is a viable dark matter candidate that avoids direct detection constrains as well as bounds from LEP and LHC Higgs measurements. The allowed scenarios were divided in two classes: the ones where all the neutralinos and charginos (except the LSP) are promptly decaying and the ones with long-lived electroweakinos. We then derived LHC limits on these scenarios by reinterpreting SUSY and LLP searches using both simplified model and full recasting with MC simulation approaches. Regarding the prompt scenarios, only certain points with an LSP mass < 200 GeV were excluded, while if winos are heavy, the limit drops to 100 GeV. Regarding the LLP scenarios, we only focused on those where long-lived charginos are present. This is because the decay products of long-lived neutralinos are typically dominated by soft photons and currently any ATLAS and CMS analysis is sensitive to the corresponding signature. Thus, we used HSCP and DT searches to derive, actually powerful, constrains on the scenarios with charged LLPs. Moreover, we found that comparable limits on electroweaknos are obtained between both reinterpretation approaches. Finally, we provided 10 benchmark points that could serve as useful guidance in future work.

In chapter 6 we discussed a proposed method to determine the orthogonality of signal regions of different analysis. If analysis are determined as uncorrelated they can be trivially combined to potentially yield stronger constrains. The method was implemented into a tool we called TACO. First results were presented for LHC analyses in the intersection between the `SModelS` and `MadAnalysis` databases, derived from events produced from simplified model topologies. In a follow up work, we wish to include also more complicated events to uncover potential correlations that could have been missed. Furthermore, as more concrete results are obtained, is our objective to implement them in standard reinterpretation tools such as `SModelS` and `MadAnalysis`. Then, orthogonal signal regions could be automatically combined.

Chapter 7 regards the usefulness of ML classifiers and regressors in HEP phenomonelogy, in particular to address the full dimensionality of BSM theories. In there, we emphasize on the importance of estimating uncertainties of ML model predictions. Also, we provided recommendations on the sustainability and reproducibilty of trained ML models. Furthermore, we presented several examples of ML applications. In particular, I was responsible for the 'Learning the production cross sections of the Inert Doublet Model' sub-project. In there, we designed a neural network with a permanent dropout implementation, with the purpose of accurately predicting, with an estimated uncertainty, the production cross sections of the inert scalar in the IDM. In general, we observe a direct proportionality between the estimated uncertainty and the relative errors of the prediction This is very important for the correct interpretation of the former. Regarding accuracy, we showed promising results. However, improvements are still required, specifically in the resonant regions. A possible way to address the issue regards the use of active learning methods.

The quest for new physics is very vivid. New search possibilities are continuously arising. An important example is the development of LLP searches that permit us to study a whole different type of collider phenomenology. The success of this endeavor undoubtedly relies on a close communication between the experimenters and theorists in our field. On the one hand, this permit us to come up with optimal search strategies. On the other, it encourages the proper preservation of LHC results so they can be reinterpreted in the context of theories not yet tested. Finally, I stress the importance of employing (and developing) modern ML techniques in HEP phenomenology. Several applications have already been discussed in the literature. They include, signal vs background classification, prediction of observables, data-driven anomaly searches, the production of generative models, etc. I believe that machine learning, with a proper treatment of uncertainties, will play an important role on future breakthroughs in the field.

Appendix A

MCMC scan: steps of the implementation

The algorithm starts from a random uniformly drawn point, computes $-\log(L)$ denoted as $-\log(L)_{\text{old}}$, then a new point is drawn from a Gaussian distribution around the previous point, from which $-\log(L)$, denoted as $-\log(L)_{\text{new}}$, is computed. If $pp \times \log(L)_{\text{new}} \leq \log(L)_{\text{old}}$, where pp is a random number between 0 and 1, the old point is replaced by the new one and $-\log(L)_{\text{old}}$=$-\log(L)_{\text{new}}$. The next points will be drawn from a Gaussian distribution around the point that corresponds to $-\log(L)_{\text{old}}$. The steps of the implementation are the following:

1. Draw a starting point from a random uniform distribution.
2. If point lies within allowed scan range, eq. (6), compute spectrum with `SPheno`. If the compututation fails, go back to step 1 (or 9).
3. Check if $120 < m_h < 130$ GeV. If not, go back to step 1 (or 9).
4. Call `micrOMEGAs`, check if the point is excluded by LEP mass limits or invisible Z decays, or if the LSP is charged. If yes to any, go back to step 1 (or 9).
5. Compute the relic density and p_{X1T} with `micrOMEGAs`.
6. If relic density below $\Omega h^2_{Planck} + 10\% = 0.132$, save point.
7. Compute $\chi^2_{\Omega h^2}$ for relic density.
8. Compute $-\log(L)_{\text{old}} = \chi^2_{\Omega h^2} - \log(p_{X1T}) + \log(m_{LSP})$.
9. Draw a new point from a Gaussian distribution around the old one.
10. Repeat steps 2 to 7.
11. Compute $-\log(L)_{\text{new}}$.
12. Run the Metropolis–Hastings algorithm:
    pp=random.uniform(0,1.)
    If $pp \times \log(L)_{\text{new}} \leq \log(L)_{\text{old}}$:
    $\log(L)_{\text{old}}$=$\log(L)_{\text{new}}$
13. iteration++. While iteration<$n_{\text{iterations}}$: repeat steps 9 to 13.

This algorithm was run several times, starting from a different random point each time, to explore the whole parameter space defined by eq. (6).

Appendix B

Description of the signal regions considered in Chapter 6.

M_T [GeV]	p_T^{miss} [GeV]	$M_{ll} < 75$ GeV	$75 \geq M_{ll} < 105$ GeV	$M_{ll} \geq 105$ GeV
0–100	50–100	A0ASR1	A0ASR15	A0ASR32
	100–150	A0ARA2	A0ASR16	A0ASR33
	150–200	A0SRA3	A0ASR17	A0ASR34
	200-250	A0ASR4	A0ASR18	A0ASR35
	250–400	A0ASR5	A0ASR19	A0SR36
	400–500		A0ASR20	
	≥ 550		A0ASR21	
100–160	50–100	A0ASR6	A0ASR22	A0ASR37
	100-150	A0ASR7	A0ASR23	A0ASR38
	150–200	A0ASR8	A0ASR24	A0ASR39
	≥ 200	A0ASR9	A0ASR25	A0ASR40
≥ 160	50–100	A0ASR10	A0ASR26	A0ASR41
	100–150	A0ASR11	A0ASR27	A0ASR42
	150-200	A0ASR12	A0ASR28	A0ASR43
	200–250	A0ASR13	A0ASR29	A0ASR44
	250–400	A0ASR14	A0ASR30	
	≥ 400		A0SAR30	

Table B.1: Summary of the A0A signal regions in the A0 analysis, cf. Ref. [302].

M_T(GeV)	p_T^{miss}(GeV)	$M_{ll} < 100$GeV	$M_{ll} \geq 100$GeV
0-120	50-100	A0BSR1	A0BSR4
	> 100	A0BSR2	A0BSR5
> 120	> 50	A0BSR3	A0BSR6

Table B.2: Summary of the A0B signal regions in the A0 analysis, cf. Ref. [302].

p_T^{miss} [GeV]	$75 \geq M_{ll} < 105$ GeV	$M_{T2}(l_1 l_2)$[GeV]	$M_{ll} < 75$ GeV	$M_{ll} \geq 105$ GeV
50–100	A0CSR06	0-100	A0CSR01	A0CSR012
100–150	A0CSR07		A0CSR02	A0CSR013
150–200	A0CSR08		A0CSR03	A0CSR014
200–250	A0CSR09		A0CSR04	A0CSR015
250–300			A0CSR05	A0CSR016
300–400	A0CSR10			
$\geq$ 400	A0CSR11			
50–200		$\geq$ 100	A0CSR017	
$\geq$200			A0CSR018	

Table B.3: Summary of the A0C signal regions in the A0 analysis, cf. Ref. [302].

M_T [GeV]	p_T^{miss} [GeV]	$M_{ll} < 75$ GeV	$75 \geq M_{ll} < 105$ GeV	$M_{ll} \geq 105$ GeV
0–100	50–100	A0DSR1	A0DSR6	A0DSR11
	100–150	A0DSR2	A0DSR7	A0DSR12
	150–200	A0DSR3	A0DSR8	A0DSR13
	200–250	A0DSR4	A0DSR09	A0DSR14
	$\geq$250	A0DSR5	A0DSR10	
$\geq$100	50–200	A0DSR15		
	$\geq$200	A0DS016		

Table B.4: Summary of the A0D signal regions in the A0 analysis, cf. Ref. [302].

$M_{T2}(l_1, \tau)$ [GeV]	p_T^{miss} [GeV]	$M_{ll} < 60$ GeV	$60 \geq M_{ll} < 100$ GeV	$M_{ll} \geq 100$ GeV
0–100	50–100	A0ESR1	A0ESR6	A0ESR11
	100–150	A0ESR2	A0ESR7	
	150–200	A0ESR3	A0ESR8	
	200–250	A0ESR4	A0ESR9	
	$\geq$ 250	A0ESR5	A0ESR10	
$\geq$ 100	$\geq$50	A0ESR15		

Table B.5: Summary of the A0E signal regions in the A0 analysis, cf. Ref. [302].

$M_{T2}(l_1, \tau)$ [GeV]	p_T^{miss} [GeV]	$M_{ll} < 100$ GeV	$M_{ll} \geq 100$ GeV
0–100	50–100	A0FSR1	A0FSR7
	100–150	A0FSR2	A0FSR8
	150–200	A0FSR3	A0FSR9
	200–250	A0FSR4	A0FSR10
	250–300	A0FSR5	
	$\geq$ 300	A0FSR6	
$\geq$ 100	50–200	A0FSR11	
	$\geq$ 200	A0FSR12	

Table B.6: Summary of the A0F signal regions in the A0 analysis, cf. Ref. [302].

p_T^{miss} [GeV]	0 τ_h		1 τ_h	2 τ_h	
	nOSSF$\geq$2	nOSSF$<$ 2	nOSSF$\geq$ 0	nOSSF$\geq$ 2	nOSSF$<$ 2
0–50	A0GSR1	A0HSR1	A0ISR1	A0JSR1	A0KSR1
50–100	A0GSR2	A0HSR2	A0ISR2	A0JSR2	A0KSR2
100–150	A0GSR3	A0HSR3	A0ISR3	A0JSR3	A0KSR3
150–200	A0GSR4	A0HSR4	A0ISR4	A0JSR4	
$\geq$200	A0GSR5				

Table B.7: Summary of the A0(G-K) signal regions in the A0 analysis, cf. Ref. [302].

N_{jets}		0			1		
M_T [GeV]		$<$100		$>$100	$<$100		$>$100
p_T^{ll} [GeV]		$<$50	$>$50		$<$50	$>$50	
$p_T^{\text{miss}} < 100$ GeV		A0SSSR1	A0SSSR6	A0SSSR11	A0SSSR16	A0SSSR21	A0SSSR26
$100 \leq p_T^{\text{miss}} < 150$ GeV	++	A0SSSR2	A0SSSR7	A0SSSR12	A0SSSR17	A0SSSR22	A0SSSR27
	- -	A0SSSR3	A0SSSR8	A0SSSR13	A0SSSR18	A0SSSR23	A0SSSR28
$150 \leq p_T^{\text{miss}} < 200$ GeV		A0SSSR4	A0SSSR9	A0SSSR14	A0SSSR19	A0SSSR24	A0SSSR29
$p_T^{\text{miss}} \geq 200$ GeV		A0SSSR5	A0SSSR10	A0SSSR15	A0SSSR20	A0SSSR25	A0SSSR30

Table B.8: Summary of the A0SS signal regions in the A0 analysis, cf. Ref. [302].

	N_{jet}	$N_{b\text{-jet}}$	H_T [GeV]	H_T^{miss} [GeV]
A1SR1	$\geq$ 2	0	$\geq$ 500	$\geq$ 500
A1SR2	$\geq$ 3	0	$\geq$1500	$\geq$ 750
A1SR3	$\geq$ 5	0	$\geq$ 500	$\geq$500
A1SR4	$\geq$ 5	0	$\geq$ 1500	$\geq$ 750
A1SR5	$\geq$ 9	0	$\geq$ 1500	$\geq$ 750
A1SR6	$\geq$ 2	$\geq$2	$\geq$500	$\geq$500
A1SR7	$\geq$ 3	$\geq$1	$\geq$750	$\geq$750
A1SR8	$\geq$ 5	$\geq$ 3	$\geq$500	$\geq$ 500
A1SR9	$\geq$ 5	$\geq$2	$\geq$ 1500	$\geq$ 750
A1SR10	$\geq$ 5	$\geq$ 3	$\geq$750	$\geq$ 750
A1SR11	$\geq$ 7	$\geq$ 1	$\geq$300	$\geq$ 300
A1SR12	$\geq$ 5	$\geq$1	$\geq$750	$\geq$ 750

Table B.9: Summary of the signal regions in the A1 analysis, cf. Ref. [127].

$m_{T2}(l_1 l_2)$ [GeV]	100 – 140	140 – 240	$>$ 240
$E_T^{\text{miss}} > 200$ GeV	A2SR1	A2SR2	A2SR3

Table B.10: Summary of the signal regions in the A2 analysis, cf. Ref. [313].

	A3SR2jl	A3SR2jm	A3SR2jt	A3SR4jt	A3SR5j	A3SR6jm	A3SR6jt
$E_T^{\rm miss}$[GeV] $>$	200						
$p_T(j_1)$[GeV] $>$	200	300	200				
$p_T(j_2)$[GeV] $>$	200	50	200	100			
$p_T(j_3)$[GeV] $>$	-			100			
$p_T(j_4)$[GeV] $>$	-			100			
$p_T(j_5)$[GeV] $>$	-				50		
$p_T(j_6)$[GeV] $>$	-					50	
$\Delta\phi({\rm jet}_{1,2,(3)}, E_T^{\rm miss})_{\rm min} >$	0.8	0.4	0.8	0.4			
$\Delta\phi({\rm jet}_{i>3}, E_T^{\rm miss})_{\rm min} >$	-			0.2			
$E_T^{\rm miss}/\sqrt{H_T}$ [GeV$^{1/2}$] $>$	15		20	-			
Aplanarity $>$	-			0.04			
$E_T^{\rm miss}/m_{\rm eff}(N_j) >$	-			0.2	0.25		0.2
$m_{\rm eff}$(incl.) [GeV] $>$	1200	1600	2000	2200	1600	1600	2000

Table B.11: Summary of the signal regions in the A3 analysis, cf. Ref. [312].

Appendix C

Résumé Français.

C.1 Introduction.

L'été 2012 a marqué une étape importante dans l'histoire du grand collisionneur de hadrons (LHC). Les collaborations ATLAS et CMS ont annoncé l'observation d'une résonance à 125 GeV dans le spectre de di-photons, correspondant à la production résonante d'une particule scalaire, avec un niveau de confiance de 5σ. Le boson de Higgs avait été découvert. Le boson scalaire était la dernière pièce manquante du modèle standard (SM) de la physique des particules. Ainsi, le spectre des champs de la théorie a été complété. Huit ans se sont écoulés et le SM reste incontesté au LHC. Jusqu'à présent, toutes les observations des détecteurs ATLAS et CMS restent fidèles aux prédictions du SM, alors qu'aucun signe précis de déviation n'a été détecté. Cependant, nous avons de bonnes raisons de croire que le SM n'est pas la théorie finale. Intrinsèquement, plusieurs phénomènes soulèvent des questions auxquelles nous aimerions trouver une réponse: pourquoi l'échelle électrofaible et l'échelle de Planck sont-elles si éloignées?,La conservation du nombre de baryons et du nombre de leptons ne sont-elles que des symétries accidentelles?, Pourquoi n'y a-t-il pas violation de CP (charge - parité) dans le secteur QCD (Chromodynamique quantique)?, etc. De plus, il existe des observations astrophysiques et cosmologiques qui conduisent à penser qu'il existe une nouvelle physique au-delà du SM: l'asymétrie matière-antimatière, l'expansion accélérée de l'Univers et la matière noire. Finalement, le SM ne décrit que trois des quatre forces fondamentales que nous connaissons, en laissant de côté la gravité.

Pour résoudre les énigmes intrinsèques du SM et décrire les observations que le SM ne ne parvient pas à expliquer, une pléthore de théories au-delà du modèle standard (BSM) ont été proposées. Jusqu'à présent, les plus théoriquement convaincantes, sont les celles tirées du paradigme de la supersymétrie (SUSY), dans lequel pour chaque champ bosonique une contrepartie fermionique existe et vice-versa. Elles peuvent être invoquées pour résoudre la majorité, sinon la totalité, des problèmes du SM et devraient être observées au LHC. Il existe également un grand nombre d'extensions non supersymétriques, telles que des théories avec des dimensions supplémentaires, des modèles multi-Higgs et des théories avec de nouvelles symétries internes, qui sont souvent conçues pour décrire des problèmes spécifiques du SM. Dans l'ensemble, les théories BSM forment une vaste mer de possibilités qui devraient toutes être explorées, car de la nouvelle physique peut être trouvée dans tous les coins.

Un vaste programme de recherches sur la nouvelle physique a été proposé au LHC, visant à couvrir autant que possible les nouvelles théories de la physique. Cependant, l'immensité des théories et des scénarios BSM, rend impossible pour les collaborations expérimentales de poursuivre cet objectif par eux-mêmes. Ainsi, une communication étroite entre théoricien et expérimentateur est nécessaire. Cela encourage de nouvelles idées sur où chercher de la nouvelle physique. De plus, il favorise la préservation des résultats expérimentaux de telle manière qu'ils puissent être réinterprétés dans le contexte des théories au-delà de la nouvelle physique standard. C'est dans cet esprit que le forum de réinterprétation des recherches du LHC a été conçu, dans le cadre d'un effort conjoint entre expérimentateurs et théoriciens visant à tirer le meilleur parti de l'héritage du LHC.

C'est dans le cadre de la réinterprétation des résultats du LHC que cette thèse se déroule. Du côté phénoménologique, il explore la sensibilité des résultats actuels du LHC au modèle Minimal avec gauginos de Dirac (MDGSSM), une théorie SUSY au-delà de la nouvelle physique standard où les gauginos sont promus aux états Dirac. Fait intéressant, le MDGSSM présente une phénoménologie considérablement différente des modèles SUSY déjà envisagés au LHC. Les travaux correspondants ont impliqué la réinterprétation, selon différentes approches, d'une variété d'analyses du LHC. Côté développement d'outils, il concerne les nouveaux développements de l'outil de réinterprétation `SModelS` présentés dans sa version 1.2. Ma principale contribution à cette version a été le développement d'un créateur de tracés interactifs, pour faciliterl'étude des résultats de `SModelS`. De plus, dans cette thèse, nous discutons de la mise en œuvre d'un outil pour déterminer si les régions de signal de différentes analyses sont statistiquement indépendantes les unes des autres et, par conséquent, peuvent être combinées de manière triviale.

De plus, nous vivons à l'ère mondiale du big data, qui s'est sans aucun doute propagée au domaine de la physique des particules. Tant sur le domaine des collisionneurs que sur celui de l'astrophysique, une énorme quantité de données est collectée, dont l'interprétation est trop complexe pour ne pas s'appuyer sur la science des données moderne. Ainsi, les collaborations expérimentales adoptent de plus en plus (et développent) des techniques modernes d'apprentissage automatique (ML) pour leurs études. La nécessité de faire de même en phénoménologie de la physique des hautes énergies (HEP) devient de plus en plus stricte. D'une part, pour être en mesure de bien comprendre et de (ré)interpréter les résultats expérimentaux, une bonne compréhension des techniques sophistiquées qu'ils emploient est nécessaire. En outre, comme indiqué, le cadre de réinterprétation du LHC a pour objectif de couvrir la grande variété de théories BSM proposées. La plupart de ces théories sont faites d'une interaction compliquée entre leurs paramètres libres. L'introduction du ML peut certainement améliorer l'exploration de ces espaces de paramètres. De plus, le ML ouvre la possibilité de suivre le problème inverse, c'est-à-dire poursuivre les recherches basées sur les données pour trouver des anomalies dans les résultats expérimentaux, qui pourraient être interprétées plus tard dans le contexte d'une théorie BSM.

Donc, cette thèse décrit la première tentative par l'auteur, dans le sujet émergent du ML en phénoménologie HEP. Concrètement, j'ai travaillé sur l'implémentation d'un réseau neuronal pour prédire avec précision et avec une incertitude estimée, les sections efficaces de production dans le modèle de doublet inerte (IDM). Nous discutons également de l'importance de fournir des incertitudes sur les prédictions des modèles de ML et sur les recommandations pour partager tout le matériel impliqué dans la production des applications de ML. De plus, nous présentons plus d'exemples de classificateurs et régresseurs basé sur le ML et appliqués à la phénoménologie HEP.

Le manuscrit est structuré comme suit. Le chapitre 2 sert d'introduction au SM et à notre quête actuelle pour l'étendre. En ce qui concerne notre motivation à aller au-delà du SM, nous accordons une attention particulière à la matière noire, tandis que dans le cadre des théories de nouvelle physique, nous mettons l'accent sur la supersymétrie. Ensuite, le chapitre 3 présente le cadre de modèle simplifié pour interpréter les résultats du LHC, suivi d'une description des principales approches de réinterprétation des analyses du LHC. Le chapitre 4 commence par décrire le concept général de l'outil de réinterprétation de modèles simplifiés `SModelS`, pour ensuite se concentrer sur les développements présentés dans sa version la plus récente, v1.2. Dans le chapitre 5, nous allons au-delà de la nouvelle physique standard et explorons le MDGSSM dans le contexte du cadre de réinterprétation du LHC. Dans la première section, nous fournissons une introduction au modèle et nos motivations pour l'étudier. Dans la seconde, nous présentons les contraintes sur les gluinos et les squarks du modèle, dérivées de la réinterprétation des analyses LHC appropriées. Dans le troisième, nous nous tournons vers le secteur electroweakino. Nous présentons notre étude de la phénoménologie des collisionneurs de l'espace des paramètres electroweakino où le neutrino le plus léger est un candidat à la matière noire non surabondant qui échappe aux contraintes des recherches de détection directe de la matière noire, LEP et des mesures de Higgs au LHC. L'étude a été divisée en deux classes de scénarios: ceux avec seulement des électroweakinos en désintégration rapide et ceux avec des charginos et / ou des neutralnos à longue durée de vie. Ceci est suivi par le chapitre 6 où nous discutons de la mise en œuvre de TACO (Testing Analyses' COrrelations), un outil pour déterminer l'orthogonalité des région du signal (SR) à partir de différentes analyses du LHC. Ensuite, dans le chapitre 7, nous discutons des applications des régresseurs et classificateurs ML en phénoménologie HEP. Finalement, les conclusions finales sont abordées.

C.2 Sommaire des Chapitres.

C.2.1 Chapitre 2 - Le voyage au-delà du modèle standard.

Le modèle standard de la physique des particules est actuellement notre meilleure description des éléments constitutifs de la nature. Cependant, plusieurs indications nous motivent à étendre le SM. Dans l'aspect théorique, ils incluent le problème de hiérarchie, le problème de CP fort, la grande unification, etc. Au sens observationnel, la motivation la plus claire est l'existence de matière noire (DM); le SM ne peut pas décrire l'excès de matière observé dans l'Univers.

Par conséquent, plusieurs théories ont été proposées pour étendre le SM afin de répondre à ces énigmes théoriques et observationnelles. Les plus complètes sont celles tirées du contexte de la supersymétrie. Le modèle standard supersymétrique minimal (MSSM) a été largement étudié, car il est connu pour fournir des solutions au problème de hiérarchie et fournir des candidats de DM viables, entre autres propriétés. Cependant, il existe d'autres théories SUSY qui méritent de l'attention . En particulier, dans cette thèse, nous nous concentrons sur la théorie minimale SUSY où les gauginos (super partenaires des bosons de jauge) sont des états de Dirac. Finalement, notre machine principale pour étudier le SM et ses extensions possibles est le grand collisionneur de hadrons.

C.2.2 Chapitre 3 - (Re)Interprétation des recherches du LHC.

Au LHC, ATLAS et CMS ont mis en place un vaste programme de recherche de nouvelle physique. Cela peut être grossièrement classé en recherches de résonance, d'énergie manquante et de particules à longue durée de vie (LLP). Les premiers sont généraux à interpréter (effets d'interférence mis à part). Alors que les deux autres sont généralement plus complexes. Cela est principalement dû à leur optimisation dépendant du modèle et aux modèles théoriques complexes à partir desquels ils sont optimisés. Pour y remédier, ATLAS et CMS ont choisi de présenter leurs résultats dans le cadre des spectres de modèles simplifiés (SMS). Les SMS sont des ensembles de descriptions lagrangiennes efficaces, appelés modèles simplifiés, conçus pour caractériser un nouveau modèle physique avec un petit nombre de paramètres cinématiques, liés à la physique des collisionneurs, d'une manière supposée suffisante pour décrire la phénoménologie essentielle des modèles de nouvelle physique. Cela permet aux recherches du LHC de couvrir aussi largement que possible les théories BSM populaires tout en restant applicables à un plus large éventail de modèles théoriques, de manière simple. Les résultats sont ensuite présentés sous la forme de cartes de la limite supérieure sur des sections efficaces multipliées par des rapports de branchement ($\sigma \times \mathcal{B}$) et des cartes d'efficacité sur les paramètres libres des modèles simplifiés.

La variété des théories BSM est trop vaste pour que les collaborations expérimentales les couvrent d'elles-mêmes. Ainsi, il est nécessaire que les résultats du LHC soient réinterprétés pour tester des théories plus complexe ou pas encore pensé. Actuellement, il existe deux approches principales pour ce faire. La première, connue sous le nom d'approche par modèle simplifié, est rapide mais souvent conservatrice. Son idée principale est de comparer directement la limite supérieure expérimentale avec le $\sigma \times \mathcal{B}$ correspondant du modèle théorique. Alternativement, on peut également utiliser des cartes d'efficacité pour calculer les événements de signal attendus et les bornes correspondantes. L'approche du modèle simplifié suit l'hypothèse selon laquelle l'efficacité ou les limites supérieures restent approximativement valables pour un modèle générique prédisant la même signature que le modèle simplifié. La seconde approche prend plus de temps mais est généralement plus complète. Elle est connue sous le nom de réinterprétation basée sur le simulation complète d'événements (ou refonte complète). Son idée générale est de calculer les rendements de signal attendus des processus BSM qui seraient mesurés par une analyse basée sur les selections. Ceci est réalisé en appliquant les mêmes selections dans les analyses et en calculant le rapport des événements sélectionnés sur le nombre total d'événements produits. Ces événements sont produits via des générateurs d'événements Monte Carlo et la réponse du détecteur est émulée par des simulateurs dédiés. Finalement, nous notons que, bien que le processus de réinterprétation basée sur le simulation complète d'événements soit bien standardisé pour le cas de recherches d'énergie manquantes par plusieurs outils, il n'existe pas encore une méthode claire pour les recherches LLP. Néanmoins, plusieurs implémentations de recherches LLP ont été effectuées en suivant différentes approches.

C.2.3 Chapitre 4 - SModelS. Developemments récents.

La nature de l'approche SMS nous permet de dériver des contraintes sur une large variété de théories BSM. Dans `SModelS` [134, 171, 135], une procédure générale de décomposition des théories BSM, présentant une symétrie Z_2, en topologies de modèle simplifiées, est implémentée. Ceci est suivi d'une correspondance automatique entre les topologies produites et le résultat du modèle simplifié correspondant trouvé dans sa grande base de données. Avec la publication de la version 1.2 [135], `SModelS` a annoncé plusieurs nouveaux développements. Premièrement, alors que les versions précédentes étaient limitées aux signatures énergétiques manquantes et ne supposaient que des désintégrations rapides, la version actuelle prend désormais en compte la durée de vie de chaque particule Z_2-impair et prend correctement en compte les signatures de énergie manquante, des particules chargée, stable et lourde (HSCP) et des hadrons R . Deuxièmement, `SModelS` permet désormais une combinaison de régions de signal dans les résultats de la carte d'efficacité chaque fois qu'une matrice de covariance est disponible à partir de l'expérience. Troisièmement, smodelsTools fournit désormais un créateur de tracés interactifs pour visualiser facilement des résultats de `SModelS` et les comparer avec les paramètres des théories BSM.

C.2.4 Chapitre 5 - Contraintes sur le modèle minimal de Dirac gaugino.

La plupart des recherches SUSY au LHC sont effectuées dans le contexte du MSSM, où les gauginos sont des particules de Majorana. En introduisant les gauginos de Dirac, nous obtenons une phénoménologie enrichie, des différences considérables dans les signatures et les limites du LHC sont attendues par rapport au MSSM. Concrètement, dans le MDGSSM nous avons un secteur electroweakino étendu par deux neutralinos et un chargino. De plus, les sections efficaces de production sont agrandie pour les gluinos, tandis que pour les squarks, ils sont supprimés. De plus, une petite division de masse dans les deux états bino et wino peuvent conduire à la présence des LLP. Nous avons réalisé deux études pour explorer la phénoménologie des collisionneurs du secteur coloré (dans le premier) et du secteur electroweakino (dans le second).

Dans la première étude [184], nous avons étudié les limites des recherches du LHC sur les squarks et les gluinos pour quelques scénarios représentatifs. Dans le contexte de contraintes de modèle simplifiées, la grande variété de modes de désintégration possibles dans nos scénarios a conduit à des limites très faibles. La raison en est que, dans des scénarios complexes comme ceux considérés ici, seule une petite fraction de la production totale de SUSY correspond aux topologies de signaux qui sont contraintes par les résultats de modèles simplifiés disponibles. Nous avons donc confronté nos scénarios à une refonte complète de la recherche ATLAS multi-jet + MET [268] avec `MadAnalysis 5`. En comparant les limites sur nos scénarios du MDGSSM à ceux du MSSM, nous avons confirmé que les limites des squarks sont très significativement (de plusieurs centaines de GeV) supprimées par rapport au MSSM. Nous avons montré que cette déclaration est robuste même en incluant des corrections de boucle de la production. En revanche, pour les petites masses de gluino, les degré de liberté supplémentaires conduisent à des sections efficaces de production plus importantes, et donc la limite inférieure sur la masse des gluinos dans ces modèles est quelque peu plus élevée que dans le MSSM.

Dans la deuxième étude (l'article correspondant est en préparation), nous avons étudié le secteur electroweakino du MDGSSM. Nous avons exploré l'espace des paramètres où le neutralino le plus léger $\tilde{\chi}_1^0$ est un bon candidat à la DM en accord avec la dénsité relique et les contraintes de détection directe. La phénoménologie des collisionneurs des nouveaux scénarios motivés par la DM est caractérisée par le spectre du secteur EW-ino plus riche par rapport a celui du MSSM, naturellement de petites répartitions de masse et la présence fréquente de charginos et/ou de neutralinos à longue durée de vie. Nous avons dérivé des contraintes actuelles du LHC sur ces scénarios en réinterprétant les recherches SUSY et LLP réalisées par ATLAS et CMS. Pour ça, nous avons suivi une approche de modèle simplifiée et une refonte complète à l'aide de la simulation d'événements de Monte Carlo. Alors que les HSCP et les recherches des traces qui disparaissen (DT) donnent des limites assez puissantes aux scénarios avec des LLP chargés, les scénarios avec principalement des signatures E_T^{miss} restent peu contraints. En effet, les recherches SUSY ne permettent d'exclure que (certains) points avec un LSP inférieur à 200 GeV, et ça tombe à environ 100 GeV lorsque les winos sont lourds. C'est un contraste frappant avec l'image pour les contraintes sur les particules colorées, et indique que le secteur EW-ino de la théorie est probablement le plus prometteur pour les travaux futurs. Finalement, nous avons fourni un ensemble de 10 points de référenc à cette fin. En outre, nous avons constaté que le modèle simplifié et l'approche de refonte complète fournissent des limites comparables sur le secteur electroweakino du MDGSSM.

C.2.5 Chapitre 6 - Détermination des SR indépendants dans les recherches du LHC pour la nouvelle physique.

Le programme de recherche du LHC pour la nouvelle physique a produit des centaines de publications et un plus grand nombre de résultats SMS individuels. Dans certains cas, ATLAS et CMS fournissent également des matrices de covariance qui permettent une combinaison de probabilités dérivées de différentes régions de signal (SR). Ce n'est cependant pas général, et est limité aux régions de signal dans la même analyse. Néanmoins, avoir une connaissance de la corrélation entre les régions de signal est très utile, car elles permettent leur combinaison et dérivent ainsi des limites plus strictes sur les théories BSM. Avec cela comme motivation, nous avons développé une méthode probabiliste pour la détermination de paires d'analyses approximativement non corrélées. La méthode a ensuite été implémentée dans un outil que nous avons appelé TACO. Pour les résultats présentés, seuls les événements issus de topologies de modèles simplifiés ont été produits. Dans un futur projet, nous souhaitons introduire également des événements plus compliqués pour couvrir les corrélations potentielles qui pourraient être manquées par des événements basés sur des modèles simplifiés trop simplistes. Ce travail est apparu comme la contribution 16 dans le rapport du groupe de travail BSM [1] de l'atelier Les Houches 'Physics at TeV Colliders' 2019.

C.2.6 Chapitre 7 - Apprentissage automatique pratique pour la régression et la classification et les applications en phénoménologie HEP.

Ce chapitre concerne la contribution 22 du rapport du groupe de travail BSM de l'atelier Les Houches 'Physics at TeV Colliders' 2019 [1]. Ici, nous discutons des applications pratiques du ML dans la phénoménologie de la Physique des Hautes ènergies et en particulier la possibilité d'examiner les modèles de la nouvelle physique dans leur pleine dimensionnalité.

L'idée de ce projet est de simplifier la création et la réutilisation de modèles d'apprentissage automatique conçus pour la phénoménologie HEP. Pour cela, nous avons encouragé à sauvegarder le modèle ML, l'ensemble de données et le code pour former les modèles de ML. Si la construction des modèles ML peut être simplifiée, toute publication sur la phénoménologie HEP pourrait utiliser des modèles ML pour stocker les probabilités, les sections efficaces et les limites également pour les modèles HEP multidimensionnels. De plus, nous insistons sur l'importance de quantifier les incertitudes *épistémiques.* Ils concernent ceux introduits avec notre modèle ML pour l'estimateur $\hat{f}(x) \approx f(x)$. Un exemple de ce type d'incertitude est l'incertitude liée aux valeurs entraînées des paramètres (par exemple les poids d'un réseau neuronal) de l'algorithme ML. Une façon d'estimer ces incertitudes dans les réseaux de neurones consiste à appliquer *dropout* aux nœuds pendant l'inférence [331].

Finalement, à titre de preuve de concept et de faisabilité, nous avons montré divers exemples d'applications. Ici, nous ne mentionnons que celui qui était de la responsabilité de l'auteur de cette thèse: 'Apprentissage des sections efficaces de production dans le IDM. Dans ce travail, nous avons obtenu les premiers résultats de réseaux de neurones formés qui prédisent les sections efficaces de production du LHC pour les scalaires inertes dans l'IDM, avec une estimation de l'incertitude bayésienne. La prochaine étape de ce projet se concentrera sur la réduction de cette incertitude et, en s'assurant que la vraie valeur est à l'intérieur de l'intervalle d'incertitude 1 std de la prédiction, la réduction de l'erreur relative des prédictions sur tout l'espace des paramètres pour tous les processus sous considération. Une façon d'y parvenir concerne la mise en œuvre de l'apprentissage actif basé sur le *dropout* [372].

C.3 Conclusion.

Un vaste programme de recherches sur la nouvelle physique est mené par les collaborations ATLAS et CMS. Au sein de ces dernières, les résultats sont généralement interprétés dans le contexte de modèles simplifiés. Cette approche permet une compréhension plus claire des résultats et facilite notamment leur réinterprétation. Cependant, les limites de masse dérivées de modèles simplifiés peuvent changer considérablement lorsque l'on considère les scénarios plus réalistes d'une même théorie. En outre, il existe encore une grande variété de théories au-delà de la nouvelle physique standard qui ne sont pas directement couvertes par les collaborations expérimentales. Ainsi, justifiant la présence d'un cadre très actif de réinterprétation des résultats du LHC. Portée dans ce contexte, l'objectif de cette thèse était d'étudier la phénoménologie des théories au-delà de la nouvelle physique standard et de contribuer au développement d'outils pour rendre plus efficace une telle entreprise. Un autre aspect de cette thèse a porté sur les premiers pas de l'auteur sur le sujet émergent des applications ML à la phénoménologie HEP.

Dans le chapitre 4, nous avons discuté des développements présentés dans la version 1.2 de l'outil de réinterprétation `SModelS`. À savoir, il comporte désormais la combinaison de régions de signal chaque fois qu'une matrice de covariance et les cartes d'efficacité correspondantes sont fournies par les analyses LHC. Ceci est très utile pour améliorer le pouvoir contraignant qui peut être dérivé de modèles simplifiés. Une autre amélioration majeure est l'implémentation des signatures HSCP et R-hadron, étendant considérablement les types de topologies qui peuvent être testées par `SModelS`. En outre, la version 1.2 a présenté l'ajout d'un Interactive Plots Maker (créateur de tracés interactifs), un outil pour visualiser efficacement les résultats de `SModelS` et les comparer avec les paramètres du modèle théorique à l'étude. C'est dans le développement de cet outil que j'étais principalement impliqué.

Dans le chapitre 5, nous sommes allés au-delà de la nouvelle physique standard et avons exploré la phénoménologie du secteur coloré et du secteur electroweakino du MDGSSM. Il y a plusieurs motivations pour étudier ce modèle. Parmi eux, nous constatons qu'une augmentation naturelle de la masse de Higgs au premier ordre est induite. De plus, des différences importantes sur les contraintes et les signatures des collisionneurs sont attendues en ce qui concerne le MSSM.

Dans la première étude du MDGSSM, nous avons dérivé les limites du LHC sur les gluinos et les squarks dans le MDGSSM. Dans un premier temps, nous avons utilisé `SModelS` pour obtenir rapidement des limites sur les masses des sparticules colorées. Cependant, comme nous avions affaire à des scénarios complexes où les gluinos et les squarks répartissent leurs ratios de ramification sur plusieurs canaux de désintégration, les contraintes dérivées de modèles simplifiés étaient faibles. Ainsi, nous nous sommes tournés vers la refonte avec une simulation d'événements complète pour obtenir des résultats plus réalistes. Cela a nécessité la mise en œuvre et la validation de l'analyse multijet ATLAS-SUSY-2016-07 dans le cadre de `Madanalysis 5`. En comparant les bornes finalement obtenues à celles des scénarios MSSM équivalents, nous avons quantifié leurs différences. D'une part, lorsque les masses gluino sont grandes, les limites des squarks sont supprimées par rapport au MSSM. Ceci en raison d'une inversion de chiralité interdite dans la production des squarks via le processus d'échange de gluino, dans le MDGSSM. D'un autre côté, lorsque la production de gluino domine, les contraintes sont renforcées dans le cas du MDGSSM en raison des degrés de liberté supplémentaires du gluino.

Dans la deuxième étude, nous avons contraint les électroweakinos du MDGSSM. Premièrement, nous avons délimité l'espace des paramètres où le neutralino le plus léger est un candidat viable à la matière noire qui évite les contraintes de détection directes ainsi que les limites imposées par le LEP et par les mesures de Higgs au LHC. Les scénarios autorisés ont été divisés en deux classes: ceux où tous les neutralinos et charginos (sauf le LSP) se désintègrent rapidement et ceux avec des électroweakinos à longue durée de vie. Nous avons ensuite dérivé les limites du LHC sur ces scénarios en réinterprétant les recherches SUSY et LLP en utilisant à la fois un modèle simplifié et une refonte complète avec des approches de simulation de Monte Carlo. En ce qui concerne les scénarios avec electroweakinos en décomposition rapide, seuls certains points avec une LSP avec masse $<$ 200 GeV ont été exclus, tandis que si les winos sont lourds, la limite tombe à 100 GeV. En ce qui concerne les scénarios LLP, nous nous sommes concentrés uniquement sur ceux où des charginos à longue durée de vie sont présents. En effet, les produits de désintégration des neutrialinos à longue durée de vie sont généralement dominés par les photons de basse énergie et actuellement, aucune analyse dans ATLAS où CMS n'est sensible à la signature correspondante. Ainsi, nous avons utilisé les recherches HSCP et DT pour dériver des contraintes, qui s'avèrent puissantes, sur les scénarios avec des LLP chargés. De plus, nous avons constaté que des limites sur les electroweakinos obtenues par les deux approches de réinterprétation sont comparables. Enfin, nous avons fourni 10 points de référence qui pourraient servir d'orientations utiles dans les travaux futurs.

Dans le chapitre 6, nous avons discuté d'une méthode proposée pour déterminer l'orthogonalité des régions de signal de différentes analyses. Si les analyses sont déterminées comme non corrélées, elles peuvent être combinées de manière triviale pour produire potentiellement des contraintes plus fortes. La méthode a été implémentée dans un outil que nous avons appelé TACO. Les premiers résultats ont été présentés pour les analyses du LHC à l'intersection entre les bases de données de `SModelS` et de `MadAnalysis`, dérivées d'événements produits à partir de topologies de modèle simplifiées. Dans un travail de suivi, nous souhaitons également inclure des événements plus compliqués pour découvrir des corrélations potentielles qui auraient pu être manquées. De plus, à mesure que des résultats plus concrets sont obtenus, notre objectif est de les implémenter dans des outils de réinterprétation standard tels que `SModelS` et `MadAnalysis`. Ensuite, les régions de signaux orthogonales pourraient être automatiquement combinées.

Le chapitre 7 concerne l'utilité des classificateurs et régresseurs ML dans la phénoménologie HEP, en particulier pour aborder la pleine dimensionnalité des théories BSM. En particulier, nous insistons sur l'importance d'estimer les incertitudes des prédictions du modèle ML. Nous avons également fourni des recommandations sur la durabilité et la reproductibilité des modèles ML formés. De plus, nous avons présenté plusieurs exemples d'applications ML. En particulier, j'étais responsable du sous-projet 'Apprentissage des sections efficaces de production du modèle de doublet inerte'. Ainsi, nous avons conçu un réseau neuronal avec une implémentation d'abandon permanent, dans le but de prédire avec précision, avec une incertitude estimée, les sections efficaces de production du scalaire inerte dans l'IDM. En général, nous observons une proportionnalité directe entre l'incertitude estimée et les erreurs relatives de la prédiction. Ceci est très important pour l'interprétation correcte de la première. Concernant la précision, nous avons montré des résultats prometteurs. Cependant, des améliorations sont encore nécessaires, en particulier dans les régions résonantes. Un moyen possible de résoudre le problème concerne l'utilisation de méthodes d'apprentissage actives.

La quête d'une nouvelle physique est très vive. De nouvelles possibilités de recherche apparaissent sans cesse. Un exemple important est le développement de recherches LLP qui nous permettent d'étudier un tout autre type de phénoménologie des collisionneurs. Le succès de cette entreprise repose sans aucun doute sur une communication étroite entre les expérimentateurs et les théoriciens de notre domaine. D'une part, cela nous permet de trouver des stratégies de recherche optimales. D'autre part, il encourage la bonne conservation des résultats du LHC afin qu'ils puissent être réinterprétés dans le cadre de théories non encore testées. Finalement, je souligne l'importance d'employer (et de développer) des techniques modernes de ML dans la phénoménologie HEP. Je pense que l'apprentissage automatique, avec un traitement approprié des incertitudes, jouera un rôle important dans les progrès futurs de la physique des particules.

Bibliography

[1] G. Brooijmans et al. Les Houches 2019 Physics at TeV Colliders: New Physics Working Group Report. In *11th Les Houches Workshop on Physics at TeV Colliders: PhysTeV Les Houches*, 2 2020.

[2] Andrea Romanino. The Standard model of particle physics. In *9th Baikal Summer School on Physics of Elementary Particles and Astrophysics*, 2009.

[3] Mark Thomson. *Modern particle physics*. Cambridge University Press, New York, 2013.

[4] M. Mondragon. Beyond the Standard Model. *CERN Yellow Rep. School Proc.*, 4:101–124, 2018.

[5] Hyun Min Lee. Lectures on Physics Beyond the Standard Model. arXiv:1907.12409, 7 2019.

[6] B. C. Allanach. Beyond the standard model lectures. arXiv:1609.02015, 2016.

[7] Sunny Vagnozzi, Elena Giusarma, Olga Mena, Katherine Freese, Martina Gerbino, Shirley Ho, and Massimiliano Lattanzi. Unveiling ν secrets with cosmological data: neutrino masses and mass hierarchy. *Phys. Rev. D*, 96(12):123503, 2017.

[8] J. D. Vergados, H. Ejiri, and F. Šimkovic. Neutrinoless double beta decay and neutrino mass. *International Journal of Modern Physics E*, 25(11):1630007, Nov 2016.

[9] M. Aker et al. Improved upper limit on the neutrino mass from a direct kinematic method by katrin. *Phys. Rev. Lett.*, 123:221802, Nov 2019.

[10] D.Q. Adams et al. Improved Limit on Neutrinoless Double-Beta Decay in ^{130}Te with CUORE. *Phys. Rev. Lett.*, 124(12):122501, 2020.

[11] S. Schael et al. Precision electroweak measurements on the Z resonance. *Phys. Rept.*, 427:257–454, 2006.

[12] Georges Aad et al. Observation of a new particle in the search for the Standard Model Higgs boson with the ATLAS detector at the LHC. *Phys. Lett. B*, 716:1–29, 2012.

[13] Serguei Chatrchyan et al. Observation of a New Boson at a Mass of 125 GeV with the CMS Experiment at the LHC. *Phys. Lett. B*, 716:30–61, 2012.

[14] R.D. Peccei and Helen R. Quinn. CP Conservation in the Presence of Instantons. *Phys. Rev. Lett.*, 38:1440–1443, 1977.

[15] STEPHEN P. MARTIN. A supersymmetry primer. *Advanced Series on Directions in High Energy Physics*, pages 1–98, Jul 1998.

[16] A.D. Sakharov. Violation of CP Invariance, C asymmetry, and baryon asymmetry of the universe. *Sov. Phys. Usp.*, 34(5):392–393, 1991.

[17] F. Csikor, Z. Fodor, and J. Heitger. Endpoint of the hot electroweak phase transition. *Phys. Rev. Lett.*, 82:21–24, 1999.

[18] Debasish Majumdar. *Dark Matter : an Introduction.* Taylor and Francis, 2015.

[19] Stefano Profumo, Leonardo Giani, and Oliver F. Piattella. An Introduction to Particle Dark Matter. *Universe*, 5(10):213, 2019.

[20] Gianfranco Bertone, Dan Hooper, and Joseph Silk. Particle dark matter: Evidence, candidates and constraints. *Phys. Rept.*, 405:279–390, 2005.

[21] Stefano Profumo. Astrophysical Probes of Dark Matter. In *Theoretical Advanced Study Institute in Elementary Particle Physics: Searching for New Physics at Small and Large Scales*, pages 143–189, 2013.

[22] Dan Hooper. Tasi 2008 lectures on dark matter. arXiv:0901.4090, 2009.

[23] T.S. van Albada, John N. Bahcall, K. Begeman, and R. Sancisi. The Distribution of Dark Matter in the Spiral Galaxy NGC-3198. *Astrophys. J.*, 295:305–313, 1985.

[24] F. Zwicky. Die Rotverschiebung von extragalaktischen Nebeln. *Helv. Phys. Acta*, 6:110–127, 1933.

[25] Vera C Rubin, W Kent Ford Jr, and Norbert Thonnard. Rotational properties of 21 sc galaxies with a large range of luminosities and radii, from ngc 4605/r= 4kpc/to ugc 2885/r= 122 kpc. *The Astrophysical Journal*, 238:471–487, 1980.

[26] Douglas Clowe, Marusa Bradac, Anthony H. Gonzalez, Maxim Markevitch, Scott W. Randall, Christine Jones, and Dennis Zaritsky. A direct empirical proof of the existence of dark matter. *Astrophys. J. Lett.*, 648:L109–L113, 2006.

[27] G. Hinshaw et al. Nine-Year Wilkinson Microwave Anisotropy Probe (WMAP) Observations: Cosmological Parameter Results. *Astrophys. J. Suppl.*, 208:19, 2013.

[28] N. Aghanim et al. Planck 2018 results. VI. Cosmological parameters. arXiv:1807.06209, 7 2018.

[29] E.W. Kolb and M.S. Turner. *The Early Universe.* Frontiers in physics. Addison-Wesley, 1990.

[30] J. Silk et al. *Particle Dark Matter: Observations, Models and Searches.* Cambridge Univ. Press, Cambridge, 2010.

[31] Edward W. Kolb and Michael S. Turner. *The Early Universe*, volume 69. 1990.

[32] Gerard Jungman, Marc Kamionkowski, and Kim Griest. Supersymmetric dark matter. *Phys. Rept.*, 267:195–373, 1996.

[33] G. Belanger, F. Boudjema, A. Pukhov, and A. Semenov. MicrOMEGAs: A Program for calculating the relic density in the MSSM. *Comput. Phys. Commun.*, 149:103–120, 2002.

[34] Geneviève Bélanger, Fawzi Boudjema, Andreas Goudelis, Alexander Pukhov, and Bryan Zaldivar. micrOMEGAs5.0 : Freeze-in. *Comput. Phys. Commun.*, 231:173–186, 2018.

[35] Mihailo Backović, Kyoungchul Kong, and Mathew McCaskey. Maddm v.1.0: Computation of dark matter relic abundance using madgraph 5. *Physics of the Dark Universe*, 5-6:18–28, Dec 2014.

[36] Federico Ambrogi, Chiara Arina, Mihailo Backovic, Jan Heisig, Fabio Maltoni, Luca Mantani, Olivier Mattelaer, and Gopolang Mohlabeng. MadDM v.3.0: a Comprehensive Tool for Dark Matter Studies. *Phys. Dark Univ.*, 24:100249, 2019.

[37] P Gondolo, J Edsjö, P Ullio, L Bergström, M Schelke, and E A Baltz. Darksusy: computing supersymmetric dark matter properties numerically. *Journal of Cosmology and Astroparticle Physics*, 2004(07):008–008, Jul 2004.

[38] Torsten Bringmann, Joakim Edsjö, Paolo Gondolo, Piero Ullio, and Lars Bergström. DarkSUSY 6 : An Advanced Tool to Compute Dark Matter Properties Numerically. *JCAP*, 07:033, 2018.

[39] Lawrence J. Hall, Karsten Jedamzik, John March-Russell, and Stephen M. West. Freeze-In Production of FIMP Dark Matter. *JHEP*, 03:080, 2010.

[40] Leonard Parker. Quantized fields and particle creation in expanding universes. 1. *Phys. Rev.*, 183:1057–1068, 1969.

[41] N.D. Birrell and P.C.W. Davies. *Quantum Fields in Curved Space*. Cambridge Monographs on Mathematical Physics. Cambridge Univ. Press, Cambridge, UK, 2 1984.

[42] L.H. Ford. Gravitational Particle Creation and Inflation. *Phys. Rev. D*, 35:2955, 1987.

[43] Daniel J.H. Chung, Edward W. Kolb, and Antonio Riotto. Superheavy dark matter. *Phys. Rev. D*, 59:023501, 1998.

[44] Daniel J.H. Chung, Patrick Crotty, Edward W. Kolb, and Antonio Riotto. On the Gravitational Production of Superheavy Dark Matter. *Phys. Rev. D*, 64:043503, 2001.

[45] Yohei Ema, Ryusuke Jinno, Kyohei Mukaida, and Kazunori Nakayama. Gravitational Effects on Inflaton Decay. *JCAP*, 05:038, 2015.

[46] Yohei Ema, Ryusuke Jinno, Kyohei Mukaida, and Kazunori Nakayama. Gravitational particle production in oscillating backgrounds and its cosmological implications. *Phys. Rev. D*, 94(6):063517, 2016.

[47] Yohei Ema, Kazunori Nakayama, and Yong Tang. Production of Purely Gravitational Dark Matter. *JHEP*, 09:135, 2018.

[48] Daniel J.H. Chung, Edward W. Kolb, Antonio Riotto, and Leonardo Senatore. Isocurvature constraints on gravitationally produced superheavy dark matter. *Phys. Rev. D*, 72:023511, 2005.

[49] Daniel J.H. Chung and Hojin Yoo. Isocurvature Perturbations and Non-Gaussianity of Gravitationally Produced Nonthermal Dark Matter. *Phys. Rev. D*, 87:023516, 2013.

[50] Teresa Marrodán Undagoitia and Ludwig Rauch. Dark matter direct-detection experiments. *J. Phys. G*, 43(1):013001, 2016.

[51] E. Aprile et al. Dark Matter Search Results from a One Ton-Year Exposure of XENON1T. *Phys. Rev. Lett.*, 121(11):111302, 2018.

[52] E. Aprile et al. Observation of Excess Electronic Recoil Events in XENON1T, 6 2020. arXiv:2006.09721.

[53] Lisa Goodenough and Dan Hooper. Possible Evidence For Dark Matter Annihilation In The Inner Milky Way From The Fermi Gamma Ray Space Telescope. 10 2009.

[54] M. Ackermann et al. Searching for Dark Matter Annihilation from Milky Way Dwarf Spheroidal Galaxies with Six Years of Fermi Large Area Telescope Data. *Phys. Rev. Lett.*, 115(23):231301, 2015.

[55] Judd D. Bowman, Alan E. E. Rogers, Raul A. Monsalve, Thomas J. Mozdzen, and Nivedita Mahesh. An absorption profile centred at 78 megahertz in the sky-averaged spectrum. *Nature*, 555(7694):67–70, 2018.

[56] Adrian Signer. ABC of SUSY. *J. Phys. G*, 36:073002, 2009.

[57] H. Baer and X. Tata. *Weak scale supersymmetry: From superfields to scattering events.* Cambridge University Press, 5 2006.

[58] Ulrich Ellwanger, Cyril Hugonie, and Ana M. Teixeira. The Next-to-Minimal Supersymmetric Standard Model. *Phys. Rept.*, 496:1–77, 2010.

[59] Nima Arkani-Hamed, Lawrence J. Hall, Hitoshi Murayama, David Tucker-Smith, and Neal Weiner. Small neutrino masses from supersymmetry breaking. *Phys. Rev. D*, 64:115011, 2001.

[60] Francesca Borzumati and Yasunori Nomura. Low scale seesaw mechanisms for light neutrinos. *Phys. Rev. D*, 64:053005, 2001.

[61] JoAnne L. Hewett and Thomas G. Rizzo. Low-Energy Phenomenology of Superstring Inspired E(6) Models. *Phys. Rept.*, 183:193, 1989.

[62] Paul Langacker and Jing Wang. U(1)-prime symmetry breaking in supersymmetric E(6) models. *Phys. Rev. D*, 58:115010, 1998.

[63] Pierre Fayet. Massive Gluinos. *Phys. Lett.*, 78B:417–420, 1978.

[64] Thomas Appelquist, Hsin-Chia Cheng, and Bogdan A. Dobrescu. Bounds on universal extra dimensions. *Phys. Rev. D*, 64:035002, 2001.

[65] Kyoungchul Kong and Konstantin T. Matchev. Phenomenology of universal extra dimensions. *AIP Conf. Proc.*, 903(1):451–454, 2007.

[66] Lisa Randall and Raman Sundrum. A Large mass hierarchy from a small extra dimension. *Phys. Rev. Lett.*, 83:3370–3373, 1999.

[67] Nima Arkani-Hamed, Savas Dimopoulos, and G.R. Dvali. The Hierarchy problem and new dimensions at a millimeter. *Phys. Lett. B*, 429:263–272, 1998.

[68] Hsin-Chia Cheng, Jonathan L. Feng, and Konstantin T. Matchev. Kaluza-Klein dark matter. *Phys. Rev. Lett.*, 89:211301, 2002.

[69] Geraldine Servant and Timothy M.P. Tait. Is the lightest Kaluza-Klein particle a viable dark matter candidate? *Nucl. Phys. B*, 650:391–419, 2003.

[70] R.D. Peccei. The Strong CP problem and axions. *Lect. Notes Phys.*, 741:3–17, 2008.

[71] Leanne D. Duffy and Karl van Bibber. Axions as Dark Matter Particles. *New J. Phys.*, 11:105008, 2009.

[72] G.C. Branco, P.M. Ferreira, L. Lavoura, M.N. Rebelo, Marc Sher, and Joao P. Silva. Theory and phenomenology of two-Higgs-doublet models. *Phys. Rept.*, 516:1–102, 2012.

[73] Nilendra G. Deshpande and Ernest Ma. Pattern of Symmetry Breaking with Two Higgs Doublets. *Phys. Rev.*, D18:2574, 1978.

[74] Ernest Ma. Verifiable radiative seesaw mechanism of neutrino mass and dark matter. *Phys. Rev. D*, 73:077301, 2006.

[75] F. González Canales, A. Mondragón, M. Mondragón, U. J. Saldaña Salazar, and L. Velasco-Sevilla. Quark sector of S3 models: classification and comparison with experimental data. *Phys. Rev. D*, 88:096004, 2013.

[76] C. Espinoza, E.A. Garcés, M. Mondragón, and H. Reyes-González. The $S3$ Symmetric Model with a Dark Scalar. *Phys. Lett. B*, 788:185–191, 2019.

[77] Yuri L. Dokshitzer. Calculation of the Structure Functions for Deep Inelastic Scattering and e+ e- Annihilation by Perturbation Theory in Quantum Chromodynamics. *Sov. Phys. JETP*, 46:641–653, 1977.

[78] V.N. Gribov and L.N. Lipatov. Deep inelastic e p scattering in perturbation theory. *Sov. J. Nucl. Phys.*, 15:438–450, 1972.

[79] Guido Altarelli and G. Parisi. Asymptotic Freedom in Parton Language. *Nucl. Phys. B*, 126:298–318, 1977.

[80] Tilman Plehn. Lectures on LHC Physics. https://doi.org/10.1007/978-3-319-05942-6, 2015.

[81] Tao Han. Collider phenomenology: Basic knowledge and techniques. In *Theoretical Advanced Study Institute in Elementary Particle Physics: Physics in $D \geqq 4$*, pages 407–454, 8 2005.

[82] Tim M.P. Tait and Lian-Tao Wang. Introductory Lectures on Collider Physics. In *Theoretical Advanced Study Institute in Elementary Particle Physics: The Dark Secrets of the Terascale*, pages 375–411, 2013.

[83] Tao Han, editor. *Proceedings of Theoretical Advanced Study Institute in Elementary Particle Physics on The dawn of the LHC era (TASI 2008): Boulder, USA, June 2-27, 2008*, Hackensack, USA, 11 2010. World Scientific.

[84] Nima Arkani-Hamed, Philip Schuster, Natalia Toro, Jesse Thaler, Lian-Tao Wang, Bruce Knuteson, and Stephen Mrenna. Marmoset: The path from lhc data to the new standard model via on-shell effective theories. http://dx.doi.org/10.2172/902546, Mar 2007.

[85] Johan Alwall, Philip Schuster, and Natalia Toro. Simplified Models for a First Characterization of New Physics at the LHC. *Phys. Rev. D*, 79:075020, 2009.

[86] Waleed Abdallah et al. Reinterpretation of LHC Results for New Physics: Status and Recommendations after Run 2. arXiv:2003.07868, 3 2020.

[87] David E. Morrissey, Tilman Plehn, and Tim M.P. Tait. Physics searches at the LHC. *Phys. Rept.*, 515:1–113, 2012.

[88] Thomas Junk. Confidence level computation for combining searches with small statistics. *Nucl. Instrum. Meth. A*, 434:435–443, 1999.

[89] R. Barbier et al. R-parity violating supersymmetry. *Phys. Rept.*, 420:1–202, 2005.

[90] D.E. Lopez-Fogliani and C. Munoz. Proposal for a Supersymmetric Standard Model. *Phys. Rev. Lett.*, 97:041801, 2006.

[91] Pradipta Ghosh, Inaki Lara, Daniel E. Lopez-Fogliani, Carlos Munoz, and Roberto Ruiz de Austri. Searching for left sneutrino LSP at the LHC. *Int. J. Mod. Phys. A*, 33(18n19):1850110, 2018.

[92] C.H. Chen, Manuel Drees, and J.F. Gunion. Searching for invisible and almost invisible particles at e+ e- colliders. *Phys. Rev. Lett.*, 76:2002–2005, 1996.

[93] Scott D. Thomas and James D. Wells. Phenomenology of Massive Vectorlike Doublet Leptons. *Phys. Rev. Lett.*, 81:34–37, 1998.

[94] Paul Langacker. The Physics of Heavy Z' Gauge Bosons. *Rev. Mod. Phys.*, 81:1199–1228, 2009.

[95] David Curtin et al. Long-Lived Particles at the Energy Frontier: The MATHUSLA Physics Case. *Rept. Prog. Phys.*, 82(11):116201, 2019.

[96] Morad Aaboud et al. Search for long-lived neutral particles in pp collisions at $\sqrt{s} = 13$ TeV that decay into displaced hadronic jets in the ATLAS calorimeter. *Eur. Phys. J. C*, 79(6):481, 2019.

[97] Georges Aad et al. Search for pair-produced long-lived neutral particles decaying in the ATLAS hadronic calorimeter in pp collisions at $\sqrt{s} = 8$ TeV. *Phys. Lett. B*, 743:15–34, 2015.

[98] Georges Aad et al. Search for long-lived, weakly interacting particles that decay to displaced hadronic jets in proton-proton collisions at $\sqrt{s} = 8$ TeV with the ATLAS detector. *Phys. Rev. D*, 92(1):012010, 2015.

[99] Morad Aaboud et al. Search for long-lived, massive particles in events with displaced vertices and missing transverse momentum in $\sqrt{s} = 13$ TeV pp collisions with the ATLAS detector. *Phys. Rev. D*, 97(5):052012, 2018.

[100] Georges Aad et al. Search for massive, long-lived particles using multitrack displaced vertices or displaced lepton pairs in pp collisions at $\sqrt{s} = 8$ TeV with the ATLAS detector. *Phys. Rev. D*, 92(7):072004, 2015.

[101] Albert M Sirunyan et al. Search for new long-lived particles at $\sqrt{s} = 13$ TeV. *Phys. Lett. B*, 780:432–454, 2018.

[102] Albert M Sirunyan et al. Search for long-lived particles decaying into displaced jets in proton-proton collisions at $\sqrt{s} = 13$ TeV. *Phys. Rev. D*, 99(3):032011, 2019.

[103] Vardan Khachatryan et al. Search for Long-Lived Neutral Particles Decaying to Quark-Antiquark Pairs in Proton-Proton Collisions at $\sqrt{s} = 8$ TeV. *Phys. Rev. D*, 91(1):012007, 2015.

[104] Vardan Khachatryan et al. Search for long-lived particles that decay into final states containing two electrons or two muons in proton-proton collisions at $\sqrt{s} = 8$ TeV. *Phys. Rev. D*, 91(5):052012, 2015.

[105] Search for long-lived particles that decay into final states containing two muons, reconstructed using only the CMS muon chambers. Technical Report CMS-PAS-EXO-14-012, CERN, Geneva, 2015.

[106] Search for displaced leptons in the e-mu channel. Technical Report CMS-PAS-EXO-16-022, CERN, Geneva, 2016.

[107] Morad Aaboud et al. Search for long-lived particles in final states with displaced dimuon vertices in pp collisions at $\sqrt{s} = 13$ TeV with the ATLAS detector. *Phys. Rev. D*, 99(1):012001, 2019.

[108] Juliette Alimena et al. Searching for Long-Lived Particles beyond the Standard Model at the Large Hadron Collider. arXiv:1903.04497, 3 2019.

[109] Search for heavy stable charged particles with 12.9 fb^{-1} of 2016 data. Technical Report CMS-PAS-EXO-16-036, CERN, Geneva, 2016.

[110] Serguei Chatrchyan et al. Searches for Long-Lived Charged Particles in pp Collisions at $\sqrt{s}$=7 and 8 TeV. *JHEP*, 07:122, 2013.

[111] Morad Aaboud et al. Search for heavy charged long-lived particles in the ATLAS detector in 36.1 fb^{-1} of proton-proton collision data at $\sqrt{s} = 13$ TeV. *Phys. Rev. D*, 99(9):092007, 2019.

[112] Morad Aaboud et al. Search for heavy charged long-lived particles in proton-proton collisions at $\sqrt{s} = 13$ TeV using an ionisation measurement with the ATLAS detector. *Phys. Lett. B*, 788:96–116, 2019.

[113] Georges Aad et al. Searches for heavy long-lived charged particles with the ATLAS detector in proton-proton collisions at $\sqrt{s} = 8$ TeV. *JHEP*, 01:068, 2015.

[114] Morad Aaboud et al. Search for long-lived charginos based on a disappearing-track signature in pp collisions at $\sqrt{s} = 13$ TeV with the ATLAS detector. *JHEP*, 06:022, 2018.

[115] Albert M Sirunyan et al. Search for disappearing tracks as a signature of new long-lived particles in proton-proton collisions at $\sqrt{s} = 13$ TeV. *JHEP*, 08:016, 2018.

[116] JoAnne L. Hewett, Ben Lillie, Manuel Masip, and Thomas G. Rizzo. Signatures of long-lived gluinos in split supersymmetry. *JHEP*, 09:070, 2004.

[117] W. Kilian, T. Plehn, P. Richardson, and E. Schmidt. Split supersymmetry at colliders. *Eur. Phys. J. C*, 39:229–243, 2005.

[118] Glennys R. Farrar and Pierre Fayet. Phenomenology of the Production, Decay, and Detection of New Hadronic States Associated with Supersymmetry. *Phys. Lett. B*, 76:575–579, 1978.

[119] Howard Baer, King-man Cheung, and John F. Gunion. A Heavy gluino as the lightest supersymmetric particle. *Phys. Rev. D*, 59:075002, 1999.

[120] Georgios Choudalakis. On hypothesis testing, trials factor, hypertests and the BumpHunter. In *PHYSTAT 2011*, 1 2011.

[121] Johan Alwall, My-Phuong Le, Mariangela Lisanti, and Jay G. Wacker. Searching for Directly Decaying Gluinos at the Tevatron. *Phys. Lett. B*, 666:34–37, 2008.

[122] Johan Alwall, My-Phuong Le, Mariangela Lisanti, and Jay G. Wacker. Model-Independent Jets plus Missing Energy Searches. *Phys. Rev. D*, 79:015005, 2009.

[123] Daniele Alves. Simplified Models for LHC New Physics Searches. *J. Phys. G*, 39:105005, 2012.

[124] Hideki Okawa. Interpretations of SUSY Searches in ATLAS with Simplified Models. In *Particles and fields. Proceedings, Meeting of the Division of the American Physical Society, DPF 2011, Providence, USA, August 9-13, 2011*, 10 2011.

[125] Serguei Chatrchyan et al. Interpretation of Searches for Supersymmetry with Simplified Models. *Phys. Rev. D*, 88(5):052017, 2013.

[126] Jalal Abdallah et al. Simplified Models for Dark Matter Searches at the LHC. *Phys. Dark Univ.*, 9-10:8–23, 2015.

[127] Albert M Sirunyan et al. Search for supersymmetry in multijet events with missing transverse momentum in proton-proton collisions at 13 TeV. *Phys. Rev.*, D96(3):032003, 2017.

[128] Sascha Caron, Jong Soo Kim, Krzysztof Rolbiecki, Roberto Ruiz de Austri, and Bob Stienen. The BSM-AI project: SUSY-AI generalizing LHC limits on supersymmetry with machine learning. *Eur. Phys. J.*, C77(4):257, 2017.

[129] Andy Buckley, Christoph Englert, James Ferrando, David J. Miller, Liam Moore, Michael Russell, and Chris D. White. Constraining top quark effective theory in the LHC Run II era. *JHEP*, 04:015, 2016.

[130] Jonathan M. Butterworth, David Grellscheid, Michael Krämer, Björn Sarrazin, and David Yallup. Constraining new physics with collider measurements of Standard Model signatures. *JHEP*, 03:078, 2017.

[131] Luc Darmé, Benjamin Fuks, and Mark Goodsell. Cornering sgluons with four-top-quark events. *Phys. Lett.*, B784:223–228, 2018.

[132] Morad Aaboud et al. Measurement of detector-corrected observables sensitive to the anomalous production of events with jets and large missing transverse momentum in *pp* collisions at $\sqrt{\mathbf{s}} = \mathbf{13}$ TeV using the ATLAS detector. *Eur. Phys. J. C*, 77(11):765, 2017.

[133] Federico Ambrogi, Sabine Kraml, Suchita Kulkarni, Ursula Laa, Andre Lessa, and Wolfgang Waltenberger. On the coverage of the pMSSM by simplified model results. *Eur. Phys. J. C*, 78(3):215, 2018.

[134] Sabine Kraml, Suchita Kulkarni, Ursula Laa, Andre Lessa, Wolfgang Magerl, Doris Proschofsky-Spindler, and Wolfgang Waltenberger. SModelS: a tool for interpreting simplified-model results from the LHC and its application to supersymmetry. *Eur. Phys. J.*, C74:2868, 2014.

[135] Federico Ambrogi, Juhi Dutta, Jan Heisig, Sabine Kraml, Suchita Kulkarni, Ursula Laa, Andre Lessa, Philipp Neuhuber, Humberto Reyes-González, Wolfgang Waltenberger, and et al. Smodels v1.2: Long-lived particles, combination of signal regions, and other novelties. *Computer Physics Communications*, 251:106848, Jun 2020.

[136] Philip Bechtle, Oliver Brein, Sven Heinemeyer, Georg Weiglein, and Karina E. Williams. HiggsBounds: Confronting Arbitrary Higgs Sectors with Exclusion Bounds from LEP and the Tevatron. *Comput. Phys. Commun.*, 181:138–167, 2010.

[137] Philip Bechtle, Oliver Brein, Sven Heinemeyer, Oscar Stål, Tim Stefaniak, Georg Weiglein, and Karina E. Williams. HiggsBounds – 4: Improved Tests of Extended Higgs Sectors against Exclusion Bounds from LEP, the Tevatron and the LHC. *Eur. Phys. J. C*, 74(3):2693, 2014.

[138] Felix Kahlhoefer, Alexander Mück, Stefan Schulte, and Patrick Tunney. Interference effects in dilepton resonance searches for Z' bosons and dark matter mediators. *JHEP*, 03:104, 2020.

[139] Philip Ilten, Yotam Soreq, Mike Williams, and Wei Xue. Serendipity in dark photon searches. *JHEP*, 06:004, 2018.

[140] J. Alwall, R. Frederix, S. Frixione, V. Hirschi, F. Maltoni, O. Mattelaer, H. S. Shao, T. Stelzer, P. Torrielli, and M. Zaro. The automated computation of tree-level and next-to-leading order differential cross sections, and their matching to parton shower simulations. *JHEP*, 07:079, 2014.

[141] R. Frederix, S. Frixione, V. Hirschi, D. Pagani, H.-S. Shao, and M. Zaro. The automation of next-to-leading order electroweak calculations. *JHEP*, 07:185, 2018.

[142] Andy Buckley, James Ferrando, Stephen Lloyd, Karl Nordström, Ben Page, Martin Rüfenacht, Marek Schönherr, and Graeme Watt. LHAPDF6: parton density access in the LHC precision era. *Eur. Phys. J.*, C75:132, 2015.

[143] Johan Alwall et al. A Standard format for Les Houches event files. *Comput. Phys. Commun.*, 176:300–304, 2007.

[144] Torbjorn Sjostrand, Stephen Mrenna, and Peter Z. Skands. PYTHIA 6.4 Physics and Manual. *JHEP*, 05:026, 2006.

[145] Torbjörn Sjöstrand, Stefan Ask, Jesper R. Christiansen, Richard Corke, Nishita Desai, Philip Ilten, Stephen Mrenna, Stefan Prestel, Christine O. Rasmussen, and Peter Z. Skands. An Introduction to PYTHIA 8.2. *Comput. Phys. Commun.*, 191:159–177, 2015.

[146] M. Bahr et al. Herwig++ Physics and Manual. *Eur. Phys. J. C*, 58:639–707, 2008.

[147] T. Gleisberg, Stefan. Hoeche, F. Krauss, M. Schonherr, S. Schumann, F. Siegert, and J. Winter. Event generation with SHERPA 1.1. *JHEP*, 02:007, 2009.

[148] Enrico Bothmann et al. Event Generation with Sherpa 2.2. *SciPost Phys.*, 7(3):034, 2019.

[149] Matt Dobbs and Jorgen Beck Hansen. The HepMC C++ Monte Carlo event record for High Energy Physics. *Comput. Phys. Commun.*, 134:41–46, 2001.

[150] J. de Favereau, C. Delaere, P. Demin, A. Giammanco, V. Lemaître, A. Mertens, and M. Selvaggi. DELPHES 3, A modular framework for fast simulation of a generic collider experiment. *JHEP*, 02:057, 2014.

[151] Christian Bierlich et al. Robust Independent Validation of Experiment and Theory: Rivet version 3. *SciPost Phys.*, 8:026, 2020.

[152] Andy Buckley, Deepak Kar, and Karl Nordström. Fast simulation of detector effects in Rivet. *SciPost Phys.*, 8:025, 2020.

[153] Manuel Drees, Herbi Dreiner, Daniel Schmeier, Jamie Tattersall, and Jong Soo Kim. CheckMATE: Confronting your Favourite New Physics Model with LHC Data. *Comput. Phys. Commun.*, 187:227–265, 2015.

[154] Daniel Dercks, Nishita Desai, Jong Soo Kim, Krzysztof Rolbiecki, Jamie Tattersall, and Torsten Weber. CheckMATE 2: From the model to the limit. *Comput. Phys. Commun.*, 221:383–418, 2017.

[155] Jong Soo Kim, Daniel Schmeier, Jamie Tattersall, and Krzysztof Rolbiecki. A framework to create customised LHC analyses within CheckMATE. *Comput. Phys. Commun.*, 196:535–562, 2015.

[156] Eric Conte, Benjamin Fuks, and Guillaume Serret. MadAnalysis 5, A User-Friendly Framework for Collider Phenomenology. *Comput. Phys. Commun.*, 184:222–256, 2013.

[157] Eric Conte and Benjamin Fuks. Confronting new physics theories to LHC data with MADANALYSIS 5. *Int. J. Mod. Phys.*, A33(28):1830027, 2018.

[158] B. Dumont, B. Fuks, S. Kraml, S. Bein, G. Chalons, E. Conte, S. Kulkarni, D. Sengupta, and C. Wymant. Toward a public analysis database for LHC new physics searches using MADANALYSIS 5. *Eur. Phys. J.*, C75(2):56, 2015.

[159] Jack Y. Araz, Benjamin Fuks, and Georgios Polykratis. Simplified fast detector simulation in MadAnalysis 5. 6 2020.

[160] Csaba Balázs et al. ColliderBit: a GAMBIT module for the calculation of high-energy collider observables and likelihoods. *Eur. Phys. J. C*, 77(11):795, 2017.

[161] Peter Athron et al. GAMBIT: The Global and Modular Beyond-the-Standard-Model Inference Tool. *Eur. Phys. J. C*, 77(11):784, 2017. [Addendum: Eur.Phys.J.C 78, 98 (2018)].

[162] Andy Buckley, Jonathan Butterworth, Leif Lonnblad, David Grellscheid, Hendrik Hoeth, James Monk, Holger Schulz, and Frank Siegert. Rivet user manual. *Comput. Phys. Commun.*, 184:2803–2819, 2013.

[163] G. Brooijmans et al. Les Houches 2017: Physics at TeV Colliders New Physics Working Group Report. In *10th Les Houches Workshop on Physics at TeV Colliders*, 3 2018.

[164] Sezen Sekmen and Gokhan Ünel. CutLang: A Particle Physics Analysis Description Language and Runtime Interpreter. *Comput. Phys. Commun.*, 233:215–236, 2018.

[165] Gokhan Unel, Sezen Sekmen, and Anna Monica Toon. CutLang: a cut-based HEP analysis description language and runtime interpreter. In *19th International Workshop on Advanced Computing and Analysis Techniques in Physics Research: Empowering the revolution: Bringing Machine Learning to High Performance Computing*, 9 2019.

[166] G. Brooijmans et al. Les Houches 2015: Physics at TeV colliders - new physics working group report. In *9th Les Houches Workshop on Physics at TeV Colliders*, 5 2016.

[167] Sezen Sekmen, Gokhan Unel, and Harrison Prosper. ADL4HEP/ADLLHCanalyses: LHC analyses with ADL. `https://github.com/ADL4HEP/ADLLHCanalyses`, March 2020. DOI: 10.5281/zenodo.3708262 (v1.0.0).

[168] Yanou Cui and Brian Shuve. Probing Baryogenesis with Displaced Vertices at the LHC. *JHEP*, 02:049, 2015.

[169] Search for long-lived neutral particles decaying to dijets. Technical Report CMS-PAS-EXO-12-038, CERN, Geneva, 2013.

[170] Benjamin Fuks, editor. *Proceedings of the first MadAnalysis 5 workshop on LHC recasting in Korea*, 6 2018.

[171] Federico Ambrogi, Sabine Kraml, Suchita Kulkarni, Ursula Laa, Andre Lessa, Veronika Magerl, Jory Sonneveld, Michael Traub, and Wolfgang Waltenberger. SModelS v1.1 user manual: Improving simplified model constraints with efficiency maps. *Comput. Phys. Commun.*, 227:72–98, 2018.

[172] Charanjit K. Khosa, Sabine Kraml, Andre Lessa, Philipp Neuhuber, and Wolfgang Waltenberger. SModelS database update v1.2.3. arXiv:2005.00555, 5 2020.

[173] The CMS Collaboration. Simplified likelihood for the re-interpretation of public CMS results. Technical Report CMS-NOTE-2017-001. CERN-CMS-NOTE-2017-001, CERN, Geneva, Jan 2017.

[174] Andy Buckley, Matthew Citron, Sylvain Fichet, Sabine Kraml, Wolfgang Waltenberger, and Nicholas Wardle. The Simplified Likelihood Framework. *JHEP*, 04:064, 2019.

[175] Alexander L. Read. Presentation of search results: The CL(s) technique. *J. Phys.*, G28:2693–2704, 2002. [,11(2002)].

[176] Glen Cowan, Kyle Cranmer, Eilam Gross, and Ofer Vitells. Asymptotic formulae for likelihood-based tests of new physics. *Eur. Phys. J. C*, 71:1554, 2011. [Erratum: Eur.Phys.J.C 73, 2501 (2013)].

[177] https://docs.scipy.org/doc/scipy/reference/generated/scipy.optimize.brentq.html.

[178] https://smodels.readthedocs.io/en/stable/index.html.

[179] Albert M Sirunyan et al. Search for supersymmetry in proton-proton collisions at 13 TeV using identified top quarks. *Phys. Rev. D*, 97(1):012007, 2018.

[180] Search for supersymmetry in events with at least one soft lepton, low jet multiplicity, and missing transverse momentum in proton-proton collisions at $\sqrt{s} = 13$ TeV. Technical Report CMS-PAS-SUS-16-052, CERN, Geneva, 2017.

[181] Jan Heisig, Andre Lessa, and Loic Quertenmont. Simplified Models for Exotic BSM Searches. *JHEP*, 12:087, 2015.

[182] Jan Heisig, Sabine Kraml, and Andre Lessa. Constraining new physics with searches for long-lived particles: Implementation into SModelS. *Phys. Lett.*, B788:87–95, 2019.

[183] Vardan Khachatryan et al. Constraints on the pMSSM, AMSB model and on other models from the search for long-lived charged particles in proton-proton collisions at sqrt(s) = 8 TeV. *Eur. Phys. J. C*, 75(7):325, 2015.

[184] Guillaume Chalons, Mark D. Goodsell, Sabine Kraml, Humberto Reyes-González, and Sophie L. Williamson. LHC limits on gluinos and squarks in the minimal Dirac gaugino model. *JHEP*, 04:113, 2019.

[185] Mark D. Goodsell, Sabine Kraml, Humberto Reyes-González, and Sophie L. Williamson. Constraining Electroweakinos in the Minimal Dirac Gaugino Model. arXiv:2007.08498, 7 2020.

[186] Patrick J. Fox, Ann E. Nelson, and Neal Weiner. Dirac gaugino masses and supersoft supersymmetry breaking. *JHEP*, 08:035, 2002.

[187] Stephen P. Martin. Nonstandard Supersymmetry Breaking and Dirac Gaugino Masses without Supersoftness. *Phys. Rev.*, D92(3):035004, 2015.

[188] I. Jack and D. R. T. Jones. Quasiinfrared fixed points and renormalization group invariant trajectories for nonholomorphic soft supersymmetry breaking. *Phys. Rev.*, D61:095002, 2000.

[189] Mark D. Goodsell. Two-loop RGEs with Dirac gaugino masses. *JHEP*, 01:066, 2013.

[190] Daniele S. M. Alves, Jamison Galloway, Matthew McCullough, and Neal Weiner. Goldstone Gauginos. *Phys. Rev. Lett.*, 115(16):161801, 2015.

[191] Daniele S. M. Alves, Jamison Galloway, Matthew McCullough, and Neal Weiner. Models of Goldstone Gauginos. *Phys. Rev.*, D93(7):075021, 2016.

[192] Asimina Arvanitaki, Masha Baryakhtar, Xinlu Huang, Ken van Tilburg, and Giovanni Villadoro. The Last Vestiges of Naturalness. *JHEP*, 03:022, 2014.

[193] I. Antoniadis, K. Benakli, A. Delgado, and M. Quiros. A New gauge mediation theory. *Adv. Stud. Theor. Phys.*, 2:645–672, 2008.

[194] John Ellis, Jérémie Quevillon, and Verónica Sanz. Doubling Up on Supersymmetry in the Higgs Sector. *JHEP*, 10:086, 2016.

[195] Karim Benakli, Mark D. Goodsell, and Sophie L. Williamson. Higgs alignment from extended supersymmetry. *Eur. Phys. J.*, C78(8):658, 2018.

[196] Karim Benakli, Yifan Chen, and Gaëtan Lafforgue-Marmet. R-symmetry for higgs alignment without decoupling. *The European Physical Journal C*, 79(2), Feb 2019.

[197] Graham D. Kribs, Erich Poppitz, and Neal Weiner. Flavor in supersymmetry with an extended R-symmetry. *Phys. Rev.*, D78:055010, 2008.

[198] Ricky Fok and Graham D. Kribs. μ to e in R-symmetric Supersymmetry. *Phys. Rev.*, D82:035010, 2010.

[199] Emilian Dudas, Mark Goodsell, Lucien Heurtier, and Pantelis Tziveloglou. Flavour models with Dirac and fake gluinos. *Nucl. Phys.*, B884:632–671, 2014.

[200] Matti Heikinheimo, Moshe Kellerstein, and Veronica Sanz. How Many Supersymmetries? *JHEP*, 04:043, 2012.

[201] Graham D. Kribs and Adam Martin. Supersoft Supersymmetry is Super-Safe. *Phys. Rev.*, D85:115014, 2012.

[202] Graham D. Kribs and Adam Martin. Dirac Gauginos in Supersymmetry – Suppressed Jets + MET Signals: A Snowmass Whitepaper. arXiv:1308.3468, 2013.

[203] Giovanni Grilli di Cortona, Edward Hardy, and Andrew J. Powell. Dirac vs Majorana gauginos at a 100 TeV collider. *JHEP*, 08:014, 2016.

[204] Joseph Polchinski and Leonard Susskind. Breaking of Supersymmetry at Intermediate-Energy. *Phys. Rev.*, D26:3661, 1982.

[205] L. J. Hall and Lisa Randall. U(1)-R symmetric supersymmetry. *Nucl. Phys.*, B352:289–308, 1991.

[206] Ann E. Nelson, Nuria Rius, Veronica Sanz, and Mithat Unsal. The Minimal supersymmetric model without a mu term. *JHEP*, 08:039, 2002.

[207] Santiago De Lope Amigo, Andrew E. Blechman, Patrick J. Fox, and Erich Poppitz. R-symmetric gauge mediation. *JHEP*, 01:018, 2009.

[208] K. Benakli and M. D. Goodsell. Dirac Gauginos in General Gauge Mediation. *Nucl. Phys.*, B816:185–203, 2009.

[209] K. Benakli and M. D. Goodsell. Dirac Gauginos and Kinetic Mixing. *Nucl. Phys.*, B830:315–329, 2010.

[210] K. Benakli and M. D. Goodsell. Dirac Gauginos, Gauge Mediation and Unification. *Nucl. Phys.*, B840:1–28, 2010.

[211] Linda M. Carpenter. Dirac Gauginos, Negative Supertraces and Gauge Mediation. *JHEP*, 09:102, 2012.

[212] Graham D. Kribs, Takemichi Okui, and Tuhin S. Roy. Viable Gravity-Mediated Supersymmetry Breaking. *Phys. Rev.*, D82:115010, 2010.

[213] Steven Abel and Mark Goodsell. Easy Dirac Gauginos. *JHEP*, 06:064, 2011.

[214] Rhys Davies, John March-Russell, and Matthew McCullough. A Supersymmetric One Higgs Doublet Model. *JHEP*, 04:108, 2011.

[215] Karim Benakli, Mark D. Goodsell, and Ann-Kathrin Maier. Generating mu and Bmu in models with Dirac Gauginos. *Nucl. Phys.*, B851:445–461, 2011.

[216] Jan Kalinowski. Phenomenology of R-symmetric supersymmetry. *Acta Phys. Polon.*, B42:2425–2432, 2011.

[217] Claudia Frugiuele and Thomas Gregoire. Making the Sneutrino a Higgs with a $U(1)_R$ Lepton Number. *Phys. Rev.*, D85:015016, 2012.

[218] Enrico Bertuzzo and Claudia Frugiuele. Fitting Neutrino Physics with a $\mathrm{U}(1)_R$ Lepton Number. *JHEP*, 05:100, 2012.

[219] Rhys Davies. Dirac gauginos and unification in F-theory. *JHEP*, 10:010, 2012.

[220] Riccardo Argurio, Matteo Bertolini, Lorenzo Di Pietro, Flavio Porri, and Diego Redigolo. Holographic Correlators for General Gauge Mediation. *JHEP*, 08:086, 2012.

[221] Riccardo Argurio, Matteo Bertolini, Lorenzo Di Pietro, Flavio Porri, and Diego Redigolo. Exploring Holographic General Gauge Mediation. *JHEP*, 10:179, 2012.

[222] Claudia Frugiuele, Thomas Gregoire, Piyush Kumar, and Eduardo Ponton. 'L=R' - $U(1)_R$ as the Origin of Leptonic 'RPV'. *JHEP*, 03:156, 2013.

[223] Claudia Frugiuele, Thomas Gregoire, Piyush Kumar, and Eduardo Ponton. 'L=R' – $U(1)_R$ Lepton Number at the LHC. *JHEP*, 05:012, 2013.

[224] Karim Benakli, Mark D. Goodsell, and Florian Staub. Dirac Gauginos and the 125 GeV Higgs. *JHEP*, 06:073, 2013.

[225] H. Itoyama and Nobuhito Maru. D-term Triggered Dynamical Supersymmetry Breaking. *Phys. Rev.*, D88(2):025012, 2013.

[226] Sabyasachi Chakraborty and Sourov Roy. Higgs boson mass, neutrino masses and mixing and keV dark matter in an $U(1)_R-$ lepton number model. *JHEP*, 01:101, 2014.

[227] Csaba Csaki, Jessica Goodman, Riccardo Pavesi, and Yuri Shirman. The $m_D - b_M$ problem of Dirac gauginos and its solutions. *Phys. Rev.*, D89(5):055005, 2014.

[228] H. Itoyama and Nobuhito Maru. 126 GeV Higgs Boson Associated with D-term Triggered Dynamical Supersymmetry Breaking. *Symmetry*, 7(1):193–205, 2015.

[229] Hugues Beauchesne and Thomas Gregoire. Electroweak precision measurements in supersymmetric models with a U$(1)_R$ lepton number. *JHEP*, 05:051, 2014.

[230] Enrico Bertuzzo, Claudia Frugiuele, Thomas Gregoire, and Eduardo Ponton. Dirac gauginos, R symmetry and the 125 GeV Higgs. *JHEP*, 04:089, 2015.

[231] Mark D. Goodsell and Pantelis Tziveloglou. Dirac Gauginos in Low Scale Supersymmetry Breaking. *Nucl. Phys.*, B889:650–675, 2014.

[232] Daniel Busbridge. Constrained Dirac gluino mediation. arXiv:1408.4605, 2014.

[233] Sabyasachi Chakraborty, AseshKrishna Datta, and Sourov Roy. $h \to \gamma\gamma$ in U$(1)_R$ - lepton number model with a right-handed neutrino. *JHEP*, 02:124, 2015. [Erratum: JHEP09,077(2015)].

[234] Philip Dießner, Jan Kalinowski, Wojciech Kotlarski, and Dominik Stöckinger. Higgs boson mass and electroweak observables in the MRSSM. *JHEP*, 12:124, 2014.

[235] Ran Ding, Tianjun Li, Florian Staub, Chi Tian, and Bin Zhu. Supersymmetric standard models with a pseudo-Dirac gluino from hybrid F - and D -term supersymmetry breaking. *Phys. Rev.*, D92(1):015008, 2015.

[236] Linda M. Carpenter and Jessica Goodman. New Calculations in Dirac Gaugino Models: Operators, Expansions, and Effects. *JHEP*, 07:107, 2015.

[237] Philip Diessner, Jan Kalinowski, Wojciech Kotlarski, and Dominik Stöckinger. Two-loop correction to the Higgs boson mass in the MRSSM. *Adv. High Energy Phys.*, 2015:760729, 2015.

[238] Philip Diessner, Jan Kalinowski, Wojciech Kotlarski, and Dominik Stöckinger. Exploring the Higgs sector of the MRSSM with a light scalar. *JHEP*, 03:007, 2016.

[239] Philip Diessner, Wojciech Kotlarski, Sebastian Liebschner, and Dominik Stöckinger. Squark production in R-symmetric SUSY with Dirac gluinos: NLO corrections. *JHEP*, 10:142, 2017.

[240] G. Belanger, K. Benakli, M. Goodsell, C. Moura, and A. Pukhov. Dark Matter with Dirac and Majorana Gaugino Masses. *JCAP*, 0908:027, 2009.

[241] K. Benakli, M. Goodsell, F. Staub, and W. Porod. Constrained minimal Dirac gaugino supersymmetric standard model. *Phys. Rev.*, D90(4):045017, 2014.

[242] Mark D. Goodsell, Manuel E. Krauss, Tobias Müller, Werner Porod, and Florian Staub. Dark matter scenarios in a constrained model with Dirac gauginos. *JHEP*, 10:132, 2015.

[243] Karim Benakli, Luc Darmé, Mark D. Goodsell, and Julia Harz. The Di-Photon Excess in a Perturbative SUSY Model. *Nucl. Phys.*, B911:127–162, 2016.

[244] Philip Diessner. *Phenomenological Study of the Minimal R-symmetric Supersymmetric Standard Sodel.* PhD thesis, Dresden, Tech. U., 2016.

[245] Carlos Alvarado, Antonio Delgado, and Adam Martin. Constraining the R-symmetric chargino NLSP at the LHC. *Phys. Rev.*, D97(11):115044, 2018.

[246] Tilman Plehn and Tim M. P. Tait. Seeking Sgluons. *J. Phys.*, G36:075001, 2009.

[247] S. Y. Choi, M. Drees, J. Kalinowski, J. M. Kim, E. Popenda, and P. M. Zerwas. Color-Octet Scalars of N=2 Supersymmetry at the LHC. *Phys. Lett.*, B672:246–252, 2009.

[248] S. Y. Choi, J. Kalinowski, J. M. Kim, and E. Popenda. Scalar gluons and Dirac gluinos at the LHC. *Acta Phys. Polon.*, B40:2913–2922, 2009.

[249] S. Y. Choi, D. Choudhury, A. Freitas, J. Kalinowski, J. M. Kim, and P. M. Zerwas. Dirac Neutralinos and Electroweak Scalar Bosons of N=1/N=2 Hybrid Supersymmetry at Colliders. *JHEP*, 08:025, 2010.

[250] Dorival Goncalves-Netto, David Lopez-Val, Kentarou Mawatari, Tilman Plehn, and Ioan Wigmore. Sgluon Pair Production to Next-to-Leading Order. *Phys. Rev.*, D85:114024, 2012.

[251] Chien-Yi Chen, Ayres Freitas, Tao Han, and Keith S. M. Lee. Heavy Color-Octet Particles at the LHC. *JHEP*, 05:135, 2015.

[252] Lana Beck, Freya Blekman, Didar Dobur, Benjamin Fuks, James Keaveney, and Kentarou Mawatari. Probing top-philic sgluons with LHC Run I data. *Phys. Lett.*, B746:48–52, 2015.

[253] Wojciech Kotlarski. Sgluons in the same-sign lepton searches. *JHEP*, 02:027, 2017.

[254] Wojciech Kotlarski. Scalar color octets and triplets in the SUSY with R-symmetry. *J. Phys. Conf. Ser.*, 873(1):012043, 2017.

[255] C. Patrignani et al. Review of Particle Physics. *Chin. Phys.*, C40(10):100001, 2016.

[256] S. Y. Choi, M. Drees, A. Freitas, and P. M. Zerwas. Testing the Majorana Nature of Gluinos and Neutralinos. *Phys. Rev.*, D78:095007, 2008.

[257] Florian Staub. SARAH 3.2: Dirac Gauginos, UFO output, and more. *Comput. Phys. Commun.*, 184:1792–1809, 2013.

[258] Florian Staub. From Superpotential to Model Files for FeynArts and CalcHep/CompHep. *Comput.Phys.Commun.*, 181:1077–1086, 2010.

[259] Florian Staub. Automatic Calculation of supersymmetric Renormalization Group Equations and Self Energies. *Comput.Phys.Commun.*, 182:808–833, 2011.

[260] Florian Staub. SARAH 4 : A tool for (not only SUSY) model builders. *Comput. Phys. Commun.*, 185:1773–1790, 2014.

[261] Mark D. Goodsell, Stefan Liebler, and Florian Staub. Generic calculation of two-body partial decay widths at the full one-loop level. *Eur. Phys. J.*, C77(11):758, 2017.

[262] W. Porod and F. Staub. SPheno 3.1: Extensions including flavour, CP-phases and models beyond the MSSM. *Comput. Phys. Commun.*, 183:2458–2469, 2012.

[263] Mark D. Goodsell, Kilian Nickel, and Florian Staub. Two-Loop Higgs mass calculations in supersymmetric models beyond the MSSM with SARAH and SPheno. *Eur. Phys. J.*, C75(1):32, 2015.

[264] M. Goodsell, K. Nickel, and F. Staub. Generic two-loop Higgs mass calculation from a diagrammatic approach. *Eur. Phys. J.*, C75(6):290, 2015.

[265] Johannes Braathen, Mark D. Goodsell, and Florian Staub. Supersymmetric and non-supersymmetric models without catastrophic Goldstone bosons. *Eur. Phys. J.*, C77(11):757, 2017.

[266] Zenodo dataset, `https://zenodo.org/record/2422747`.

[267] Guillaume Chalons and Humberto Reyes-Gonzalez. MadAnalysis 5 implementation of ATLAS-SUSY-16-07 (arXiv:1712.02332), 2018. `http://doi.org/10.7484/INSPIREHEP.DATA.56DC.PPE2`.

[268] Morad Aaboud et al. Search for squarks and gluinos in final states with jets and missing transverse momentum using 36/fb of sqrt(s)=13 TeV pp collision data with the ATLAS detector. *Phys. Rev.*, D97(11):112001, 2018.

[269] W. Beenakker, R. Hopker, M. Spira, and P. M. Zerwas. Squark and gluino production at hadron colliders. *Nucl. Phys.*, B492:51–103, 1997.

[270] `https://www.uni-muenster.de/Physik.TP/~akule_01/nnllfast/doku.php`.

[271] H. Goldberg. Constraint on the Photino Mass from Cosmology. *Phys. Rev. Lett.*, 50:1419, 1983. [Erratum: Phys.Rev.Lett. 103, 099905 (2009)].

[272] John R. Ellis, J.S. Hagelin, Dimitri V. Nanopoulos, Keith A. Olive, and M. Srednicki. Supersymmetric Relics from the Big Bang. *Nucl. Phys. B*, 238:453–476, 1984.

[273] N. Arkani-Hamed, A. Delgado, and G.F. Giudice. The Well-tempered neutralino. *Nucl. Phys. B*, 741:108–130, 2006.

[274] Clifford Cheung, Lawrence J. Hall, David Pinner, and Joshua T. Ruderman. Prospects and Blind Spots for Neutralino Dark Matter. *JHEP*, 05:100, 2013.

[275] Andreas Birkedal-Hansen and Brent D. Nelson. The Role of Wino content in neutralino dark matter. *Phys. Rev. D*, 64:015008, 2001.

[276] Andreas Birkedal-Hansen and Brent D. Nelson. Relic neutralino densities and detection rates with nonuniversal gaugino masses. *Phys. Rev. D*, 67:095006, 2003.

[277] Howard Baer, Azar Mustafayev, Eun-Kyung Park, and Stefano Profumo. Mixed wino dark matter: Consequences for direct, indirect and collider detection. *JHEP*, 07:046, 2005.

[278] Howard Baer, Tadas Krupovnickas, Azar Mustafayev, Eun-Kyung Park, Stefano Profumo, and Xerxes Tata. Exploring the BWCA (bino-wino co-annihilation) scenario for neutralino dark matter. *JHEP*, 12:011, 2005.

[279] Natsumi Nagata, Hidetoshi Otono, and Satoshi Shirai. Probing Bino-Wino Coannihilation at the LHC. *JHEP*, 10:086, 2015.

[280] Joseph Bramante, Nishita Desai, Patrick Fox, Adam Martin, Bryan Ostdiek, and Tilman Plehn. Towards the Final Word on Neutralino Dark Matter. *Phys. Rev.*, D93(6):063525, 2016.

[281] Guang Hua Duan, Ken-Ichi Hikasa, Jie Ren, Lei Wu, and Jin Min Yang. Probing bino-wino coannihilation dark matter below the neutrino floor at the LHC. *Phys. Rev. D*, 98(1):015010, 2018.

[282] Ken Hsieh. Pseudo-Dirac bino dark matter. *Phys. Rev. D*, 77:015004, 2008.

[283] Werner Porod. SPheno, a program for calculating supersymmetric spectra, SUSY particle decays and SUSY particle production at e+ e- colliders. *Comput. Phys. Commun.*, 153:275–315, 2003.

[284] Guillaume Chalons, Mark D. Goodsell, Sabine Kraml, Humberto Reyes-Gonzalez, and Sophie L. Williamson. Dirac gaugino benchmark points from arXiv:1812.09293, December 2018.

[285] D. Barducci, G. Belanger, J. Bernon, F. Boudjema, J. Da Silva, S. Kraml, U. Laa, and A. Pukhov. Collider limits on new physics within micrOMEGAs_4.3. *Comput. Phys. Commun.*, 222:327–338, 2018.

[286] Genevieve Belanger, Ali Mjallal, and Alexander Pukhov. Recasting direct detection limits within micrOMEGAs and implication for non-standard Dark Matter scenarios. 2020.

[287] M. Tanabashi et al. Review of Particle Physics. *Phys. Rev.*, D98(3):030001, 2018.

[288] Sabine Kraml, Tran Quang Loc, Dao Thi Nhung, and Le Duc Ninh. Constraining new physics from Higgs measurements with Lilith: update to LHC Run 2 results. *SciPost Phys.*, 7(4):052, 2019.

[289] Modified SARAH-SPheno code for the Dirac Gaugino model including neutralino/chargino decays to pions, July 2020.

[290] C.H. Chen, Manuel Drees, and J.F. Gunion. A Nonstandard string / SUSY scenario and its phenomenological implications. *Phys. Rev. D*, 55:330–347, 1997. [Erratum: Phys.Rev.D 60, 039901 (1999)].

[291] Johann H. Kuhn and A. Santamaria. Tau decays to pions. *Z. Phys. C*, 48:445–452, 1990.

[292] C.H. Chen, Manuel Drees, and J.F. Gunion. Addendum/erratum for 'searching for invisible and almost invisible particles at e^+e^- colliders' [hep-ph/9512230] and 'a nonstandard string/SUSY scenario and its phenomenological implications' [hep-ph/9607421]. 2 1999.

[293] Federico Ambrogi, Juhi Dutta, Jan Heisig, Sabine Kraml, Suchita Kulkarni, Ursula Laa, Andre Lessa, Philipp Neuhuber, Humberto Reyes-González, Wolfgang Waltenberger, and Matthias Wolf. SModelS v1.2: long-lived particles, combination of signal regions, and other novelties. 2018.

[294] Georges Aad et al. Search for chargino-neutralino production with mass splittings near the electroweak scale in three-lepton final states in $\sqrt{s} = 13$ TeV pp collisions with the ATLAS detector. *Phys. Rev. D*, 101(7):072001, 2020.

[295] Georges Aad et al. Search for direct production of electroweakinos in final states with one lepton, missing transverse momentum and a Higgs boson decaying into two b-jets in (pp) collisions at $\sqrt{s} = 13$ TeV with the ATLAS detector. 2019.

[296] Georges Aad et al. Search for electroweak production of charginos and sleptons decaying into final states with two leptons and missing transverse momentum in $\sqrt{s} = 13$ TeV pp collisions using the ATLAS detector. *Eur. Phys. J.*, C80(2):123, 2020.

[297] A. M. Sirunyan et al. Combined search for electroweak production of charginos and neutralinos in proton-proton collisions at $\sqrt{s} = 13$ TeV. *JHEP*, 03:160, 2018.

[298] Benjamin Fuks and Subhadeep Mondal. MadAnalysis 5 implementation of the CMS search for supersymmetry in the multilepton channel with 35.9 fb^{-1} of 13 TeV LHC data (CMS-SUS-16-039). 10.7484/INSPIREHEP.DATA.HE48.D9HD.1, 2018.

[299] Benjamin Fuks. Re-implementation of the soft lepton + missing energy analysis of CMS (35.9 fb^{-1}; CMS-SUS-16-048). DOI:10.14428/DVN/YA8E9V, 2020.

[300] Mark Goodsell. MadAnalysis 5 implementation of the ATLAS search for electroweakinos in $1\,\mathrm{lepton} + \mathrm{H}(\to \mathrm{b}\bar{\mathrm{b}}) + \mathrm{E}_{\mathrm{T}}^{\mathrm{miss}}$ final states with 139 fb^{-1} of 13 TeV LHC data (ATLAS-SUSY-2019-08), 2020. awaiting DOI ....

[301] Eric Conte, Béranger Dumont, Benjamin Fuks, and Chris Wymant. Designing and recasting LHC analyses with MadAnalysis 5. *Eur. Phys. J.*, C74(10):3103, 2014.

[302] A. M. Sirunyan et al. Search for electroweak production of charginos and neutralinos in multilepton final states in proton-proton collisions at $\sqrt{s} = 13$ TeV. *JHEP*, 03:166, 2018.

[303] Albert M Sirunyan et al. Search for new physics in events with two soft oppositely charged leptons and missing transverse momentum in proton-proton collisions at $\sqrt{s} = 13$ TeV. *Phys. Lett. B*, 782:440–467, 2018.

[304] Johan Alwall, Claude Duhr, Benjamin Fuks, Olivier Mattelaer, Deniz Gizem Öztürk, and Chia-Hsien Shen. Computing decay rates for new physics theories with FeynRules and MadGraph5_aMC@NLO. *Comput. Phys. Commun.*, 197:312–323, 2015.

[305] 2018.

[306] 2018.

[307] Albert M Sirunyan et al. Search for disappearing tracks in proton-proton collisions at $\sqrt{s} = 13$ TeV. *Phys. Lett. B*, 806:135502, 2020.

[308] Sergey Alekhin et al. A facility to Search for Hidden Particles at the CERN SPS: the SHiP physics case. *Rept. Prog. Phys.*, 79(12):124201, 2016.

[309] Morad Aaboud et al. Search for chargino-neutralino production using recursive jigsaw reconstruction in final states with two or three charged leptons in proton-proton collisions at $\sqrt{s} = 13$ TeV with the ATLAS detector. *Phys. Rev. D*, 98(9):092012, 2018.

[310] 2020.

[311] Juhi Dutta, Sabine Kraml, Andre Lessa, and Wolfgang Waltenberger. SModelS extension with the CMS supersymmetry search results from Run 2. *LHEP*, 1(1):5–12, 2018.

[312] Morad Aaboud et al. Search for squarks and gluinos in final states with jets and missing transverse momentum at $\sqrt{s} = 13$ TeV with the ATLAS detector. *Eur. Phys. J.*, C76(7):392, 2016.

[313] Albert M Sirunyan et al. Search for top squarks and dark matter particles in opposite-charge dilepton final states at $\sqrt{s} = 13$ TeV. *Phys. Rev.*, D97(3):032009, 2018.

[314] Neil D. Christensen, Priscila de Aquino, Celine Degrande, Claude Duhr, Benjamin Fuks, Michel Herquet, Fabio Maltoni, and Steffen Schumann. A Comprehensive approach to new physics simulations. *Eur. Phys. J.*, C71:1541, 2011.

[315] Peter Z. Skands et al. SUSY Les Houches accord: Interfacing SUSY spectrum calculators, decay packages, and event generators. *JHEP*, 07:036, 2004.

[316] Andy Buckley, Benjamin Fuks, Humberto Reyes-González, Wolfgang Waltenberger, and Sophie Williamson. Complementary data for LH2019 contribution 'Determination of Independent Signal Regions in LHC Searches for New Physics'. https://doi.org/10.5281/zenodo.3634740, February 2020.

[317] Anja Butter, Tilman Plehn, and Ramon Winterhalder. How to GAN LHC Events. *SciPost Phys.*, 7(6):075, 2019.

[318] Anja Butter, Tilman Plehn, and Ramon Winterhalder. How to GAN Event Subtraction. 12 2019.

[319] Marco Bellagente, Anja Butter, Gregor Kasieczka, Tilman Plehn, and Ramon Winterhalder. How to GAN away Detector Effects. *SciPost Phys.*, 8(4):070, 2020.

[320] Sydney Otten, Sascha Caron, Wieske de Swart, Melissa van Beekveld, Luc Hendriks, Caspar van Leeuwen, Damian Podareanu, Roberto Ruiz de Austri, and Rob Verheyen. Event generation and statistical sampling for physics with deep generative models and a density information buffer, 2019.

[321] Bobak Hashemi, Nick Amin, Kaustuv Datta, Dominick Olivito, and Maurizio Pierini. LHC analysis-specific datasets with Generative Adversarial Networks. 2019, arXiv:1901.05282.

[322] Riccardo Di Sipio, Michele Faucci Giannelli, Sana Ketabchi Haghighat, and Serena Palazzo. DijetGAN: A Generative-Adversarial Network Approach for the Simulation of QCD Dijet Events at the LHC. *JHEP*, 08:110, 2020.

[323] Anja Butter and Tilman Plehn. Generative Networks for LHC events. 8 2020.

[324] Richard D. Ball et al. Parton distributions for the LHC Run II. *JHEP*, 04:040, 2015.

[325] Andrew J. Larkoski, Ian Moult, and Benjamin Nachman. Jet Substructure at the Large Hadron Collider: A Review of Recent Advances in Theory and Machine Learning. 2017.

[326] Anja Butter et al. The Machine Learning Landscape of Top Taggers. *SciPost Phys.*, 7:014, 2019.

[327] Johann Brehmer, Kyle Cranmer, Gilles Louppe, and Juan Pavez. Constraining Effective Field Theories with Machine Learning. *Phys. Rev. Lett.*, 121(11):111801, 2018.

[328] Andrea Coccaro, Maurizio Pierini, Luca Silvestrini, and Riccardo Torre. The DNNLikelihood: enhancing likelihood distribution with Deep Learning. arXiv:1911.03305, 2019.

[329] Benjamin Nachman. A guide for deploying Deep Learning in LHC searches: How to achieve optimality and account for uncertainty. *SciPost Phys.*, 8:090, 2020.

[330] Sascha Caron, Tom Heskes, Sydney Otten, and Bob Stienen. Constraining the Parameters of High-Dimensional Models with Active Learning. *Eur. Phys. J.*, C79(11):944, 2019.

[331] Yarin Gal and Zoubin Ghahramani. Dropout as a bayesian approximation: Representing model uncertainty in deep learning. arXiv:1506.02142, 2015.

[332] F. Pedregosa, G. Varoquaux, A. Gramfort, V. Michel, B. Thirion, O. Grisel, M. Blondel, P. Prettenhofer, R. Weiss, V. Dubourg, J. Vanderplas, A. Passos, D. Cournapeau, M. Brucher, M. Perrot, and E. Duchesnay. Scikit-learn: Machine learning in Python. *Journal of Machine Learning Research*, 12:2825–2830, 2011.

[333] `https://scikit-learn.org/stable/modules/model_persistence.html`.

[334] Yann LeCun and Corinna Cortes. MNIST handwritten digit database. http://yann.lecun.com/exdb/mnist/, 2010.

[335] Andrea Dal Pozzolo, Olivier Caelen, A. Johnson Reid, and Gianluca Bontempi. Calibrating probability with undersampling for unbalanced classification. *Symposium on Computational Intelligence and Data Mining (CIDM), IEEE*, 2015.

[336] Faruk Diblen, Jisk Attema, Rena Bakhshi, Sascha Caron, Luc Hendriks, and Bob Stienen. spot: Open source framework for scientific data repository and interactive visualization. *SoftwareX*, 9:328–331, Jan 2019.

[337] Michael Bridges, Kyle Cranmer, Farhan Feroz, Mike Hobson, Roberto Ruiz de Austri, and Roberto Trotta. A Coverage Study of the CMSSM Based on ATLAS Sensitivity Using Fast Neural Networks Techniques. *JHEP*, 03:012, 2011.

[338] A. Buckley, A. Shilton, and M. J. White. Fast supersymmetry phenomenology at the Large Hadron Collider using machine learning techniques. *Comput. Phys. Commun.*, 183:960–970, 2012.

[339] Philip Bechtle, Sebastian Belkner, Daniel Dercks, Matthias Hamer, Tim Keller, Michael Krämer, Björn Sarrazin, Jan Schütte-Engel, and Jamie Tattersall. SCYNet: Testing supersymmetric models at the LHC with neural networks. *Eur. Phys. J.*, C77(10):707, 2017.

[340] Sydney Otten, Krzysztof Rolbiecki, Sascha Caron, Jong-Soo Kim, Roberto Ruiz De Austri, and Jamie Tattersall. DeepXS: Fast approximation of MSSM electroweak cross sections at NLO. *Eur. Phys. J.*, C80(1):12, 2020.

[341] W. Beenakker, R. Hopker, and M. Spira. PROSPINO: A Program for the production of supersymmetric particles in next-to-leading order QCD. arXiv:hep-ph/9611232, 1996.

[342] Anders Kvellestad, Steffen Maeland, and Inga Strümke. Signal mixture estimation for degenerate heavy Higgses using a deep neural network. *Eur. Phys. J.*, C78(12):1010, 2018.

[343] Sven Bollweg, Manuel Haussmann, Gregor Kasieczka, Michel Luchmann, Tilman Plehn, and Jennifer Thompson. Deep-Learning Jets with Uncertainties and More. *SciPost Phys.*, 8(1):006, 2020.

[344] Gregor Kasieczka, Michel Luchmann, Florian Otterpohl, and Tilman Plehn. Per-Object Systematics using Deep-Learned Calibration. 3 2020.

[345] Gianfranco Bertone, Marc Peter Deisenroth, Jong Soo Kim, Sebastian Liem, Roberto Ruiz de Austri, and Max Welling. Accelerating the BSM interpretation of LHC data with machine learning. *Phys. Dark Univ.*, 24:100293, 2019.

[346] Gianfranco Bertone, Nassim Bozorgnia, Jong Soo Kim, Sebastian Liem, Christopher McCabe, Sydney Otten, and Roberto Ruiz de Austri. Identifying WIMP dark matter from particle and astroparticle data. *JCAP*, 1803:026, 2018.

[347] Gregor Kasieczka, Tilman Plehn, Jennifer Thompson, and Michael Russel. Top quark tagging reference dataset, March 2019.

[348] Q. R. Ahmad et al. Direct evidence for neutrino flavor transformation from neutral current interactions in the Sudbury Neutrino Observatory. *Phys. Rev. Lett.*, 89:011301, 2002.

[349] Y. Ashie et al. A Measurement of atmospheric neutrino oscillation parameters by SUPER-KAMIOKANDE I. *Phys. Rev.*, D71:112005, 2005.

[350] Ernest Ma. Pathways to naturally small neutrino masses. *Phys. Rev. Lett.*, 81:1171–1174, 1998.

[351] Yi Cai, Juan Herrero-Garcia, Michael A. Schmidt, Avelino Vicente, and Raymond R. Volkas. From the trees to the forest: a review of radiative neutrino mass models. *Front.in Phys.*, 5:63, 2017.

[352] Yi Cai, Tao Han, Tong Li, and Richard Ruiz. Lepton Number Violation: Seesaw Models and Their Collider Tests. *Front.in Phys.*, 6:40, 2018.

[353] A. Abada et al. FCC-hh: The Hadron Collider. *Eur. Phys. J. ST*, 228(4):755–1107, 2019.

[354] A. Abada et al. HE-LHC: The High-Energy Large Hadron Collider. *Eur. Phys. J. ST*, 228(5):1109–1382, 2019.

[355] Jogesh C. Pati and Abdus Salam. Lepton Number as the Fourth Color. *Phys. Rev.*, D10:275–289, 1974. [Erratum: Phys. Rev.D11,703(1975)].

[356] Rabindra N. Mohapatra and Jogesh C. Pati. Left-Right Gauge Symmetry and an Isoconjugate Model of CP Violation. *Phys. Rev.*, D11:566–571, 1975.

[357] R. N. Mohapatra and Jogesh C. Pati. A Natural Left-Right Symmetry. *Phys. Rev.*, D11:2558, 1975.

[358] G. Senjanovic and Rabindra N. Mohapatra. Exact Left-Right Symmetry and Spontaneous Violation of Parity. *Phys. Rev.*, D12:1502, 1975.

[359] Goran Senjanovic. Spontaneous Breakdown of Parity in a Class of Gauge Theories. *Nucl. Phys.*, B153:334–364, 1979.

[360] Wai-Yee Keung and Goran Senjanovic. Majorana Neutrinos and the Production of the Right-handed Charged Gauge Boson. *Phys. Rev. Lett.*, 50:1427, 1983.

[361] Richard Ruiz. Lepton Number Violation at Colliders from Kinematically Inaccessible Gauge Bosons. *Eur. Phys. J.*, C77(6):375, 2017.

[362] Miha Nemevsek, Fabrizio Nesti, and Goran Popara. Keung-Senjanovic process at the LHC: From lepton number violation to displaced vertices to invisible decays. *Phys. Rev.*, D97(11):115018, 2018.

[363] Giovanna Cottin, Juan Carlos Helo, and Martin Hirsch. Searches for light sterile neutrinos with multitrack displaced vertices. *Phys. Rev.*, D97(5):055025, 2018.

[364] Manimala Mitra, Richard Ruiz, Darren J. Scott, and Michael Spannowsky. Neutrino Jets from High-Mass W_R Gauge Bosons in TeV-Scale Left-Right Symmetric Models. *Phys. Rev.*, D94(9):095016, 2016.

[365] Olivier Mattelaer, Manimala Mitra, and Richard Ruiz. Automated Neutrino Jet and Top Jet Predictions at Next-to-Leading-Order with Parton Shower Matching in Effective Left-Right Symmetric Models. arXiv:1610.08985, 2016.

[366] Valerio Bertone, Stefano Carrazza, Nathan P. Hartland, and Juan Rojo. Illuminating the photon content of the proton within a global PDF analysis. *SciPost Phys.*, 5(1):008, 2018.

[367] Pierre Artoisenet, Rikkert Frederix, Olivier Mattelaer, and Robbert Rietkerk. Automatic spin-entangled decays of heavy resonances in Monte Carlo simulations. *JHEP*, 03:015, 2013.

[368] Yoshua Bengio and Yann LeCun, editors. *4th International Conference on Learning Representations, ICLR 2016, San Juan, Puerto Rico, May 2-4, 2016, Conference Track Proceedings*, 2016.

[369] Genevieve Belanger, Beranger Dumont, Andreas Goudelis, Bjorn Herrmann, Sabine Kraml, and Dipan Sengupta. Dilepton constraints in the Inert Doublet Model from Run 1 of the LHC. *Phys. Rev.*, D91(11):115011, 2015.

[370] D. Bellhouse. Area estimation by point-counting techniques. *Biometrics 37*, no. 2:303–312, 1981.

[371] A. Goudelis, B. Herrmann, and O. Stål. Dark matter in the Inert Doublet Model after the discovery of a Higgs-like boson at the LHC. *JHEP*, 09:106, 2013.

[372] Evgenii Tsymbalov, Maxim Panov, and Alexander Shapeev. Dropout-based active learning for regression. *Analysis of Images, Social Networks and Texts*, pages 247–258, 2018.

[373] Peter Athron et al. Status of the scalar singlet dark matter model. *Eur. Phys. J.*, C77(8):568, 2017.

[374] Peter Athron et al. Global fits of GUT-scale SUSY models with GAMBIT. *Eur. Phys. J.*, C77(12):824, 2017.

[375] Peter Athron et al. A global fit of the MSSM with GAMBIT. *Eur. Phys. J.*, C77(12):879, 2017.

[376] Peter Athron, Jonathan M. Cornell, Felix Kahlhoefer, James Mckay, Pat Scott, and Sebastian Wild. Impact of vacuum stability, perturbativity and XENON1T on global fits of $\mathbb{Z}_2$ and $\mathbb{Z}_3$ scalar singlet dark matter. *Eur. Phys. J.*, C78(10):830, 2018.

[377] Peter Athron et al. Global analyses of Higgs portal singlet dark matter models using GAMBIT. *Eur. Phys. J.*, C79(1):38, 2019.

[378] Peter Athron et al. Combined collider constraints on neutralinos and charginos. *Eur. Phys. J.*, C79(5):395, 2019.

[379] Sebastian Hoof, Felix Kahlhoefer, Pat Scott, Christoph Weniger, and Martin White. Axion global fits with Peccei-Quinn symmetry breaking before inflation using GAMBIT. *JHEP*, 03:191, 2019. [Erratum: JHEP11,099(2019)].

[380] Marcin Chrzaszcz, Marco Drewes, Tomás E. Gonzalo, Julia Harz, Suraj Krishnamurthy, and Christoph Weniger. A frequentist analysis of three right-handed neutrinos with GAMBIT. arXiv:1908.02302, 2019.

[381] Diederik P. Kingma and Jimmy Ba. Adam: A Method for Stochastic Optimization. *arXiv e-prints*, page arXiv:1412.6980, Dec 2014.

Abstract. The ATLAS and CMS collaborations has been putting forward an extensive program of searches for new physics, aiming to cover new physics theories as much as possible. The results of these searches are typically interpreted in the context of popular models or simplified model topologies. However, there exist a plethora of non-minimal, non-standard or less-known BSM theories and scenarios that are not directly covered by the experimental analyses. Thus, the importance of a framework of LHC reinterpretation to test any of such beyond vanilla theories. Is within this spirit that this thesis unfolds. It concerns two aspects: phenomenology of beyond vanilla new physics and the further development of dedicated tools.

On the tools development side, we describe recent developments of the `SModelS` package, a tool for interpreting simplified models results from the LHC. Furthermore, we present a new tool to determine if signal regions from different analyses are statistically independent from each other and hence, can be trivially combined. On the phenomenological side, we explore the collider phenomenology of a very interesting alternative to the Minimal Supersymmetric Standard Model: The Minimal Dirac Gaugino Supersymmetric Standard Model (MDGSSM). First, we derive current LHC limits on the gluinos and squarks of the model. Second, we delimit the parameter space of the MDGSSM electroweakino sector where the lightest neutralino is a viable DM candidate, to then constrain the emerging scenarios on the light of supersymmetry and long lived particle searches.

Finally, this thesis also regards machine learning (ML) applications to HEP phenomenology. Among other examples, we present a neural network to accurately predict, with an estimated uncertainty, the production cross sections of the inert doublet model. Furthermore, we discuss the importance of providing uncertainties on ML predictions and provide recommendations for sharing all the material involved in the production of ML applications.

Résumé. Les collaborations ATLAS et CMS proposent un vaste programme de recherche de nouvelle physique, visant à couvrir autant que possible les théories de la nouvelle physique. Les résultats de ces recherches sont généralement interprétés dans le contexte de modèles populaires ou de topologies des modèles simplifiées. Cependant, il existe une pléthore de théories et de scénarios BSM non minimales, non standard ou moins connues qui ne sont pas directement couverts par les analyses expérimentales. Ainsi, l'importance d'un cadre de réinterprétation du LHC pour tester ces théories au-delà de la nouvelle physique standard. C'est dans cet esprit que se déroule cette thèse. Il considère deux aspects: la phénoménologie et le développement d'outils dédiés.

En concernant le développement d'outils, nous décrivons les développements récents de l'outil de réinterprétation `SModelS`, un outil d'interprétation des résultats des modèles simplifiés du LHC De plus, nous présentons un noveau outil pour déterminer si les régions de signal de différentes analyses sont statistiquement indépendantes les unes des autres et, par conséquent, peuvent être combinées de manière triviale. Sur l'aspect phénoménologique, nous explorons la phénoménologie aux collisionneurs d'une théorie au-delà de la nouvelle physique standard très intéressante: le modèle minimal avec gauginos de Dirac (MDGSSM). Dans un premier temps, nous dérivons des limites de courant sur les gluinos et les squarks du modèle. Dans une deuxième étude, nous délimitons l'espace des paramètres du secteur électroweakino du MDGSSM où le neutralino le plus léger est un candidat à la matière noire viable, suivi par la contrainte des scénarios émergents à la lumière des recherches de supersymétrie et de particules à vie longue.

Finalement, cette thèse concerne également les applications d'apprentissage automatique à la phénoménologie HEP. Entre autres exemples, nous présentons un réseau neuronal pour prédire avec précision, et avec une incertitude estimée, les sections efficaces de production du modèle de doublet inerte. En outre, nous discutons de l'importance de fournir des incertitudes sur les prédictions des modèles ML et formulons des recommandations pour partager tout le matériel impliqué dans la production des applications de ML.